Where Tori Fear to Tread: Hypermassive Neutron Star Remnants and Absolute Event Horizons
or
Topics in Computational General Relativity

Thesis by

Jeffrey Daniel Kaplan

In Partial Fulfillment of the Requirements

for the Degree of

Doctor of Philosophy

California Institute of Technology

Pasadena, California

2014

(Defended July 1, 2013)

To my family

Acknowledgements

First I thank my advisor Christian Ott for his time, advising, and support (moral *and* grant related). Particularly his pushing me to 'just get stuff done' in the face of challenges and technical difficulties (yes, even debugging `fortran-77` code). I can say with certainty that learning to do this will be one of the most valuable things I've learned during my time spent at Caltech.

I do not think I could have made it through graduate school without the friendships I developed here at Caltech. Peter Brooks, Jeff Flanigan, Kari Hodge, Richard Norte and Steven Privitera, your support have made these six long years bearable, sometimes even enjoyable. Although far from Pasadena, Peter Chung, Tony Evans, Kristen Jones Unger, Vivian Leung, Erin and Brian Favia and Zoe Mindell were always available when I needed someone to listen. Speaking of always available, thanks to the folks over at `#casualteam`; okay you were probably somewhat of a distraction, but you were perhaps a necessary one.

Thank you to my research collaborators and TAPIR group members: Mike Cohen, Tony Chu, David Nichols, Fan Zhang, Kristen Boydstun, Yi-Chen Hu, Iryna Butsky, John Wendell, Sarah Gossan, Huan Yang, Francois Foucart, Curran Muhlberger, Dan Hemberger, Roland Haas, Mark Scheel, Béla Szilágyi, Andrew Benson, and Professors Kip Thorne, Yanbei Chen, Saul Teukolsky, and Matt Duez. It was a humbling experience to work with so many brilliant people. It may be a long time before I fully appreciate how privileged I was to be able to converse and conduct research with all of you. I want to give a special thanks to the co-authors of the thermal support paper: Christian Ott, Evan O'Connor, Kenta Kiuchi, Luke Roberts and Matt Duez; I appreciated your fast turn around on comments for the paper. Evan O'Connor, thank you for being such a damn good person and officemate. Although you may deny it, your support and companionship was essential to my sanity. The same goes for Aaron Zimmerman; (though not my officemate) your constant availability and our conversations during the past six months of 'thesis crunch' have been invaluable.

Finally, thank you to my family, to whom I dedicate this thesis. To my siblings (old), Jess, (and new) Rob and Amber. To my aunts and uncles, Fran, Mike, Janet, and Rob. To my grandparents, Jaclyn, Louis, Clara and Phil. And to the Westlund family tree. And saving the best for last, to my mother and father, Deborah and David. You all have made an *essential* contribution to my thesis through your nurturing, love, support, advice and inspiration. I love you.

Abstract

Computational general relativity is a field of study which has reached maturity only within the last decade. This thesis details several studies that elucidate phenomena related to the coalescence of compact object binaries. Chapters 2 and 3 recounts work towards developing new analytical tools for visualizing and reasoning about dynamics in strongly curved spacetimes. In both studies, the results employ analogies with the classical theory of electricity and magnetism, first (Ch. 2) in the post-Newtonian approximation to general relativity and then (Ch. 3) in full general relativity though in the absence of matter sources. In Chapter 4, we examine the topological structure of absolute event horizons during binary black hole merger simulations conducted with the `SpEC` code. Chapter 6 reports on the progress of the `SpEC` code in simulating the coalescence of neutron star-neutron star binaries, while Chapter 7 tests the effects of various numerical gauge conditions on the robustness of black hole formation from stellar collapse in `SpEC`. In Chapter 5, we examine the nature of pseudospectral expansions of non-smooth functions motivated by the need to simulate the stellar surface in Chapters 6 and 7. In Chapter 8, we study how thermal effects in the nuclear equation of state effect the equilibria and stability of hypermassive neutron stars. Chapter 9 presents supplements to the work in Chapter 8, including an examination of the stability question raised in Chapter 8 in greater mathematical detail.

Contents

Acknowledgements **iv**

Abstract **v**

1 Overview and historical summary **1**

1.1 Introduction 1

1.2 Re: The Title *or* A Literary Aside 1

1.3 Summary 2

1.3.1 Early work 2

1.3.2 Intermediate work: EH No Tori 3

1.3.3 `SpEC-hydro` work 4

1.3.4 On thermal effects in hypermassive neutron stars 5

I Work in (a) vacuum **7**

2 Post-Newtonian Approximation in Maxwell-Like Form **8**

2.1 Introduction 8

2.2 The DSX Maxwell-Like Formulation of 1PN Theory 10

2.3 Specialization to a Perfect Fluid 12

2.4 Momentum Density, Flux, and Conservation 13

2.5 Energy Conservation 15

2.6 Gravitational Potentials in the Vacuum of a System of Compact, Spinning Bodies . . 16

2.7 Conclusion 17

3 Frame-Dragging Vortexes and Tidal Tendexes Attached to Colliding Black Holes: Visualizing the Curvature of Spacetime **21**

3.1 Introduction 21

3.2 Vortexes and Tendexes in Black-Hole Horizons 22

3.3 3D vortex and tendex lines 23

3.4 Vortex and Tendex Evolutions in Binary Black Holes 24
3.5 Conclusions 27

4 On Toroidal Horizons in Binary Black Hole Inspirals 31
4.1 Introduction 31
4.2 Identification of Crossover Points 33
4.3 Event horizons from numerical simulations of binary black hole mergers 36
4.4 Topological structure of the Event Horizon for inspiraling and merging black holes . 38
4.5 Topological Structure of Simulated Event Horizons 43
4.5.1 Equal-mass non-spinning merger 44
4.5.2 2:1 mass ratio with 'randomly' oriented spins 46
4.5.2.1 Pre-merger: $t = 124.200M^*$ 47
4.5.2.2 Merger: $t = 124.355M^*$ 49
4.5.2.3 Post-merger: $t = 124.400M^*$ 49
4.5.3 Discussion on the numerical analysis of topological features 53
4.6 Conclusion 53

II Work with [that] matter[s] 58

5 Behavior of Pseudospectral Coefficients in the Presence of a Non-smoothness 59
5.1 Motivation 59
5.2 Preliminaries and theoretical background 60
5.2.1 Expected convergence of the metric at the stellar surface 60
5.2.2 The 'pseudo' in pseudospectral methods 61
5.2.3 Measures of the truncation error 62
5.3 Methods 62
5.4 Results 63
5.5 Discussion and concluding remarks 65

6 Simulations of neutron star-neutron star inspirals with `SpEC` 70
6.1 Introduction 70
6.1.1 NSNS coalescence and gravitational waves 70
6.1.2 Short gamma-ray bursts and other electromagnetic counterparts 73
6.1.3 `SpEC` 73
6.2 Methods and initial data 74
6.2.1 Code details 74
6.2.2 Initial data 76

6.3 Results . . . 77
6.4 Discussion and conclusions . . . 79

7 Black hole formation from isolated neutron stars in SpEC 86
7.1 Literature review and introduction . . . 86
7.2 Methods and numerical setup . . . 87
7.2.1 Hydrodynamics grid . . . 87
7.2.2 Spectral grid and methods . . . 88
7.2.3 Time evolution and grid-to-grid communication . . . 88
7.2.4 Equation of state . . . 89
7.2.5 Hydrodynamic evolution equations . . . 89
7.2.6 Generalized harmonic equations . . . 91
7.2.7 Excision of nascent black hole . . . 91
7.3 Gauge equations, conditions, and methods . . . 92
7.3.1 Harmonic and generalized harmonic gauge . . . 92
7.3.2 Damped harmonic gauge for numerical evolutions . . . 93
7.3.3 Imposing damped harmonic gauge in SpEC simulations . . . 94
7.4 Initial Models and physical setup . . . 95
7.4.1 Methods . . . 95
7.4.2 Models . . . 96
7.4.3 Code parameters . . . 96
7.5 Results and discussion . . . 96
7.A Plots documenting the robustness of the simulations . . . 99
7.A.1 Convergence of simulations . . . 99
7.A.2 Gravitational waves from collapse . . . 99
7.B Definition of the 3-Velocity . . . 99
7.C Resolving the constraint equations . . . 102

8 The Influence of Thermal Pressure on Hypermassive Neutron Star Merger Remnants 107
8.1 Introduction . . . 108
8.2 Methods and Equations of State . . . 110
8.2.1 Equations of State . . . 110
8.2.2 Temperature and Composition Parametrizations . . . 115
8.2.3 Spherically Symmetric Equilibrium Models . . . 117
8.2.4 Axisymmetric Equilibrium Models . . . 117
8.3 Results: Spherically Symmetric Models . . . 119

8.4 Results: Axisymmetric Models in Rotational Equilibrium 123
8.4.1 Uniformly Rotating Configurations 123
8.4.2 Differentially Rotating Configurations 125
8.5 Discussion and comparison with 3D NSNS simulations 130
8.5.1 The Stability of HMNS Equilibrium Sequences 130
8.5.2 The Secular Evolution of HMNS from Mergers 132
8.5.3 Comparison with NSNS Merger Simulations 134
8.6 Summary and Conclusions 138
8.A Temperature Parametrizations 141
8.B Solving for the Electron Fraction 143

9 Supplements to The Influence of Thermal Pressure on Hypermassive Neutron Star Merger Remnants 150

9.1 Expanded discussion on the stability of HMNS equilibrium sequences 150
9.1.1 Review on established applications of the turning-point method to neutron star stability 150
9.1.2 Applying the turning-point method in more general cases 153
9.1.3 Approximate turning points for alternate tuples of conserved quantities 155
9.2 Properties of quasitoroidal models 156
9.2.1 Criterion which implies a model must be quasitoroidal 156
9.2.2 The fluid element at $\rho_{\mathrm{b,max}}$ is freely falling. 158
9.2.3 Maximum of the centrifugal support with differential rotation 158
9.3 Changes in energy and density of a configuration 159
9.4 Relation of average density to mass-shed centrifugal support 160
9.5 Newtonian estimate of angular momentum at coalescence 161

Chapter 1

Overview and historical summary

1.1 Introduction

The content of this thesis contains chapters of two different natures, both with the goal of summarizing the research I have accomplished during my time as a graduate student in the TAPIR (Theoretical AstroPhysics Including Relativity) group. One kind consists of works published or recently submitted for publication to which I have made a significant contribution: Chapters 2, 3, 4, and 8. These works are reproduced in their entirety, and my specific role in these works will be detailed here in Chapter 1. The other style of chapter contains work which is unpublished or unfinished work, involving the `SpEC-hydro` numerical relativity code (Chapters 5, 6 and 7). The primary goal of these chapters is to not only showcase the scientific results of this work, but also to document it so that `SpEC-hydro` researchers have a record of the numerical experiments I have conducted. Finally, Chapter 9 contains supplementary materials to the paper reproduced in Chapter 8.

The style of this overview chapter will be somewhat in in the form of a historical overview, as this will assist in detailing the specific contributions I have made to each work. It will also give me the chance to mention some non-scientific contributions which I feel have had a significant impact on the SXS collaboration.

1.2 Re: The Title *or* A Literary Aside

Though unconventional, the title of this thesis is appropriate on several levels. *Tori* is the plural of torus which is the mathematical term for a 'donut' shape; formally it defines a topology which is homeomorphic to the Cartesian product of two circles, $S^1 \times S^1$. In Chapter 4, we study the topological structure of event horizons in binary black hole mergers, and find no evidence for a toroidal (donut) shape. Chapter 8 examines equilibrium configurations of hypermassive neutron star remnants. Here, our investigations originally led us to believe that the enhancement seen

in the masses of these stellar configurations, due to differential rotation, was related to the stars beginning to take on a toroidal-like shape; these shapes, which look somewhat like that of a red-blood cell, are referred to as *quasitoroidal*. However, after further investigation, we found quasitoroidal morphologies to be astrophysically unrealistic configurations and not of great relevance to our study. Hence, I've happened to conduct numerical studies of compact objects "Where Tori Fear to Tread."

Additionally, the phrase is a reference to the famous line of the the poem *An Essay on Criticism* by Alexander Pope: "For fools rush in where angels fear to tread." The verse is a parable noting that the naive will often venture into situations that shrewd and more experienced will avoid. Directly applied to the studies I've conducted, this line could be twisted into the statement: "A fool may rush to the conclusion that toroidal shapes are significant to these topics; however a thorough investigation has revealed that tori are unimportant here." However, I find the verse's meaning to be personally significant as the parable represents perhaps the most important lesson I have learned during my graduate studies, that of the intrinsic value of experience. For me, this lesson takes many forms, one of which is the understanding that the hard work invested into tasks and projects which do not pan out is not wasted. Instead, such labor has intrinsic value in the experience it provides. The unstructured nature and long duration of graduate study is, essentially, for gaining experience in accomplishing tasks at the cutting edge of human knowledge. While many tasks and investigations in research may seem futile, pointless, or without motivation, perhaps such unstructured study is the only manner in which to prepare one for the task of uncovering new knowledge.

So I suppose it's a good thing I went grad school, otherwise I'd be going around with the foolish impression that the outcome of compact object coalescence is some sort of toroidal structure...

1.3 Summary

1.3.1 Early work

My initial work in the TAPIR group consisted of research led by Kip Thorne and Yanbei Chen in developing methods of visualizing and understanding the spacetimes observed in numerical simulations of binary black hole mergers. The first approach to this involved using gauge dependent local measures of gravitational field energy and momentum, along with their respective integral conservation laws in an attempt to understand the dynamics of merging binary black holes. Chapter 2, originally published as [2] is a particular formulation of the post-Newtonian approximation in a form designed to resemble Maxwell's equations in form and function. It was conceived and first organized by Kip Throne; David Nichols and I repeated and refined Kip's calculations, and I presented the work at the April 2009 meeting of the American Physical Society.

I was also an author on the paper *Momentum flow in black-hole binaries. II. Numerical simulations of equal-mass, head-on mergers with antiparallel spins* [3], which is not reproduced in this

thesis. For this work, I was trained by Michael Cohen on the use of the event horizon finder which he wrote for the `SpEC` code. For the work, I calculated the event horizon for the `SpEC` head-on, anti-aligned spinning binary black hole merger simulated by Geoffrey Lovelace, as well as assisted in calculating the surface integral of field momentum over the event horizon surface. This calculation is illustrated in Figs. 13 and 14 of the work. Additionally, since the workflow for the event horizon finder code (from initial data generation through post-processing) was very much experimental at the time, I formalized and automated the process via scripts.

Another approach developed by our collaboration is that of representing the general relativistic gravitational field in terms of *vortex and tendex lines*. Chapter 3 reproduces our collaboration's submission to Physical Review Letters [5]. Here I distinctly remember my contribution as checking the signs in the physical interpretations of the tidal and frame-drag fields (paragraph 2 of Sec. 3.1)! I also contributed to the fine-tuning of Fig. 3.2 [1], and the calculation of the event horizon surface in Fig. 3.1. The website companion pages; I did those too. Sincerely though, it was a pleasure and an honor to be a part of an analytical and numerical collaboration so talented that I could just barely keep up with their insights. Additionally, I was an author on the first in a series of follow up papers, which I have also chosen not to reproduce in this thesis [4].

1.3.2 Intermediate work: EH No Tori

Chapter 4 is a reproduction of the work published in Physical Review D entitled *On Toroidal Horizons in Binary Black Hole Inspirals* [1]. The work consisted of previously unpublished material in the thesis of Michael Cohen. The event-horizon finding code, algorithm for identification of crossover points, investigation of the equal-mass BBH merger and analysis of the generic topological structure of binary black hole mergers was done by Mike. Upon this solid foundation, my task was to examine the 'generic' BBH merger and verify that the conclusions drawn by Mike were robust. I accomplished this by calculating event horizon of the 'generic' merger for different spatial, temporal and simulation data resolutions. In addition, I thought carefully about what it would mean to resolve a topological feature of a numerical simulation. I subsequently developed a precise criterion for how one could, in principle, determine whether or not a numerically located event horizon shows evidence for the presence of a toroidal topology. Mark Scheel carefully examined our results and, as always, powered us through when code bugs became too challenging. To this date (almost two years later!), no one has found evidence for a toroidal event horizon in the slicing of their fully relativistic BBH merger simulations.

[1] particularly exciting was that this figure appeared on the cover of Physical Review Letters

1.3.3 SpEC-hydro work

In the spring of 2009, just before Christian Ott became an Assistant Professor at Caltech (at the time, he was a post-doc in the TAPIR group), he inquired if any student was interested in investigating neutron star-neutron star coalescence with the SpEC code. As a young grad student, I thought that this would be a good opportunity to use my experience with SpEC (at the time calculating event horizons) to work on research that had a wider range of astrophysical applications[2]. Later the following summer I shipped off to Cornell for a week to learn the methods of the budding SpEC-hydro code being written by Matt Duez and Francois Foucart. Conveniently enough, Curran Muhlberger had just written code to calculate NSNS initial data, and before October 2009, I was using SpEC-hydro to evolve some orbiting neutron stars. How, you might ask, did I end up in June of 2013 with no SpEC-hydro NSNS publication? Of course, there were distractions with the previously mentioned projects, and, uh... 'general grad-studentyness'. However, I'd like to think that those were not the major reasons for the difficulty in progress with NSNSs in SpEC-hydro. Here I will explain my thoughts on the issue.

(I) The coupling of shock-capturing high-resolution finite-differencing methods and pseudospectral methods proved to be more delicate than was anticipated (cf. Ch. 5 for one example): it took nearly a year after first starting the simulations to achieve inspirals which were convergent in resolution. One problem identified here was that the PPM reconstruction scheme seemed to produce gridpoint-to-gridpoint variations in the density. Once we switched to the smoother WENO reconstruction scheme, we started to make progress on the convergence issue.

(II) The development of the SpEC-hydro code rapidly diverged from many major practices in the vacuum SpEC code during its initial phases. To be frank, its development ended up somewhat rushed and without consideration for multiple users. That is, it was particularly specialized to BHNS coalescences. This issue seemed to stem from the fact that the SpEC code itself is a complex piece of software with a high learning curve. I never completely 'dove in' to the SpEC-hydro code, deconstructing it and voraciously determining its every nuance and feature. In retrospect, this is what I now feel would have been necessary to have generated more results. In an attempt to mitigate future student's reluctance to 'dive into' the SpEC code, reduce bugs and propagate best practices, I took the initiative to lead the 2011 Summer SpEC coding class. The 9 week informal video conferenced course was a success: taught by Professors and Senior Researchers, approximately 20 students across more than four universities participated with a completion rate for the optional assignments of $> 50\%$. Though this course could only scratch the surface of the SpEC code, the course materials are currently the standard for introducing new researchers to writing software for SpEC.

[2] get back to my roots, so to speak: in undergrad at Northwestern I conducted my undergraduate research in the theoretical astrophysics group under the guidance of Vicky Kalogera

(III) Communication and propagation of best practices across collaborating research groups proved difficult. For more than a year after starting the project, I was the only `SpEC-hydro` collaborator who was not at Cornell (and for slightly more than two years I was the only `SpEC-hydro` collaborator at Caltech). Additionally, those who were readily available to advise me, were primarily focused on the vacuum `SpEC` code. This meant that I was primarily assisted by those who used the same codebase, but a very different branch of the code. One step I took in order to address the communication issue was to introduce the use of issue-tracking software to the collaboration. Though the use of bug-tracking software was probably an inevitability for the collaboration, my initiative in its initial setup certainly hastened its arrival. The `trac` software I installed now has over 540 opened tickets, 420 closed tickets, and continues to be in active use by the collaboration.

(IV) Technical developments necessary for the robust simulation of NSNS coalescence needed to be accomplished. While the necessity of new technology is necessary for any experimental science, it was perhaps under-appreciated that new technical developments which were unique to the NSNS coalescence problem (i.e. not shared by the BHNS evolutions) had yet to be innovated. These included the 'dual box' regridder method, pushed by Béla Szilágyi and written by Francois Foucart. This was necessary in order to accomplish the long inspiral which is the subject of Chapter 6. Although, this subsequently required infrastructure (developed by Roland Haas) to merge the two grids into a single grid and continue evolution to black hole formation. Speaking of which, the formation of a new black hole is a good example of a phenomenon which may be present during the coalescence of two neutron stars, but is not present BHNS binaries. The technical feat of forming a new black hole in `SpEC-hydro` is the subject of Chapter 7.

1.3.4 On thermal effects in hypermassive neutron stars

In September of 2012, Christian Ott was inspired to investigate the subject of thermal pressure support in hypermassive neutron stars (HMNSs) via examining the maximum masses of neutron star equilibrium models for 'hot' temperatures ($\sim 10s$ of MeV for neutron stars) using realistic tabulated equations of state. Originally intended to be a one week investigation, I was put to the task of calculating rotating equilibrium models of HMNS using the code of Cook, Shapiro and Teukolsky. Nine months later, the study has lead to perhaps the most interesting result included in this thesis. This study is the subject of the paper reproduced in Chapter 8, which is intended for submission to The Astrophysical Journal on the same date as the submission proofs of this thesis.

One of the first aspects I noticed of the properties of equilibrium models with significant differential rotation was the correlation between very massive models with $\rho_{\rm b,max}$ around nuclear saturation density (2.7×10^{14} g/cm^3) and a *quasitoroidal* morphology of the model. While, investigations into this correlation never matured into causation, I was still able to derive a few nice analytical results regarding the properties of quasitoroidal equilibrium models (cf. Sec. 9.2). The fundamental puzzle

we were exploring was that results in the literature of 3D NSNS simulations indicated that thermal support was important in stabilizing HMNSs from gravitational collapse. However the properties of the 1D and 2D equilibrium sequences we were calculating implied that thermal effects were essentially *irrelevant* to the maximum mass supported by rotation and the nuclear equation of state. I was led to the resolution of this discrepancy through my efforts attempting to understand how one might reason about the stability of the equilibrium models we had constructed. This led me to construct sequences of constant baryonic mass models and examine a primitive version of Fig. 8.11. Figure 8.11 shows that, for varied temperatures and magnitudes of differential rotation, all constant baryonic mass equilibrium sequences reach a minimum in their energy (gravitational mass) within a small window of maximum densities. After much blank staring at the figure, I came to the realization which was to become the major result of the work: a picture of the secular evolution of HMNSs in which this density regime should mark the transition from a stable HMNS to one which is unstable to gravitational collapse. With this new framework, we were able develop a coherent picture which reconciled the results found in the literature with those of our equilibrium models; this work is discussed in Chapter 8.

Bibliography

[1] M. I. Cohen, J. D. Kaplan, and M. A. Scheel. Toroidal horizons in binary black hole inspirals. *Phys. Rev. D*, 85(2):024031, January 2012.

[2] J. D. Kaplan, D. A. Nichols, and K. S. Thorne. Post-Newtonian approximation in Maxwell-like form. *Phys. Rev. D*, 80(12):124014, December 2009.

[3] G. Lovelace, Y. Chen, M. Cohen, J. D. Kaplan, D. Keppel, K. D. Matthews, D. A. Nichols, M. A. Scheel, and U. Sperhake. Momentum flow in black-hole binaries. II. Numerical simulations of equal-mass, head-on mergers with antiparallel spins. *Phys. Rev. D*, 82(6):064031, September 2010.

[4] D. A. Nichols, R. Owen, F. Zhang, A. Zimmerman, J. Brink, Y. Chen, J. D. Kaplan, G. Lovelace, K. D. Matthews, M. A. Scheel, and K. S. Thorne. Visualizing spacetime curvature via frame-drag vortexes and tidal tendexes: General theory and weak-gravity applications. *Phys. Rev. D*, 84(12):124014, December 2011.

[5] R. Owen, J. Brink, Y. Chen, J. D. Kaplan, G. Lovelace, K. D. Matthews, D. A. Nichols, M. A. Scheel, F. Zhang, A. Zimmerman, and K. S. Thorne. Frame-Dragging Vortexes and Tidal Tendexes Attached to Colliding Black Holes: Visualizing the Curvature of Spacetime. *Physical Review Letters*, 106(15):151101, April 2011.

Part I

Work in (a) vacuum

Chapter 2

Post-Newtonian Approximation in Maxwell-Like Form

The equations of the *linearized* first post-Newtonian approximation to general relativity are often written in "gravitoelectromagnetic" Maxwell-like form, since that facilitates physical intuition. Damour, Soffel and Xu (DSX) (as a side issue in their complex but elegant papers on relativistic celestial mechanics) have expressed the first post-Newtonian approximation, *including all nonlinearities*, in Maxwell-like form. This paper summarizes that DSX Maxwell-like formalism (which is not easily extracted from their celestial mechanics papers), and then extends it to include the post-Newtonian (Landau-Lifshitz-based) gravitational momentum density, momentum flux (i.e. gravitational stress tensor) and law of momentum conservation in Maxwell-like form. The authors and their colleagues have found these Maxwell-like momentum tools useful for developing physical intuition into numerical-relativity simulations of compact binaries with spin.

Originally published as Jeffrey D. Kaplan, David A. Nichols, and Kip S. Thorne. Post-Newtonian approximation in Maxwell-like form, Phys. Rev. D 80, 124014

2.1 Introduction

In 1961, Robert L. Forward [1] (building on earlier work of Einstein [2, 3] and especially Thirring [4, 5]) wrote the *linearized, slow-motion approximation to general relativity* in a form that closely resembles Maxwell's equations; and he displayed this formulation's great intuitive and computational power. In the half century since then, this Maxwell-like formulation and variants of it have been widely explored and used; see, e.g., [6–13] and references therein.

In 1965–69 S. Chandrasekhar [14, 15] formulated the *first post-Newtonian (weak-gravity, slow-motion) approximation to general relativity* in a manner that has been widely used for astrophysical

calculations during the subsequent 40 years. When linearized, this first post-Newtonian (1PN) approximation can be (and often is) recast in Maxwell-like form.

In 1991, T. Damour, M. Soffel and C. Xu (DSX; [16]) extended this Maxwell-like 1PN formalism to include all 1PN nonlinearities (see also Sec. 13 of Jantzen, Carini and Bini [17]). DSX did so as a tool in developing a general formalism for the celestial mechanics of bodies that have arbitrary internal structures and correspondingly have external gravitational fields characterized by two infinite sets of multipole moments. (For a generalization to scalar-tensor theories, see [18].) In 2004, Racine and Flanagan [19] generalized DSX to a system of compact bodies (e.g. black holes) that have arbitrarily strong internal gravity.

During the past 18 months, we and our colleagues have been exploring the flow of gravitational field momentum in numerical-relativity simulations of compact, spinning binaries [20, 21]. In their inspiral phase, these binaries' motions and precessions can be described by the 1PN approximation,[1] and we have gained much insight into their dynamics by using the 1PN DSX Maxwell-like formalism, *extended* to include Maxwell-like momentum density, momentum flux, and momentum conservation.[2]

In this paper, we present that extension of DSX,[3] though with two specializations: (i) we fix our coordinates (gauge) to be fully harmonic instead of maintaining the partial gauge invariance of DSX, and (ii) we discard all multipole moments of the binaries' bodies except their masses and their spin angular momenta, because for black holes and neutron stars, the influences of all other moments are numerically much smaller than 1.5PN order.

The DSX celestial-mechanics papers [16, 22–24] are so long and complex that it is not easy to extract from them the bare essentials of the DSX Maxwell-like 1PN formalism. For the benefit of researchers who want those bare essentials and want to see how they are related to more conventional approaches to 1PN theory, we summarize them before presenting our momentum extension, and we do so for a general stress-energy tensor, for a perfect fluid, and for a system of compact bodies described by their masses and spins.

This paper is organized as follows: In Sec. 2.2 we summarize the basic DSX equations for 1PN theory in Maxwell-like form. In Sec. 2.3 we specialize the DSX formalism to a perfect fluid and make contact with the conventional 1PN notation. In Sec. 2.4 we extend DSX by deriving the (Landau-Lifshitz-based) density and flux of gravitational momentum in terms of the DSX gravitoelectric and gravitomagnetic fields and by writing down the law of momentum conservation in terms of them.

[1] For black-hole and neutron-star binaries, the influences of spin that interest us are formally 1PN, but because of the bodies' compactness (size of order Schwarzschild radius), they are numerically 1.5PN.

[2] A referee has pointed out to us that some papers in the rich literature on the Maxwell-like formulation of linearized 1PN theory, e.g. [10], argue that the Maxwell analogy is physically useful only for stationary phenomena. Our spinning-binary application [20] of the momentum-generalized DSX formalism is a counterexample.

[3] When we carried out our analysis and wrote it up in the original version of this paper, we were unaware of the Maxwell-like formalism in DSX [16]; see our preprint at `http://xxx.lanl.gov/abs/0808.2510v1` When we learned of DSX from Luc Blanchet, we used it to improve our Maxwell-like treatment of gravitational momentum (by replacing our definition for the gravitoelectric field by that of DSX) and we rewrote this paper to highlight the connection to DSX.

(It is this that we have found so useful for gaining intuition into numerical-relativity simulations of inspiraling, spinning binaries [20, 21].) In Sec. 2.5 we briefly discuss energy conservation. In Sec. 2.6, relying on Racine and Flanagan [19], we specialize to the vacuum in the near zone of a system made from compact bodies with arbitrarily strong internal gravity. Finally, in Sec. 2.7 we summarize the DSX formalism and our extension of it both for a self-gravitating fluid and for a system of compact bodies.

Throughout this paper, we set $G = c = 1$, Greek letters run from 0 to 3 (spacetime) and Latin from 1 to 3 (space), and we use the notation of field theory in flat space in a 3+1 split, so spatial indices are placed up or down equivalently and repeated spatial indices are summed whether up or down or mixed. We use bold-face italic characters to represent spatial vectors, i.e. $\boldsymbol{w}$ is the bold-face version of w_j.

2.2 The DSX Maxwell-Like Formulation of 1PN Theory

Damour, Soffel and Xu (DSX [16]) express the 1PN metric in terms of two gravitational potentials, a scalar w and a vector w_j:

$$\begin{aligned} g_{00} &= -e^{-2w} = -1 + 2w - 2w^2 + O(U_N^3) \,, \\ g_{0i} &= -4w_i + O(U_N^{5/2}) \,, \\ g_{ij} &= \delta_{ij} e^{2w} = \delta_{ij}(1 + 2w) + O(U_N^2) \end{aligned} \tag{2.1}$$

[DSX Eqs. (3.3)]. The Newtonian limit of w is $U_N =$ (Newtonian gravitational potential), and w_i is of order $U_N^{3/2}$:

$$w = U_N + O(U_N^2) \,, \quad w_i = O(U_N^{3/2}) \,. \tag{2.2}$$

The harmonic gauge condition implies that

$$w_{,t} + w_{j,j} = 0 \tag{2.3}$$

[DSX Eq. (3.17a)]; here and throughout commas denote partial derivatives. Using this gauge condition (which DSX do not impose), the 1PN Einstein field equations take the following remarkably simple form:

$$\nabla^2 w - \ddot{w} = -4\pi(T^{00} + T^{jj}) + O(U_N^3/\mathcal{L}^2) \,, \tag{2.4a}$$

$$\nabla^2 w_i = -4\pi T^{0i} + O(U_N^{5/2}/\mathcal{L}^2) \tag{2.4b}$$

[DSX Eqs. (3.11)]. Here $T^{\alpha\beta}$ is the stress-energy tensor of the source (which we specialize below to

a perfect fluid), ∇^2 is the flat-space Laplacian (i.e. $\nabla^2 w = w_{,jj}$), repeated indices are summed, dots denote time derivatives (i.e. $\ddot{w} = w_{,tt}$), and $\mathcal{L}$ is the lengthscale on which w varies.

Following DSX, we introduce the 1PN *gravitoelectric field* $\boldsymbol{g}$ (denoted $\boldsymbol{e}$ or $\boldsymbol{E}$ by DSX , depending on the context) and *gravitomagnetic field* $\boldsymbol{H}$ (denoted $\boldsymbol{b}$ or $\boldsymbol{B}$ by DSX):

$$\boldsymbol{g} = \boldsymbol{\nabla} w + 4\dot{\boldsymbol{w}} + O(U_N^3/\mathcal{L}) \,, \tag{2.5a}$$

$$\boldsymbol{H} = -4\boldsymbol{\nabla} \times \boldsymbol{w} + O(U_N^{5/2}/\mathcal{L}) \,. \tag{2.5b}$$

[DSX Eqs. (3.21)].

The Einstein equations (2.4) and these definitions imply the following 1PN Maxwell-like equations for $\boldsymbol{g}$ and $\boldsymbol{H}$:

$$\boldsymbol{\nabla} \cdot \boldsymbol{g} = -4\pi(T^{00} + T^{jj}) - 3\ddot{w} + O(gU_N^2/\mathcal{L}) \,, \tag{2.6a}$$

$$\boldsymbol{\nabla} \times \boldsymbol{g} = -\dot{\boldsymbol{H}} + O(gU_N^2/\mathcal{L}) \,, \tag{2.6b}$$

$$\boldsymbol{\nabla} \cdot \boldsymbol{H} = 0 + O(HU_N/\mathcal{L}) \,, \tag{2.6c}$$

$$\boldsymbol{\nabla} \times \boldsymbol{H} = -16\pi T^{0i}\boldsymbol{e}_i + 4\dot{\boldsymbol{g}} + O(HU_N/\mathcal{L}) \tag{2.6d}$$

[DSX Eqs. (3.22)]. Here $\boldsymbol{e}_i$ is the unit vector in the i direction.

In terms of $\boldsymbol{g}$ and $\boldsymbol{H}$, the geodesic equation for a particle with ordinary velocity $\boldsymbol{v} = d\boldsymbol{x}/dt$ takes the following form [Eq. (7.17) of DSX, though in a less transparently "Lorentz-force"-like form there]:

$$\frac{d}{dt}\left[\left(1 + 3U_N + \tfrac{1}{2}\boldsymbol{v}^2\right)\boldsymbol{v}\right] = \left(1 - U_N + \tfrac{3}{2}\boldsymbol{v}^2\right)\boldsymbol{g} + \boldsymbol{v} \times \boldsymbol{H} + O(gU_N^2) \,. \tag{2.7}$$

Note that the spatial part of the particle's 4-momentum is $m\boldsymbol{u} = m(1 + U_N + \frac{1}{2}\boldsymbol{v}^2)\boldsymbol{v}$ at 1PN order. This accounts for the coefficient $1 + U_N + \frac{1}{2}\boldsymbol{v}^2$ on the left-hand side of Eq. (2.7). The remaining factor $2U_N$ is related to the difference between physical lengths and times, and proper lengths and times. In the linearized, very-low-velocity approximation, this geodesic equation takes the "Lorentz-force" form $d\boldsymbol{v}/dt = \boldsymbol{g} + \boldsymbol{v} \times \boldsymbol{H}$, first deduced (so far as we know) in 1918 by Thirring [4], motivated by Einstein's 1913 [2] insights about similarities between electromagnetic theory and his not-yet-perfected general relativity theory.

The 1PN deviations of the geodesic equation (2.7) from the usual Lorentz-force form might make one wonder about the efficacy of the DSX definition of $\boldsymbol{g}$. That efficacy will show up most strongly when we explore the gravitational momentum density in Sec. 2.4 below.

2.3 Specialization to a Perfect Fluid

We now depart from DSX by specializing our source to a perfect fluid and making contact with a set of 1PN gravitational potentials that are widely used. We pay special attention to connections with a paper by Pati and Will [27] because that paper will be our foundation, in Sec. 2.4, for computing the density and flux of gravitational field momentum.

We describe our perfect fluid in the following standard notation: ρ_o = (density of rest mass), Π =(internal energy per unit rest mass, i.e. specific internal energy), P = (pressure), all as measured in the fluid's local rest frame; $v_j \equiv dx^j/dt$ = (fluid's coordinate velocity).

Following Blanchet and Damour [28], and subsequently Pati and Will (Eqs. (4.13), (4.3) of [27]), we introduce a post-Newtonian variant U of the Newtonian potential, which is sourced by $T^{00}+T^{jj}$: $\nabla^2 U = -4\pi(T^{00}+T^{jj})$. Accurate to 1PN order, the source is [see Eq. (2.18d)]

$$T^{00}+T^{jj} = \rho_o(1+\Pi+2\boldsymbol{v}^2+2U_N+3P/\rho_o)\ , \tag{2.8}$$

where U_N is the Newtonian limit of U

$$U_N(\boldsymbol{x},t) = \int \frac{\rho_o(\boldsymbol{x}',t)}{|\boldsymbol{x}-\boldsymbol{x}'|} d^3x'\ . \tag{2.9a}$$

Correspondingly, U can be written as

$$U = \int \frac{\rho_o(1+\Pi+2\boldsymbol{v}^2+2U_N+3P/\rho_o)}{|\boldsymbol{x}-\boldsymbol{x}'|} d^3x'\ . \tag{2.9b}$$

Here and below the fluid variables and gravitational potentials in the integrand are functions of $(\boldsymbol{x}',t)$ as in Eq. (2.9a). In Eq. (2.9a) for U_N, ρ_o can be replaced by any quantity that agrees with ρ_o in the Newtonian limit, e.g. by the post-Newtonian "conserved mass density" ρ_* of Eq. (2.13b) below. We also introduce Chandrasekhar's Post-Newtonian scalar gravitational potential χ (Eq. (44) of [14]), which is sourced by $2U_N$, $\nabla^2\chi = -2U_N$ or equivalently

$$\chi = -\int \rho_o|\boldsymbol{x}-\boldsymbol{x}'|d^3x'\ . \tag{2.10}$$

Pati and Will use the notation $-X$ for χ (Eqs. (4.14), (4.12a) and (4.3) of [27]).

It is straightforward to show that the 1PN solution to the wave equation (2.4a) for the DSX scalar potential w is

$$w = U - \frac{1}{2}\ddot{\chi}\ ; \tag{2.11}$$

and the 1PN solution to the Laplace equation (2.4b) for the DSX vector potential w_j is

$$w_j = \int \frac{\rho_o v_j}{|\boldsymbol{x} - \boldsymbol{x}'|} d^3x' \ . \tag{2.12}$$

The fluid's evolution is governed by rest-mass conservation, momentum conservation, and energy conservation.

The 1PN version of rest-mass conservation takes the following form:

$$\rho_{*,t} + \boldsymbol{\nabla} \cdot (\rho_* \boldsymbol{v}) = 0 \ , \tag{2.13a}$$

where

$$\rho_* = \rho_o u^0 \sqrt{-g} = \rho_o (1 + \tfrac{1}{2}\boldsymbol{v}^2 + 3U) \tag{2.13b}$$

(Eqs. (117) and (118) of Chandrasekhar [14]). Here u^0 is the time component of the fluid's 4-velocity and g is the determinant of the covariant components of the metric.

We shall discuss momentum conservation and energy conservation in the next two sections.

We note in passing that Chandrasekhar and many other researchers write their 1PN spacetime metric in a different gauge from our harmonic one. The two gauges are related by a change of time coordinate

$$t_{\rm C} = t_{\rm H} - \tfrac{1}{2}\dot{\chi} \ , \tag{2.14a}$$

and correspondingly the metric components in the two gauges are related by

$$g^{\rm C}_{00} = g^{\rm H}_{00} + \ddot{\chi} \ , \quad g^{\rm C}_{0j} = g^{\rm H}_{0j} + \tfrac{1}{2}\dot{\chi}_{,j} \ . \tag{2.14b}$$

Here C refers to the Chandrasekhar gauge and H to our harmonic gauge. DSX write their equations in forms that are invariant under the gauge change (2.14).

2.4 Momentum Density, Flux, and Conservation

We now turn to our extension of the DSX formalism to include a Maxwell-like formulation of gravitational momentum density, momentum flux, and momentum conservation. Following Chandrasekhar [15], Pati and Will [27] and others, we adopt the Landau-Lifshitz pseudotensor as our tool for formulating these concepts.

From Pati and Will's 2PN harmonic-gauge Eqs. (2.6), (4.4b) and (4.4c) for the pseudotensor, one can deduce the following 1PN expressions for the the gravitational momentum density and

momentum flux (stress) in terms of the DSX gravitoelectric and gravitomagnetic fields $\boldsymbol{g}$ and $\boldsymbol{H}$:

$$(-g)t^{0j}_{\rm LL}\boldsymbol{e}_j = -\tfrac{1}{4\pi}\boldsymbol{g}\times\boldsymbol{H} + \tfrac{3}{4\pi}\dot{U}_N\boldsymbol{g}\ , \tag{2.15a}$$

$$(-g)t^{ij}_{\rm LL} = \tfrac{1}{4\pi}(g_ig_j - \tfrac{1}{2}\delta_{ij}g_kg_k) + \tfrac{1}{16\pi}(H_iH_j - \tfrac{1}{2}\delta_{ij}H_kH_k) - \tfrac{3}{8\pi}\dot{U}_N^2\delta_{ij}\ . \tag{2.15b}$$

Each equation is accurate up to corrections of order U_N times the smallest term on the right side (2PN corrections).

For comparison, in flat spacetime the electromagnetic momentum density is $\frac{1}{4\pi}\boldsymbol{E}\times\boldsymbol{B}$ and the momentum flux is $\frac{1}{4\pi}(E_iE_j-\frac{1}{2}\delta_{ij}E_kE_k)+\frac{1}{4\pi}(B_iB_j-\frac{1}{2}\delta_{ij}B_kB_k)$. *Aside from a sign in Eq. (2.15a) and the two terms involving $\dot{U}_N$, the gravitational momentum flux and density (2.15) are identical to the electromagnetic ones with $\boldsymbol{E}\to\boldsymbol{g}$ and $\boldsymbol{B}\to\boldsymbol{H}$.* Therefore, by analogy with the electromagnetic case, there are *gravitational tensions* $|\boldsymbol{g}|^2/8\pi$ and $|\boldsymbol{H}|^2/8\pi$ parallel to gravitoelectric and gravitomagnetic field lines, and *gravitational pressures* of this same magnitude orthogonal to the field lines. This makes the gravitoelectric and gravitomagnetic fields $\boldsymbol{g}$ and $\boldsymbol{H}$ powerful tools for building up physical intuition about the distribution and flow of gravitational momentum. We use them for that in our studies of compact binaries [20], relying heavily on Eqs. (2.15).

Here are some hints for deducing Eqs. (2.15) from Pati and Will [27] (henceforth PW): (i) Show that the last two terms in (2.6) of PW are of 2PN order for $\{\alpha,\beta\}=\{0j\}$ or $\{ij\}$ and so can be ignored, whence $16\pi(-g)t^{\alpha\beta}_{\rm LL}=\Lambda^{\alpha\beta}$. (ii) Show that our notation is related to that of PW by $\chi=-X$, U the same, $w=U-\frac{1}{2}\ddot{\chi}=\frac{1}{4}(N+B)-\frac{1}{8}(N+B)^2$ [for the last of these cf. PW (5.2), (5.4a,c)], and at Newtonian order $U_N=\frac{1}{4}N$. (iii) In PW (4.4b,c) for $\Lambda^{\alpha\beta}$, keep only the Newtonian and 1PN terms: the first curly bracket in (4.4b) and first and second curly brackets in (4.4c). Rearrange those terms so they involve only $\boldsymbol{K}$, $N+B$ and the Newtonian-order N, use the above translation of notation and use the definitions (2.5) of $\boldsymbol{g}$ and $\boldsymbol{H}$. Thereby, bring PW (4.4b,c) into the form (2.15).

In the Landau-Lifshitz formalism, the local law of 4-momentum conservation $T^{j\mu}{}_{;\mu}=0$ takes the form

$$[(-g)(T^{j\mu}+t^{j\mu}_{\rm LL})]_{,\mu}=0 \tag{2.16}$$

(Eqs. (20.23a) and (20.19) of [29], or (100.8) of [30]). Here (as usual), commas denote partial derivatives, and semicolons denote covariant derivatives. *This is the conservation law that we use in our studies of momentum flow in compact binaries* [20].

When dealing with material bodies (e.g. in DSX) rather than with the vacuum outside compact bodies, an alternative Maxwell-like version of momentum conservation is useful. Specifically, using

expressions (2.15) and $(-g) = 1 + 4U_N$ [from Eq. (2.1) with $w = U_N$ at leading order], and using the field equations (2.6) for $\boldsymbol{g}$ and $\boldsymbol{H}$, the conservation law (2.16) can be rewritten in the following simple Lorentz-force-like form (Eq. (4.3) of Damour, Soffel and Xu's Paper II [22])

$$\begin{aligned}&[(1+4U_N)T^{i0}]_{,t} + [(1+4U_N)T^{ij}]_{,j} \\ &\quad = (T^{00}+T^{jj})g_i + \epsilon_{ijk}T^{0j}H_k \; .\end{aligned} \tag{2.17}$$

Here the Levi-Civita tensor ϵ_{ijk} produces a cross product of the momentum density with the gravitomagnetic field. For comparison, in flat spacetime, the momentum conservation law for a charged medium interacting with electric and magnetic fields E_i and B_i has the form $T^{i0}{}_{,t} + T^{ij}{}_{,j} = \rho_e E_i + \epsilon_{ijk}J_jB_k$, where ρ_e is the charge density and J_j the charge flux (current density). *The right-hand side of Eq. (2.17) (the gravitational force density) is identical to that in the electromagnetic case, with* $\rho_e \to (T^{00}+T^{jj})$, $J_j \to T^{0j}$, $\boldsymbol{E} \to \boldsymbol{g}$, *and* $\boldsymbol{B} \to \boldsymbol{H}$. Again, this makes $\boldsymbol{g}$ and $\boldsymbol{H}$ powerful foundations for gravitational intuition.

For a perfect fluid, the components of the 1PN stress-energy tensor, which appear in the momentum conservation law (2.17), are (Eqs. (20) of Chandrasekhar [14])

$$T^{00} = \rho_o(1+\Pi+\boldsymbol{v}^2+2U_N) \; , \tag{2.18a}$$

$$T^{i0} = \rho_o(1+\Pi+v^2+2U_N+P/\rho_o)v_j \; , \tag{2.18b}$$

$$\begin{aligned}T^{ij} &= \rho_o(1+\Pi+\boldsymbol{v}^2+2U_N+P/\rho_o)v_iv_j \\ &\quad +P(1-2U_N)\delta_{ij} \; ,\end{aligned} \tag{2.18c}$$

$$T^{00}+T^{jj} = \rho(1+\Pi+2\boldsymbol{v}^2+2U_N+3P/\rho_o) \; . \tag{2.18d}$$

2.5 Energy Conservation

For a perfect fluid, the exact (not just 1PN) law of energy conservation, when combined with mass conservation and momentum conservation, reduces to the first law of thermodynamics $d\Pi/dt = -Pd(1/\rho_o)/dt$; so whenever one needs to invoke energy conservation, the first law is the simplest way to do so. For this reason, and because deriving the explicit form of 1PN energy conservation $[(-g)(T^{0\mu}+t^{0\mu}_{\rm LL})]_{,\mu} = 0$ is a very complex and delicate task (cf. Sec. VI of [31]), we shall not write it down here.

However, we *do* write down the Newtonian law of energy conservation in harmonic gauge, since we will occasionally need it in our future papers. Chandrasekhar calculated $(-g)(T^{0\mu}+t^{0\mu}_{\rm LL})$ in [15]; his Eqs. (48) and (57) are the time-time and time-space components, respectively. When one

writes the expressions in terms of the "conserved rest-mass density" ρ_* [Eq. (2.13b)] and in our Maxwell-like form, Newtonian conservation of energy states that

$$\begin{aligned}&\left[\rho_*(1+\Pi+\frac{1}{2}v^2+3U_N)-\frac{7}{8\pi}\boldsymbol{g}\cdot\boldsymbol{g}\right]_{,t}\\&+\boldsymbol{\nabla}\cdot\left[\rho_*\boldsymbol{v}(1+\Pi+\frac{P}{\rho}+\frac{1}{2}v^2+3U_N)\right.\\&\left.+\frac{3}{4\pi}\dot{U}_N\boldsymbol{g}-\frac{1}{4\pi}\boldsymbol{g}\times\boldsymbol{H}\right]=0\,.\end{aligned}\tag{2.19}$$

While this equation is perfectly correct, it expresses Newtonian energy conservation in terms of the post-Newtonian gravitomagnetic field $\boldsymbol{H}$. It is possible to rewrite the $\boldsymbol{H}$-dependent term using the relationship, $\nabla\cdot[-1/(4\pi)(\boldsymbol{g}\times\boldsymbol{H})]=\nabla\cdot[-4U_NT^{0j}\boldsymbol{e}_j+(1/\pi)U_N\dot{\boldsymbol{g}}]$, which is accurate up to corrections of order $\boldsymbol{g}\cdot\dot{\boldsymbol{H}}$. This relationship can be found by applying Eq. (2.6b) once and (2.6d) twice, in combination with elementary vector-calculus identities. The statement of Newtonian energy conservation then depends only upon the Newtonian potential and its gradient and time derivative:

$$\begin{aligned}&\left[\rho_*(1+\Pi+\frac{1}{2}v^2+3U_N)-\frac{7}{8\pi}\boldsymbol{g}\cdot\boldsymbol{g}\right]_{,t}\\&+\boldsymbol{\nabla}\cdot\left[\rho_*\boldsymbol{v}(1+\Pi+\frac{P}{\rho}+\frac{1}{2}v^2-U_N)\right.\\&\left.+\frac{3}{4\pi}\dot{U}_N\boldsymbol{g}+\frac{1}{\pi}U_N\dot{\boldsymbol{g}}\right]=0\,.\end{aligned}\tag{2.20}$$

Notice that going from Eq. (2.19) to Eq. (2.20) involves adding a divergence-free piece to the energy flux, so it entails changing how the energy flux is localized — a change that strictly speaking takes the energy flux out of harmonic gauge.

If the coefficients of the gravitational terms in Eq. (2.20) look unfamiliar, it is because even at Newtonian order, the density and flux of gravitational energy are gauge-dependent. In some other gauge, they will be different; see Box 12.3 of [32].

2.6 Gravitational Potentials in the Vacuum of a System of Compact, Spinning Bodies

For a system of compact, spinning bodies (neutron stars or black holes), the gravitational potentials U_N, U, w_i and χ in the vacuum between the bodies take the following forms (in a slightly different

harmonic gauge than the one used in Sec. 2.3 for fluids):

$$U_N = \sum_A \frac{M_A}{r_A} , \tag{2.21a}$$

$$U = \sum_A \frac{M_A}{r_A}\left(1 + \tfrac{3}{2}\boldsymbol{v}_A^2 - \sum_{B\neq A}\frac{M_B}{r_{AB}}\right) + 2\sum_A \frac{\epsilon_{ijk} v_A^i S_A^j n_A^k}{{r_A}^2} , \tag{2.21b}$$

$$\chi = -\sum_A M_A r_A , \tag{2.21c}$$

$$w = U - \frac{1}{2}\ddot{\chi} , \tag{2.21d}$$

$$w_i = \sum_A \frac{M_A v_A^i}{r_A} + \frac{1}{2}\sum_A \frac{\epsilon_{ijk} S_A^j n_A^k}{{r_A}^2} , \tag{2.21e}$$

Here the notation is that of Sec. IV of Thorne and Hartle [26]: the sum is over the compact bodies labeled by capital Latin letters A, B; M_A, S_A^j and v_A^j are the mass, spin angular momentum and coordinate velocity of body A; r_A is the coordinate distance from the field point to the center of mass of body A; r_{AB} is the coordinate distance between the centers of mass of bodies A and B; n_A^j is the unit vector pointing from the center of mass of body A to the field point; and ϵ_{ijk} is the Levi-Civita tensor.

Equations (2.21) for the potentials can be deduced by comparing our 1PN spacetime metric coefficients [Eqs. (2.1), (2.11)] with those in Eqs. (2.4), (5.11) and (5.14) of Racine and Flanagan [19] or in Eqs. (4.4) of Thorne and Hartle [26].[4]

2.7 Conclusion

In our Maxwell-like formulation of the 1PN approximation to general relativity for fluid bodies, the evolution of the fluid and gravitational fields is governed by: (i) the law of momentum conservation (2.17), (2.18) (which can be thought of as evolving the fluid velocity v_j); (ii) the law of mass conservation (2.13) (which can be thought of as evolving the mass density ρ_o); (iii) the equation of state $P(\rho_o)$ and first law of thermodynamics $d\Pi = -Pd(1/\rho_o)$ (which determine P and Π once ρ_o is known); Eqs. (2.9), (2.12), (2.10) for the gravitational potentials U, χ, and w_j; and Eqs. (2.5) or (2.6) for the gravitoelectric and gravitomagnetic fields $\boldsymbol{g}$, $\boldsymbol{H}$.

[4]Racine and Flanagan specialize DSX to a system of compact bodies with a complete set of nonzero multipole moments. We neglect all moments except the bodies' masses and spins (see fifth paragraph of Sec. 2.1). Our notation is related to that of Racine and Flanagan by $U_N = -\Phi$, $w = U - \frac{1}{2}\ddot{\chi} = -(\Phi + \psi), w_i = -\frac{1}{4}\zeta_i$. The Racine-Flanagan derivation of Eqs. (2.21) avoids considering the internal structures of the bodies and it therefore is directly valid for black holes. The Thorne-Hartle derivation relies on the pioneering analysis of Einstein, Infeld and Hoffman [33] which uses a fluid description of the bodies' interiors. Thorne and Hartle extend Eqs. (2.21) to black holes by the equivalent of Damour's "effacement" considerations, Sec. 6.4 of [25].

When specialized to a system of compact bodies, e.g. a binary made of black holes or neutron stars, the system is governed by: (i) 1PN equations of motion and precession for the binary (not given in this paper; see, e.g., Eqs. (4.10), (4.11) and (4.14) of [26]); (ii) momentum flow within the binary as described by the Landau-Lifshitz pseudotensor (2.15) and its conservation law (2.16), in which the gravitoelectric and gravitomagnetic fields are expressed as sums over the bodies via Eqs. (2.21) and (2.5); and (iii) other tools developed by Landau and Lifshitz (Sec. 100 of [30]). We are finding this formalism powerful in gaining insight into compact binaries [20].

Acknowledgments

For helpful discussions we thank Yanbei Chen and Drew Keppel. We also thank Luc Blanchet for bringing references [28] and [16] to our attention, and anonymous referees for helpful critiques and suggestions. This research was supported in part by NSF grants PHY-0601459 and PHY-0653653 and by a Caltech Feynman Fellowship to JDK.

Bibliography

[1] R. L. Forward, Proc. IRE **49**, 892 (1961).

[2] A. Einstein, Phys. Z. **14**, 1261 (1913).

[3] A. Einstein, *Four Lectures on the Theory of Relativity* held at Princeton University in May 1921, English Translation by Edwin Plimpton Adams (London, Meutuen, 1922; Princeton University Press, 1923); reproduced as Document 71 in *The Collected Papers of Albert Einstein*, **7** (Princeton University Press, 2002); see pp. 100–103.

[4] H. Thirring, Phys. Z. **19**, 204 (1918).

[5] H. Thirring, Phys. Z. **19**, 33 (1918); and H. Thirring and J. Lense, Phys. Z. **19**, 156 (1918); English translations in B. Mashhoon, F.W. Hehl and D. S. Theiss, Gen. Rel. Grav. **16**, 711 (1984).

[6] V. B. Braginsky, C. M. Caves and K. S. Thorne, Phys. Rev. D **15**, 2047 (1977).

[7] R. M. Wald, *General Relativity* (University of Chicago Press, Chicago, 1984), Sec. 4.4a.

[8] B. Mashhoon, Phys. Lett. A **173**, 347 (1993).

[9] B. Mashhoon, F. Gronwald and H. I. M. Lichtenegger, Lect. Notes Phys. **562**, 83 (2001).

[10] S. J. Clark and R. W. Tucker, Class. Quant. Grav. **17**, 4125 (2000).

[11] B. Mashhoon, Class. Quant. Grav. **25** 085014 (2008).

[12] E. Goulart and F. T. Falciano, J. Gen. Rel. Grav., submitted; arXiv:0807.2777

[13] L. F. O. Costa and C. A. R. Herdeiro Phys. Rev. D **78**, 024021 (2008).

[14] S. Chandrasekhar, Astrophys. J. **142**, 1488 (1965); also available as Paper 6 in S. Chandrasekhar, *Selected Papers, Volume* **5***, Relativistic Astrophysics* (University of Chicago Press, Chicago, 1990).

[15] S. Chandrasekhar, Astrophys. J. **158**, 45 (1969); also available as Paper 7 in S. Chandrasekhar, *Selected Papers, Volume* **5***, Relativistic Astrophysics* (University of Chicago Press, Chicago, 1990).

[16] T. Damour, M. Soffel, C. Xu, Phys. Rev. D **43**, 3273 (1991).

[17] R.T. Jantzen, P. Carini and D. Bini, Ass. Phys. **215**, 1 (1992).

[18] S. Kopeikin and I. Vlasov, Phys. Reports **400**, 209 (2004).

[19] E. Racine and E.E. Flanagan, Phys. Rev. D **71**, 044010 (2005).

[20] Y. Chen, D. G. Keppel, D. A. Nichols and K. S. Thorne, Phys. Rev. D, submitted (2009); arXiv:0902.4077.

[21] G. Lovelace, Y. Chen, M. Cohen, J.D. Kaplan, D. Keppel, K.D. Matthews, D.A. Nichols, M.A. Scheel, and U. Sperhake, Phys. Rev. D, submitted (2009); arXiv:0907.0869.

[22] T. Damour, M. Soffel, C. Xu, Phys. Rev. D **45**, 1017 (1992).

[23] T. Damour, M. Soffel, C. Xu, Phys. Rev. D **47**, 3124 (1993).

[24] T. Damour, M. Soffel, C. Xu, Phys. Rev. D **49**, 618 (1994).

[25] T. Damour, Chapter 6 in *Three Hundred Years of Gravitation*, eds. S.W. Hawking and W. Israel (Cambridge University Press, Cambridge, 1987).

[26] K. S. Thorne and J. B. Hartle, Phys. Rev. D **31**, 1815 (1985).

[27] M. E. Pati and C. M. Will, Phys. Rev. D **62**, 124015 (2000).

[28] L. Blanchet, T. Damour, Ann. Inst. Henri Poincaré, **50**, 337 (1989).

[29] C. W. Misner, K. S. Thorne and J. A. Wheeler, *Gravitation* (W.H. Freeman, San Francisco, 1973).

[30] L. D. Landau and E.M. Lifshitz, *Classical Theory of Fields* (Addison Wesley, Redding Mass., 1962).

[31] S. Chandrasekhar and Y. Nutku, Astrophys. J. **158**, 55 (1969); also available as Paper 8 in S. Chandrasekhar, *Selected Papers, Volume* **5**, *Relativistic Astrophysics* (University of Chicago Press, Chicago, 1990).

[32] R. D. Blandford and K. S. Thorne, *Applications of Classical Physics* (2009), available at `http://www.pma.caltech.edu/Courses/ph136/yr2008/` .

[33] A. Einstein, L. Infeld and B. Hoffman, Ann. Math. 39, 65 (1938).

Chapter 3

Frame-Dragging Vortexes and Tidal Tendexes Attached to Colliding Black Holes: Visualizing the Curvature of Spacetime

When one splits spacetime into space plus time, the spacetime curvature (Weyl tensor) gets split into an "electric" part $\mathcal{E}_{jk}$ that describes tidal gravity and a "magnetic" part $\mathcal{B}_{jk}$ that describes differential dragging of inertial frames. We introduce tools for visualizing $\mathcal{B}_{jk}$ (frame-drag vortex lines, their vorticity, and vortexes) and $\mathcal{E}_{jk}$ (tidal tendex lines, their tendicity, and tendexes), and also visualizations of a black-hole horizon's (scalar) vorticity and tendicity. We use these tools to elucidate the nonlinear dynamics of curved spacetime in merging black-hole binaries.

Originally published as Robert Owen, Jeandrew Brink, Yanbei Chen, Jeffrey D. Kaplan, Geoffrey Lovelace, Keith D. Matthews, David A. Nichols, Mark A. Scheel, Fan Zhang, Aaron Zimmerman, and Kip S. Thorne. Phys. Rev. Lett. 106, 151101 (2011)

3.1 Introduction

When one foliates spacetime with spacelike hypersurfaces, the Weyl curvature tensor $C_{\alpha\beta\gamma\delta}$ (same as Riemann in vacuum) splits into "electric" and "magnetic" parts $\mathcal{E}_{jk} = C_{\hat{0}j\hat{0}k}$ and $\mathcal{B}_{jk} = \frac{1}{2}\epsilon_{jpq}C^{pq}{}_{k\hat{0}}$ (see e.g. [1] and references therein); both $\mathcal{E}_{jk}$ and $\mathcal{B}_{jk}$ are spatial, symmetric, and trace-free. Here the indices are in the reference frame of "orthogonal observers" who move orthogonal to the space slices; $\hat{0}$ is their time component, ϵ_{jpq} is their spatial Levi-Civita tensor, and throughout we use

units with $c = G = 1$.

Because two orthogonal observers separated by a tiny spatial vector $\boldsymbol{\xi}$ experience a relative tidal acceleration $\Delta a_j = -\mathcal{E}_{jk}\xi^k$, $\mathcal{E}_{jk}$ is called the *tidal field*. And because a gyroscope at the tip of $\boldsymbol{\xi}$ precesses due to frame dragging with an angular velocity $\Delta\Omega_j = \mathcal{B}_{jk}\xi^k$ relative to inertial frames at the tail of $\boldsymbol{\xi}$, we call $\mathcal{B}_{jk}$ the *frame-drag field*.

3.2 Vortexes and Tendexes in Black-Hole Horizons

For a binary black hole, our space slices intersect the 3-dimensional (3D) event horizon in a 2D horizon with inward unit normal $\mathbf{N}$; so $\mathcal{B}_{NN}$ is the rate the frame-drag angular velocity around $\mathbf{N}$ increases as one moves inward through the horizon. Because of the connection between rotation and vorticity, we call $\mathcal{B}_{NN}$ the horizon's *frame-drag vorticity*, or simply its *vorticity*.

Because $\mathcal{B}_{NN}$ is boost-invariant along $\mathbf{N}$ [2], the horizon's vorticity is independent of how fast the orthogonal observers fall through the horizon, and is even unchanged if the observers hover immediately above the horizon (the FIDOs of the "black-hole membrane paradigm" [3]).

Figure 3.1 shows snapshots of the horizon for two identical black holes with transverse, oppositely directed spins $\mathbf{S}$, colliding head on. Before the collision, each horizon has a negative-vorticity region (red) centered on $\mathbf{S}$, and a positive-vorticity region (blue) on the other side. We call these regions of concentrated vorticity *horizon vortexes*. Our numerical simulation [4] shows the four vortexes being transferred to the merged horizon (Fig. 3.1b), then retaining their identities, but sloshing between positive and negative vorticity and gradually dying, as the hole settles into its final Schwarzschild state; see the movie in Ref. [5].

Because $\mathcal{E}_{NN}$ measures the strength of the tidal-stretching acceleration felt by orthogonal observers as they fall through (or hover above) the horizon, we call it the horizon's *tendicity* (a word coined by David Nichols from the Latin *tendere*, "to stretch"). On the two ends of the merged horizon in Fig. 3.1b there are regions of strongly enhanced tendicity, called *tendexes*; cf. Fig. 3.5

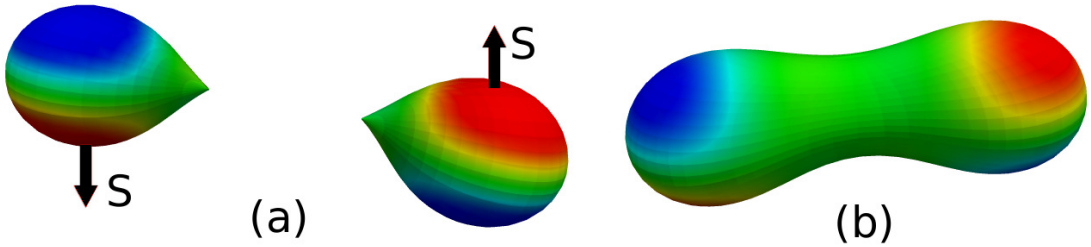

Figure 3.1: Vortexes (with positive vorticity blue, negative vorticity red) on the 2D event horizons of spinning, colliding black holes, just before and just after merger. (From the simulation reported in [4].)

below.

An orthogonal observer falling through the horizon carries an orthonormal tetrad consisting of her 4-velocity $\mathbf{U}$, the horizon's inward normal $\mathbf{N}$, and transverse vectors $\mathbf{e_2}$ and $\mathbf{e_3}$. In the null tetrad $\mathbf{l} = (\mathbf{U} - \mathbf{N})/\sqrt{2}$ (tangent to horizon generators), $\mathbf{n} = (\mathbf{U} + \mathbf{N})/\sqrt{2}$, $\mathbf{m} = (\mathbf{e_2} + i\mathbf{e_3})/\sqrt{2}$, and $\mathbf{m}^*$, the Newman-Penrose Weyl scalar Ψ_2 [6] is $\Psi_2 = (\mathcal{E}_{NN} + i\mathcal{B}_{NN})/2$. Here we use sign conventions of [7], appropriate for our (- +++) signature.

Penrose and Rindler [8] define a complex scalar curvature $\mathcal{K} = \mathcal{R}/4 + i\mathcal{X}/4$ of the 2D horizon, with $\mathcal{R}$ its intrinsic (Ricci) scalar curvature (which characterizes the horizon's shape) and $\mathcal{X}$ proportional to the 2D curl of its Hájíček field [9] (the space-time part of the 3D horizon's extrinsic curvature). Penrose and Rindler show that $\mathcal{K} = -\Psi_2 + \mu\rho - \lambda\sigma$, where ρ, σ, μ, and λ are spin coefficients related to the expansion and shear of the null vectors $\mathbf{l}$ and $\mathbf{n}$, respectively. In the limit of a shear- and expansion-free horizon (e.g. a quiescent black hole; Fig. 3.2a,b,c), $\mu\rho - \lambda\sigma$ vanishes, so $\mathcal{K} = -\Psi_2$, whence $\mathcal{R} = -2\mathcal{E}_{NN}$ and $\mathcal{X} = -2\mathcal{B}_{NN}$. As the dimensionless spin parameter a/M of a quiescent (Kerr) black hole is increased, the scalar curvature $\mathcal{R} = -2\mathcal{E}_{NN}$ at its poles decreases, becoming negative for $a/M > \sqrt{3}/2$; see the blue spots on the poles in Fig. 3.2b compared to solid red for the nonrotating hole in Fig. 3.2a. In our binary-black-hole simulations, the contributions of the spin coefficients to $\mathcal{K}$ on the apparent horizons are small [$L2$-norm $\lesssim 1\%$] so $\mathcal{R} \simeq -2\mathcal{E}_{NN}$ and $\mathcal{X} \simeq -2\mathcal{B}_{NN}$, except for a time interval $\sim 5M_{\rm tot}$ near merger. Here $M_{\rm tot}$ is the binary's total mass. On the event horizon, the duration of spin-coefficient contributions $> 1\%$ is somewhat longer, but we do not yet have a good measure of it.

Because $\mathcal{X}$ is the 2D curl of a 2D vector, its integral over the 2D horizon vanishes. Therefore, positive-vorticity regions must be balanced by negative-vorticity regions; it is impossible to have a horizon with just one vortex. By contrast, the Gauss-Bonnet theorem says the integral of $\mathcal{R}$ over the 2D horizon is 8π (assuming S_2 topology), which implies the horizon tendicity $\mathcal{E}_{NN}$ is predominantly negative (because $\mathcal{E}_{NN} \simeq -\mathcal{R}/2$ and $\mathcal{R}$ is predominantly positive). Many black holes have negative horizon tendicity everywhere (an exception is Fig. 3.2b), so their horizon tendexes must be distinguished by deviations of $\mathcal{E}_{NN}$ from a horizon-averaged value.

3.3 3D vortex and tendex lines

The frame-drag field $\mathcal{B}_{jk}$ is symmetric and trace free and therefore is fully characterized by its three orthonormal eigenvectors $\mathbf{e}_{\tilde{j}}$ and their eigenvalues $\mathcal{B}_{\tilde{1}\tilde{1}}$, $\mathcal{B}_{\tilde{2}\tilde{2}}$ and $\mathcal{B}_{\tilde{3}\tilde{3}}$. We call the integral curves along $\mathbf{e}_{\tilde{j}}$ *vortex lines*, and their eigenvalue $\mathcal{B}_{\tilde{j}\tilde{j}}$ those lines' *vorticity*, and we call a concentration of vortex lines with large vorticity a *vortex*. For the tidal field $\mathcal{E}_{jk}$ the analogous quantities are *tendex lines*, *tendicity* and *tendexes*. For a nonrotating (Schwarzschild) black hole, we show a few tendex lines in Fig. 3.2a; and for a rapidly-spinning black hole (Kerr metric with $a/M = 0.95$) we show

tendex lines in Fig. 3.2b and vortex lines in Fig. 3.2c.

If a person's body (with length ℓ) is oriented along a positive-tendicity tendex line (blue in Fig. 3.2a), she feels a head-to-foot compressional acceleration $\Delta a = |\text{tendicity}|\ell$; for negative tendicity (red) it is a stretch. If her body is oriented along a positive-vorticity vortex line (blue in Fig. 3.2c), her head sees a gyroscope at her feet precess clockwise with angular speed $\Delta\Omega = |\text{vorticity}|\ell$, and her feet see a gyroscope at her head also precess clockwise at the same rate. For negative vorticity (red) the precessions are counterclockwise.

For a nonrotating black hole, the stretching tendex lines are radial, and the squeezing ones lie on spheres (Fig. 3.2a). When the hole is spun up to $a/M = 0.95$ (Fig. 3.2b), its toroidal tendex lines acquire a spiral, and its poloidal tendex lines, when emerging from one polar region, return to the other polar region. For any spinning Kerr hole (e.g. Fig. 3.2c), the vortex lines from each polar region reach around the hole and return to the same region. The red vortex lines from the red north polar region constitute a *counterclockwise vortex*: the blue ones from the south polar region constitute a *clockwise vortex*.

As a dynamical example, consider a Schwarzschild black hole's fundamental odd-parity $l = m = 2$ quasinormal mode of pulsation, which is governed by Regge-Wheeler perturbation theory [10] and has angular eigenfrequency $\omega = (0.74734 - 0.17792i)/2M$, with M the hole's mass. From the perturbation equations, we have deduced the mode's horizon vorticity: $\mathcal{B}_{NN} = \Re\{9\sin^2\theta/(2i\omega M^3)\exp[2i\phi - i\omega(\tilde{t}+2M)]\}$. (Here $\tilde{t}$ is the ingoing Eddington-Finklestein time coordinate, and the mode's Regge-Wheeler radial eigenfunction $Q(r)$ is normalized to unity near the horizon.) At time $\tilde{t} = 0$, this $\mathcal{B}_{NN}$ exhibits four horizon vortexes [red and blue in Fig. 3.2d], centered on the equator at $(\theta, \phi) = (\pi/2, 1.159 + k\pi/2)$ $(k = 0, 1, 2, 3)$, and with central vorticities $\mathcal{B}_{NN} = -(-1)^k 39.22/(2M)^2$. From analytic formulae for $\mathcal{B}_{jk}$ and a numerical $Q(r)$, we have deduced the equatorial-plane red vortex lines and vorticities shown in Fig. 3.2d. As time $\tilde{t}$ passes, the vortexes rotate counterclockwise, so they resemble water splayed out from a turning sprinkler. The transition from near zone to wave zone is at $r \sim 4M$ (near the outermost part of the second contour line). As one moves into the wave zone, each of the red vortexes is smoothly transformed into a gravitational-wave trough and the 3D vortexes that emerge from the blue horizon vortexes (concentrated in the dark region of this figure) are transformed into gravitational-wave crests.

3.4 Vortex and Tendex Evolutions in Binary Black Holes

We have explored the evolution of frame-drag vortexes and tidal tendexes in numerical simulations of three binary black holes (BBHs) that differ greatly from each other.

Our first simulation (documented in Ref. [4]; movies in Ref. [5]) is the head-on, transverse-spin merger depicted in Fig. 3.1 above, with spin magnitudes $a/M = 0.5$. As the holes approach each

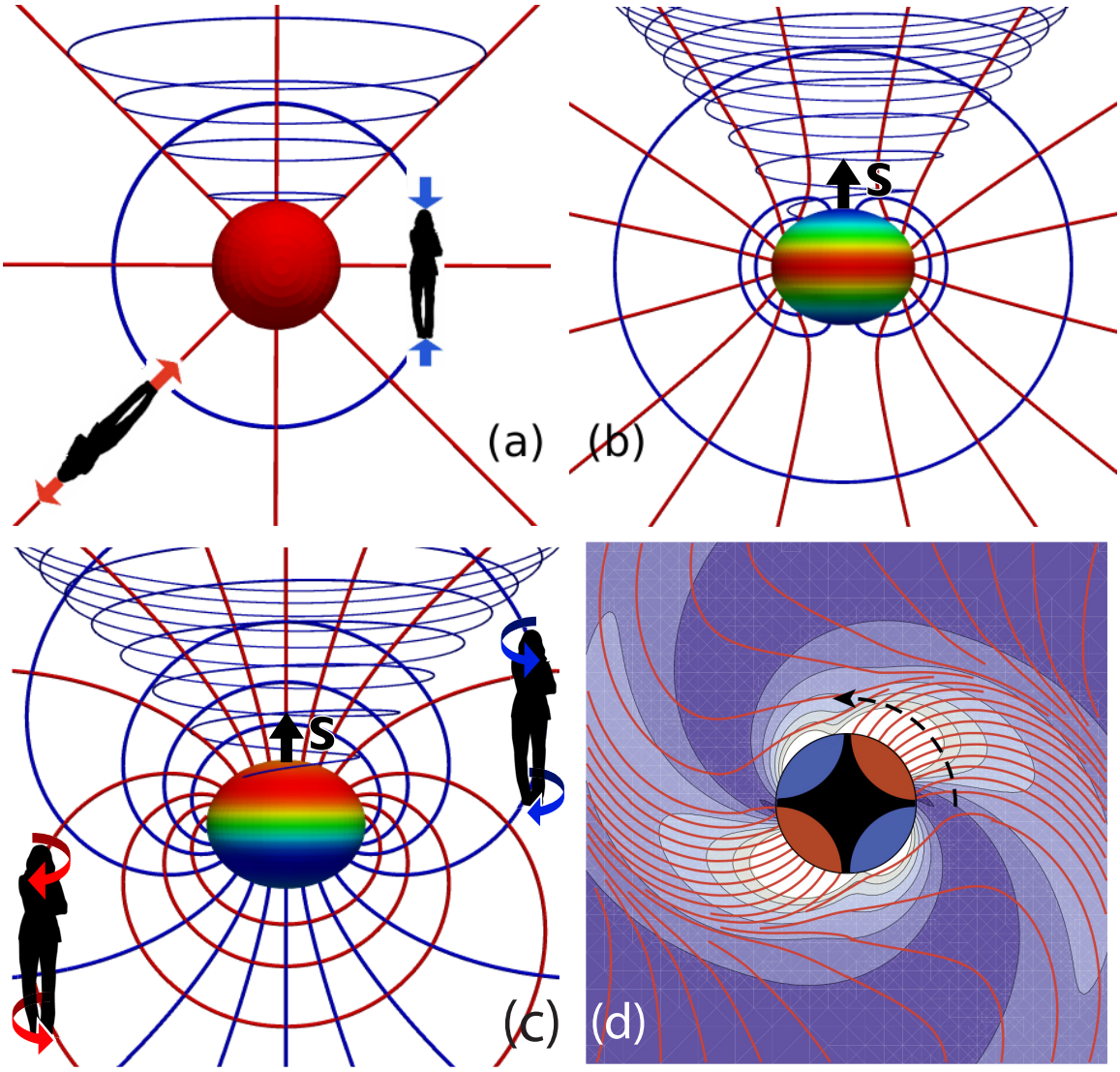

Figure 3.2: Four different black holes, with horizons colored by their tendicity (upper two panels) or vorticity (lower two panels), ranging from most negative (red) to most positive (blue); and with a Kerr-Schild horizon-penetrating foliation (Exercise 33.8 of Ref. [18]). (a) A nonrotating black hole and its tendex lines; negative-tendicity lines are red, and positive blue. (b) A rapidly rotating (Kerr) black hole, with spin $a/M = 0.95$, and its tendex lines. (c) The same Kerr black hole and its vortex lines. (d) Equatorial plane of a nonrotating black hole that is oscillating in an odd-parity $l = m = 2$ quasinormal mode, with negative-vorticity vortex lines emerging from red horizon vortexes. The lines' vorticities are indicated by contours and colors; the contour lines, in units $(2M)^{-2}$ and going outward from the hole, are -10, -8, -6, -4, -2.

other then merge, their 3D vortex lines, which originally link a horizon vortex to itself on a single hole (Fig. 3.2c), reconnect so on the merged hole they link one horizon vortex to the other of the same polarity (Fig. 3.3a). After merger, the near-zone 3D vortexes slosh (their vorticity oscillates between positive and negative), generating vortex loops (Fig. 3.3b) that travel outward as gravitational waves.

Our second simulation (documented in Ref. [**?**]; movies in Ref. [11]) is the inspiral and merger

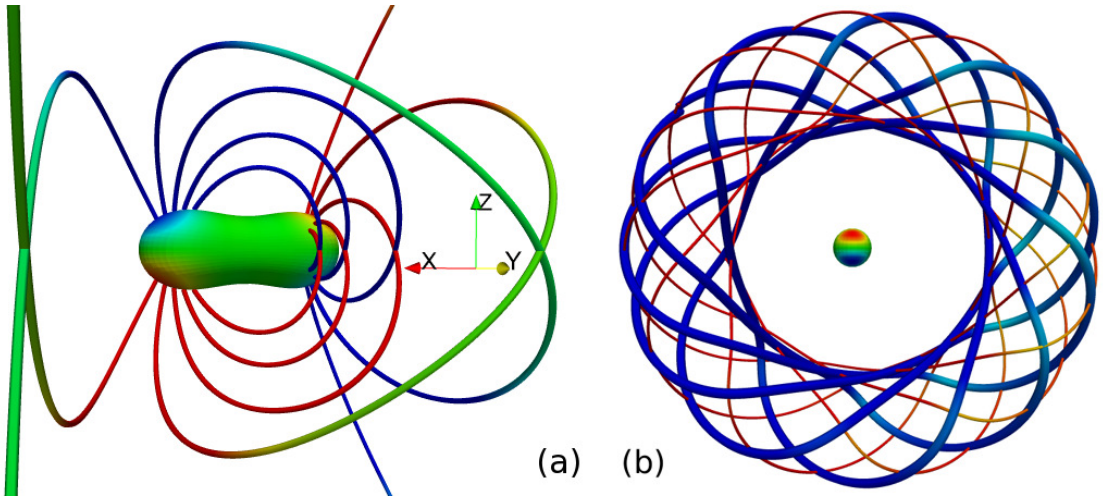

Figure 3.3: Head-on, transverse-spin simulation: (a) Shortly after merger, vortex lines link horizon vortexes of same polarity (red to red; blue to blue). Lines are color coded by vorticity (different scale from horizon). (b) Sloshing of near-zone vortexes generates vortex loops traveling outward as gravitational waves; thick and thin lines are orthogonal vortex lines.

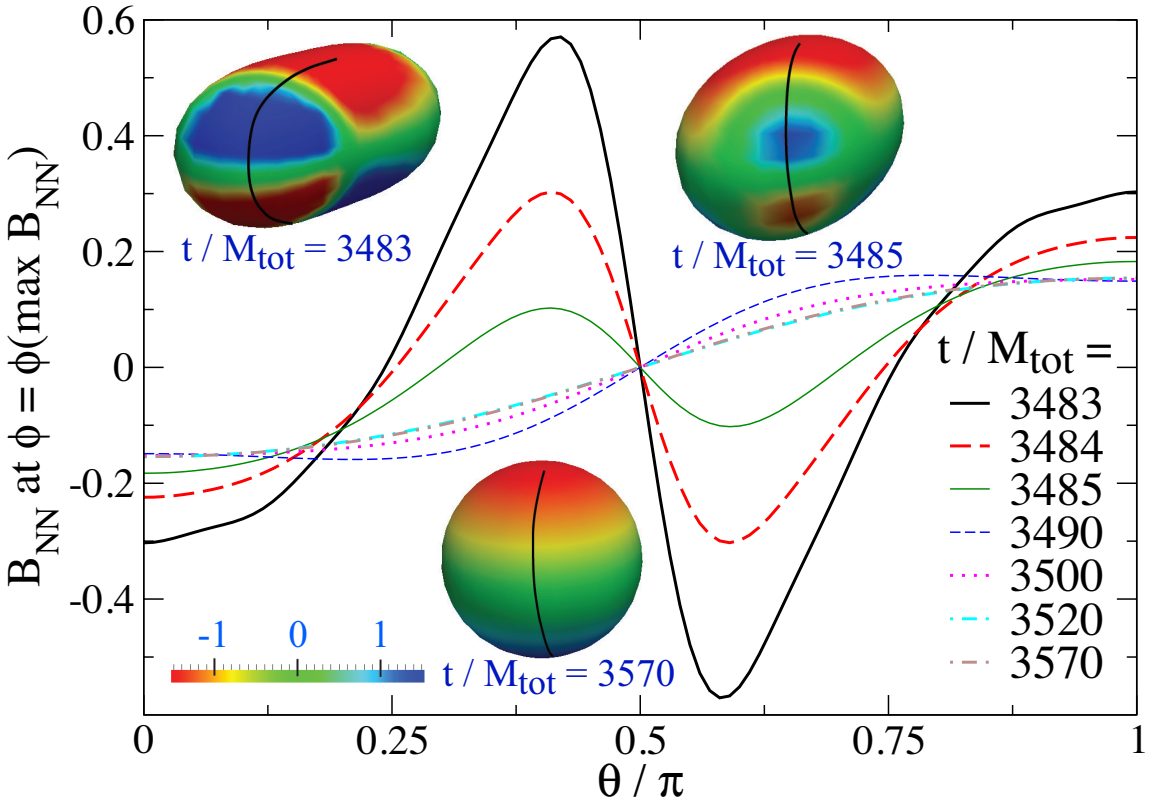

Figure 3.4: Insets: snapshots of the common apparent horizon for the $a/M = 0.95$ anti-aligned simulation, color coded with the horizon vorticity B_{NN}. Graphs: B_{NN} as a function of polar angle θ at the azimuthal angle ϕ that bisects the four vortexes (along the black curves in snapshots).

of two identical, fast-spinning holes ($a/M = 0.95$) with spins antialigned to the orbital angular momentum. Figure 3.4 shows the evolution of the vorticity $\mathcal{B}_{NN}$ on the common apparent horizon beginning just after merger (at time $t/M_{\rm tot} = 3483$), as seen in a frame that co-rotates with the small horizon vortexes. In that frame, the small vortexes (which arise from the initial holes' spins) appear to diffuse into the two large central vortexes (which arise from the initial holes' orbital angular momentum), annihilating some of their vorticity. (This is similar to the diffusion and annihilation of magnetic field lines with opposite polarity threading a horizon [3].) Making this heuristic description quantitative, or disproving it, is an important challenge.

Our third simulation (see movies in Ref. [12]) is a variant of the "extreme-kick" merger studied by Campanelli et al. [13] and others [14, 15]: two identical holes, merging from an initially circular orbit, with oppositely directed spins $a/M = 0.5$ lying in the orbital (x, y) plane. In this case, the vortexes and tendexes in the merged hole's (x, y) plane rotate as shown in Fig. 3.2d. We have tuned the initial conditions to make the final hole's kick (nearly) maximal, in the $+z$ direction. The following considerations explain the origin of this maximized kick:

In a plane gravitational wave, all the vortex and tendex lines with nonzero eigenvalues lie in the wave fronts and make angles of 45 degrees to each other (bottom inset of Fig. 3.5.) For vectors $\boldsymbol{E}$ (parallel to solid, positive-tendicity tendex line) and $\boldsymbol{B}$ (parallel to dashed, positive-vorticity vortex line), $\boldsymbol{E} \times \boldsymbol{B}$ is in the wave's propagation direction.

Now, during and after merger, the black hole's near-zone rotating tendex lines (top left inset in Fig. 3.5) acquire accompanying vortex lines as they travel outward into the wave zone and become gravitational waves; and the rotating near-zone vortex lines acquire accompanying tendex lines. Because of the evolution-equation duality between $\mathcal{E}_{ij}$ and $\mathcal{B}_{ij}$, the details of this wave formation are essentially the same for the rotating tendex and vortex lines. Now, in the near zone, the vectors $\boldsymbol{E}$ and $\boldsymbol{B}$ along the tendex and vortex lines (Fig. 3.5) make the same angle with respect to each other as in a gravitational wave (45 degrees) and have $\boldsymbol{E} \times \boldsymbol{B}$ in the $-z$ direction. This means that the gravitational waves produced by the rotating near-zone tendex lines and those produced by the rotating near-zone vortex lines will superpose constructively in the $-z$ direction and destructively in the $+z$ direction, leading to a maximized gravitational-wave momentum flow in the $-z$ direction and maximized black-hole kick in the $+z$ direction. An extension of this reasoning shows that the black-hole kick velocity is sinusoidal in twice the angle between the merged hole's near-zone rotating vortexes and tendexes, in accord with simulations.

3.5 Conclusions

In our BBH simulations, the nonlinear dynamics of curved spacetime appears to be dominated by (i) the transfer of spin-induced frame-drag vortexes from the initial holes to the final merged hole, (ii)

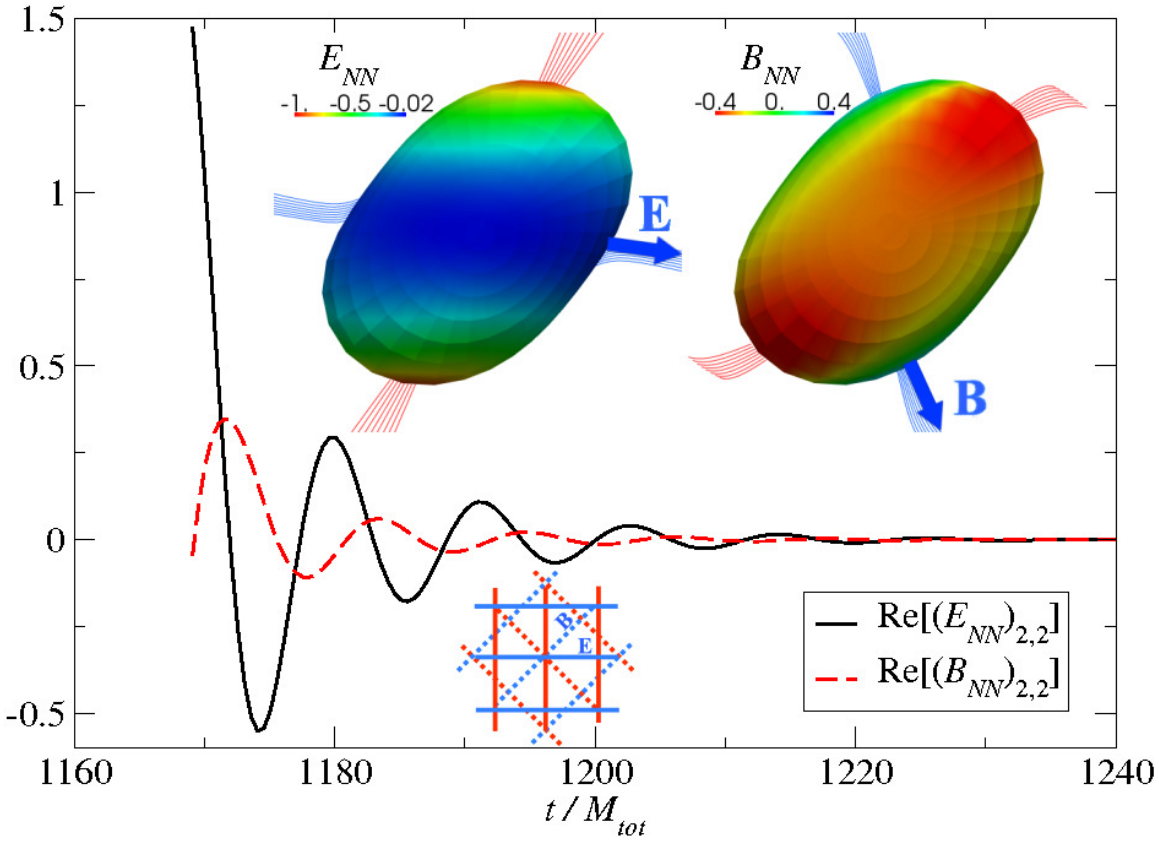

Figure 3.5: Bottom inset: tendex and vortex lines for a plane gravitational wave; $\boldsymbol{E} \times \boldsymbol{B}$ is in the propagation direction. Upper two insets: for the "extreme-kick simulation", as seen looking down the merged hole's rotation axis ($-z$ direction): the apparent horizon color coded with the horizon tendicity (left inset) and vorticity (right inset), and with 3D vortex lines and tendex lines emerging from the horizon. The tendexes with the most positive tendicity (blue; $\boldsymbol{E}$) lead the positive-vorticity vortexes (blue, $\boldsymbol{B}$) by about 45° as they rotate counterclockwise. This 45° lead is verified in the oscillating curves, which show the rotating $\mathcal{B}_{NN}$ and $\mathcal{E}_{NN}$ projected onto a nonrotating $\ell = 2$, $m = 2$ spherical harmonic.

the creation of two large vortexes on the merged hole associated with the orbital angular momentum, (iii) the subsequent sloshing, diffusion, and/or rotational motion of the spin-induced vortexes, (iv) the formation of strong negative $\mathcal{E}_{NN}$ poloidal tendexes on the merged horizon at the locations of the original two holes, associated with the horizon's elongation, and a positive $\mathcal{E}_{NN}$ tendex at the neck where merger occurs, and (v) the oscillation, diffusion, and/or circulatory motion of these tendexes.

We *conjecture* that there is no other important dynamics in the merger and ringdown of BBHs. If so, there are important consequences: (i) This could account for the surprising simplicity of the BBH gravitational waveforms predicted by simulations. (ii) A systematic study of frame-drag vortexes and tidal tendexes in BBH simulations may produce improved understanding of BBHs, including their waveforms and kicks. The new waveform insights may lead to improved functional forms for waveforms that are tuned via simulations to serve as templates in LIGO/VIRGO data analysis.

(iii) Approximation techniques that aim to smoothly cover the full spacetime of BBH mergers (e.g. the combined Post-Newtonian and black-hole-perturbation theory method [16]) might be made to capture accurately the structure and dynamics of frame-drag vortexes and tidal tendexes. If so, these approximations may become powerful and accurate tools for generating BBH waveforms.

Acknowledgements.—We thank Larry Kidder and Saul Teukolsky for helpful discussions. Our simulations have been performed using the Spectral Einstein Code (`SpEC`) [18]. This research was supported by NSF grants PHY-0601459, PHY-0653653, PHY-0960291, PHY-0969111, PHY-1005426, and CAREER grant PHY-0956189, by NASA grants NNX09AF97G and NNX09AF96G, and by the Sherman Fairchild Foundation, the Brinson Foundation, and the David and Barbara Groce fund.

Bibliography

[1] R. Maartens and B. A. Bassett, Class. Quantum Grav. **15**, 705 (1998).

[2] R. H. Price and K. S. Thorne, Phys. Rev. D **33**, 330915 (1986).

[3] K. S. Thorne, R. H. Price, and D. A. MacDonald, *Black Holes: The Membrane Paradigm* (Yale University Press, New Haven and London, 1986).

[4] G. Lovelace, Y. Chen, M. Cohen, J. D. Kaplan, D. Keppel, K. D. Matthews, D. A. Nichols, M. A. Scheel, and U. Sperhake, Phys. Rev. D **82**, 064031 (2010), `arXiv:0907.0869`.

[5] `http://www.black-holes.org/headon05aa.html`.

[6] E. Newman and R. Penrose, J. Math. Phys. **3**, 566 (1962), URL `http://link.aip.org/link/?JMP/3/566/1`.

[7] V. P. Frolov and I. D. Novikov, *Black Hole Physics: Basic Concepts and New Developments* (Kluwer, 1998).

[8] R. Penrose and W. Rindler, *Spinors and Space-time, Volume 1* (Cambridge University Press, Cambridge, 1992).

[9] T. Damour, in *Proceedings of the Second Marcel Grossman Meeting on General Relativity*, edited by R. Ruffini (North-Holland Publishing Company, Amsterdam, 1982), pp. 587–606.

[10] S. Chandrasekhar and S. Detweiler, Proc. R. Soc. A **344**, 441 (1975).

[11] `http://www.black-holes.org/inspiral95aa.html`.

[12] `http://www.black-holes.org/extreme-kick.html`.

[13] M. Campanelli, C. O. Lousto, Y. Zlochower, and D. Merritt, Phys. Rev. Lett. **98**, 231102 (2007), gr-qc/0702133.

[14] J. A. Gonzalez, M. D. Hannam, U. Sperhake, B. Brügmann, and S. Husa, Phys. Rev. Lett. **98**, 231101 (2007), gr-qc/0702052.

[15] C. O. Lousto and Y. Zlochower, Phys. Rev. D. **83**, 024003 (2011), arXiv:1011.0593.

[16] D. A. Nichols and Y. Chen, Phys. Rev. D **82**, 104020 (2010), 1007.2024.

[17] C. W. Misner, K. S. Thorne, and J. A. Wheeler, *Gravitation* (Freeman, New York, New York, 1973).

[18] http://www.black-holes.org/SpEC.html.

Chapter 4

On Toroidal Horizons in Binary Black Hole Inspirals

We examine the structure of the event horizon for numerical simulations of two black holes that begin in a quasicircular orbit, inspiral, and finally merge. We find that the spatial cross section of the merged event horizon has spherical topology (to the limit of our resolution), despite the expectation that generic binary black hole mergers in the absence of symmetries should result in an event horizon that briefly has a toroidal cross section. Using insight gained from our numerical simulations, we investigate how the choice of time slicing affects both the spatial cross section of the event horizon and the locus of points at which generators of the event horizon cross. To ensure the robustness of our conclusions, our results are checked at multiple numerical resolutions. 3D visualization data for these resolutions are available for public access online. We find that the structure of the horizon generators in our simulations is consistent with expectations, and the lack of toroidal horizons in our simulations is due to our choice of time slicing.

Originally published as Michael I. Cohen, Jeffrey D. Kaplan, and Mark A. Scheel. Toroidal horizons in binary black hole inspirals, Phys. Rev. D 85, 024031 (2012)

4.1 Introduction

It has long been known that a stationary black hole must have spherical topology [1]. For a non-stationary black hole, that is, one undergoing dynamical evolution, the situation is more complicated: the intersection of the event horizon and a given spatial hypersurface may be toroidal instead of spherical [2]; In fact, Siino has shown that event horizons may have topology of arbitrary genus [3, 4]. Event horizons with initially-toroidal topologies have been observed in numerical simulations of the collapse of rotating star clusters [5, 6].

A number of theorems restrict the conditions under which horizons can have toroidal topology; for instance, the torus must close up fast enough so that no light ray from past null infinity can pass through the torus and reach future null infinity [7, 8]. Additionally, it has been conjectured that for all toroidal horizons, a new spacetime foliation can be chosen so that the intersection of the horizon with each slice of the foliation has spherical topology [8].

The recent ability of numerical relativity to simulate the merger of two black holes (see refs. [9, 10] for recent reviews) provides a laboratory for studying the structure of event horizons that are far from stationary. Husa and Winicour predicted [11] that a brief toroidal phase should occur generically in binary black hole mergers, but until recently most numerical investigations of event horizons utilized some degree of symmetry. Diener [12] investigated event horizons in non-symmetric black hole collisions, including those of three black holes, but he did not have sufficient numerical resolution to determine whether a toroidal phase occurs in his simulations. More recently, Ponce [13] et. al. examined the merger of ring of eight black holes initially at rest and also found no evidence of a toroidal event horizon.

In this paper, we investigate the event horizons from two numerical simulations run with the `SpEC` [14] code by building on the work presented in the thesis of Michael Cohen [15]. The first simulation follows two black holes of (initially) zero spin and equal mass from a quasicircular orbit, through merger and ringdown [16, 17]. The second simulation is similar, but fully generic: the mass ratio is 2:1, and the initial spins of magnitude $a/M \simeq 0.4$ are not aligned with each other or with the initial orbital plane [18]. Table 4.1 lists parameters of these two simulations, and also parameters of two previous simulations for which the detailed shape of the event horizon was discussed in earlier works [19, 20].

For all of these simulations, we find the event horizon by the method described in Ref. [19]: we choose a set of outgoing null geodesics that lie on the apparent horizon of the remnant black hole at the end of the simulation when the spacetime is nearly stationary, and we integrate these geodesics backwards in time. These geodesics exponentially converge onto the event horizon, so we will refer to them as *generators* of the horizon even though they are only (very good) approximations to the true generators.

It is important to note that the event horizon is only a subset of the surface generated by these generators. Under subsequent evolution backwards in time, some of the generators leave the horizon at points where they meet other generators[21, 22]. These meeting points have been studied extensively [6, 11, 23] and can be separated into two types: *caustics*, at which neighboring generators focus and converge, and *crossover points*, at which non-neighboring generators cross. Much of the work in studying the structure of the event horizon in numerical simulations involves identifying the crossover and caustic points, so as to determine when the generators are on or off the horizon. In this work we make an effort to clarify the structure of event horizon caustics and crossovers for the

cases of spatial slices with and without a toroidal event horizon surface.

Of course, any numerical study of event horizons is limited by several different sources of numerical error. Consequently, the identification of caustic and crossover points must be carefully analyzed to ensure that one's conclusions are not tainted by discretization errors. Discretization error could arise from, for example, both the 3+1 spacetime resolution of the underlying black hole simulation, *and/or* the 2+1 spacetime resolution of the event horizon hypersurface. Accordingly, one important goal of this work is to investigate whether our conclusions are robust when we change the (relatively high) spatial and temporal resolution of our event horizons.

We note that it is not always easy to visualize the event horizon's topological structure from the two-dimensional screenshots we can include in this work. Therefore, we make our event horizon data for the generic merger, Run 2 from Table 4.1, available online for the reader to explore at `http://www.black-holes.org/onToroidalHorizonsData.html`. Included are detailed instructions on how to visualize and compare the event horizon data for different resolutions using freely available 3D visualization software [24]. Also included there are saved state and camera view files allowing the reader to jump to the views displayed in this work, providing the ability for the reader to see the event horizons as they are featured in this paper's figures [25].

The organization of this paper is as follows: In Section 4.2 we present modifications to our event-horizon finder [19] that allow us to detect crossover points, i.e. intersections of non-neighboring horizon generators. In Section 4.3 we apply this method to find the event horizon of two binary black hole simulations in which the black holes merge after inspiraling from an initially quasicircular orbit. We find that the merged horizon has spherical topology to the limit of our numerical accuracy. In Section 4.4 we review the structure of crossover points and caustics in binary black hole collisions. We show how toroidal horizon cross sections are possible in black hole collisions without symmetry, and how the existence of toroidal cross sections depends on the choice of time slicing. In Section 4.5 we identify the crossover points and caustics of the horizon generators for our numerical simulations, and show that they are consistent with expectations for generic binary black hole mergers. In particular, we infer that there should exist a different slicing of our numerical spacetime such that a toroidal horizon is present for a finite coordinate time. We summarize our findings and conclude in Section 4.6.

4.2 Identification of Crossover Points

A key challenge in computing an event horizon is to accurately determine when each of the generators being tracked merges onto the horizon. The set of merger points can be classified into two types: caustics, which occur when neighboring generators focus and converge, and crossovers, which occur when non-neighboring generators cross. The set of crossover points generically forms a two-

Run	M_A/M_B	$\vec{S}_A/M_A^2$	$\vec{S}_B/M_B^2$	Type	Ref
1	1	0	0	orbit	[16, 17]
2	2	$-0.4(\hat{z}+\hat{y})/\sqrt{2}$	$0.2(\hat{z}-\hat{x})/\sqrt{2}$	orbit	[18]
3	1	0	0	head-on	[19]
4	1	$0.5\hat{z}$	$-0.5\hat{z}$	head-on	[20]

Table 4.1: Binary black hole simulations for which we have investigated the topology of the event horizon. Listed are mass ratios, initial spins, and whether the black holes are colliding head-on or are initially in quasicircular orbit. The first two simulations are discussed in the present paper, and for these the $\hat{z}$ direction is parallel to the initial orbital angular momentum; the last two simulations are head-on collisions along the $\hat{x}$ direction, and are discussed in refs [19] and [20].

dimensional subset of the three-dimensional event horizon hypersurface, (see Figure 4.3 right panel), and the set of caustics generically forms the boundary of the set of crossovers [11, 23].

In previous applications of our event-horizon finder it sufficed to search only for caustics and not for crossover points. Ref. [19] treated only axisymmetric head-on black hole collisions, for which all crossovers are also caustics (cf. Run 3 of Table 4.1). Interestingly, we found that for spinning, head-on black hole collisions (cf. Run 4 of Table 4.1) [20], despite the lack of pure axisymmetry, the set of crossover points is also composed entirely of caustics. However, for finding the event horizon of a binary black hole system that inspirals and merges, we find it is necessary to develop a technique for detecting crossover points.

On any given spacelike slice, the set of generators forms a smooth, closed two-dimensional surface that may self-intersect (at crossover points and/or caustics). We detect caustics by monitoring the local area element on this surface [19]; the area element vanishes at caustics. In order to detect crossover points, we model this surface as a set of triangles, and we check whether each generator has passed through each triangle between the current and the previous time step.

To define these triangles, we note that the surface of generators can be mapped to a two-sphere with standard polar coordinates $u \in [0, \pi], v \in [0, 2\pi)$ in such a way so that each generator is tied to a specific value of u and v for all time. The generators are placed on a grid in (u, v) space, and the triangles are defined on this grid. Thus the property "neighbor-ness" (i.e. knowing which geodesics are to the left/right/above/below any given geodesic) is maintained throughout the simulation. We choose the grid points in (u, v) space to be the collocation points of a pseudospectral expansion in spherical harmonics of order L, and we use this L to describe the numerical resolution of the event horizon finder. There are no geodesics at the poles $u = 0$ and $u = \pi$, so for the purpose of defining triangles we place artificial points there (the simulation coordinates x, y, z of such a pole point are defined as the mean of the x, y, z coordinates of the nearest neighboring geodesics). Thus each triangle near the pole is formed from the artificial pole point plus two points that represent geodesics. The number of geodesics in a surface of resolution L is $2(L+1)^2$, and the number of triangles in the surface is $4(L+1)^2$. The algorithm compares every triangle with every geodesic

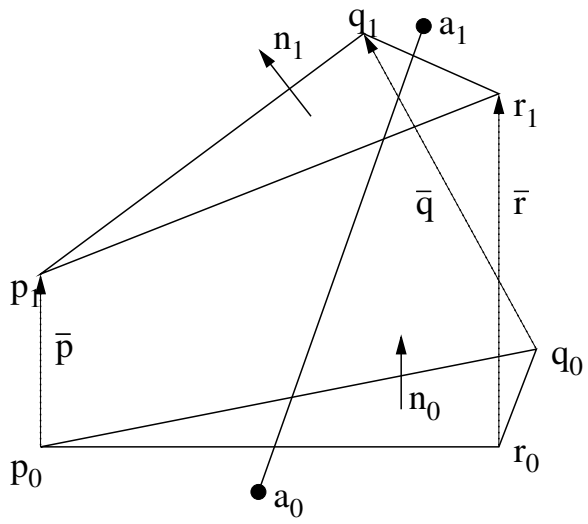

Figure 4.1: Crossover-detection algorithm illustrated by a geodesic crossing a moving triangle. Points p_0, q_0, and r_0 form the triangle at time t_0, and points p_1, q_1, and r_1 form the triangle at time t_1. Likewise points a_0 and a_1 represent the geodesic at times t_0 and t_1.

point, to determine whether the geodesic has passed through that triangle between the current and previous time step. Therefore, if the number of geodesics on the horizon is N, the number of triangles is $2N$, and the computational cost of the algorithm scales as $\mathcal{O}(N^2) = \mathcal{O}(L^4)$.

Determining whether the point has passed through the triangle proceeds as follows (see Figure 4.1 for a diagram): Suppose that the positions of the three geodesics that comprise the vertexes of the triangle at time t_0 are p_0, q_0, r_0, and the position of the potentially intersecting geodesic is a_0. At time t_1 , one time step later, these positions are p_1, q_1, r_1 and a_1. We assume that the geodesics move linearly in space during the short interval between time t_0 and t_1. Thus $p(t) = p_0 + t(p_1 - p_0) = p_0 + t\bar{p}$, and similarly for q, p and a. We now define the normal of the triangle at time t_0

$$n_0 = (q_0 - p_0) \times (r_0 - p_0), \tag{4.1}$$

where we have assumed that the orientation of the triangle points is anti-clockwise. As a function of time, the normal is

$$\begin{aligned} n(t) &= (q(t) - p(t)) \times (r(t) - p(t)) \\ &= (q_0 - p_0 + t(\bar{q} - \bar{p})) \times (r_0 - p_0 + t(\bar{r} - \bar{p})) \\ &= (q_0 - p_0) \times (r_0 - p_0) + t[(\bar{q} - \bar{p}) \times (r_0 - p_0) + \\ &\quad (q_0 - p_0) \times (\bar{r} - \bar{p})] + t^2(\bar{q} - \bar{p}) \times (\bar{r} - \bar{p}). \end{aligned} \tag{4.2}$$

Since $p_0, q_0, r_0, \bar{p}, \bar{q}, \bar{r}$ are known quantities, we can write Equation 4.2 as

$$n(t) = n_0 + \alpha t + \beta t^2. \tag{4.3}$$

Now, any given plane P has the property that

$$\forall i \in P, \qquad i \cdot n_P = D, \tag{4.4}$$

where D is a constant, and n_P is the normal of the plane. Now, $D(t) = p(t) \cdot n(t)$, a cubic equation, so our geodesic $a(t)$ and the triangle $\{p, q, r\}(t)$ are coplanar at times t that satisfy the equation

$$p(t) \cdot n(t) - a(t) \cdot n(t) = n(t) \cdot (p(t) - a(t)) = 0. \tag{4.5}$$

Equation 4.5 is a cubic with algebraic roots, which can be solved for analytically. For every root found between $t_0 < t \leq t_1$, it is a simple matter to check whether $a(t_{\text{root}})$ is within the triangle $\{p, q, r\}(t_{\text{root}})$, rather than merely being co-planar.

There are a few special cases to be checked, such as ensuring that the geodesic being tested for intersection is not one of the geodesics that make up the triangle, or cases for which the cubic equation is degenerate, but the algorithm itself is quite robust and effective. Although the algorithm is, as mentioned above, $\mathcal{O}(N^2)$, the expense of the algorithm is mitigated by two factors. Firstly, since the algorithm involves analytically solving an at most cubic equation, the run time of each individual instance is very small, on the order of microseconds. Secondly, the looping condition is sufficiently simple that it can be parallelized over multiple cores without any significant CPU overhead. In practice, with typical resolutions of between $30,000$ & $60,000$ geodesics, the run time is not prohibitive.

4.3 Event horizons from numerical simulations of binary black hole mergers

Husa and Winicour [11] posit that mergers of binary black holes in a non-axisymmetric configuration generically result in an intermediate toroidal state of the event horizon. Previously (cf. Runs 3 and 4 of Table 4.1) we have found that merger occurs at a single point in not only the axisymmetric head-on merger [19], but also the head-on spinning merger [20] (where axisymmetry is broken). Therefore, we were strongly motivated to determine the topological behavior of the event horizon for mergers of black holes that inspirals from an initially quasicircular orbit, where axisymmetry is broken in no uncertain terms.

Figure 4.2 shows the event horizons from two numerical simulations of binary black hole coales-

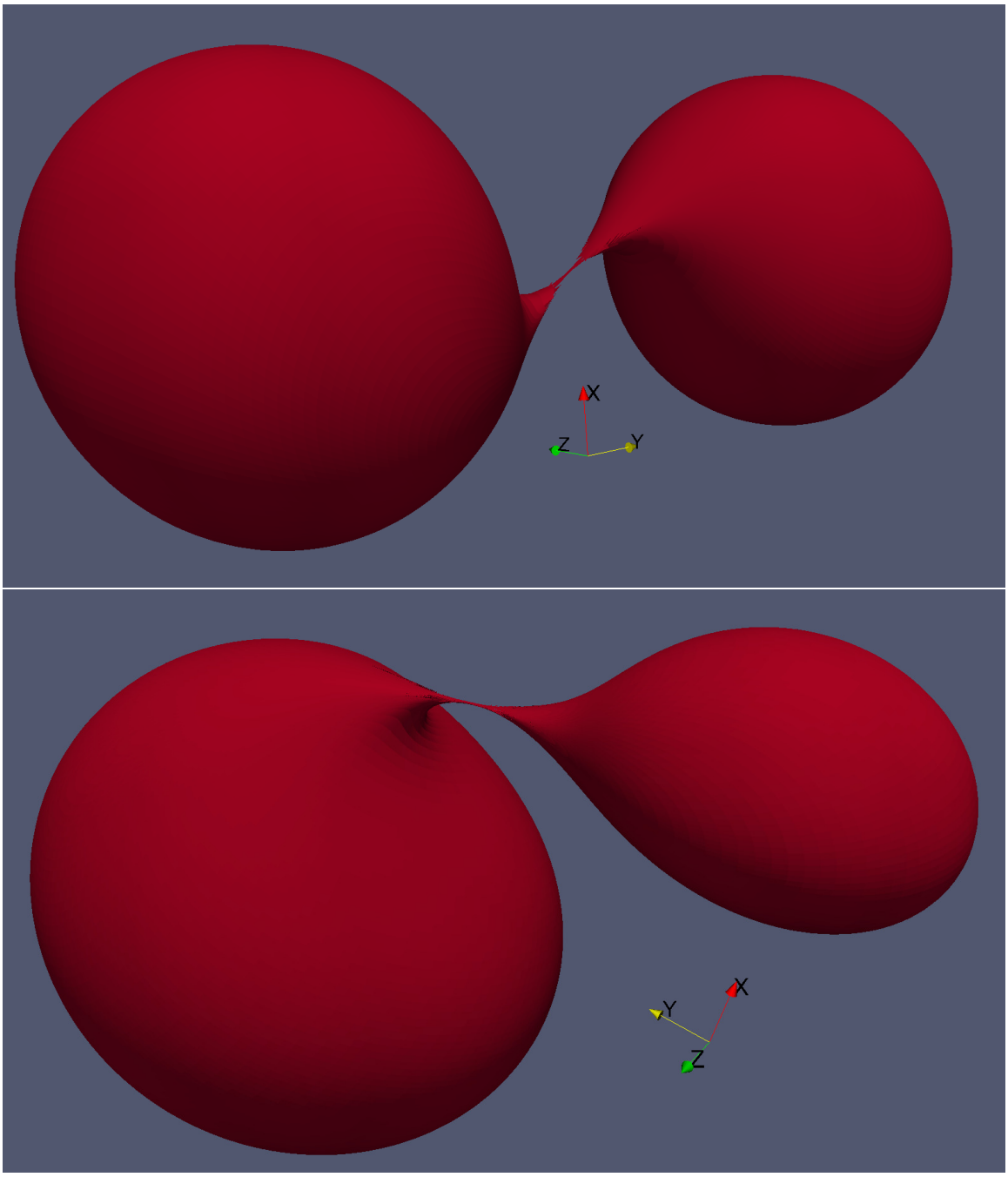

Figure 4.2: *Color online.* Slices through the event horizon at the exact point of merger to within numerical accuracy. **Upper panel:** Equal-mass non-spinning 16-orbit inspiral, Run 1 of Table 4.1, at $t/M = 3902.897$; the point of merger is $t_{\rm merger}/M = 3902.897 \pm 0.006$. Here M is the sum of the ADM masses. **Lower panel:** Generic merger, Run 2 of Table 4.1, at $t/M = 117.145$; the point of merger is $t_{\rm merger}/M = 117.145 \pm 0.005$. The error estimates come from the time resolution of our event horizon finder (i.e. our EH finder time step is $\sim 0.005M$); note that the merger occurs at the same time (within this error bound) for both medium and high resolutions of the numerical relativity simulations. At earlier times the two black hole horizons are disjoint. No toroids are evident in the limit of our accuracy.

cence, at the time of merger. In the top panel, the two black holes start in a quasicircular orbit, and have equal masses and initially zero spins; details of this simulation were published in Ref. [16]. The bottom panel shows a fully generic situation: again the black holes start in a quasicircular orbit, but the mass ratio is 2:1, and the initial spins have magnitude $a/M \simeq 0.4$ and are not aligned with each other or with the initial orbital plane. This simulation is "case F" of Ref. [18]. For both of these simulations, we find the generators of the event horizon using the "geodesic method" of [19]. We integrate generators backwards in time, and when we find that generators leave the event horizon, either through caustics (as determined by the vanishing of the local area element of the surface of generators [19]) or through crossover points (as determined by the method described in Section 4.2) we flag them as having left the horizon. Figure 4.2 plots only those generators that are on the horizon at the time of merger. In both the equal-mass and generic cases, our results show that the event horizons merge at a point, with no intermediate toroidal phase to the limit of our numerical accuracy.

4.4 Topological structure of the Event Horizon for inspiraling and merging black holes

In order to understand why no toroidal intermediate stage is found in our simulations, we need to further understand the topological structure of the event horizon null hypersurface in the case of a binary inspiral and merger. In [11], Husa and Winicour consider two sets of points. One set, labeled $\mathcal{C}$, is the set of all caustic points in the spacetime where neighboring event horizon geodesics cross. The other set of points, $\mathcal{X}$, is the set of all crossover points in the spacetime, where non-neighboring event horizon geodesics cross. They show that the set of points $\mathcal{X}$ is an open 2-surface on the event horizon null hypersurface $\mathcal{N}$, and that this set is bounded by the caustic set $\mathcal{C}$. They further show that the behavior of this 2-surface of caustic/crossover points is governed by the topology of the merger. In an axisymmetric prolate merger (such as our headon case), the 2-surface is reduced by the symmetry, resulting in the single boundary line of caustic points we see as being the "inseam" of the "pair of pants," as shown in the left panel of Figure 4.3. In the non-axisymmetric case, the set of caustic and crossover points is a 2-surface on the event horizon, as shown in the case of a binary black hole inspiral in the right panel of Figure 4.3 (where we show the merger in a corotating frame).

The question of whether toroidal horizons can be found in the intermediate stages of binary black hole merger can be answered by considering the various ways in which these "pair of pants" diagrams can be sliced. The fact that the set caustic/crossover points $\mathcal{C} \cup \mathcal{X}$ is a spacelike 2-surface on a non-axisymmetric event horizon hypersurface (and, for an axisymmetric case, the line of points $\mathcal{C}$ is a spacelike line) provides some freedom in the allowed spacelike slicings of this surface.

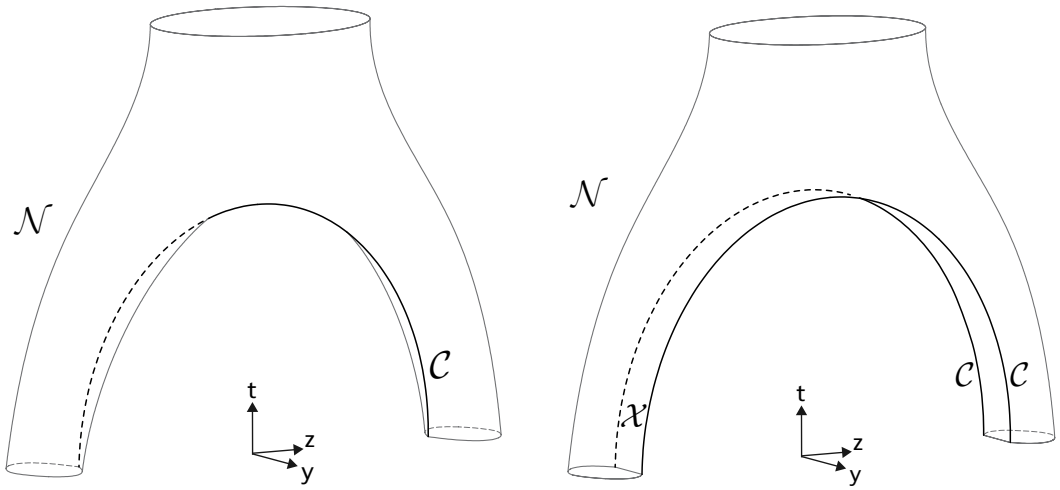

Figure 4.3: Diagrams of the event horizon null hypersurface, $\mathcal{N}$, in axisymmetric and non-axisymmetric mergers. The merger is along the z-axis. In both panels, the regions $\mathcal{C} \cup \mathcal{X}$ are spacelike. **Left panel:** In the axisymmetric case, the caustic/crossover set is reduced to a single line of caustic points, the "inseam" of the "pair of pants," labeled $\mathcal{C}$. The x direction is suppressed but, since the x and y directions are identical for axisymmetry, the diagram would be unchanged if we were to suppress y in favor of x. **Right panel:** In the non-axisymmetric case, such as an inspiral (where we have "unwound" the legs of the "pair of pants" by going to a corotating frame), the set of crossover points $\mathcal{X}$ is two-dimensional, bounded on both sides by "inseams" $\mathcal{C}$. Unlike the axisymmetric case, here the x and y directions are not identical. Since the caustic/crossover set of points is a 2-surface, the diagram we would obtain by suppressing y in favor of x would look identical to the left panel, except that the single "inseam" would be composed of crossover points.

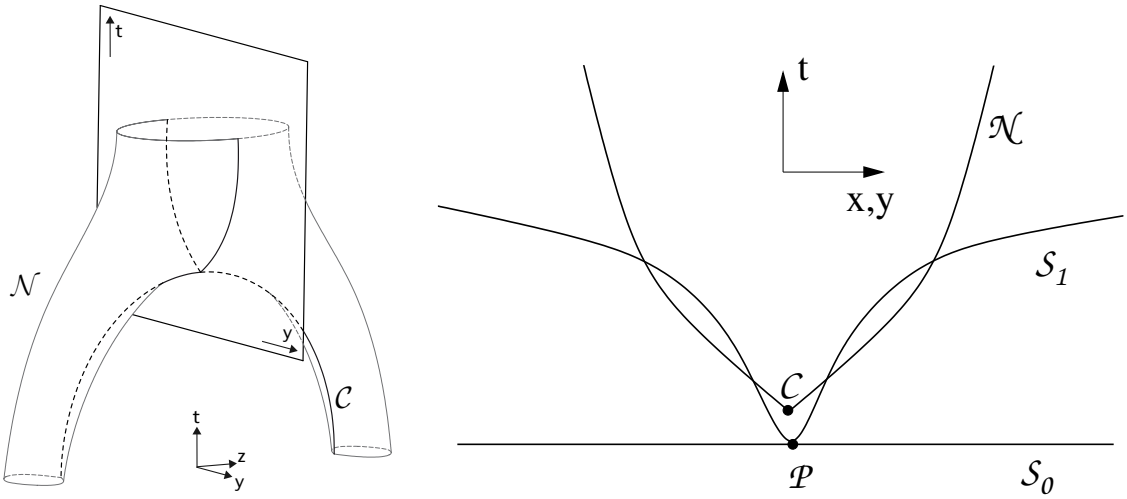

Figure 4.4: A 2-dimensional slice through the event horizon null hypersurface, $\mathcal{N}$, in an axisymmetric merger. The horizontal direction in the right panel could be either x or y. We attempt to construct a slice $\mathcal{S}_1$ in x (or y) from point $\mathcal{P}$ that intersects the black hole. This slice is clearly not spacelike. Since $\mathcal{N}$ is spacelike only at $\mathcal{C}$, only a slice such as $\mathcal{S}_0$ that does not intersect the black hole can be both spacelike and pass through $\mathcal{P}$.

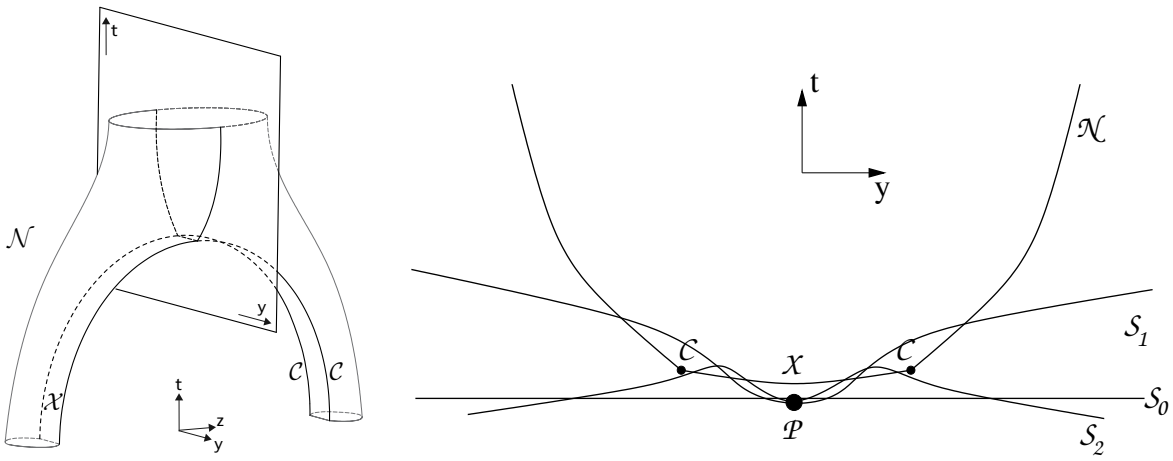

Figure 4.5: A 2-dimensional slice through the event horizon null hypersurface, $\mathcal{N}$, in a non-axisymmetric merger. Unlike the previous figure, the horizontal direction in the right panel is not interchangeable between x and y. We construct three slices $\mathcal{S}_0, \mathcal{S}_1, \mathcal{S}_2$ from the starting point $\mathcal{P}$. These slices intersect the event horizon in different ways. Since $\mathcal{C} \cup \mathcal{X}$ is spacelike, all these slices are spacelike. Although exaggerated for effect, the tangent to $\mathcal{X}$ in the t-y plane becomes null at $\mathcal{C}$ (see [6]).

Let us first consider whether a nontrivial topology might be obtained in the axisymmetric case. In order to do so, we need to consider how such a slice may be constructed. Clearly, if we were to construct "horizontal" spatial slices of the null hypersurface in the left panel of Figure 4.3, we would produce a slicing in which the merger occurred at a point. However, we can attempt to construct slices in which the lapse is somewhat retarded near the "crotch." In Figure 4.4 we examine a 2-dimensional slice in $\{t, y\}$ through the center of the hypersurface. It is clear that if we choose a central point for the slice before the merger of the black holes, we cannot extend a spacelike slice from this central point in either the x or y directions in such a way as to encounter the black holes. Only in the z direction can we encounter the black holes.

This changes however, when we consider the non-axisymmetric case. In this case, the x and y directions are different, as shown in the right panel of Figure 4.3. In Figure 4.5 we show a $\{t, y\}$ 2-slice of the event horizon. The event horizon, $\mathcal{N}$, is spacelike both at $\mathcal{C}$, and along the line $\mathcal{X}$. Thus, given a point $\mathcal{P}$ below the "crotch" of the event horizon, we can construct three distinct slices, each with different behavior. Slice $\mathcal{S}_0$ does not encounter the event horizon at all in the y direction. Slice $\mathcal{S}_1$ encounters the event horizon four times: twice in the null region, and twice in the spacelike region. Finally, slice $\mathcal{S}_2$ encounters the event horizon four times in the spacelike region. Note that in the x direction, the slice through the event horizon is identical to slice $\mathcal{S}_0$ of Figure 4.4 (except that the "inseam" is part of the crossover set $\mathcal{X}$ instead of the caustic set $\mathcal{C}$). Therefore, if we slice our spacetime using slices $\mathcal{S}_1$ or $\mathcal{S}_2$, our slice encounters the event horizon four times in the z and y directions, and not at all in the x direction. This is precisely a toroidal intermediate stage. Such

slices can be seen in three dimensions $\{t, y, z\}$ in Figure 4.6.

We now consider what the event horizon looks like in three spatial dimensions $\{x, y, z\}$ on each of the slices $\mathcal{S}_0$, $\mathcal{S}_1$, or $\mathcal{S}_2$ of Figures 4.5 and 4.6. The top panel of Figure 4.7 shows the intersection of the event horizon with the slice $\mathcal{S}_0$. Compare with Figure 4.6, which shows the same slice in the dimensions $\{t, y, z\}$. The slice $\mathcal{S}_0$ does not encounter the event horizon in the $x - y$ plane; this plane lies between the two black holes. On each black hole, the slice $\mathcal{S}_0$ encounters the two-dimensional crossover set $\mathcal{X}$ along a one-dimensional curve, and this curve is bounded by two caustic points from the set $\mathcal{C}$.

In contrast, the intersection of the event horizon with the slice $\mathcal{S}_1$ is shown in the middle panel of Figure 4.7. Compare with Figure 4.6, which shows the same slice in the dimensions $\{t, y, z\}$. This is a toroidal cross section of the horizon. Slice $\mathcal{S}_1$ intersects the event horizon four times along the y axis: the outer two points are in the null region of the horizon $\mathcal{N}$ and the inner two are in the spacelike crossover set $\mathcal{X}$. Note that the inner edge of the torus *is made up entirely of crossover points from the set* $\mathcal{X}$ and does not include caustic points nor points in the set $\mathcal{N}$. The existence of an isolated set of crossovers that cannot be connected to caustics is a key signature of a toroidal horizon.

The bottom panel of Figure 4.7 shows the intersection of the event horizon with the slice $\mathcal{S}_2$, which is shown in the $\{t, y\}$ directions in Figure 4.5. This slice also produces a torus. Slice $\mathcal{S}_2$ intersects the event horizon four times along the y axis, and each of these intersections is a crossover point in $\mathcal{X}$. As was the case for slice $\mathcal{S}_1$, the inner edge of the torus for slice $\mathcal{S}_2$ also consists entirely of crossover points. The outer edge of the event horizon intersects the two-dimensional crossover set $\mathcal{X}$ along two one-dimensional curves, and each of these curves is bounded by caustic points on each end.

It is important to note another distinction between the behavior of slices $\mathcal{S}_1$ and $\mathcal{S}_2$ in Figures 4.5 and 4.7. When a slice intersects the event horizon at a point that is a member of $\mathcal{C} \cup \mathcal{X}$, that point is the point where two generators of the event horizon pass through each other as they merge onto the event horizon. Consequently, that point is not a smooth part of the event horizon. If instead the slice intersects the event horizon at a point not in $\mathcal{C} \cup \mathcal{X}$, that point is a smooth part of the event horizon. Therefore, $\mathcal{S}_1$ corresponds to a toroidal intermediate stage where the torus has a non-smooth (i.e. sharp) inner edge and a smooth outer edge, and $\mathcal{S}_2$ corresponds to a stage where both the outside and the inside of the torus are sharp-edged. There also exists the possibility of a slice that looks like $\mathcal{S}_1$ in the positive y direction and looks like $\mathcal{S}_2$ in the negative y direction or vice versa; on such a slice the outer edge of the torus will be sharp on one side and smooth on the other.

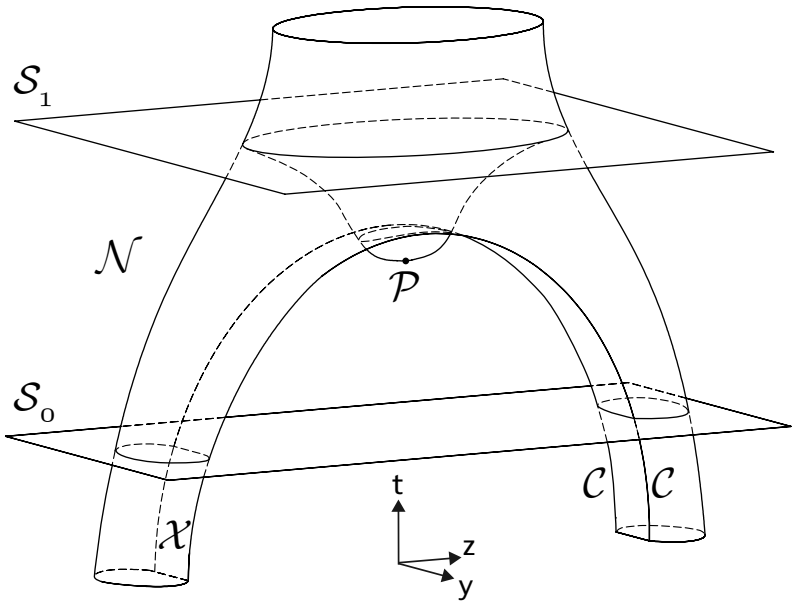

Figure 4.6: A 3-dimensional representation of slices $\mathcal{S}_0$ and $\mathcal{S}_1$ from Figure 4.5. Here we see the continuation of each slice in the z direction. The event horizon is toroidal on slice $\mathcal{S}_1$; the center of the torus is $\mathcal{P}$. The toroidal region is the part of $\mathcal{S}_1$ that has dipped through the crossover region $\mathcal{X}$.

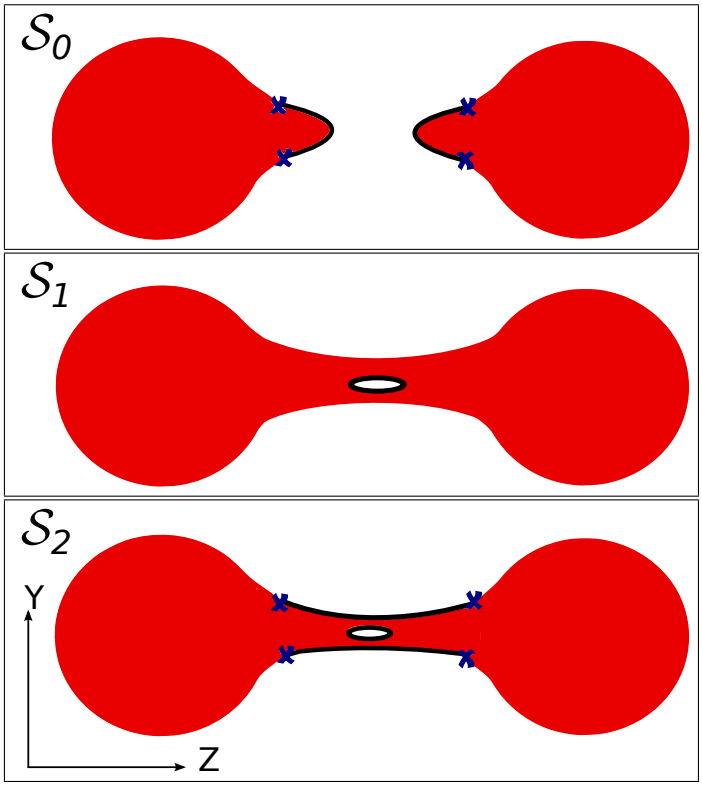

Figure 4.7: *Color online.* Cartoon illustrations of spatial slices $\mathcal{S}_0$, $\mathcal{S}_1$, and $\mathcal{S}_2$ of Figures 4.5 and 4.6. Null generators currently on the horizon are in red; linear sets of crossovers merging onto the horizon are indicated by black lines, and the location of caustic points are denoted by blue Xs.

4.5 Topological Structure of Simulated Event Horizons

Having shown how an appropriate choice of slicing yield spatial slices in which the event horizon is toroidal, we now hope to convince the reader that, up to the limit of our numerical resolution, we see no signs of a toroidal event horizon in the slicing of our simulations. In greater generality, we would like to answer the following question: What is the structure of caustic and crossover points for the simulations we have performed, and how do those results relate to the structure discussed in the previous section?

We can use Figure 4.6 to predict the structure of caustic and crossover points for an early slice through the event horizon of a non-axisymmetric merger. Unlike the axisymmetric case, where all geodesics merge onto the event horizon at a point, an early slice of the non-axisymmetric merger, say slice $\mathcal{S}_0$ in Figure 4.6, should show each black hole with a linear cusp on its surface, through which geodesics merge onto the horizon. The cusp should be composed of crossover points, except that the boundaries of the cusp should be caustic points. At a later time, the two black holes will merge, and whether or not a torus is formed depends on how the slice intersects the set of caustics and crossovers, as seen in Figure 4.7.

To clarify let us first state a precise condition for the presence or absence of a toroidal event horizon: A slice *without* a toroidal event horizon has the following property: For every crossover point on the horizon, there exists a path from that crossover point to a caustic point, such that the path passes through only crossover points (cf. Figure 4.7). For a slice *with* a toroidal event horizon, there exist crossover points on the horizon that are disconnected from all caustics, in the sense that no path can be drawn along crossovers that reaches a caustic. For example, in slices $\mathcal{S}_1$ and $\mathcal{S}_2$ of Figure 4.7, the crossover points on the inner edge of the torus are disconnected from all caustics.

A slicing of spacetime where the event horizon is never toroidal will appear like slice $\mathcal{S}_0$ at early times. Approaching merger, the two disjoint crossover sets will extend into "duck bill" shapes and then meet at a point, forming an "X" shape at the exact point of merger. After merger, the crossover set will then disconnect and will look like the outer edges of the horizon of slice $\mathcal{S}_2$ (with no torus in the middle). At even later times, each disjoint crossover set on the outer edge of the horizon will shrink to a single caustic point and then disappear.

A slicing of spacetime in which the event horizon is toroidal will also look like slice $\mathcal{S}_0$ at early times. But at times approaching merger, the disjoint crossover sets will meet at *two* (or more) points instead of one. If these meeting points are the caustics, then just after merger these caustics will disappear, leaving a ring of crossovers, and the horizon will look like slice $\mathcal{S}_1$ of Figure 4.7. If instead these meeting points are crossover points, then the crossover set will form a double "X" shape at merger, and after merger, the crossovers in the middle will form a ring, and the horizon will look like slice $\mathcal{S}_2$ of Figure 4.7. In this latter case, each disjoint crossover set on the outer edge of the

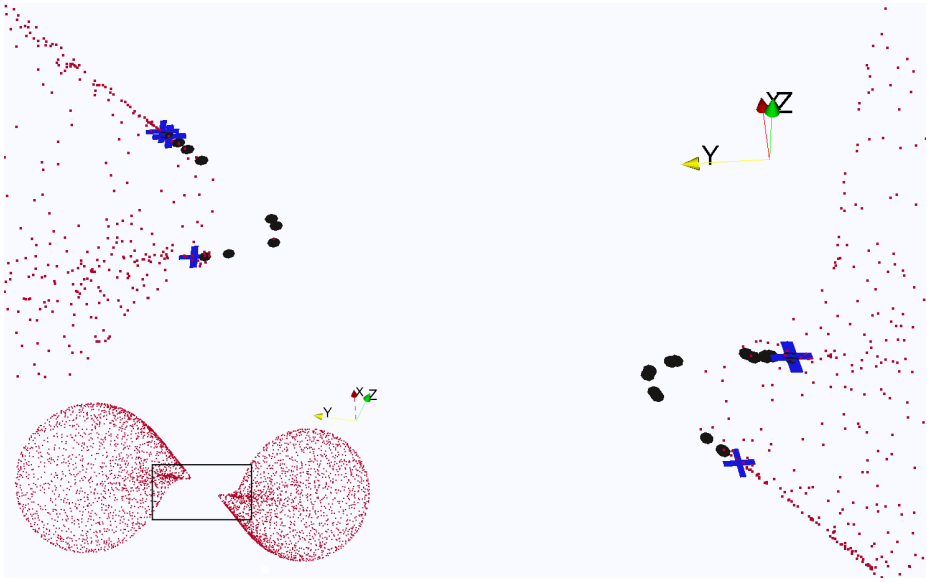

Figure 4.8: *Color online.* A snapshot of the geodesics being followed by the event horizon finder at time $t/M = t_{\rm merger}/M - 0.067$, for the equal-mass inspiral. The small dots are geodesics currently on the event horizon. The larger points, either crosses or circles, represent geodesics in the process of merging onto the event horizon. Crosses represent points merging through caustic points, while circles represent points merging through crossovers. In this slice, the cusp on the black hole is linear, and composed of crossover points with caustics at the end points.

horizon will eventually shrink to a single caustic point and then disappear. Furthermore, the central ring of crossovers will eventually shrink to a single point and disappear. If the disappearance of the crossovers on the horizon edge occurs before the disappearance of the central ring of crossovers, then for some time the horizon will look like slice $\mathcal{S}_1$ of Figure 4.7.

Comparing these predictions with the results of a simulation of finite numerical resolution requires care, since single points (such as the point of merger or the single caustic points that bound the crossover sets) cannot be found with infinite precision. We will discuss these limitations in the concluding paragraphs of this section. Let us now analyze the two numerical simulations studied here in detail.

4.5.1 Equal-mass non-spinning merger

In Figures 4.8–4.10,[1] we examine our simulation of the coalescence of two equal-mass non-spinning black holes. This simulation clearly displays the characteristics of a non-axisymmetric merger: the black holes do indeed have linear cusps on their surfaces, and we find caustic points occuring at the edges of the cusps.

Figure 4.8 shows generators before the point of merger. At this time, our slicing is consistent

[1]The axes in all snapshots are *not* the same as the axes denoted in Figures 4.3–4.7. They correspond to the coordinate axes of the binary black hole merger simulations and illustrate the relative camera angle between snapshots.

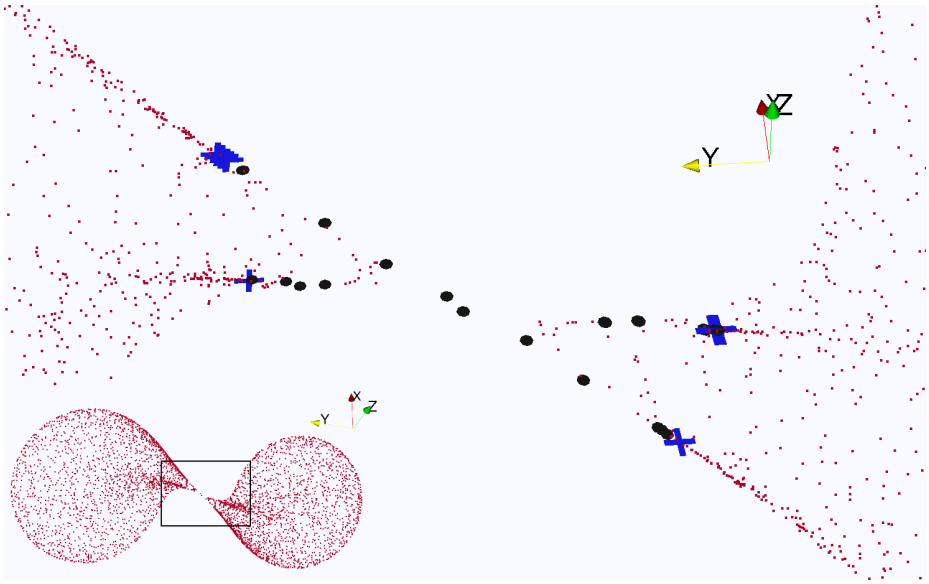

Figure 4.9: *Color online.* A snapshot of the geodesics being followed by the event horizon finder at time $t/M = t_{\rm merger}/M$, the exact point of merger (to within numerical error) in the equal-mass inspiral simulation. Labels are the same as in Figure 4.8. Although finding the exact point of merger is difficult given limited numerical time accuracy, we can extrapolate the "X" shape of the cusps to see that the merger point is clearly a crossover point.

with slices parallel to $\mathcal{S}_0$ in Figure 4.5. These slices correspond to late enough times that they have encountered the horizon's linear cusps but early enough times that they have not yet encountered points $\mathcal{C}$ in Figure 4.5. The event horizon slices show a "bridge" extending partway between the black holes, with cusps along each side. Each cusp is a line of crossover points on one of the black holes, anchored at each end by a caustic point.

At the precise point of merger (Figure 4.9) our slicing remains consistent with slices parallel to $\mathcal{S}_0$ in Figure 4.5. In this figure, slices parallel to $\mathcal{S}_0$ encounter the crossover region at slightly earlier times than they encounter the caustic lines. Therefore, at merger, the slice will intersect the horizon at one point (a crossover point) in the y direction, and this point is where the linear cusps on the individual black holes meet. Consequently, the slice at the point of merger is expected to have a rough "X" shape of crossover points, meeting at the merger point, and anchored at the edges of the black hole cusps by caustic points. In Figure 4.9, we see that this is indeed the case. Note that if our slicing were similar to slice $\mathcal{S}_1$ in Figure 4.5 rather than slice $\mathcal{S}_0$, the linear cusps of the individual black holes would meet at two points rather than one, and these two points would be the caustic points at the boundary of the cusps. Similarly, if our slicing were similar to slice $\mathcal{S}_2$ in Figure 4.5, the cusps on the individual black holes would again meet at two points, and these would be crossover points. According to Figure 4.5, presumably there should exist slicings in which the two black holes would first touch at multiple points and form horizons of arbitrary genus.

After merger, the "X" shape of the merger has disconnected, resulting in two line segments of

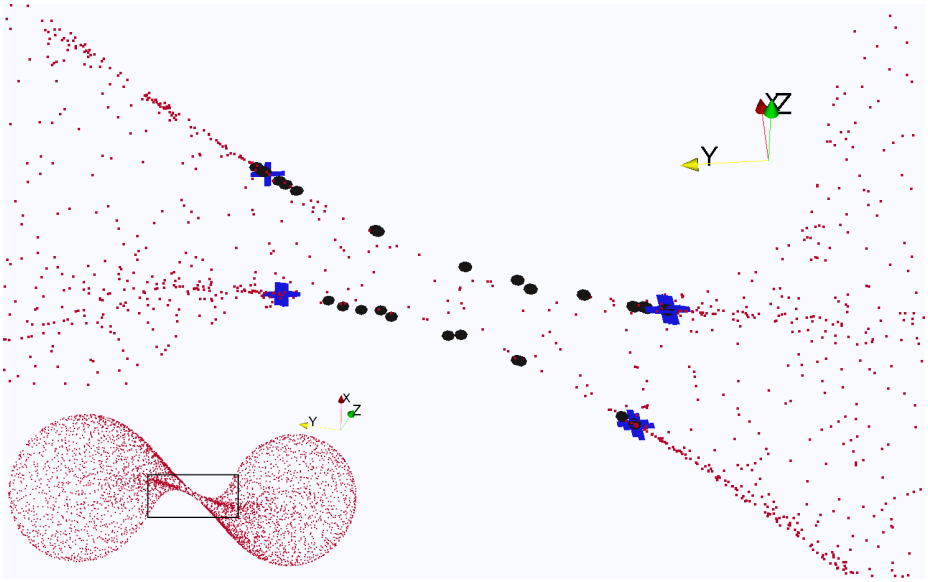

Figure 4.10: *Color online.* A snapshot of the geodesics being followed by the event horizon finder at time $t/M = t_{\rm merger}/M + 0.039$, shortly after merger, for the equal-mass inspiral. Labels are the same as in Figure 4.8. The "bridge" between the two black holes has two lines of merger points running on either side of it, with the majority being crossover points anchored by caustics at either end.

crossover points still bounded by caustics. This is clearly visible in Figure 4.10.

Note that in Figures 4.8–4.10, we sometimes find multiple caustic points at the edge of the crossover set, rather than a single caustic point; this appears to be an effect of the finite tolerance of the algorithm that we use to identify caustic points. Similarly, we sometimes find caustic points that are slightly outside the crossover set, as in Figure 4.10. This too appears to be a finite-resolution effect. For the generic run below, we will present horizon figures computed with different number of geodesics in order to better understand this effect.

4.5.2 2:1 mass ratio with 'randomly' oriented spins

Here we examine in detail the topological structure of a generic binary black hole merger, Run 2 of Table 4.1. As noted earlier, this simulation corresponds to "case F" of Ref. [18]. We use the term 'generic' to highlight the fact that this simulation lacks degeneracies in the parameter space of possible binary black hole mergers. While the equal-mass non-spinning simulation is symmetric in the masses and spin parameters of the black hole, and therefore has a few spatial symmetries, this generic simulation possesses no such symmetries. Even though the Kerr parameter a/M of both holes is the same, their spin angular momenta differ by a factor of 4 due to their mass difference.

The lack of symmetries for the generic binary black hole configuration make it more difficult to detect or exclude the presence of a torus. To see this, consider one of the symmetries of the equal-mass merger: a rotation by π about the direction of the orbital angular momentum. Because of this

symmetry, the horizon finder needs to use only half the number of geodesics that would be required for a generic run: for every geodesic that is integrated backwards in time, another geodesic (with a position rotated by π along the direction of the orbital angular momentum) is effectively obtained 'for free'. Conversely, for a run without symmetries, it is necessary to use far more geodesics in the event horizon finder.

We will now examine the event horizon of the 'generic' merger at several spacetime locations that are important to the topological structure of the event horizon. Again, contrast this to the equal-mass merger, where there is only one spacetime region of interest to the topology of the horizon: the region and location where the common event horizon is first formed, and the associated cusp on the individual horizons.

For each of these spacetime locations we have investigated the consistency of the observed topological structure for several different numerical resolutions; specifically, we have run our event horizon finder using different spatial and temporal resolutions for the $2 + 1$ event horizon hypersurface, as well as on two of the different resolutions used to evolve the $3 + 1$ generic binary black hole merger simulation. We find no qualitative differences between the resolutions. In particular, though there appear to be features where a crossover point exists beyond the boundary or 'anchor' of a caustic, these features are not convergent with resolution. That is, upon going from a lower to higher resolution, it is possible to find an 'anchoring' caustic point for the apparently anomalous crossover. See Figure 4.12 for a clear demonstration of this phenomenon.

In the following sections, we examine the effect of two different spatial resolutions of our EH finder using a fine time resolution with a Δt of $0.005M^*$: one resolution with $2(119+1)^2$ geodesics ($L = 119$), and a higher spatial resolution using $2(191+1)^2$ geodesics ($L = 191$). Here M^* is nearly the total mass of the black holes on our evolution grid, M; $M^* = M/1.06157$ where M is the the sum of the Christodoulou masses of the black holes; we use this notation here as all detailed event horizon calculations are done before scaling with the Christodoulou masses. Though we do not show them here, the results from the event horizon finding using a different time step, and from using a different background simulation resolution can be found online at `http://www.black-holes.org/onToroidalHorizonsData.html`. Also included at that location are detailed instructions on how to visualize the data in the same way in which we present it in this paper [25].

4.5.2.1 Pre-merger: $t = 124.200M^*$

First, we examine the structure of the cusps on each black hole's individual event horizons at a time before merger[2]. Figure 4.11 displays a screenshot of this for two spatial resolutions used, focusing on the cusp on the larger black hole. Note that the resolution displayed here is much higher than in the equal-mass non-spinning case, and that we need to plot a much smaller region than

[2]Where merger is defined by the earliest time for which there is a common event horizon

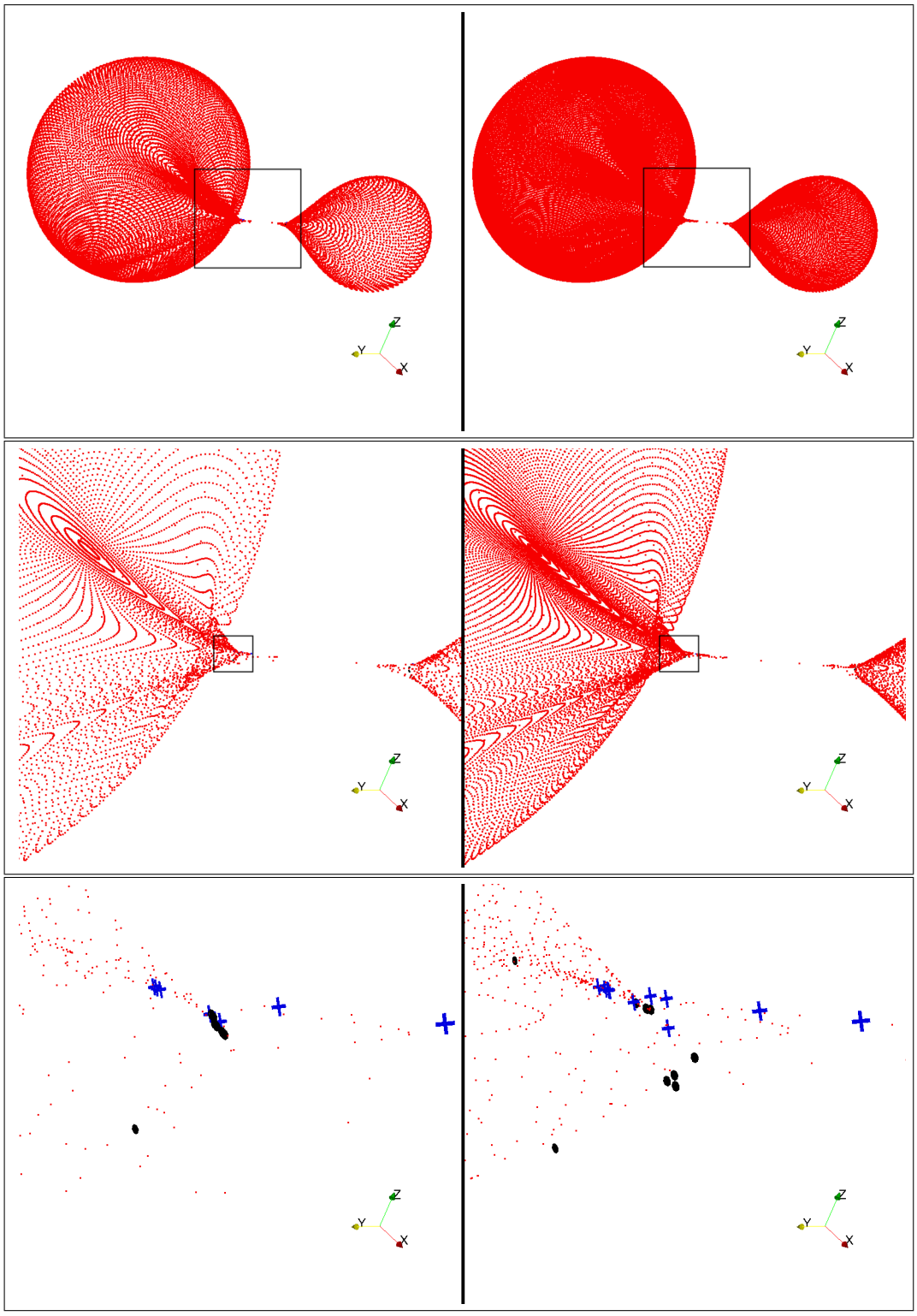

Figure 4.11: *Color online.* Generators of the event horizon at $t = 124.200M^*$. Current generators are shown as red points, and generators that are in the process of merging onto the event horizon are shown either as blue crosses (caustics), or larger black dots (crossovers). The left panel is computed using an apparent horizon finder resolution of of $L = 119$, and the right panel uses a resolution of $L = 191$. The lower panels are successive enlargements of the upper panels, focusing on the cusp near the larger black hole.

in Figures 4.8–4.10 in order to visualize the structure of the cusp. Unfortunately, the topological structure of the event horizon is not as clearly discernible as in the equal-mass non-spinning case. A close examination of the data in 3D using the free visualization software ParaView [24] reveals that there do not appear to be any 'isolated sets' of crossovers, i.e. crossovers not anchored by caustics. It is very difficult to make this clear using static screenshots in a standard article, and so we have made the visualization data available publicly for inspection at `http://www.black-holes.org/onToroidalHorizonsData.html`, and encourage the curious reader to view the cusp in 3D [25].

Figure 4.12 displays the cusp on the smaller black hole at the same time. Here, one can clearly see an example of the limits of our current method of discretization of the event horizon surface: while we cannot see proper 'anchoring' caustics using a resolution of $L = 119$ (left), we find the expected 'anchoring' caustics using higher resolution ($L = 191$, right). To the limit of the $2 + 1$ resolution of our event horizon surface, we find only one connected set of crossovers on each black hole near their respective cusps.

4.5.2.2 Merger: $t = 124.355M^*$

Our second time of interest occurs at the merger of the individual event horizons. Figure 4.13 illustrates the merger by showing screenshots of the coalescing bridge at three consecutive time steps. At merger, the black points indicating crossovers appear to form a "fat X" with finite width at the center, however this is likely a limitation of our finite temporal resolution; crossover points can only be flagged as as such if they join the horizon sometime between two time steps. In the limit of infinite spatial and temporal resolution, we would expect the same merger behavior as in the equal-mass non-spinning merger; i.e., the crossovers will be topologically one dimensional and form an "X" shape at merger (albeit a horizontally squished "X"). As in the equal-mass case, the point of merger occurs at a crossover.

4.5.2.3 Post-merger: $t = 124.400M^*$

Finally, we focus at a time after merger: when the final geodesics join horizon (or, in the backwards-in-time language of event horizon finding, when the *first* geodesics *leave* the horizon). Figure 4.14 shows the common bridge between horizons, along with two linear cusps anchored by caustics. The asymmetry of the simulation is clear here: the cusp to the right of the bridge is closing faster than the cusp on the left. The cusp on the left is closing in the direction along the bridge because caustics on either side are approaching each other, and it is closing in the transverse direction because the locus of crossovers is shrinking and moving out from the center of the bridge. As we follow this picture further in time, the cusp on the right displays the same qualitative behavior.

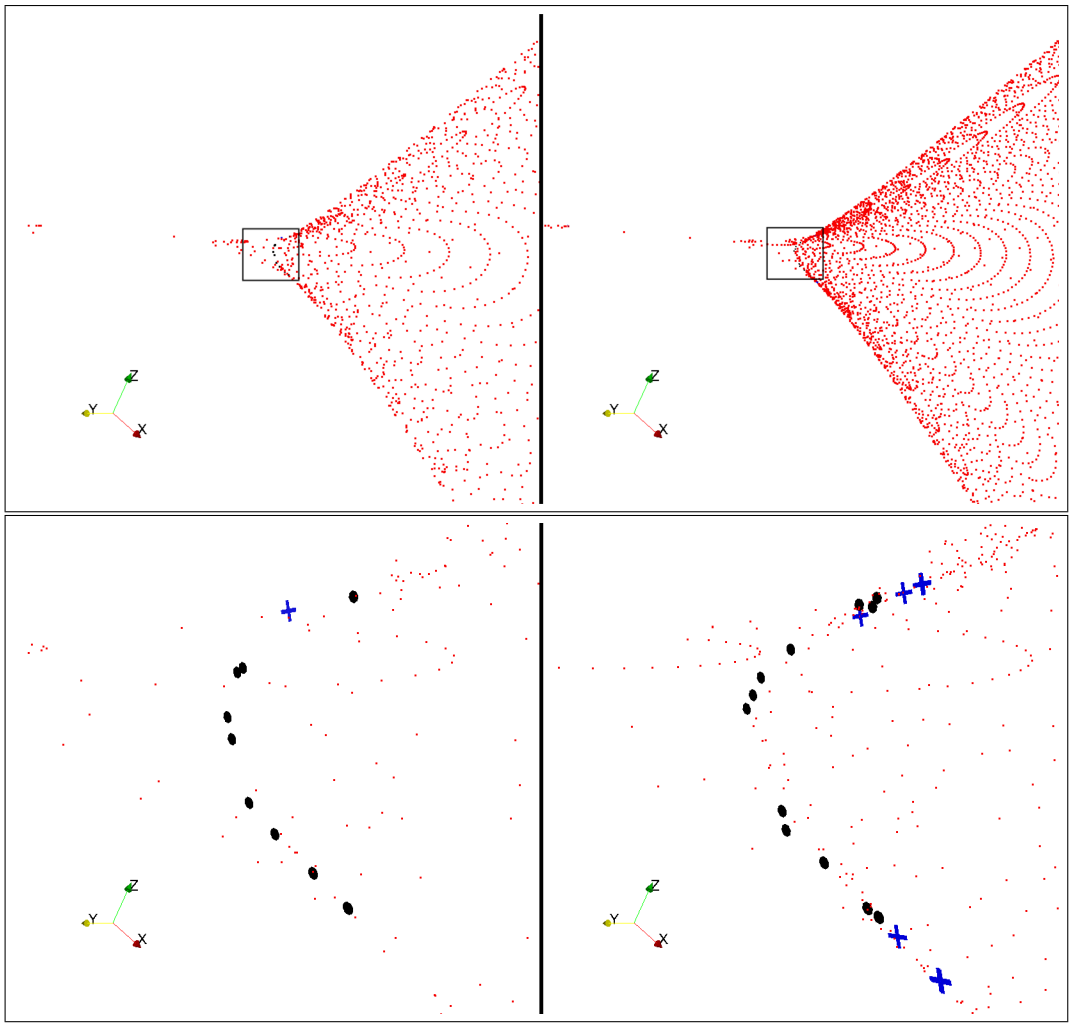

Figure 4.12: *Color online.* Same as the lower panels of Figure 4.11, except focusing on cusp on the smaller black hole.

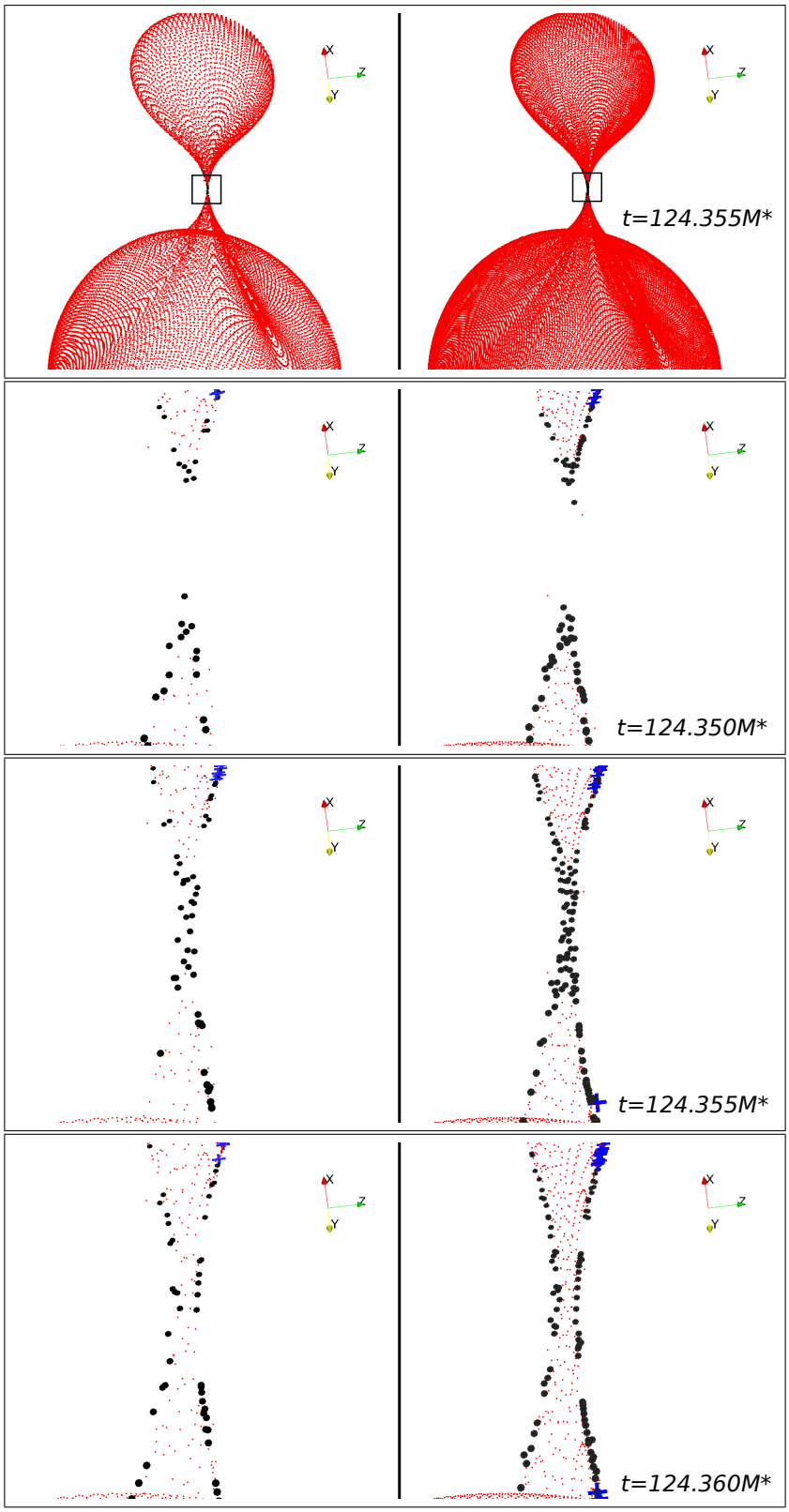

Figure 4.13: *Color online.* Same color coding and resolutions as in Figure 4.11, except shown at times very close to and surrounding the merger. Merger is localized to between times $t = 124.355M^*$ and $t = 124.360M^*$ (bottom row). The left side of each frame displays resolution $L = 119$, and the right side of each frame shows resolution $L = 191$.

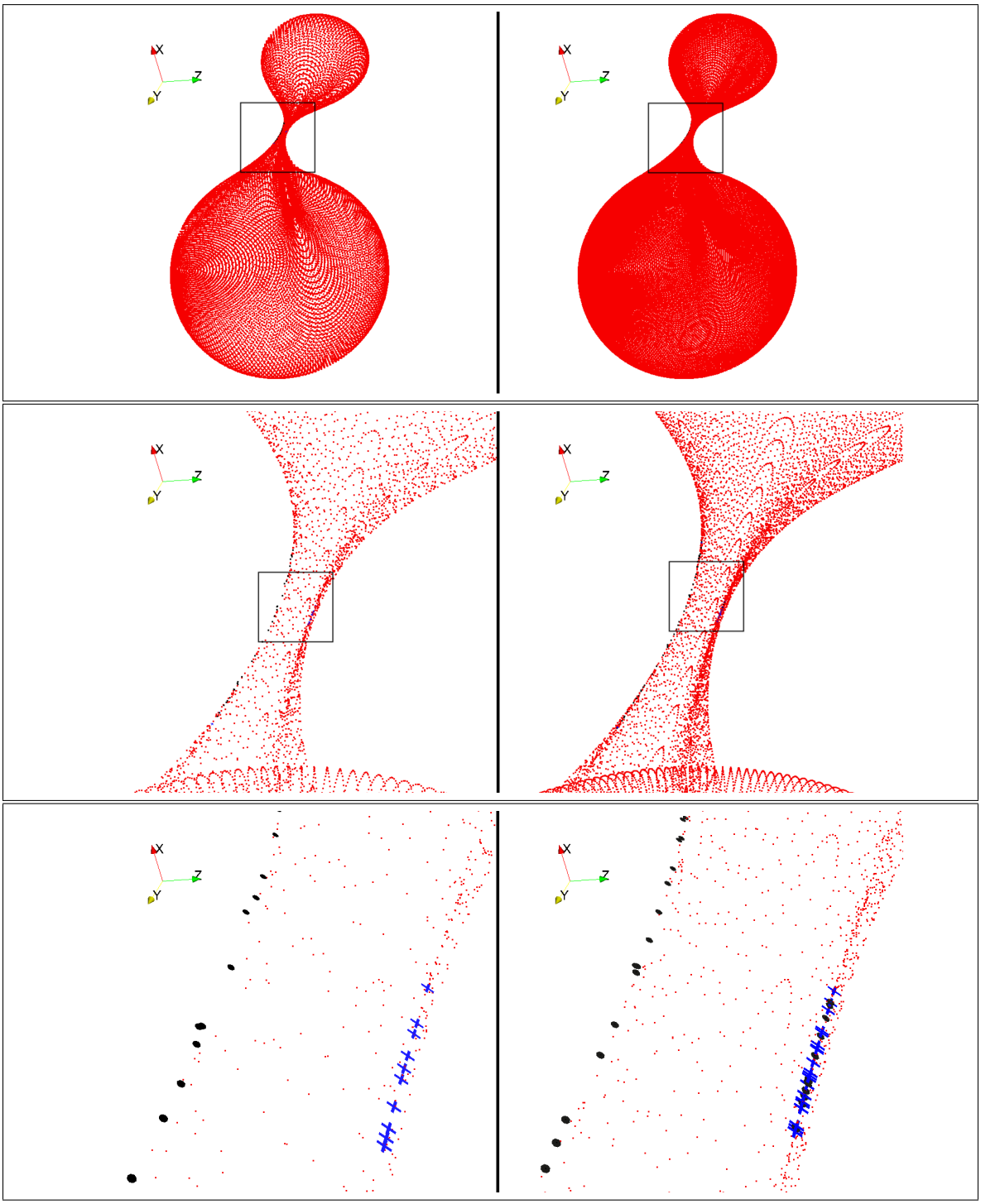

Figure 4.14: *Color online.* Same as Figure 4.11 but at time $t = 124.400M^*$. The crossover set on the left side of the bridge connecting the holes extends past the extents of the lower screenshot and is bounded by caustics that are outside the view of the frame. Also, on the right edge of the bridge, note the extended line of caustics and the presence of crossovers between the caustics. This appears to be the effect of finite resolution in the event horizon finder, since the appearance is different in the right and left panels. Such numerical phenomena suggest the need for advanced techniques such as adaptive refinement of geodesic placement if we wish to completely resolve event horizon features at a reasonable computational cost.

4.5.3 Discussion on the numerical analysis of topological features

Figures 4.11–4.14 illustrate why it is difficult to formulate a precise numerical condition that tells us the scale to which we can exclude the presence of a toroidal structure; in the generic case, it is difficult at times to say that we have even identified all connected components of the set of crossovers and caustics visually and qualitatively. In particular, though the distribution of geodesics is well spaced on the spherical apparent horizon at late times (which serves as the initial data for our event horizon finder), this does not ensure a uniform distribution of geodesics on the event horizon surface at earlier times. Thus, as one can see in Figure 4.14, the crossover points are not uniformly distributed along the line of the cusp. How do we know these crossover points are of the same connected component? Remember, if the crossover points in this region are members of at least two distinct connected components, and there are no "anchoring" caustic points in their neighborhood, it would indicate the presence of a toroidal event horizon! Runs at different resolutions indicate that our visual and qualitative identification of the crossover and caustic structure is consistent with a single linear cusp, but the structure is still only resolved up to the *largest* separation of crossover points in the cusp. We note that the implementation of adaptive geodesic placement in our event horizon finder is likely necessary to resolve these sorts of issues. We therefore choose to postpone the issue of a quantitative and precise bound on the scale to which we can exclude a toroidal event horizon to future work.

It is clear, however, from these results that our simulation is consistent with the topological structure discussed by Husa and Winicour in [11], and outlined in Section 4.4 above. Our slicing corresponds to slices parallel to $\mathcal{S}_0$ in Figures 4.4–4.6 through the structure of the event horizon, but this does not preclude the possibility of other spacelike slicings producing toroidal intermediate stages during merger.

4.6 Conclusion

In this work, we have taken the first steps in examining the topological structure of event horizons in generic binary black hole merger simulations. We focus on determining the topology of the two dimensional event horizon surface as it appears on spacelike slices of numerical relativity simulations. In particular, we concentrate on the presence or absence of a toroidal event horizon, as previous work [3, 4, 11] has suggested that the existence of a toroidal horizon should appear generically in non-axisymmetric mergers of black holes. In order to sharpen the discussion on toroidal horizons, we examine the caustic and crossover structure of the event horizon from a theoretical (Sec 4.4) and numerical (Sec 4.5) point of view. Following Husa and Winicour [11], we emphasize the distinction between caustic points, where neighboring (infinitesimally separated) geodesics cross and join the horizon, and crossover points, where geodesics separated by a finite angle cross and join the horizon.

Note that the union of caustics and crossovers are the 'crease set' discussed in the work of Siino [3, 4]. We now would like to recount the main topics we have discussed:

1. First, in Sections 4.1–4.3 we have described improvements in our event horizon finding code and summarized the topological results for event horizons found from `SpEC` binary black hole mergers. We describe our algorithm (which scales like $\mathcal{O}(N^2)$ where N is the number of horizon generators) to detect crossover points, and we find that the computational cost is not prohibitive for finding the event horizons of binary black hole mergers.

2. In Section 4.4, we reviewed the caustic and crossover structure of the event horizons of binary black hole mergers for the axisymmetric and generic cases. Concentrating on spatial slicings that result in toroidal event horizons, we diagram slices of the event horizon in multiple spatial and temporal directions in order to elucidate the caustic and crossover structure present in the cases of toroidal and non-toroidal event horizons.

3. Subsequently, in our introduction to Section 4.5, we have discussed a necessary condition for a spatial slice of the event horizon surface to be toroidal: the existence of a maximally path-connected set of crossover points that is disconnected from all caustic points.

4. Finally, we presented a detailed analysis of the event horizons found numerically from two inspiraling binary black hole simulations. We find in all cases that the intersection of the event horizon with any of our constant-time spatial hypersurfaces is topologically spherical rather than toroidal. Despite the lack of toroids, the structure of caustics and crossovers in our simulations are consistent with Husa & Winicour [11]. We paid particular attention to analyzing the generic merger for consistency when varying several different numerical resolutions. Though only two resolutions are compared in this paper, we have made public the visualization data for all four resolutions of the generic merger that we examined [25]. We encourage the reader to view at least one of our data sets in 3D, as this is perhaps the most powerful way to gain insight into the behavior of the event horizons from our simulations.

For the simulations presented here, it is difficult to compute a precise upper limit on the size of any tori that might exist in the exact solution but are too small for us to detect in the simulations. The main reason for this difficulty is that our ability to resolve features of the event horizon depends not only on the numerical resolution used to solve Einstein's equations, but also on the resolution of the algorithm used to find and classify event horizon generators. The latter resolution dominates in the examples presented here. This is because in our current method, the geodesics are located on a fixed computational mesh that is chosen at the beginning of the backwards-in-time geodesic integration (i.e. at late times). We suggest that the best way to tackle this issue would be to devise an event horizon finding algorithm with *iterative* or *adaptive* geodesic resolution and placement. Thus, one

could build into the adaptive method a target precision with which to resolve caustic and crossover sets. Though challenging, such an approach would allow one to investigate the topological structure of numerical event horizons to a much higher precision, while also providing a solid quantitative measure of the precision to which features are resolved.

Before we conclude, we would like to discuss a few important open questions about how the slicing condition used in our numerical simulations relates to the topological structure of the observed spatial cross sections of the event horizon: 1) Can an existing simulation be re-sliced to produce a toroidal cross section of the event horizon? 2) Alternatively, could the gauge conditions of our generalized harmonic evolution code be modified in order to produce a binary black hole merger in a spatial slicing with a toroidal event horizon? 3) Why have recent numerical simulations of merging black holes *not* produced slicings with a toroidal horizon when it has been thought that an intermediate toroidal phase should be relatively generic? The answer to the first question is clearly 'yes'. Previous work in the literature [3, 4, 6, 11] shows that it is possible to have a spacelike slicing of a dynamical event horizon with a toroidal topology, and that the question of whether the horizon is toroidal depends on how the spacelike slice intersects the spacelike crossover set $\mathcal{X}$, as we review in Section 4.4.

Questions 2) & 3), however, are far more mysterious and are ripe for future investigation. Is the lack of toroids in our simulations endemic to the types of foliations used in numerical relativity as a whole, or just to the generalized harmonic [18, 26, 27] gauge conditions we currently use in the `SpEC` code? It would be interesting to see if a toroidal event horizon phase could be produced from the same initial data used in our current simulations by modifying gauge conditions in such a way as to retard the lapse function near the merger point of the black holes. So far our attempts to do so have been unsuccessful. Hence, it has been speculated that some property of those numerical gauge choices that yield stable binary black hole evolutions also avoids slicings in which the event horizon is toroidal.

Acknowledgments

We would like to thank Saul Teukolsky, Jeff Winicour, and Aaron Zimmerman for useful discussions on toroidal horizons. We would especially like to thank Jeandrew Brink for a careful reading of a draft of this manuscript and many useful suggestions for improvement. Thanks to Nick Taylor for experimenting with modified gauge conditions designed to retard the lapse function. We would also like to acknowledge Fan Zhang and Béla Szilágyi for interesting thoughts on why our numerical slicings have not resulted in toroidal event horizons. J.K. would like to thank David Nichols for a useful discussion on the numerical resolution of a toroidal horizon. M.C. would like to thank Matt Robbins and Joerg Wachner for designing Figures 4.3–4.6. This work was supported in part by grants from

the Sherman Fairchild Foundation and from the Brinson Foundation, by NSF Grants PHY-1068881 and PHY-1005655, by NASA Grant NNX09AF97G, and by NASA APT Grant NNX11AC37G.

Bibliography

[1] S. W. Hawking, Commun. Math. Phys. **25**, 152 (1972).

[2] D. Gannon, Gen. Relativ. Gravit. **7**, 219 (1976).

[3] M. Siino, Prog. Theor. Phys. **99**, 1 (1998).

[4] M. Siino, Phys. Rev. D **58**, 104016 (1998).

[5] S. A. Hughes, C. R. Keeton, P. Walker, K. T. Walsh, S. L. Shapiro, and S. A. Teukolsky, Phys. Rev. D **49**, 4004 (1994).

[6] S. L. Shapiro, S. A. Teukolsky, and J. Winicour, Phys. Rev. D **52**, 6982 (1995).

[7] J. L. Friedman, K. Schleich, and D. M. Witt, Phys. Rev. Lett. **71**, 1486 (1993).

[8] J. L. Friedman and A. Higuchi, Ann. Phys. **15**, 109 (2006).

[9] J. M. Centrella, J. G. Baker, B. J. Kelly, and J. R. van Meter, Rev. Mod. Phys. **82**, 3069 (2010).

[10] S. T. McWilliams, Class. Quant. Grav. **28**, 134001 (2011), `arXiv:1012.2872`.

[11] S. Husa and J. Winicour, Phys. Rev. D **60**, 084019 (1999), `gr-qc/9905039`, URL `http://prola.aps.org/abstract/PRD/v60/i8/e084019`.

[12] P. Diener, Class. Quantum Grav. **20**, 4901 (2003).

[13] M. Ponce, C. Lousto, and Y. Zlochower, Classical and Quantum Gravity **28**, 145027 (2011), `arXiv:1008.2761`.

[14] `http://www.black-holes.org/SpEC.html`.

[15] M. I. Cohen, Ph.D. thesis, California Institute of Technology (2011), URL `http://thesis.library.caltech.edu/5984/`.

[16] M. Scheel, M. Boyle, T. Chu, L. Kidder, K. Matthews and H. Pfeiffer, Phys. Rev. D **79**, 024003 (2009), `arXiv:gr-qc/0810.1767`.

[17] M. Boyle, D. A. Brown, L. E. Kidder, A. H. Mroué, H. P. Pfeiffer, M. A. Scheel, G. B. Cook, and S. A. Teukolsky, Phys. Rev. D **76**, 124038 (2007).

[18] B. Szilagyi, L. Lindblom, and M. A. Scheel, Phys. Rev. D **80**, 124010 (2009), `arXiv:0909.3557`.

[19] M. Cohen, H. P. Pfeiffer, and M. A. Scheel, Class. Quant. Grav. **26**, 035005 (2009), `arXiv:0809.2628`.

[20] G. Lovelace, Y. Chen, M. Cohen, J. D. Kaplan, D. Keppel, K. D. Matthews, D. A. Nichols, M. A. Scheel, and U. Sperhake, Phys. Rev. D **82**, 064031 (2010).

[21] S. W. Hawking and G. F. R. Ellis, *The large scale structure of space-time* (Cambridge University Press, Cambridge, England, 1973).

[22] R. M. Wald, *General Relativity* (University of Chicago Press, Chicago and London, 1984).

[23] L. Lehner, N. Bishop, R. Gomez, B. Szilagyi, and J. Winicour, Phys. Rev. D **60**, 044005 (1999).

[24] *ParaView - Open Source Scientific Visualization*, http://www.paraview.org/.

[25] `http://www.black-holes.org/onToroidalHorizonsData.html`.

[26] L. Lindblom, M. A. Scheel, L. E. Kidder, R. Owen, and O. Rinne, Class. Quantum Grav. **23**, S447 (2006).

[27] L. Lindblom and B. Szilágyi, Phys. Rev. D **80**, 084019 (2009).

Part II

Work with [that] matter[s]

Chapter 5

Behavior of Pseudospectral Coefficients in the Presence of a Non-smoothness

---

First publication. Jeffrey D. Kaplan (2013)

5.1 Motivation

In the `SpEC` code, the metric fields ψ_{ab} near a neutron star or black-hole (or in general any geometry with a spherical configuration), are represented in terms of basis functions which are the product of scalar spherical harmonics (representing the angular dependence) with Chebyshev polynomials (representing the radial dependence). As mentioned in [2], the fields which describe the matter in general relativistic binaries are not smooth. In general, any strong shocks in the flows represent points where the density is discontinuous. Even in the quasi-stationary inspiral of the binary where there are no shocks, the stellar surface will be a point where $d\rho/dr$, the derivative of the density in the radial direction as measured from the center of the star, will not be continuous.[1] Therefore the spectral convergence of the radial dependence of the metric fields will be disturbed the most by a lack of smoothness. In this chapter we examine the convergence behavior of the radial dependence of the metric functions in the presence of a stellar surface by considering the toy problem of expanding a non-smooth function (defined on the interval $x \in [-1, 1]$) in a pseudospectral expansion on a Chebyshev basis.

The analysis of our toy problem focuses on showing why, for a function which is non-smooth (a term short for 'not infinitely differentiable'), a small increase in the number of terms of the spectral expansion (one or two) can result in an *increase* of the error of the approximation. This behavior

[1] In the case of a realistic neutron star, the presence of a solid crust will make the surface even less smooth and the density ρ itself will be discontinuous.

was relatively foreign to those who worked exclusively on simulating binary black holes with SpEC. The evolution system employed in SpEC was carefully formulated as to preserve the smoothness of evolutions beginning from smooth initial data [7], which allows SpEC's vacuum code takes full advantage of the spectral convergence of infinitely differentiable functions. We hypothesize that the unexpected behavior of the truncation error has to do with the change in the location of the stellar surface (non-smoothness) *relative to* the location of the collocation points. While the location of the surface does not change with resolution, the location of the collocation points *do*. We illustrate that a shift along the x axis does not change the ordering of errors with resolution for infinitely differentiable functions, but *does* change the ordering of errors in the presence of a non-smooth point.

5.2 Preliminaries and theoretical background

5.2.1 Expected convergence of the metric at the stellar surface

Let us introduce a few formal definitions necessary to discuss the smoothness of the metric fields, which are spectrally represented in the SpEC code, in the presence of matter. A function $f(x)$ is said to be C^k (short for "of differentiability class C^k") at a point x if its derivatives up to $f^{(k)}(x)$ exist at the point x (and where the notation f super k denotes the k'th derivative of f with respect to x). We will generally use the C^k to refer to functions which are C^k for all points in its domain but not C^{k+1}; that is, we will will say a function is C^k to indicate that it is k, but not $k+1$ times differentiable at at least one point in its domain. A function f(x) is said to be 'smooth' if it is infinitely differentiable at all points in its domain; in this case we may say the function is C^∞.

As discussed in Sec. 5.1, the stellar surface is only C^0 in density in the radial direction. What does this imply about the differentiability of the metric fields? Einstein's equation relates the metric fields to the matter fields by,

$$R_{ab} = 8\pi(T_{ab} - \frac{1}{2}\psi_{ab}T), \tag{5.1}$$

where R_{ab} is the Ricci tensor, and T_{ab} is the stress energy tensor. For a perfect fluid,

$$T_{ab} = \rho_{\rm b} h u_a u_b + P\psi_{ab}, \tag{5.2}$$

with $\rho_{\rm b}$ the baryon density, h the specific enthalpy, u_a the fluid 4-velocity, and P the pressure. We use Eqs. 5.1 & 5.2 to relate the differentiability of the density, to the differentiability of the metric schematically in the following way:

$$\boldsymbol{R} \sim \partial\boldsymbol{\psi} + \partial\partial\boldsymbol{\psi} \sim \boldsymbol{T} \sim \rho_{\rm b}. \tag{5.3}$$

That is, a combination of first and second derivatives of the metric, $\boldsymbol{\psi}$, are directly proportional to the density $\rho_{\rm b}$. Thus, since the density at the star's surface is C^0, in general, we would not expect the metric at this stellar surface to be any more differentiable than C^1.

The lure of spectral methods is that they exhibit geometric, (aka. "exponential" or *spectral*) convergence; the series coefficients, a_n, decrease faster than $1/n^\ell$ for any finite power of ℓ for C^∞ (infinitely differentiable) functions. Here, ℓ is known as the algebraic order of convergence. However, if the function expanded is only C^k, how will the order of convergence of a Chebyshev series differ? The answer may be deduced from the "Fourier Asymptotic Coefficient Expansion" (FACE) explained in Sec. 2.9 of Boyd (2009)[1]. For a C^k function, the algebraic order of convergence ℓ of the spectral coefficients will be:

$$\ell = k + 2. \tag{5.4}$$

That is, the spectral coefficients, a_n for a C^k function will converge as $O(1/n^{k+2})$. Consequently, for the radial basis coefficients of the metric fields in `SpEC`, we should expect no better than $O(1/n^3)$ convergence in the presence of a stellar surface.

However, if a function is C^∞ over the domain of its expansion, Eq. 5.4 tells us that its coefficients will converge geometrically: the order of magnitude of the coefficients will decrease exponentially with increasing coefficient number, n.

5.2.2 The 'pseudo' in pseudospectral methods

`SpEC` uses a particular brand of spectral methods called the *pseudospectral* method.[2] In the pseudospectral method, the spectral basis set has an associated set of gridpoints known as "collocation" points. The spectral coefficients of a function $f(x)$ in the pseudospectral method are determined by requiring that the truncated series equal $f(x)$ at each collocation point. The collocation points for the Chebyshev basis may be one of two choices: (i) the 'Roots' (aka. the "Gauss-Chebyshev" points) or (ii) the 'Extrema-plus-Endpoints' (aka. the "Gauss-Lobatto" points). In `SpEC`, we commonly use the 'Extrema-plus-Endpoints' gridpoints which, for an expansion of order N (of $N+1$ terms), are defined by,

$$x_i = -\cos\frac{\pi i}{N} \quad i = 0, \ldots, N. \tag{5.5}$$

Note that this means that, for expansions of different order, *a different set of collocation points will be employed.* We shall see in Sec. 5.4 that this feature is intimately involved with the convergence phenomena we are studying.

[2]This discussion of pseudospectral methods relies heavily on Boyd (2001) [1]. It is a concise, entertaining and accessible work which I highly recommend to anyone working with a pseudospectral code. In addition to being quite inexpensive to purchase as a hard copy, it is also available as a PDF for no cost on the web.

In the absence of any a-priori knowledge of the geometry of the problem being studied, the Chebyshev basis is essentially the optimal basis set for describing non-periodic smooth functions on 'the interval $x \in [-1,1]$' (hereafter referred to as simply "the interval"). Any function which is defined on a different, finite, domain may be mapped to the interval to facilitate the spectral expansion.

5.2.3 Measures of the truncation error

Now we need some way of quantifying the error incurred when we discretize the function $f(x)$ by representing it as a truncated series of Chebyshev polynomials of N'th order. If the N'th partial sum of the Chebyshev series approximating the function $f(x)$ with coefficients a_n $(n = 0, \ldots, N)$ is denoted $f_N(x; a_n)$, then we write the residual of the expansion as,

$$R(x; a_n) = f(x) - f_N(x; a_n). \tag{5.6}$$

In the following section, we examine two different measures of the truncation error calculated from the residual. The first is the L_2 norm of the residual calculated as,

$$L_2||R(x; a_n)|| = \sqrt{\int_{-1}^{1} R(x; a_n)^2 dx}. \tag{5.7}$$

It in some sense represents the 'root-mean-squared error' incurred by truncation. The second is maximum difference between the function and its N'th order expansion:

$$L_\infty||R(x; a_n)|| = \max |R(x; a_n)|. \tag{5.8}$$

This is the L_∞ norm of the residual. We examine both of these error measures as the formal properties of the two norms may differ significantly. Recall, for example, the presence of "Gibb's phenomena" oscillations in the Fourier series of a step function; in this example, the L_∞ norm of the error diverges as $N \to \infty$, while the L_2 norm converges to zero. Both of these two norms are commonly used in `SpEC` evolutions to measure the magnitude of the violation in the Einstein constraint equations.

5.3 Methods

We would like to test the hypothesis that the shifting location of the collocation points is responsible for lack of strict convergence in the truncation error with resolution for non-smooth functions. To accomplish this, we have constructed a toy code to expand 1D functions on the interval in terms of a Chebyshev series via the pseudospectral method. It is designed to match the behavior of `SpEC`

as closely as possible. We therefore have followed Kidder et al. (2000) [6] in our calculation of the spectral coefficients, a_n ($n = 0, \ldots, N$ where N is the order of the expansion), at the 'Extrema-plus-Endpoints' ("Gauss-Lobatto") collocation points given in Eq. 5.5.

We examine the pseudospectral expansions of consecutive orders $N = 9$, 10, & 11 for three functions [3]: An arbitrary C^∞ function,

$$f_{C^\infty}(x) = \tanh(x^2)\left[\sin\left(\frac{2\pi x}{3}\right)\right]^{13/9}. \tag{5.9}$$

The Heaviside lambda ('triangle') function, which is not differentiable at $x = 0$ and thus C^0,

$$f_{C^0}(x) = \begin{cases} 1+x & : x \leq 0, \\ 1-x & : x > 0, \end{cases} \tag{5.10}$$

and a function whose derivative is (essentially) the Heaviside lambda function and is consequently C^1,

$$f_{C^1}(x) = \begin{cases} x^2 & : x \leq 0, \\ -x^2 & : x > 0. \end{cases} \tag{5.11}$$

We then 'sweep' the functions along the interval by applying a horizontal shift $s \in [-1, 1]$. This offsets the location of the non-smooth point (for $f_{C^1}(x)\&f_{C^0}(x)$) from $x = 0$ to $x = s$. For each expansion order $N = 9$, 10, & 11, we calculate the L_2 and L_∞ norms of the residual and plot them vs. the offset s. Also on these plots, we use vertical lines to indicate the location of the collocation points for each expansion order allowing one to observe the effects of the relative difference between the location of the 'kink' (the non-smooth point) and the collocation points.

The author has made the toy code used in this study publicly available as a piece of experimental python routines at `https://github.com/jeffdk/PySpEx`. It uses the `numpy, scipy` and `matplotlib` [5] libraries. To run the code, execute 'python ExplorePsuedospectralExpansions.py'. Absolutely no warranty is provided.

5.4 Results

First in Fig. 5.1 we plot a representation of the smooth function, Eq. 5.9, in spectral and physical space for an offset value, $s = -0.26$. One may observe from the right hand panel showing the physical space of the function that the function and its truncated approximations are virtually indistinguishable. Figure 5.2 shows the L_2 (left panel) and L_∞ (right panel) norms of the residual for this smooth function. We may observe that no matter what the value of the horizontal shift,

[3] We choose these orders as they are in the range of commonly used orders for the radial Chebyshev basis functions in `SpEC`.

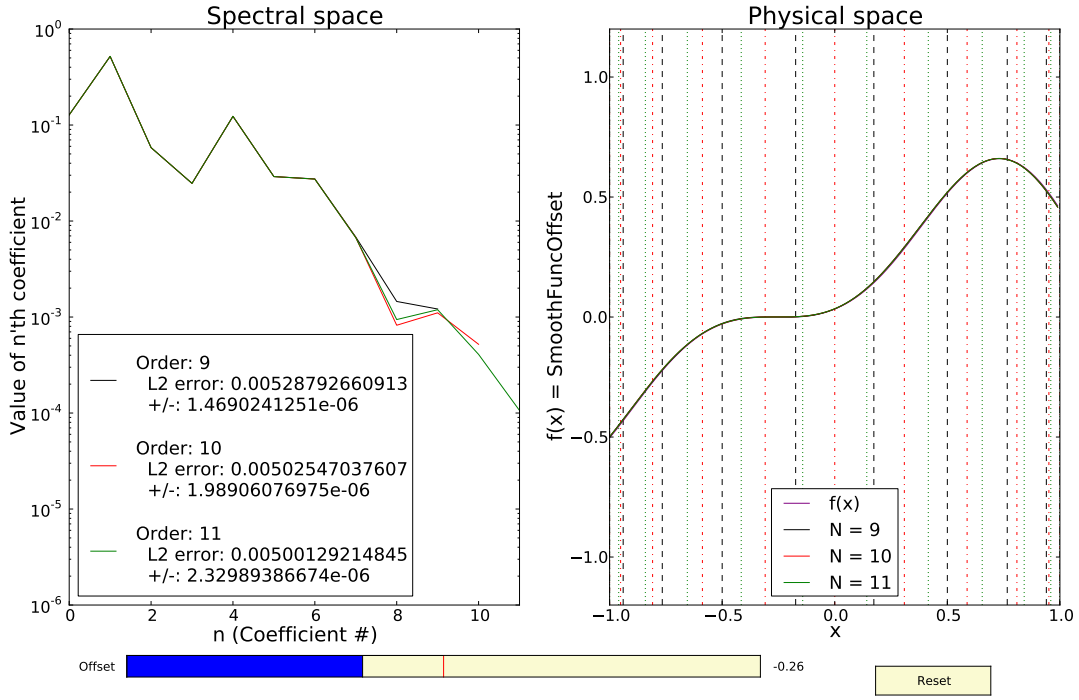

Figure 5.1: Spectral (**left panel**) and physical (**right panel**) representations of the truncated expansions for the smooth function Eq. 5.9. Note that the values of the spectral coefficients agree until about the $n = 7$ coefficient.

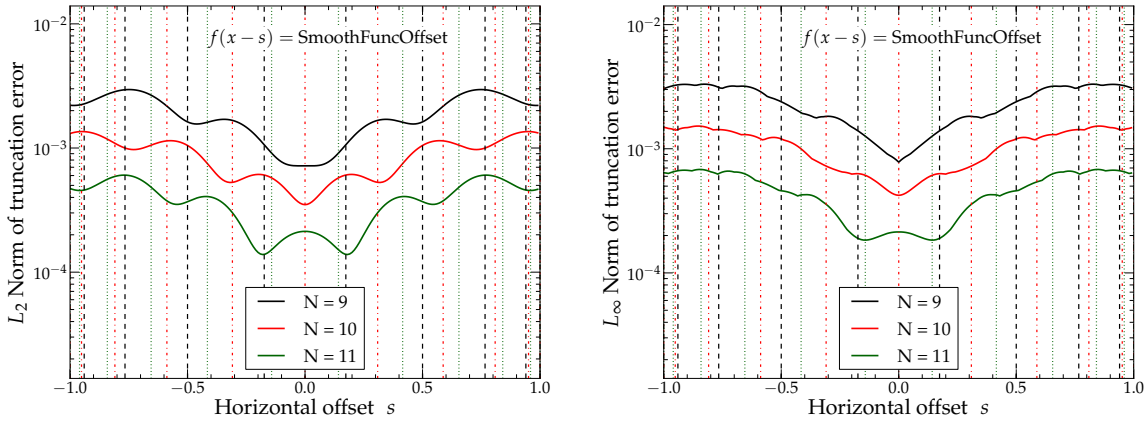

Figure 5.2: Integral norms over x for truncated expansion residuals of the C^∞ function Eq. 5.9 vs. the horizontal shift parameter s. The **left panel** shows the L_2 norm and **right panel** displays the L_∞ norm. The collocation points for the $N = 9$, 10, & 11 order expansions are show as black dashed, red dash-dotted, and green dotted vertical lines respectively. There is some variation in the error as a function of s, but overall the geometric convergence of the series may be observed; the curves are, on average, offset by a constant multiplicative factor.

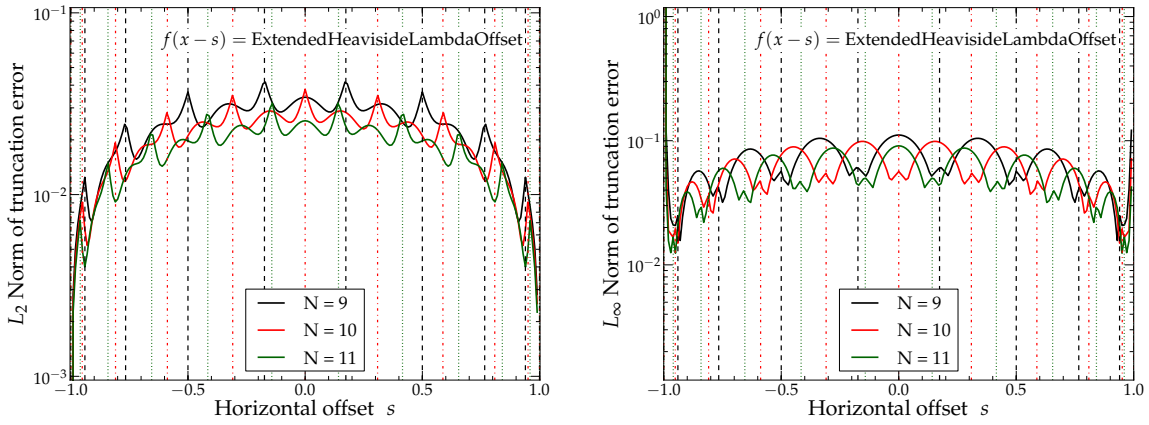

Figure 5.3: The same as Fig.5.2 but for the residuals of the truncated expansions of the C^0 function Eq. 5.10. The 'kink' limits the series coefficients to $O(1/n^2)$ convergence and results in closely spaced curves. Additionally there is significant variation in the values of the curves as a function of s; we note that the features of this variation are closely related to the positions of the collocation points.

s, is, there is always strict convergence observed. That is, the errors are consistently lower as the resolution is increased.

One may correspondingly see that in Figs. 5.4 & 5.3, that strict convergence is *not* observed for the non-smooth functions $f_{C^1}(x)\&f_{C^0}(x)$. Particularly, we note that the ordering of (both L_2 and L_∞) errors with resolution is lost for all three expansion orders for the C^0 function. While we do see significant variation in the errors due to the position of collocation points for these non-smooth functions, the magnitude of the variation at a fixed resolution does not seem to be significantly different from the variation in the smooth function. The major difference is that the average error levels for the different resolutions is significantly closer due to the algebraic orders of convergence.

These results do show that increasing the order of the Chebyshev expansion for a non-smooth function may *increase* rather than *reduce* the error, and that in some sense this variation is necessarily because of the change of collocation points used in the expansion. Technically, our hypothesis that the lack of strict convergence for the metric fields in the `SpEC` code in the presence of a stellar surface can result from the change in collocation points between resolutions may be considered confirmed. However, the heart of the issue is that the order of convergence of the Chebyshev series is *severely* reduced (from geometric to algebraic) once a 'kink' of any order is introduced. Once this happens, an increase in resolution by a few points (i.e. increasing the order of expansion by 1-3), will have a negligible effect on the error for moderate to large resolutions.

5.5 Discussion and concluding remarks

The results illustrated in Sec. 5.4 have several implications for the evolution of stellar surfaces in the `SpEC` code. First, it emphasizes that the spectral grid (on which the metric is evolved) must be

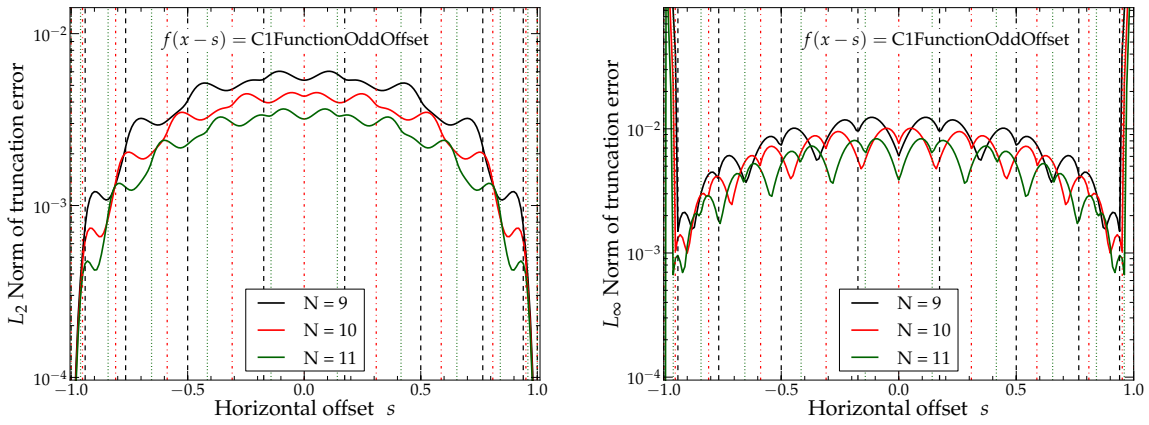

Figure 5.4: The same as Fig. 5.2 but for the residuals of the truncated expansions of the C^1 function Eq. 5.11. Compared to the truncation errors of the expansions for the C^0 function show in Fig. 5.3, there is better convergence, and less variation in the errors. However we note there is still enough variation to prevent a strict convergence of the L_∞ error with resolution for many offsets s.

'specially configured' for subdomains containing the stellar surface. By this we mean that change in number of gridpoints with resolution level must be by a multiplicative factor in these subdomains, instead of an additive factor which is the norm in binary black hole vacuum simulations. Otherwise, the truncation error will not converge at a fast enough rate to ensure robust convergence of the simulation with resolution level. This has proven to be much more difficult to implement in practice than it would first seem. First, it requires knowing which subdomain contains the stellar surface. This may change with time if a star undergoes gravitational collapse, or if coordinate mappings used to track a binary inspiral shrink the grid significantly in the star's inertial frame. In theory, this could be accomplished using the spectral adaptive mesh refinement routine (AMR) implemented in `SpEC`. To ensure robust behavior of the AMR routine, we suggest a specialized AMR driver be designed for adjusting the resolution for this purpose. Second, it is found in practice that having significantly different grid resolutions in adjacent subdomains can result in large constraint violations at the subdomain boundaries which can become the dominant source of error in a simulation. This effect could be mitigated by gradually reducing the resolution in subdomains further and further from the stellar surface, but such a strategy adds significant computational cost to the simulation. Finally, since `SpEC` uses an explicit time-stepping scheme, increasing the resolution, (and hence decreasing the grid spacing) significantly anywhere on the grid will decrease the time-stepping rate via the Courant condition. Perhaps this limitation may be mitigated by employing the Kosloff/Tal-Ezer mapping which relaxes the clustering of Chebyshev collocation points near the subdomain boundaries (see Sec 16.9 of Boyd (2001)[1]).

Another technique which is employed when spectral methods are used to solve elliptic equations for the initial data used in the simulations of compact objects is to fix the location of the stellar

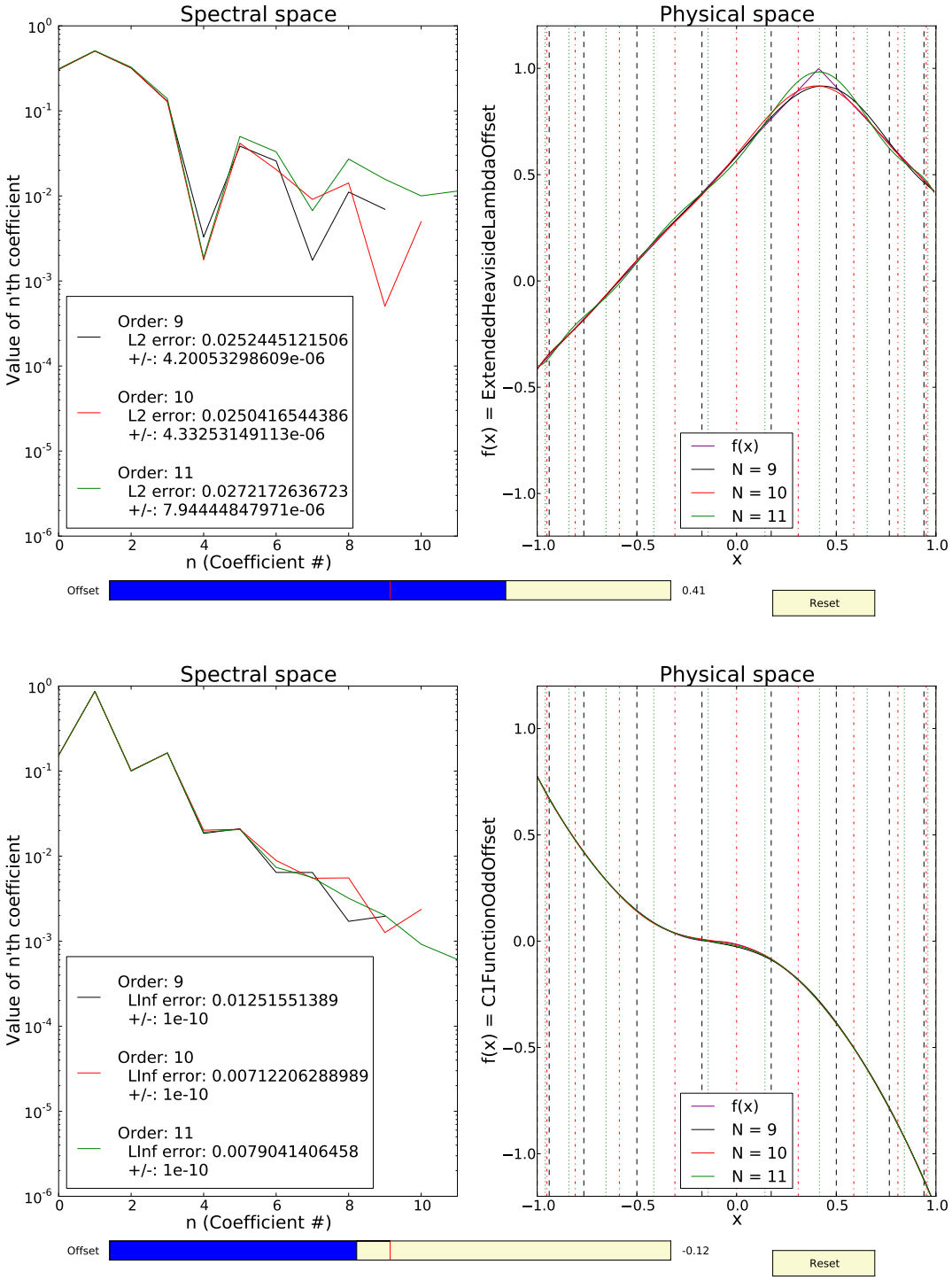

Figure 5.5: Same as Fig. 5.1, but for the C^0 (**top**) and C^1 functions (**bottom**). Note the spectral coefficients start differing after the $n = 3$ coefficient (C^0 **top left**) and the $n = 5$ coefficient (C^1 **bottom left**) respectively.

surface (the non-smooth point) to a subdomain boundary [3, 8]. This works effectively in the iterative solutions where one of the steps in the solution procedure does this explicitly. However, this is more challenging in a dynamical simulation where the location of the stellar surface may constantly change. In theory, this could be done with the combination of coordinate mappings and control systems which are employed in `SpEC` to control the excised region of the grid in binary black hole mergers [4]. Though originally this seemed to be the ideal solution to the issue raised in this work, the author is less bullish than he first was for this technique. One reason is illustrated by the right hand panels of Figs. 5.4 & 5.3. One can see that the L_∞ error of the expansion can diverge when the non-smooth point is located between the boundary and first interior collocation point. Although this particular case is likely related to the fact that the component pieces of the non-smooth functions $f_{C^1}(x)$ & $f_{C^0}(x)$ are simple polynomials (and thus exactly represented by a low order expansion), it illustrates the fact that small errors, or even noise in the values of a field at any collocation point can easily contaminate the expansion and reduce accuracy across the domain.

The author recommends that better diagnostic tools designed to specifically examine numerical effects that result from the coupling of multiple numerical methods. Chapter 6 of Boyd (2001) [1] begins with the quote, "One must watch the convergence of a numerical code as carefully as a father watching his four year old play near a busy road." If the dual-grid method employed by the `SpEC` hydrodynamics code is ever to be robust, I recommend the collaboration take the time to develop the tools necessary to follow Boyd's advice.

Bibliography

[1] J. Boyd. *Chebyshev and Fourier Spectral Methods, 2nd ed.* Dover Publications, Mineola, NY, USA, 2001.

[2] M. D. Duez, F. Foucart, L. E. Kidder, H. P. Pfeiffer, M. A. Scheel, and S. A. Teukolsky. Evolving black hole-neutron star binaries in general relativity using pseudospectral and finite difference methods. *Phys. Rev. D*, 78:104015, November 2008.

[3] F. Foucart, L. E. Kidder, H. P. Pfeiffer, and S. A. Teukolsky. Initial data for black hole neutron star binaries: A flexible, high-accuracy spectral method. *Phys. Rev. D*, 77:124051, June 2008.

[4] D. A. Hemberger, M. A. Scheel, L. E. Kidder, B. Szilágyi, G. Lovelace, N. W. Taylor, and S. A. Teukolsky. Dynamical excision boundaries in spectral evolutions of binary black hole spacetimes. *Classical and Quantum Gravity*, 30(11):115001, June 2013.

[5] J. D. Hunter. Matplotlib: A 2d graphics environment. *Computing In Science & Engineering*, 9(3):90–95, 2007.

[6] L. E. Kidder, M. A. Scheel, S. A. Teukolsky, E. D. Carlson, and G. B. Cook. Black hole evolution by spectral methods. *Phys. Rev. D*, 62(8):084032, October 2000.

[7] L. Lindblom, M. A. Scheel, L. E. Kidder, R. Owen, and O. Rinne. A new generalized harmonic evolution system. *Class. Quantum Grav.*, 23:447, August 2006.

[8] LORENE: Langage Objet pour la RElativité NumériquE.

Chapter 6

Simulations of neutron star-neutron star inspirals with SpEC

First publication. Jeffrey D. Kaplan (2013).

This work relied on the use of the `SpEC-hydro` code, and thus all the members of the SXS collaboration. In particular Curran Muhlberger, Matt Duez, Francois Foucart, Mark Scheel, Béla Szilágyi and Roland Haas made significant contributions to this work.

6.1 Introduction

6.1.1 NSNS coalescence and gravitational waves

The discovery of the first binary system consisting of two neutron stars represented and important landmark in the study of compact objects, close binary systems and general relativity [26]. Often called the Hulse-Taylor binary after its discoverers, the system has provided some of the most compelling evidence to date for the existence of gravitational waves and accuracy of Einstein's general relativity; the orbital separation of the binary has decayed over time at the precise rate predicted by general relativity [43, 44]. To date, at least ten [28] binary neutron star systems[1] have been discovered. Many of these systems have small enough orbital separations that neutron stars are expected to coalesce on timescales less than 1Gyr due to orbital decay from the emission of gravitational waves. The closest NSNS binary is PSR J0737-3039 which has an orbital period of less than 3 hours and has an expected time until merger of 85 million years [8].

[1] Astronomers generally refer to any binary star system with one neutron star component as a neutron-star binary; neutron-star neutron-star (NSNS) systems are referred to as 'binary neutron stars' or 'double neutron star' systems.

Gravitational waves from the coalescence of compact binaries represent the most promising candidates for the first direct observation of gravitational waves from the Laser Gravitational-Wave Observatory or LIGO [1, 3]. Close NSNS binary systems are the *only* compact object binaries which have been identified observationally; while the existence of black hole-neutron star (BHNS) and binary black hole (BBH) system is almost certain given our current picture of the evolution of binary star systems, they have yet to be identified in the field. Consequently, the rate of NSNS coalescences detectable by Advanced LIGO is the least uncertain (though BBH coalescences may have higher detection rates due to their being stronger sources at frequencies to which LIGO is the most sensitive) [2]. In addition, providing a strong field test of general relativity, a LIGO detection of a clean waveform from the inspiral and merger of two neutron stars has the potential to constrain the neutron star equation of state (EOS). As neutron stars have densities on the same order as that of an atomic nucleus[2], a more precise constraint on the neutron star EOS would yield a fascinating probe of fundamental physics. An excellent review of our current constraints and understanding of the neutron star EOS may be found in a recent review by Jim Lattimer [28].

A first order, quantitative, measurement of the neutron star equation of state may be determined from the gravitational wave signal of a NSNS coalescence in two ways. First, in the final phase of the inspiral, each neutron star will obtain a tidal deformation due to its companion which, to leading order, will result in an induced quadrupole moment. The ratio of the applied tidal field to the resulting quadrupole deformation of a NS is called the *tidal deformability* and is closely related to a parameter known as the *tidal Love number*; given a fixed NS mass, this parameter provides a quantitative measurement of the NS EOS's 'stiffness'. Hinderer and Flanagan have shown that the evolution of the orbital phase for the coalescing NSNS system is altered by an amount which is directly dependent on the tidal deformability of the NSs [15, 23, 24]. Thus the direct measurement of the progression of the orbital phase from the gravitational waveform of a NSNS coalescence can directly measure the tidal Love number of the component NSs and therefore the 'stiffness' of the NS EOS. Secondly, a NSNS merger which does not immediately collapse to a black hole will leave behind a differentially rotating, highly excited *hypermassive neutron star (HMNS) remnant* (cf. Ch. 8). As the HMNS remnant oscillates and settles down, it emits high frequency (2-4KHz) gravitational waves which produce a pronounced peak in the GW frequency spectrum. A comprehensive study by Bauswein et al. was able to find a relation between the value of this frequency peak and the radius of a $1.6M_{\odot}$ that is remarkably uniform over 38 different candidate neutron star EOSs [4]. Since the radius of a NS for a fixed mass is directly dependent on the 'stiffness' of the NS EOS, this yields a second way in which a quantitative measurement of the NS EOS may be accomplished via the gravitational wave signal from the merger of two neutron stars.

Although the latter (HMNS oscillation modes) result is more easily calculated by simulations,

[2]This density is called nuclear saturation density and has a value of 2.7×10^{14} g cm^{-3}.

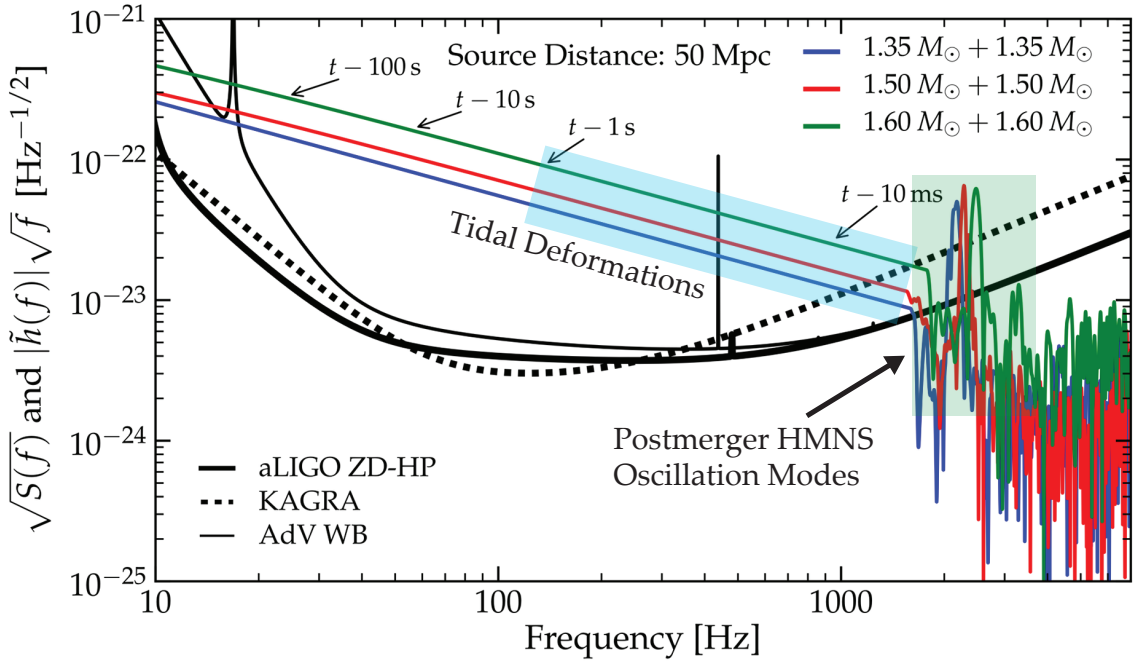

Figure 6.1: Plot courtesy of Sarah Gossan. Shows the amplitude spectral density of the design sensitivity noise floor, $\sqrt{S(f)}$, for the advanced LIGO, KAGRA, and advanced VIRGO gravitational wave detectors as black lines. Plotted as colored lines are the scaled frequency spectra, $|\tilde{h}(f)|\sqrt{f}$, of the gravitational waves from the inspiral and merger of neutron stars from the simulations by Sekiguchi et. al. [38], with the amplitude scaled for a distance to the source of 50 Mpc. The inspiral portion of the spectra are calculated via hybridization with the simulation data. As the binary inspirals and its frequency increases, it gets closer and closer to merger; the frequency at several times before merger are noted on the plot.

the former (tidal Love numbers) is more likely to be distinguished by a LIGO observation. This becomes clear when examining in Fig. 6.1 the gravitational wave frequency spectrum from a NSNS coalescence compared to the advanced LIGO noise curve. It is clear that the integral of the difference between the signal (colored lines) and the noise (black lines) is far greater for the inspiral portion where tidal deformations may be measured via the phase evolution. However, the differences in the phase evolution of the binary is more subtle than is able to be observed on this frequency plot. A NSNS binary simulation must run for many orbits and achieve high precision in the binary's orbital phase in order to measure the tidal Love numbers. This can take up to 100ms of physical evolution time, compared to ∼20ms for measuring the postmerger HMNS oscillation frequency. Bernuzzi et. al. has done an impressive study which carefully examines the precision of the inspiral and merger of an NSNS binary over 10 orbits [5]. In order to measure higher order effects beyond the tidal Love numbers from an NSNS inspiral, similar studies will have to be done which consist of more orbits and even greater phase accuracy. The initiation of such a study using the `SpEC` code is what we describe in this chapter.

6.1.2 Short gamma-ray bursts and other electromagnetic counterparts

Though gamma-ray bursts (GRBs) are the most powerful explosions observed in the universe, our understanding of their origin has only recently started to take shape [32]. GRBS are roughly divided via the duration of their light curves into two sub-populations with (very likely) different progenitors: short GRBs (SGRBs) with $T < 2$s and long GRBs with $T > 2$s [3]. In the past decade, observations have revealed that the long GRBs are often coincident with type Ic supernovae and that they likely originate from the core collapse of very massive stars [20, 25, 39]. The origin of the short subclass of GRBs however remains uncertain. Perhaps the leading candidate for the central engine powering SGRBs is the rapid accretion of matter onto a black hole resulting from a NSNS or BHNS merger [32]. The method of energy extraction for such a central engine is uncertain, but it is thought to be the result of magnetohydrodynamic processes or perhaps $\nu\bar{\nu}$ annihilation [34, 35].

6.1.3 SpEC

The Spectral Einstein Code, or SpEC, is a amalgamation of software libraries, support infrastructure and scripts for simulating compact objects (neutron stars and black holes) in full general relativity consisting of (at the time of writing) over 1.69 million lines of code. It has been in development since 2001, and currently has dozens of active collaborators across more than five universities. Over the past several years, binary black hole (BBH) merger simulations using SpEC have reached maturity and produced the highest precision evolutions of BBH inspiral and merger available to date [10, 31, 36, 40].

The high precision and impressive efficiency of the SpEC vacuum code [4] is due to its use of *multidomain spectral methods*. Spectral methods achieve exponential (geometric) convergence numerical resolution for smooth problems (cf. Ch. 5) and are thus ideal for numerical evolutions of black hole binaries with which have their singularities excised. *Excision* is a technique of numerically handling the black hole's singularity by excising the region interior to the black hole from horizon the computational domain. This works because "nothing can escape from a black hole;" one may treat the black hole's horizon as a boundary in the computational grid with an outflow boundary condition (i.e. nothing may flow *into* the numerical grid out of the black hole across its horizon).

The use of multidomain spectral methods with excision, however, comes at a large cost in the complexity of the code. Fundamentally, this is due to the fact that the computational domain must be broken up into *subdomains* which must roughly match the geometry of the fields being numerically evolved. In order to accomplish this, a general framework of coordinate mappings and

[3] However, recent work by Bromberg, Nakar, Piran & Sari has noted that the use of this heuristic to determine the progenitor of the GRB can easily result in an incorrect classification. [7]

[4] Vacuum code, or 'vacuum evolution' is commonly used as a synonym for solving Einstein's equations where the stress energy tensor vanishes; this is the case everywhere in the computational domain for evolutions of BBH coalescence.

control systems which dynamically adjust certain coordinate mappings needed to be employed [37]. In its simplest form, these mappings make the numerical grid corotate with the black holes as they orbit and inspiral. This not only facilitates the spectral convergence of the evolutions, but it is *required* in order to employ the excision technique since the black hole horizon is set as a boundary of the numerical grid. However, as researchers have pushed BBH simulations to higher spins [29], precessing orbits, and general mass ratios, the coordinate mappings and control systems required significant development and tuning [22].

`SpEC` has also been used to evolve matter fields and simulate the coalescence of black-hole neutron-star binaries [11–14, 16, 17, 19, 30]. The `SpEC` + hydrodynamics arm of the codebase (which we will refer to as `SpEC-hydro`), employs a 'dual-grid' method[5]; in the 'dual-grid' method, the metric fields are solved using pseudospectral methods on a multidomain spectral grid, and the matter fields are solved using high-resolution shock-capturing (HRSC) finite volume schemes on a Cartesian finite-difference grid. With this technique, the metric and matter fields must be communicated to the other (finite difference and spectral) grids via interpolation. The HRSC schemes of the matter grid have an algebraic order of convergence of, at maximum, fifth order ($O(1/n^5)$ for the WENO5 scheme in smooth flows), and thus require a much larger number of gridpoints to obtain the same truncation error as the geometrically converging metric fields on the spectral grid. The costly interpolation step is mitigated by the fact that the dense finite-difference grid only need cover the region of the domain where the neutron star and accretion flows exist, while the rest of the domain, including the gravitational wave 'wave-zone' need only be covered by the efficient spectral grid.

6.2 Methods and initial data

6.2.1 Code details

As the state of the `SpEC` code has and continues to be in constant development, there are yet no 'release' versions of the code. We therefore in Tab. 6.2.1 list the code revision used for this simulation. Unfortunately it is very difficult to describe the numerical resolution of `SpEC-hydro` simulations for three reasons: (i) The spacing of the gridpoints on the spectral grid are non-uniform and change from subdomain to subdomain. (ii) The coordinate mappings applied to the grid continually change the physical distances between gridpoints; this applies even for the finite-difference grid used to evolve the matter. (iii) The finite-difference grid extents are changed at discrete, dynamically determined intervals using the 'regridder' method of the code. This is designed to keep the resolution of the simulation high, but also not lose track of dynamically important matter that would otherwise flow out of the grid. Consequently, for simulations employing the `SpEC` code, the grid resolution in often

[5] also known as the "Mariage des Maillages" or "grid wedding" technique used in the `CoCoNuT` code `http://www.mpa-garching.mpg.de/hydro/COCONUT/intro.php` (see e.g. [9])

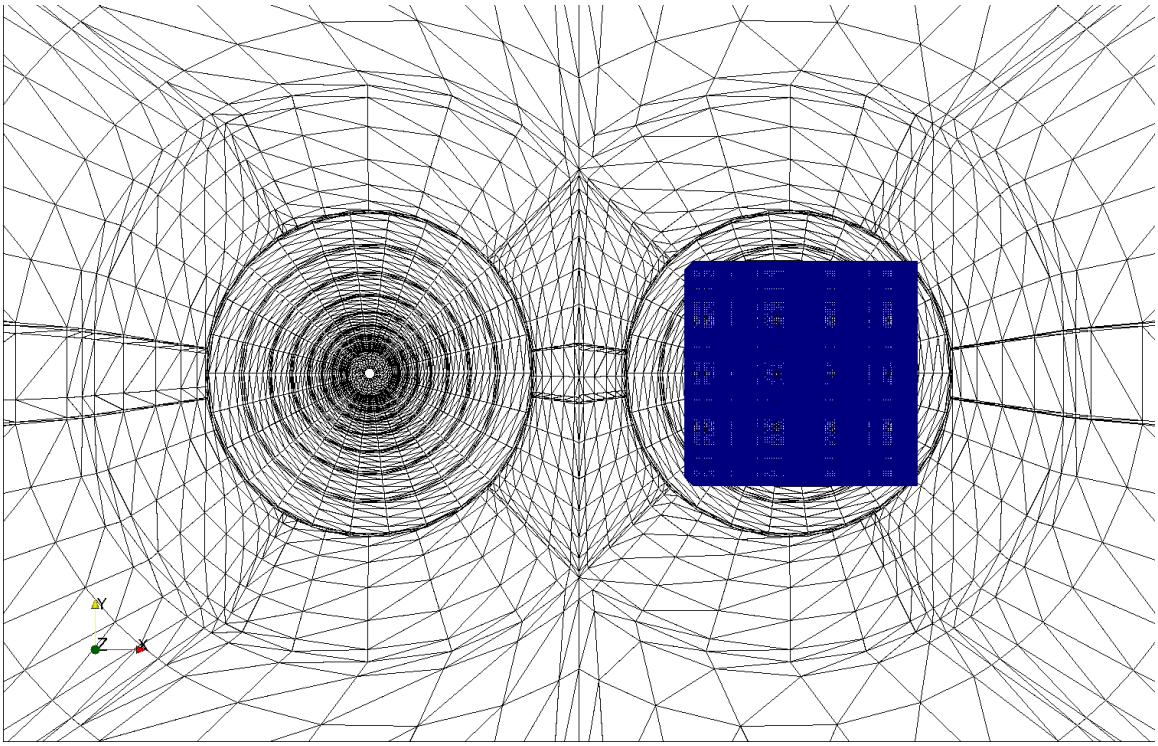

Figure 6.2: Evolution grid for the simulation (low resolution, Lev0 shown). Spectral grid is in black, and extends out ~ 10 times the size shown here into the wave-zone. The finite difference (matter) grid is shown in blue on the right. There is an identical finite difference grid for the neutron star on the left, but we have hidden it so that one may see the spectral grid inside the neutron star.

reported terms of the total number of grid-points to the one third power, $N^{1/3}$, as this measure should be approximately inverse to the linear grid spacing. We have conducted the NSNS inspiral simulation at three resolution 'levels' which we will refer to as Lev0, Lev1 and Lev2 corresponding to low, medium and high resolutions respectively. The grid resolution measures, $N^{1/3}$, for both the finite-difference matter grid and the spectral metric grid are reported for each resolution level in Tab. 6.2.1. For illustration, we show a slice in the XY of the spectral (black) and finite difference grids (blue, shown only for one neutron star) in Fig. 6.2.

Git revision:	`5f76c3b4b2192f1be8d398bee36ffcf2d2acae19`
Date linked:	Thu May 24 15:20:40 PDT 2012
Executable:	EvolveGRHydro
Machine:	zwicky
Grid resolutions:	Lev0, Lev1, Lev2
Matter grid $N^{1/3}$:	111, 135, 168
Spectral grid $N^{1/3}$:	42, 49, 56

Table 6.1: Code and resolution parameters

Description	Quantity	Value [code units]	Value [physical units]	
Coordinate separation between centers of mass	d	55.0	81.2	km
Baryon masses of each NS	$M_{\rm b}$	1.779	1.779	$M_\odot$
Circumferential radii of each NS	r_e	8.271	12.21	km
Dimensionless compaction	C	0.16	0.16	–
Initial radial decay rate	$\dot{a}$	-1.222×10^{-5}		
Initial orbital velocity	ω	0.00412	133.1	Hz
Initial eccentricity	e	7×10^{-4}	7×10^{-4}	–
Polytropic EOS scaling constant	κ	123.6		
Polytropic EOS exponent	Γ	2	2	–

Table 6.2: Initial data parameters for the simulation

6.2.2 Initial data

The initial data used for the simulation was generated within SpEC using the infrastructure developed for BHNS initial data [18]. In particular, the NSNS initial data routines were written by Curran Muhlberger at Cornell and were calibrated against the work of Gourgoulhon, Taniguchi, et al. [21, 41, 42]. These initial configurations are solved by making the approximation that the neutron stars are in *quasiequilibrium*; this approximation neglects the radiation-reaction from gravitational waves and therefore assumes the neutron stars are stationary in the corotating frame. Such configurations are *quasicircular*, that is the orbit has zero eccentricity in the quasiequilibrium approximation. Finally, the neutron stars are assumed to be *irrotational*; formally this means that the neutron star matter has zero vorticity and are non-rotating. This is a good approximation astrophysically because the internal viscosity and tidal forces on the neutron stars is too small to synchronize them to corotation as they inspiral [27].

The process of binary inspiral via gravitational radiation tends to circularize (remove eccentricity) from the binary orbit. Thus any astrophysical NSNS binaries near coalescence are expected to be completely circular. However, quasicircular orbits generated by initial data codes generally have non-zero eccentricity. This is because they do not account for the small amount of radial decay of the orbit via gravitational radiation. Thus to obtain initial data which is as eccentricity-free as possible, a small radial velocity may be specified in the initial data code to adjust the orbit. These adjustments are determined iteratively via evolution of the initial data, measurement of the orbital dynamics, and adjustment of the initial data parameters. The initial data we use has gone through three iterations of this procedure based on the radial velocity adjustment technique [18, 33]. In Table 6.2, we list the parameters describing the initial data used for the evolution. The values listed have been adjusted via the iterative eccentricity reduction procedure; without adjustment, the orbital eccentricity of the configuration would have been $e = 0.028$.

6.3 Results

Here we present the inspiral portion of the binary evolution. This consists of the portion of the simulation from the initial data, $t = 0.0$, up until a couple orbits before the neutron stars merge. Practically, this point is simply when, during the simulation, we must switch from using two disconnected patches for the finite-difference matter grids, to a single grid; this is determined simply by the point at which each individual NS's matter grid touch. In our simulations this occurs after almost 21.5 orbits at a simulation time of $t = 0.11$ *seconds*. Note that this is an extremely long time when compared to NSNS simulations in the literature; for example Bernuzzi et al. [5] tracks their simulation for nine orbits which is approximately 35 ms. For comparison, the dynamical timescale for an individual neutron star is less than 0.5 ms. In Fig. 6.3 we plot the XY position of each component neutron star as calculated via their center of mass. The pristine double spiral directly illustrates the low initial eccentricity of the initial data, as well as the accelerating orbital decay as the neutron stars approach each other. At the termination of the simulation at $t = 0.11$ s, the orbital frequency of the binary has increased to 410 Hz.

Next we report on the precision with which we can measure the evolution of the orbital phase. Since we expect the observable corresponding to the orbital phase to be the gravitational waveform of the inspiral, we must analyze the phase evolution of our gravitational wave signal. The measurement of gravitational waves in a numerical simulation is a delicate issue; they are only well defined (gauge invariant) in the limit as they approach null infinity in an asymptotically flat spacetime [45]. In these simulations, we measure the Newman-Penrose scalar, Ψ_4, at several radii and extrapolate to infinity using the procedure in [6]. The Newman-Penrose scalar is related to the gravitational wave signal measured by a detector by,

$$\Psi_4 =\sim (\ddot{h}_+ - i\ddot{h}_\times), \tag{6.1}$$

where h_+ and $h_\times$ are the gravitational wave plus and cross polarizations (which are functions of the retarded time), and a dot represents time derivatives. We include the $\sim$ to indicate that the expression may vary by an overall sign and algebraic constant depending on the conventions one uses. Then, Ψ_4 is expanded in terms of spin-weighted spherical harmonics of weight -2. Since it will be the mode dominating the gravitational waveform by a sizable margin (for inspiral), it is common to study the $(l, m) = (2, 2)$ mode; from here on this is what we shall mean when we refer to the waveform.

After the expansion and extrapolation procedure, the phase of the waveform, and subsequently, the difference in phase between resolutions (as a function of retarded time) may be calculated. We plot the difference in orbital phase as a function of the simulation retarded time in Fig. 6.4. There one can see that the absolute magnitude of the phase error begins to rise exponentially as the

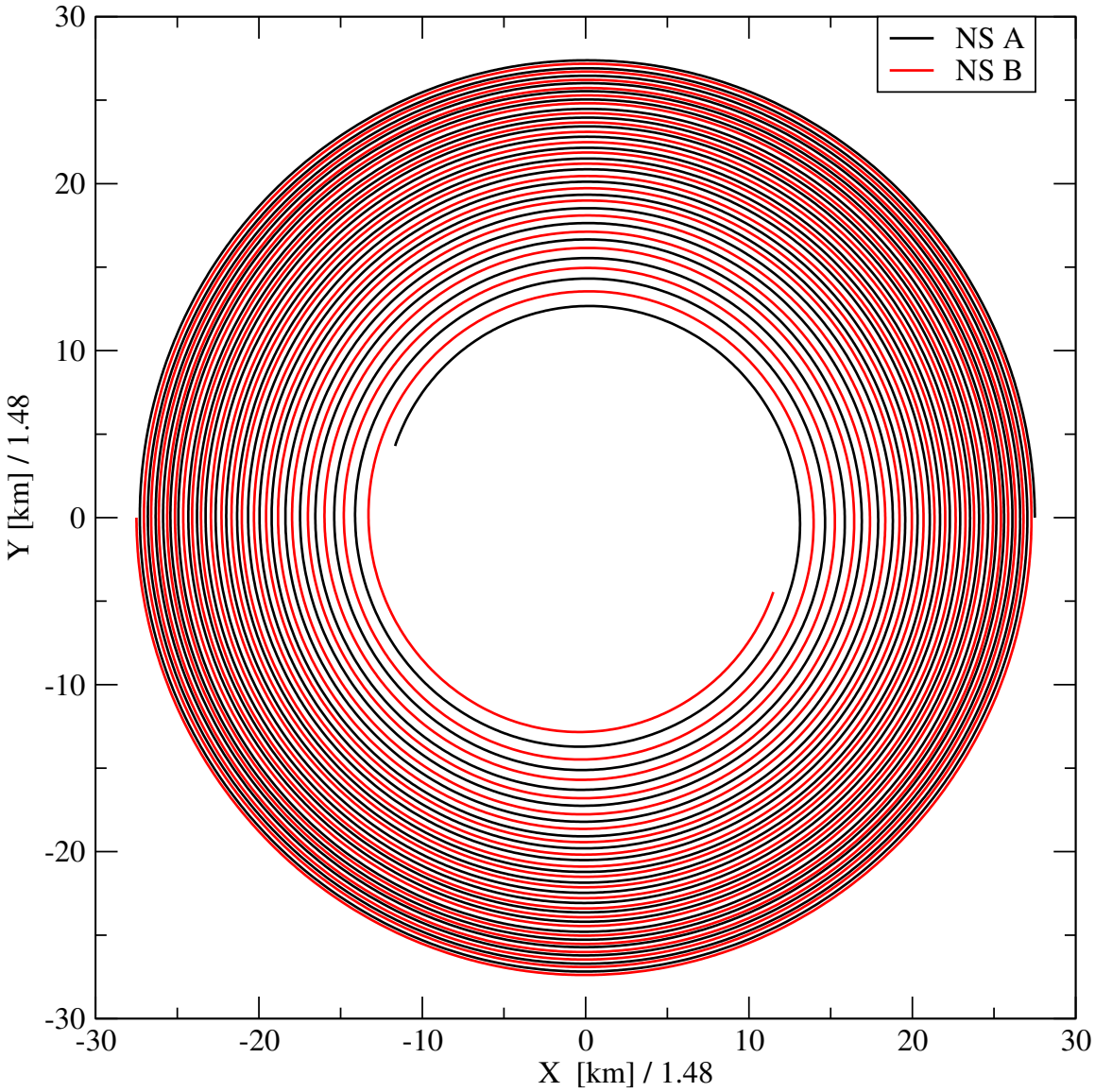

Figure 6.3: Shows orbital tracks of the center of mass of each neutron star. Shown for the high-resolution (Lev2) simulation. The axes scale factor of 1.48 corresponds to the conversion factor between lengths in $G = c = M_\odot = 1$ units and kilometers.

binary approaches merger. By the end of inspiral, the difference in phase between the medium and low resolutions (Lev1 - Lev0) has reached 2 radians while the difference between medium and high resolutions approaches 1 radian. While these could be expressed as a percentage difference over the total orbit, it would be misleading to do so because the phase error accumulates much more rapidly towards the end of inspiral. This phase error may be somewhere between on the same order to one magnitude worse than that reported by Bernuzzi et al. [5].

6.4 Discussion and conclusions

While the length of the NSNS inspiral we have simulated is longer than publications in the literature, we cannot claim to have achieved a precision which is better than that of Bernuzzi et al. [5]. However, is a the phase error on the order of 1 radian in the gravitational waveform enough to measure the tidal deformability of a neutron star? First, we may obtain an approximation for the tidal Love number of our neutron stars from Fig. 1 of Flanagan (2008) [15]. Here we see that a neutron star with a radius of 12.2 km and n=1 polytropic index (same as a $\Gamma = 2$ polytropic exponent) has a Love number, λ of $\sim 5 \times 10^{36}$ g cm^2 s^2. In Fig. 4 of Hinderer et. al. (2010) [24], we see that at a gravitational wave frequency of 800 Hz[6] there should be a 2 radian change gravitational wave phase due to tidal effects at a Love number of 5×10^{36} g cm^2 s^2 and NS gravitational mass of 1.7 $M_\odot$. Thus we find that the presented numerical simulation can not make an accurate measurement of the change in orbital phase due to tidal effects; a difference on the order of 2 radians would not be distinguishable (statistically significant) given a numerical error floor on the order of 1 radian.

Consequently, there is much room for improvement on this work. First, improving the precision in numerical phase by 2 - 3 orders of magnitude would allow for the study of effects of higher order than the tidal deformation, including non-linear corrections to the orbital phase from general relativity. Ideally, an improvement of at least one order of magnitude could be made, which would allow a numerical calculation of the phase correction due to tidal deformations. Efforts to improve the phase precision are currently underway by using newer `SpEC` technology, including the use of adaptive mesh refinement for the spectral grid.

Additionally, work is ongoing on ensuring the robustness on the merger and post-merger phases of evolution. Many infrastructure and grid changes must occur during this process and it is highly non-trivial to automate and ensure the robustness of the `SpEC-hydro` code during this process. While the merger, black hole formation, and ring down have been accomplished for this particular simulation, the infrastructure has yet to be applied to other NSNS inspiral simulations. The issue of black hole formation in `SpEC-hydro` was not attempted before the study of NSNS mergers was initiated; black holes which existed in simulation initial data were simulated in BHNS studies with

[6]This corresponds to our binary at the end of our simulation since at that time, its orbital frequency is 410 Hz, and there are two full gravitational wave cycles per orbit of a binary.

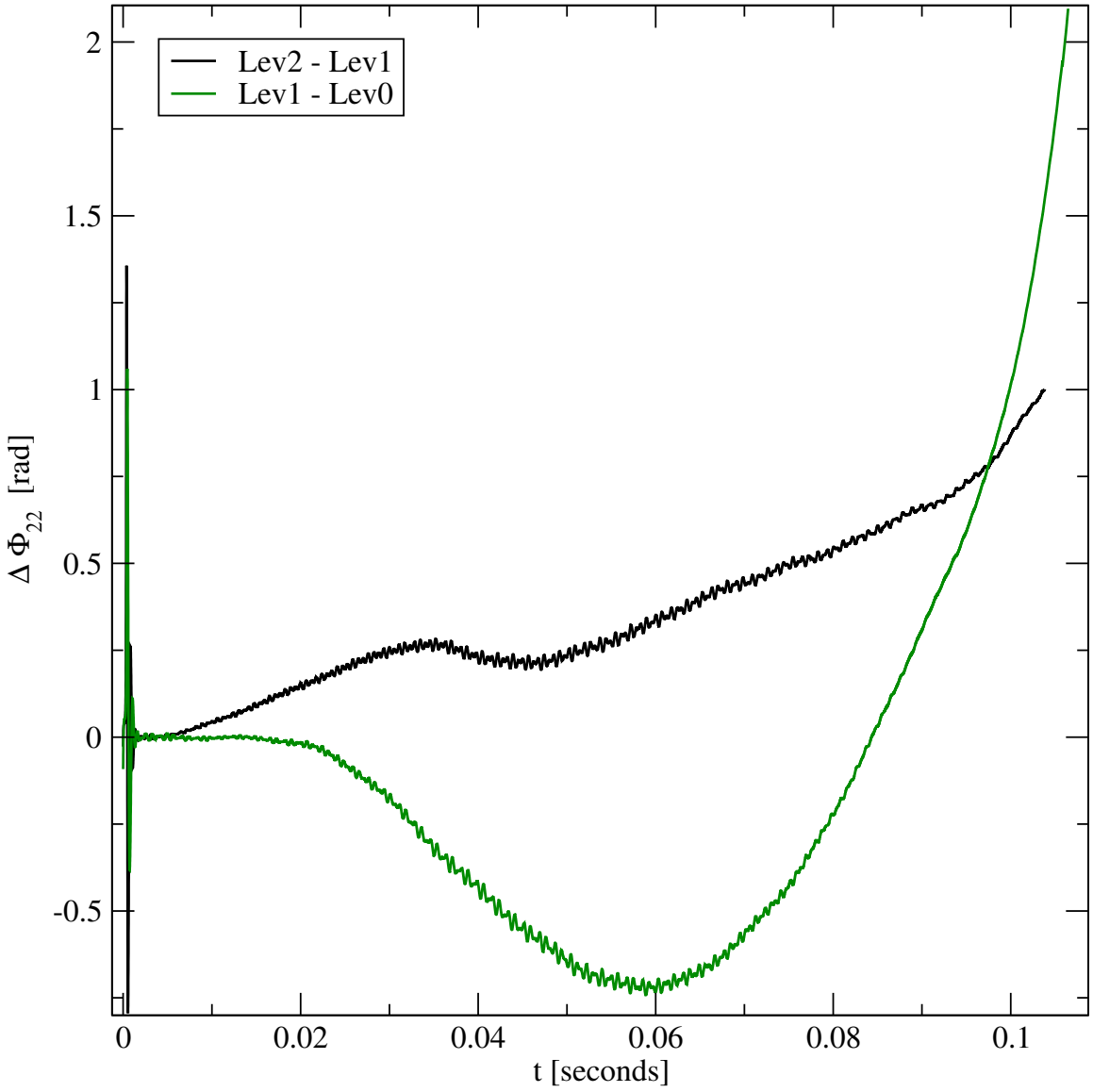

Figure 6.4: The difference between successive simulation resolutions of the gravitational wave phase of the dominant $(l, m) = (2, 2)$ mode as a function of simulation time in seconds. The initial spike corresponds to junk radiation created from the relaxation of the initial data on the grid. The persistent low amplitude high-frequency oscillations of the curves are due to finite-difference derivatives of the numerical data used in the extrapolation of the waveform and subsequent calculation of the orbital phase.

SpEC-hydro, but new black holes from gravitational collapse of matter had not yet been studied. In the next chapter, we present work on ensuring the robust simulation of black hole formation in SpEC-hydro, since the ability to capture gravitational collapse to a black hole is crucial in the merger phase of a NSNS coalescence.

Bibliography

[1] http://www.ligo.caltech.edu/. The Laser Gravitational Wave Observatory.

[2] J. Abadie et al. (LIGO Scientific Collaboration and Virgo Collaboration). Predictions for the Rates of Compact Binary Coalescences Observable by Ground-based Gravitational-wave Detectors. *Class. Quantum Grav.*, 27:173001, September 2010.

[3] B. P. Abbott, R. Abbott, R. Adhikari, P. Ajith, B. Allen, G. Allen, R. S. Amin, S. B. Anderson, W. G. Anderson, M. A. Arain, and et al. LIGO: the Laser Interferometer Gravitational-Wave Observatory. *Reports on Progress in Physics*, 72(7):076901, July 2009.

[4] A. Bauswein, H.-T. Janka, K. Hebeler, and A. Schwenk. Equation-of-state dependence of the gravitational-wave signal from the ring-down phase of neutron-star mergers. *Phys. Rev. D*, 86(6):063001, September 2012.

[5] S. Bernuzzi, M. Thierfelder, and B. Brügmann. Accuracy of numerical relativity waveforms from binary neutron star mergers and their comparison with post-Newtonian waveforms. *Phys. Rev. D*, 85(10):104030, 2012.

[6] M. Boyle, A. Buonanno, L. E. Kidder, A. H. Mroue, Y. Pan, H. P. Pfeiffer, and M. A. Scheel. High-accuracy numerical simulation of black-hole binaries: Computation of the gravitational-wave energy flux and comparisons with post-Newtonian approximants. *Phys. Rev. D*, 78:104020, 2008.

[7] O. Bromberg, E. Nakar, T. Piran, and R. Sari. Short versus Long and Collapsars versus Non-collapsars: A Quantitative Classification of Gamma-Ray Bursts. *Astrophys. J.*, 764:179, February 2013.

[8] M. Burgay, N. D'Amico, A. Possenti, R. N. Manchester, A. G. Lyne, B. C. Joshi, M. A. McLaughlin, M. Kramer, J. M. Sarkissian, F. Camilo, V. Kalogera, C. Kim, and D. R. Lorimer. An increased estimate of the merger rate of double neutron stars from observations of a highly relativistic system. *Nature*, 426:531–533, December 2003.

[9] P. Cerdá-Durán, J. A. Font, L. Antón, and E. Müller. A new general relativistic magnetohydrodynamics code for dynamical spacetimes. *Astron. & Astrophys.*, 492:937, December 2008.

[10] T. Chu, H. P. Pfeiffer, and M. A. Scheel. High accuracy simulations of black hole binaries: Spins anti-aligned with the orbital angular momentum. *Phys. Rev. D*, 80:124051, December 2009.

[11] M. B. Deaton, M. D. Duez, F. Foucart, E. O'Connor, C. D. Ott, L. E. Kidder, C. D. Muhlberger, M. A. Scheel, and B. Szilagyi. Black Hole-Neutron Star Mergers with a Hot Nuclear Equation of State: Outflow and Neutrino-Cooled Disk for a Low-Mass, High-Spin Case. *ArXiv e-prints*, April 2013.

[12] M. D. Duez. Numerical relativity confronts compact neutron star binaries: a review and status report. *Class. Quantum Grav.*, 27:114002, June 2010.

[13] M. D. Duez, F. Foucart, L. E. Kidder, C. D. Ott, and S. A. Teukolsky. Equation of state effects in black hole-neutron star mergers. *Class. Quantum Grav.*, 27:114106, June 2010.

[14] M. D. Duez, F. Foucart, L. E. Kidder, H. P. Pfeiffer, M. A. Scheel, and S. A. Teukolsky. Evolving black hole-neutron star binaries in general relativity using pseudospectral and finite difference methods. *Phys. Rev. D*, 78:104015, November 2008.

[15] É. É. Flanagan and T. Hinderer. Constraining neutron-star tidal Love numbers with gravitational-wave detectors. *Phys. Rev. D*, 77:021502, January 2008.

[16] F. Foucart, M. B. Deaton, M. D. Duez, L. E. Kidder, I. MacDonald, C. D. Ott, H. P. Pfeiffer, M. A. Scheel, B. Szilagyi, and S. A. Teukolsky. Black hole-neutron star mergers at realistic mass ratios: Equation of state and spin orientation effects. *Accepted for publication in Phys. Rev. D.; arXiv:1212.4810*, December 2012.

[17] F. Foucart, M. D. Duez, L. E. Kidder, M. A. Scheel, B. Szilagyi, and S. A. Teukolsky. Black hole-neutron star mergers for $10M_{\odot}$ black holes. *Phys. Rev. D*, 85(4):044015, 2012.

[18] F. Foucart, L. E. Kidder, H. P. Pfeiffer, and S. A. Teukolsky. Initial data for black hole neutron star binaries: A flexible, high-accuracy spectral method. *Phys. Rev. D*, 77:124051, June 2008.

[19] Francois Foucart, Matthew D. Duez, Lawrence E. Kidder, and Saul A. Teukolsky. Black hole-neutron star mergers: effects of the orientation of the black hole spin. *Phys. Rev. D*, 83:024005, 2011.

[20] A. S. Fruchter, A. J. Levan, L. Strolger, P. M. Vreeswijk, S. E. Thorsett, D. Bersier, I. Burud, J. M. Castro Cerón, A. J. Castro-Tirado, C. Conselice, T. Dahlen, H. C. Ferguson, J. P. U. Fynbo, P. M. Garnavich, R. A. Gibbons, J. Gorosabel, T. R. Gull, J. Hjorth, S. T. Holland, C. Kouveliotou, Z. Levay, M. Livio, M. R. Metzger, P. E. Nugent, L. Petro, E. Pian, J. E. Rhoads, A. G. Riess, K. C. Sahu, A. Smette, N. R. Tanvir, R. A. M. J. Wijers, and S. E.

Woosley. Long γ-ray bursts and core-collapse supernovae have different environments. *Nature*, 441:463–468, May 2006.

[21] Eric Gourgoulhon, Philippe Grandclement, Keisuke Taniguchi, Jean-Alain Marck, and Silvano Bonazzola. Quasiequilibrium sequences of synchronized and irrotational binary neutron stars in general relativity. I. Method and tests. *Phys. Rev. D*, 63:064029, 2001.

[22] D. A. Hemberger, M. A. Scheel, L. E. Kidder, B. Szilágyi, G. Lovelace, N. W. Taylor, and S. A. Teukolsky. Dynamical excision boundaries in spectral evolutions of binary black hole spacetimes. *Classical and Quantum Gravity*, 30(11):115001, June 2013.

[23] T. Hinderer. Tidal Love Numbers of Neutron Stars. *Astrophys. J.*, 677:1216, April 2008.

[24] T. Hinderer, B. D. Lackey, R. N. Lang, and J. S. Read. Tidal deformability of neutron stars with realistic equations of state and their gravitational wave signatures in binary inspiral. *Phys. Rev. D*, 81(12):123016, June 2010.

[25] J. Hjorth, J. Sollerman, P. Møller, J. P. U. Fynbo, S. E. Woosley, C. Kouveliotou, N. R. Tanvir, J. Greiner, M. I. Andersen, A. J. Castro-Tirado, J. M. Castro Cerón, A. S. Fruchter, J. Gorosabel, P. Jakobsson, L. Kaper, S. Klose, N. Masetti, H. Pedersen, K. Pedersen, E. Pian, E. Palazzi, J. E. Rhoads, E. Rol, E. P. J. van den Heuvel, P. M. Vreeswijk, D. Watson, and R. A. M. J. Wijers. A very energetic supernova associated with the γ-ray burst of 29 March 2003. *Nature*, 423:847–850, June 2003.

[26] R. A. Hulse and J. H. Taylor. Discovery of a pulsar in a binary system. *Astrophys. J. Letters*, 195:L51–L53, January 1975.

[27] C. S. Kochanek. Coalescing binary neutron stars. *Astrophys. J.*, 398:234, October 1992.

[28] J. M. Lattimer. The Nuclear Equation of State and Neutron Star Masses. *Ann. Rev. Nuc. Part. Sc.*, 62:485, November 2012.

[29] G. Lovelace, M. Boyle, M. A. Scheel, and B. Szilágyi. High-accuracy gravitational waveforms for binary black hole mergers with nearly extremal spins. *Class. Quantum Grav.*, 29(4):045003, 2012.

[30] G. Lovelace, M. D. Duez, F. Foucart, L. E. Kidder, H. P. Pfeiffer, M. A. Scheel, and B. Szilagyi. Massive disk formation in the tidal disruption of a neutron star by a nearly extremal black hole. *ArXiv e-prints*, February 2013.

[31] A. H. Mroue, M. A. Scheel, B. Szilagyi, H. P. Pfeiffer, M. Boyle, D. A. Hemberger, L. E. Kidder, G. Lovelace, S. Ossokine, N. W. Taylor, A. Zenginoglu, L. T. Buchman, T. Chu, E. Foley,

M. Giesler, R. Owen, and S. A. Teukolsky. A catalog of 171 high-quality binary black-hole simulations for gravitational-wave astronomy. *ArXiv e-prints*, April 2013.

[32] E. Nakar. Short-hard gamma-ray bursts. *Phys. Reports*, 442:166, April 2007.

[33] H. P. Pfeiffer, D. A. Brown, L. E. Kidder, L. Lindblom, G. Lovelace, and M. A. Scheel. Reducing orbital eccentricity in binary black hole simulations. *Clas. Quantum Grav.*, 24:59, June 2007.

[34] S. Rosswog and M. Liebendörfer. High-resolution calculations of merging neutron stars—II. Neutrino emission. *MNRAS*, 342:673, July 2003.

[35] S. Rosswog, E. Ramirez-Ruiz, and M. B. Davies. High-resolution calculations of merging neutron stars—III. Gamma-ray bursts. *Mon. Not. Roy. Astron. Soc.*, 345:1077, 2003.

[36] M. A. Scheel, M. Boyle, T. Chu, L. E. Kidder, K. D. Matthews, and H. P. Pfeiffer. High-accuracy waveforms for binary black hole inspiral, merger, and ringdown. *Phys. Rev. D*, 79:024003, January 2009.

[37] M. A. Scheel, H. P. Pfeiffer, L. Lindblom, L. E. Kidder, O. Rinne, and S. A. Teukolsky. Solving Einstein's equations with dual coordinate frames. *Phys. Rev. D*, 74:104006, November 2006.

[38] Y. Sekiguchi, K. Kiuchi, K. Kyutoku, and M. Shibata. Gravitational Waves and Neutrino Emission from the Merger of Binary Neutron Stars. *Phys. Rev. Lett.*, 107(5):051102, July 2011.

[39] K. Z. Stanek, T. Matheson, P. M. Garnavich, P. Martini, P. Berlind, N. Caldwell, P. Challis, W. R. Brown, R. Schild, K. Krisciunas, M. L. Calkins, J. C. Lee, N. Hathi, R. A. Jansen, R. Windhorst, L. Echevarria, D. J. Eisenstein, B. Pindor, E. W. Olszewski, P. Harding, S. T. Holland, and D. Bersier. Spectroscopic Discovery of the Supernova 2003dh Associated with GRB 030329. *Astrophys. J. Letters*, 591:L17–L20, July 2003.

[40] Bela Szilagyi, Lee Lindblom, and Mark A. Scheel. Simulations of Binary Black Hole Mergers Using Spectral Methods. *Phys. Rev. D*, 80:124010, 2009.

[41] K. Taniguchi and E. Gourgoulhon. Quasiequilibrium sequences of synchronized and irrotational binary neutron stars in general relativity. III. Identical and different mass stars with γ=2. *Phys. Rev. D*, 66(10):104019, November 2002.

[42] K. Taniguchi and E. Gourgoulhon. Various features of quasiequilibrium sequences of binary neutron stars in general relativity. *Phys. Rev. D*, 68(12):124025, December 2003.

[43] J. H. Taylor and J. M. Weisberg. A new test of general relativity - Gravitational radiation and the binary pulsar PSR 1913+16. *Astrophys. J.*, 253:908–920, February 1982.

[44] J. H. Taylor and J. M. Weisberg. Further experimental tests of relativistic gravity using the binary pulsar PSR 1913 + 16. *Astrophys. J.*, 345:434, October 1989.

[45] R. M. Wald. *General Relativity.* Chicago: USA, University of Chicago Press, 1984.

Chapter 7

Black hole formation from isolated neutron stars in SpEC

First publication. Jeffrey D. Kaplan (2013).

This work relied on the use of the `SpEC-hydro` code, and thus all the members of the SXS collaboration. In particular Curran Muhlberger, Matt Duez, Francois Foucart, Mark Scheel, Béla Szilágyi and Roland Haas made significant contributions to this work.

7.1 Literature review and introduction

The collapse of rotating neutron stars to black holes is a prime example of a astrophysical problem which requires the full machinery of a robust numerical relativity code in order to capture. The first 3D simulations of collapsing neutron stars were done by Shibata, Baumgarte for uniformly rotating stars [27]. Shibata & Shapiro also performed axisymmetric collapse simulations of uniformly rotating supramassive neutron stars at the mass-shedding limit, finding that, for a wide range of polytropic equations of state, almost no matter was left outside the resulting Kerr black hole ($< 10^{-3}$ of the initial mass remained)[26, 28].

Between 2003 and 2006, Duez et al. expanded on the work of Shibata et al. using an independent code [11–13] for evolutions in axisymmetry and full 3+1 general relativity. Here Duez significantly expanded the physical parameter space by exploring differentially rotating HMNS and their collapse, including a 3D 'supra-Kerr' model; a model with angular momentum J, divided by gravitational mass, M, squared greater than 1: $J/M^2 > 1$. More recently, the collapse of differentially rotating neutron stars has been revisited since first studied by Duez et al. The simulation of gravitational collapse for differentially rotating HMNS models and the artificially induced collapse of a 'supra-Kerr' model was repeated by by Giacomazzo et al. [16], and Saijo & Hawke examined the general

relativistic dynamics after a black hole was formed[25].

Baiotti et al. [2–4] subsequently developed a 3+1 code, concentrating on studying the gravitational physics of rotating neutron star collapse. They investigated measurements of the final Kerr black hole mass and spin via both the apparent and event horizons along with the dynamical horizon framework[2]. They also investigated the gravitational wave signal emitted from collapse via RWZ wave extraction at finite radius[3, 4]. Additionally, they investigated the growth of non-axisymmetric, high $\beta = T/|W|$ instabilities (i.e. the dynamical bar-mode instability), and its gravitational wave signal [5].

Also interesting in the context of rotating neutron stars is the 'low $T/|W|$' instability, first discovered in Newtonian gravity by Centrella et al. [7] and further investigated by Saijo, Baumgarte & Shapiro [24]. Ott et al. found this instability to be relevant in Newtonian simulations of supernova stellar core collapse starting from astrophysically realistic initial data. Non-axisymmetric instabilities are of great interest in the literature, and have been studied by numerous authors in fully general relativistic simulations [9, 20, 33].

The main goal of this work is to develop and document the computational methods used to simulate the formation of a black hole from conventional matter in the generalized harmonic framework. To our knowledge, dynamical evolution from before, through, and after black hole formation from perfect fluid matter has not been well documented in the past literature of generalized harmonic evolutions. We find that the results of Sorkin's simulations in axisymmetry, that a damped-wave gauge is particularly robust for black hole formation [30], are also true in 3+1 generalized harmonic evolutions. [1]

7.2 Methods and numerical setup

In this section we detail some of the numerical methods and evolution equations used for the collapse simulations. Here we jump straight into the methods; an introduction to these methods and the `SpEC-hydro` code can be found in Secs. 6.1.3 and 6.2.1.

7.2.1 Hydrodynamics grid

Our hydrodynamics grid consists of multiple overlapping unigrid blocks. In these simulation, the total extents of the grid cover 1.50 times the surface of the star in each of the x, y, and z directions. Our resolution is specified in terms of spacing of the gridpoints in meters. For the TOV simulations starting from spherically symmetric initial data, we employ octant symmetry (reflection across the x, y, and z axes to reduce the computational cost, and use low, medium and high resolutions of

[1] Also see Choptuik and Pretorius [8] who use a damped-harmonic gauge for ultrarelativistic collisions of complex scalar fields.

$[200, 150, 100]$ meters. With rotating stars starting from axisymmetric initial data, we use reflection symmetry about the z axis, and use resolutions of $[300, 250, 200]$ meters. The entire grid is divided into blocks of no larger than approximately 30^3 points per block for parallelization. The blocks overlap for 3 points each to prevent the necessity of using one sided derivative stencils at internal block boundaries (i.e. our number of 'ghost zones' is 3).

7.2.2 Spectral grid and methods

We evolve the metric variables using pseudospectral methods on what we call the spectral grid. The spectral grid extends out to an (arbitrary but large) radius of 38 times the equatorial stellar radius for and is divided into eighteen spectral subdomains. On each subdomain the metric variables (each component of each tensor) are expanded in terms of a set of three-dimensional scalar basis functions. The gridpoints of each subdomain are then chosen such that they lie on the zeros of the basis functions, (or an equivalent set; cf. Ch. 5). For all subdomains except for the central subdomain, we use a basis function consisting of the product of Chebyshev polynomials in the radial direction, and scalar spherical harmonics for the angular directions. The central subdomain uses a filled ball which avoids placing a point at the center point (which is singular in the angular directions) by using a spectral expansion involving one-sided Jacobi polynomials [21]. For all subdomains we use the same order of spherical harmonic L for the expansion, as this places the gridpoints at subdomain boundaries in precisely the same location and therefore eliminates the need for interpolation when communicating between subdomains. The angular grid has $[L + 1, 2(L + 1)]$ points in the $[\theta,\phi]$ directions and is uniformly spaced in $[\cos\theta,\phi]$.

For the TOV simulations, we do not increase the angular resolution when increasing the resolution level of the simulation, and keep it fixed at $L = 6$ (yielding a $[\theta,\phi]$ resolution in terms of gridpoints of [7,14]). This is because the simulation is physically spherically symmetric, and the addition of extra modes tends to add extra numerical noise with no resolution benefit. In the rotating stellar evolutions, we use angular resolutions with Ls of $[10, 12, 14]$ for low, medium and high resolutions respectively.

7.2.3 Time evolution and grid-to-grid communication

The metric and hydro variables time-stepped separately on their respective grids using a Runge-Kutta method of order 3. Ideally, one would communicate the updated hydro variables to the metric grid and vice-versa after each Runge-Kutta substep. However, we find that communication between grids can result in grid-to-grid communication dominating the computational time of our simulations. In order to reduce the amount of communication between grids required, we use previous time-step data to do a linear, forwards-in-time extrapolation of the metric data on the hydrodynamics grid

to calculate the values of the metric at intermediate Runge-Kutta steps on the hydrodynamics grid (again, the same goes for determining values of the hydrodynamic variables on the spectral grid at intermediate Runge-Kutta steps). The time stepper is an adaptive, dense stepper, which allows our simulations to step as closely as possible to the Courant-limit (see, e.g. [22]).

7.2.4 Equation of state

We choose the analytic 'gamma-law' EOS for this study with a choice of $\Gamma = 2.$ and polytropic constant, $\kappa = 100$. The motivation for this choice was to use the same EOS and initial data as the studies by Baiotti and Giacomazzo [3, 16]. The details of evolution for the EOS can be found in Sec 2.B of Duez et al. [10].

7.2.5 Hydrodynamic evolution equations

We use code described in Duez et. al. [10], for which the hydro evolution equations can be found in Shibata. et al. [29] (hereafter STU). Hydro conservative variables (evolved variables, from [10] Sec. 2.B):

$$\rho_* = \alpha\sqrt{g}u^0\rho_b, \tag{7.1}$$

$$\tau = \alpha^2\sqrt{g}T^{00} - \rho_*, \tag{7.2}$$

$$S_k = \alpha\sqrt{g}T^0_k, \tag{7.3}$$

where α is the lapse, g is the determinant of the spatial metric, ρ_b is the baryon (rest mass) density, u^0 is the time component of the fluid 4-velocity, and T is the stress energy tensor. Note that in Duez et. al. [10] and other works the symbol D is used for the conservative density, here referred to as ρ_*. The evolution equations are Eqs. 2.8-2.10 of STU [29]:

$$\begin{aligned}
\partial_t\rho_* + \partial_i\left(\rho_* v^i\right) &= 0, \\
\partial_t\left(\rho_* e^*\right) + \partial_i\left[\rho_* e^* v^i + P\sqrt{g}\left(v^i + \beta^i\right)\right] &= \\
\alpha\sqrt{g}PK + \frac{\rho_*}{u^0 h}hu_i hu_j K^{ij} - \rho_* hu_i g^{ij}\nabla_j\alpha & \\
\partial_t\left(\rho_* hu_j\right) + \partial_i\left(\rho_* v^i hu_j + P\alpha\sqrt{g}\delta^i_j\right) &= \\
-\rho_*\left[wh\partial_j\alpha - hu_i\partial_j\beta^i + \frac{1}{2u^0 h}hu_k hu_l\partial_j g^{kl}\right] & \\
+P\partial_j\left(\alpha\sqrt{g}\right). &
\end{aligned}$$

Here P is pressure, h is the specific enthalpy,

$$h = 1 + \epsilon + P/\rho_b, \tag{7.4}$$

with ϵ the specific internal energy, v^i is the 3-velocity of the fluid, e^* is a relativistic specific mass-energy density,

$$e^* = hw - \frac{P}{\rho_b w}, \tag{7.5}$$

with w the Lorentz factor of the fluid,

$$w = \alpha u^0, \tag{7.6}$$

β^i is the shift vector, K^{ij} the extrinsic curvature with trace K, and ∇_j is the covariant derivative with respect to the three metric, g_{ij}.

Our implementation of these equations is slightly different than in STU as our energy variable τ (Eq. 7.2) differs from STU by a subtraction of the conserved density, ρ_*. Thus our evolution equation for the energy differs from STU by a subtraction of the equation of mass conservation. Our evolution equations as they are written in the code are:

$$\partial_t \rho_* = -\partial_j F^j_{\rho_*}, \tag{7.7}$$

$$\begin{aligned} \partial_t \tau = &- \partial_j F^j_\tau + \alpha P \sqrt{g} K \\ &+ g^{ij} S_i \partial_j \alpha + \frac{\alpha}{\rho_* w h} S_i S_j g^{in} g^{jl} K_{nl}, \end{aligned} \tag{7.8}$$

$$\begin{aligned} \partial_t S_i = &-\partial_j F^j_{S_i} + P\sqrt{g}\left(\partial_i \alpha + \alpha \frac{\partial_i \sqrt{g}}{\sqrt{g}}\right) \\ &-\rho_* w h \partial_i \alpha + S_j \partial_i \beta^j - \frac{1}{2}\frac{\alpha}{\rho_* w h} S_j S_k \partial_i g^{jk}. \end{aligned} \tag{7.9}$$

Here we have explicitly separated the flux terms, $\partial_j F^j$, from the source terms, as the divergence of the sources are solved for using a HLL Riemann solver [1]. The flux terms are as follows:

$$F^j_{\rho_*} = w\sqrt{g}\rho_b v^j, \tag{7.10}$$

$$F^j_\tau = w\sqrt{g}\rho_b v^j (wh - 1) + \sqrt{g} P \beta^j, \tag{7.11}$$

$$F^j_{S_i} = w\sqrt{g}\rho_b h u_i v^j + \delta^j_i P\alpha. \tag{7.12}$$

7.2.6 Generalized harmonic equations

We evolve Einstein's equations with the generalized harmonic evolution system as presented in Lindblom et al. 2006 [18]. Our four-metric is, ψ_{ab} and we denote it's derivatives as $\Phi_{iab} = \partial_i \psi_{ab}$ and $\Pi_{ab} = -t^c \partial_c \psi_{ab}$. The first-order representation which includes terms for constraint damping are Eqs. (35-37) of Ref [18] (which uses $\{N, N^i\}$ instead of $\{\alpha, \beta^i\}$ for the lapse and shift functions):

$$\partial_t \psi_{ab} - (1+\gamma_1)\beta^k \partial_k \psi_{ab} = -\alpha \Pi_{ab} - \gamma_1 \beta^i \Phi_{iab}, \tag{7.13}$$

$$\begin{aligned}
\partial_t \Pi_{ab} - &\beta^k \partial_k \Pi_{ab} + \alpha g^{ik} \partial_k \Phi_{iab} - \gamma_1\gamma_2 \beta^k \partial_k \psi_{ab} \\
=& 2\alpha \psi^{cd} \left(g^{ij} \Phi_{ica} \Phi_{jdb} - \Pi_{ca}\Pi_{db} - \psi^{ef}\Gamma_{ace}\Gamma_{bdf} \right) \\
&- 2\alpha \nabla_{(a} H_{b)} - \frac{1}{2}\alpha t^c t^d \Pi_{cd}\Pi_{ab} - \alpha t^c \Pi_{ci} g^{ij} \Phi_{iab} \\
&+ \alpha\gamma_0 \left[2\delta^c{}_{(a} t_{b)} - \psi_{ab} t^c \right] (H_c + \Gamma_c) - \gamma_1\gamma_2 \beta^i \Phi_{iab} \\
&- 2\alpha \left(T_{ab} - \frac{1}{2}\psi_{ab} T^{cd} \psi_{cd} \right),
\end{aligned} \tag{7.14}$$

$$\begin{aligned}
\partial_t \Phi_{iab} - &\beta^k \partial_k \Phi_{iab} + \alpha \partial_i \Pi_{ab} - \alpha\gamma_2 \partial_i \psi_{ab} \\
=& \frac{1}{2}\alpha t^c t^d \Phi_{icd} \Pi_{ab} + \alpha g^{jk} t^c \Phi_{ijc} \Phi_{kab} - \alpha\gamma_2 \Phi_{iab},
\end{aligned} \tag{7.15}$$

where γ_0, γ_1, and γ_2 are constraint damping parameters. The parameter γ_0 is the same as used by Pretorius [23] and damps the two-index constraint (i.e., violations of Eq. 7.14). The parameter γ_2 serves the same purpose for the three-index constraint (i.e., it damps violations of Eq. 7.15). Finally, the parameter γ_1 controls the characteristic speed of certain constraint violating modes; in certain situations it is beneficial to set it to values deviating slightly from unity, causing the constraint violating modes to propagate off the grid. Here t^a denotes the unit timelike normal vector to the spatial slice (often denoted n^a in ADM literature). Note our Eq. 7.14 also includes the matter source terms which are not included in Eq. (36) of [18].

7.2.7 Excision of nascent black hole

Once an apparent horizon pops into existence on the spatial slice, we excise the region inside the horizon before the code crashes due to the impending formation of a singularity. We use the same

set of scripts and methods used in `SpEC` binary black hole evolutions in order to perform the excision and transition to a black hole evolution. This method relies on locating the apparent horizon at several timesteps. The kinematics of the apparent horizon over these several steps provides enough information to initialize the coordinate mappings necessary to lock the grid boundary onto the rapidly expanding horizon. For our evolutions, we choose 8 steps with a $\Delta t = 0.25$ (except for the H3 model, where we must use $\Delta t = 0.10$ to avoid the code crashing before enough horizon finds occur). Since we do not know precisely when an apparent horizon can first be found, we choose to start looking for an apparent horizon when $\rho_{b,max}/\rho_{b,max}|_{t=0} = 20$. In practice, we could search for an apparent horizon at all points during the simulation, however the apparent horizon finder can be computationally expensive (especially when it does not converge, which will always occur when there is no horizon), and thus we employ the stated density threshold.

7.3 Gauge equations, conditions, and methods

While the choice of gauge conditions and methods may be considered a part of the numerical methods, we have chosen to dedicate a separate section to it, as it is a crucial part of our study. The gauge freedom associated with general relativity corresponds to the invariance of physics under coordinate transformations. Since the meaning of coordinates in general relativity is determined by the metric, the meaning of the coordinates labeling the gridpoints in a numerical relativity simulation may be constantly changing as the simulation evolves. Consequently, for a numerical relativity simulation, the choice of coordinates *and some choice about their evolution in time* corresponds to a choice of gauge. Finding a suitable 'gauge condition' has proven to be one of the most challenging aspects for numerical relativists to work out in their simulations of black holes.

7.3.1 Harmonic and generalized harmonic gauge

The harmonic gauge is so named because it imposes the condition that each coordinate x^a, satisfies the covariant scalar wave equation:

$$\nabla^c \nabla_c x^a = 0. \tag{7.16}$$

This coordinate condition has been widely used in the literature for analytical studies of relativity[2]. The *generalized harmonic* coordinate condition was first studied by Garfinkle in 2002 [15]. In generalized harmonic coordinates, an arbitrary *gauge source function* H^a is specified:

$$\nabla^c \nabla_c x^a = H^a. \tag{7.17}$$

[2]It is employed, for example, in Ch.2 of this thesis.

Then, a specification for H^a in terms of coordinate and metric variables corresponds to a choice of gauge. This is the basis for the 'generalized harmonic evolution system' employed in `SpEC`[18]. Additionally, Lindblom et al. [17, 19] have developed numerical gauge 'drivers' which allow one to specify the gauge source function in a manner which corresponds to gauge choices commonly used in other formulations of general relativity (see Ch.4 of the text by Baumgarte & Shapiro[6] for a discussion of common gauge choices).

7.3.2 Damped harmonic gauge for numerical evolutions

We find that a 'damped' harmonic gauge condition is necessary for robust collapse. We use the same prescription as in Szilágyi, Lindblom & Scheel [31] (hereafter as SLS) for the damped harmonic gauge. The spatial part of a generalized harmonic gauge can be written as:

$$\nabla^c \nabla_c x^i = H^i, \tag{7.18}$$

where H^i is the spatial part of H^a. The coordinate dynamics are 'damped' by choosing H^i such that it represents a damping term for the above equation. In SLS, they choose:

$$H^i = \mu_s t^i = -\mu_S \beta^i / \alpha, \tag{7.19}$$

where $1/\mu_S$ is the time scale of the damping. Equation 7.19 governs the evolution of the spatial coordinates and we refer to it as the damped harmonic *shift* condition.

For the time component of the generalized harmonic gauge, SLS note the gauge constraint yields the equation (that is, expanding the LHS of Eq. 7.17 in terms of 3+1 metric variables one obtains):

$$t^a H_a = t^a \partial_a \log\left(\frac{\sqrt{g}}{\alpha}\right) - \alpha^{-1} \partial_k \beta^k. \tag{7.20}$$

As with the spatial part of the generalized harmonic gauge source function, the time component of the gauge source function may be chosen as a damping term, this time for $\sqrt{g}/\alpha$:

$$t^a H_a = -\mu_L \log\left(\frac{\sqrt{g}}{\alpha}\right), \tag{7.21}$$

where again, μ_L is a damping factor. As Eq. 7.21 determines the temporal evolution of the coordinates; we refer to it as the damped harmonic *slicing* condition. SLS find that for highly dynamical spacetimes, that choosing:

$$\mu_S = \mu_L = \mu_0 \left[\log\left(\frac{\sqrt{g}}{\alpha}\right)\right]^2, \tag{7.22}$$

is effective for their binary black hole evolutions. Here μ_0 is a smooth order-unity function of time

which may be specified as a function of space and/or time to adjust the strength of the damping.

Equations 7.19 and 7.21 correspond to a complete choice of coordinates by fixing the spatial and time components of the gauge source function, H^a, respectively. We will refer to a gauge source function chosen in this manner as $H^a_{\rm D}$ where the 'D' denotes it is a *damped* and therefore a *dynamical* gauge source function.

7.3.3 Imposing damped harmonic gauge in SpEC simulations

For an arbitrary choice of initial data, the gauge source function, H^a, is fully determined by the coordinates of the initial data and thus has some initial value, which we will refer to as $H^a_{\rm I}$. When the initial data is interpolated to the evolution grid and the evolution is started, the gauge source function H^a must not change discontinuously from its initial value. Therefore, our specification of the gauge (which corresponds to prescribing H^a analytically) must take into account the initial value of the gauge source function $H^a_{\rm I}$. This is done in SpEC simulations by specifying the gauge in the following way:

$$H^a(t) = H^a_{\rm I} e^{-(t/\tau_{\rm off})^4} + H^a_{\rm D}\left(1 - e^{-(t/\tau_{\rm on})^4}\right), \tag{7.23}$$

where $H^a_{\rm D}$ is the dynamical damped harmonic gauge condition defined by Eqs. 7.19-7.22 and $\tau_{\rm off}$ & $\tau_{\rm on}$ are damping timescales chosen for the physical problem at hand. Note that $\tau_{\rm off}$ controls the rate at which the initial gauge is 'rolled off' to zero, and $\tau_{\rm on}$ controls the rate at which the damped gauge condition is 'rolled on'.

We may decompose Eq. 7.23 into its time and space components:

$$H^i(t) = H^i_{\rm I} e^{-(t/\tau_{\rm s,off})^4} + H^i_{\rm D}\left(1 - e^{-(t/\tau_{\rm s,on})^4}\right), \tag{7.24}$$

$$t^a H_a(t) = t^a H_{{\rm I}a}\, e^{-(t/\tau_{\rm t,off})^4} + t^a H_{{\rm D}a}\left(1 - e^{-(t/\tau_{\rm t,on})^4}\right). \tag{7.25}$$

This allows us to independently specify the 'roll-on' and 'roll-off' timescales for the damped harmonic *shift*, and damped harmonic *slicing* conditions, Eqs. 7.19 and 7.21 respectively.

We have investigated a series of five different gauge conditions in order to investigate the coordinate dynamics during gravitational collapse and attempt to determine what condition will be lead to the most robust simulation of black hole formation. The conditions are denoted: 'froze' for a *frozen* gauge where $H^a(t) = H^a_{\rm I}$, 'harm' for a pure *harmonic* gauge (i.e $H^a = 0$), 'shift' for a gauge where only the damped harmonic *shift* condition Eq. 7.19 is rolled on, 'slice' for a gauge where only the damped harmonic *slicing* condition Eq. 7.21 is rolled on, and 'full' for a *fully* harmonic gauge in which both the damped harmonic shift and slicing conditions are used. These gauges are

Gauge	Roll-off timescale		Roll-on timescale	
	$\tau_{\rm s,off}$	$\tau_{\rm t,off}$	$\tau_{\rm s,on}$	$\tau_{\rm t,on}$
froze	∞	∞	∞	∞
harm	10	10	∞	∞
shift	10	10	25	∞
slice	10	10	∞	25
full	10	10	25	25

Table 7.1: List of gauge conditions examined. Timescales are are from Eqs. 7.24 & 7.25 and are specified in code units. A value of ∞ corresponds to setting the exponential term corresponding to the timescale equal to unity. The subscript s stands for the *spatial* (shift) condition, and the subscript t stands for the *temporal* (slicing) condition.

listed in Tab. 7.1 In all cases but the frozen gauge, the initial gauge is rolled off by choosing a value for $\tau_{\rm s,off} = \tau_{\rm t,off} = 10.0$ (in coordinate time). This results in $H^a_{\rm I}$ being rolled off to zero within roundoff precision after $t = 30.0$.[3] For the shift only, slicing only, and fully damped harmonic gauge conditions, we use a $\tau_{\rm on}$ of 25.0 code units which is about half of the time to black hole formation, so that our damped harmonic gauge condition has fully 'kicked in' by the time of collapse and black hole formation.

7.4 Initial Models and physical setup

7.4.1 Methods

Initial data for our simulations are spherically symmetric TOV, and axisymmetric CST equilibrium models constructed as in Sec. 8.2.3 & 8.2.4. In general, if an unstable equilibrium model is evolved, the numerical truncation error will manifest as a small perturbation that will result an evolution away from the unstable equilibria. This evolution will either take the stellar model to another, stable equilibria, or proceed towards gravitational collapse to a black hole. For our study, we wish to induce a *resolved* evolution towards gravitational collapse to a black hole; that is, we do not wish our evolution to be dependent on the nature of the truncation error. The stellar models we construct, which are close to the parameter space of unstable equilibria, are 'tweaked' by *depleting* their pressure by a constant factor, f_d. However, an arbitrary change to the pressure, without modifying any of the other fluid or metric variables, may result in a configuration which violates the Einstein constraint equations. In particular, it may violate the gauge constraint equation $H_a = -\Gamma_a$, which has the effect of polluting the gauge prescription specified in Sec. 7.3.3.

Hence, we have investigated *resolving* the constraint equations after a depletion has been specified. Our first unsuccessful attempt at this was employing the `SpEC` elliptic solver to resolve the metric variables given pressure depleted configuration. While this technique worked for TOV initial

[3] In our simulations, the initial gauge imprint must be fully rolled off by the time we excise and start the ringdown portion of the run so that we may appropriately apply horizon tracking coordinate mappings at the start of ringdown.

Model	M_{ADM}	$M_{\rm b}$	$\rho_{\rm b,max}$	R_{iso}	EOS	Rot $\tilde{A}$	$r_{p/e}$
D0	1.636	1.770	3.325×10^{-3}	7.54	$\Gamma = 2$	None	1.0
D2	1.728	1.913	3.189×10^{-3}	8.21	$\Gamma = 2$	0.0	0.85
D4	1.861	2.059	3.116×10^{-3}	9.65	$\Gamma = 2$	0.0	0.65
H3	2.427	2.693	2.420×10^{-3}	8.08	$\Gamma = 2$	0.714	0.43

Table 7.2: Models evolved in this study. All units here are code units. M_{ADM} is the ADM (gravitational mass), $M_{\rm b}$ is the baryonic mass, $\rho_{\rm b,max}$ is the maximum baryon density of the configuration, R_{iso} is the coordinate radius in isotropic coordinates, Rot $\tilde{A}$ is differential rotation parameter, and $r_{p/e}$ is the axis ratio of the model.

data, we found that the convergence of the elliptic solver was extremely sensitive to the position of the stellar surface relative to the subdomain boundary chosen to be collocated with the surface. For the non-spherical, rotating CST models, we attempted to fit the surface to the subdomain boundary via a standard `SpEC` coordinate mapping. However we were never able to obtain any sort of convergence for residuals in the `SpEC` elliptic solver for these rotating configurations. In particular, we noted that the CST initial data itself *without any modification* did not satisfy the constraint equations to better than 1 part in 10^4. The constraint equations were computed on both initial data, and evolution grids in `SpEC` , as well as in the `zelmani` code. Given this error floor, which we were not able to eliminate, we were never able to have a clean system to further test the `SpEC` elliptic solver. Subsequently, we developed a novel method of 'tweaking' the hydrodynamic variables which does not modify the matter sources in the Einstein constraint equations and imitated a collapse inducing pressure depletion. We detail this method in an Appendix, Sec. 7.C.

7.4.2 Models

We evolve 3 models chosen from Baiotti et al. [3]: a TOV model, and two uniformly rotating CST models. In addition, we have obtained preliminary results with the hypermassive, differentially rotating model which we denote H3. This model is chosen to have a similar mass to the A4 model from Giacomazzo et al. 2011 [16]. The parameters specifying the models are listed in Tab. 7.2.

7.4.3 Code parameters

We document the version of `SpEC` used to run our simulations in Tab. 7.4.3. The input files used for these evolutions are the same as found in the 'InputFiles/SingleStarCollapse' directory of the `SpEC` repository for the git revision specified, except for the adjustment of a handful of run parameters.

7.5 Results and discussion

In Figures 7.1-7.2 we plot the dynamics of our collapse as a function of our gauge choice. Figures 7.1 shows the evolution of the maximum baryon density, ρ_b during the collapse simulations. One will

Git revision:	`f745013d32a48cacc4ed8ba842735693e7b07010`
Date linked:	Sat Jun 1 18:39:03 PDT 2013
Executable:	EvolveGRHydro
Machine:	zwicky

Table 7.3: Code and resolution parameters

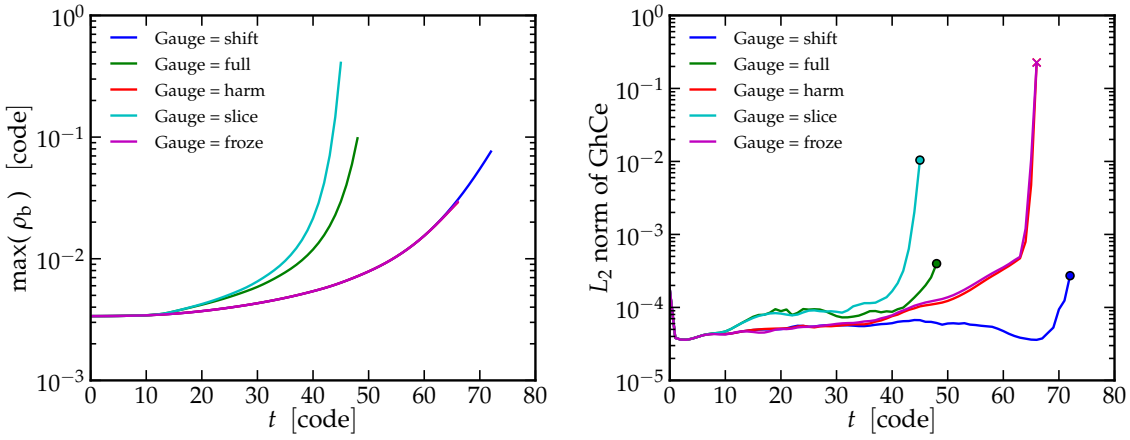

Figure 7.1: **Left panel:** Maximum baryon density for the TOV model D0. Compares runs using the five different gauge prescriptions listed in Tab. 7.1. Plot shows medium resolution (level 3). **Right panel:** L_2 norm of the normalized generalized harmonic constraints ('GhCe') for evolutions with with different gauges. Circles indicate runs which have terminated with successful apparent horizon identification, while $\times$s indicated runs which terminated due to the condition 'DataTooBig: $\tau > 100$' (for the hydrodynamic conservative energy variable τ defined in Eq. 7.2). Plot shows high resolution (level 4). Pressure depletion factor for these runs is $f_d = .85$

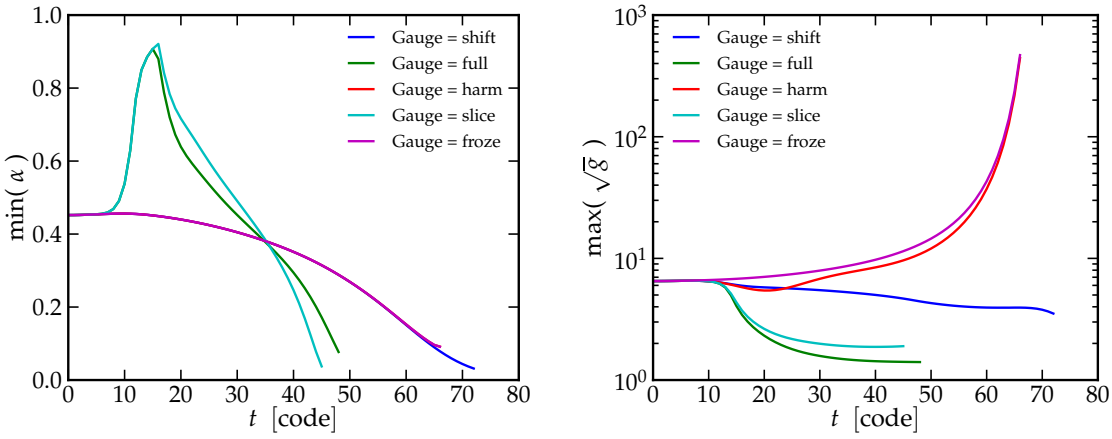

Figure 7.2: Minimum of α, the lapse (**left panel**), and maximum of the volume element, $\sqrt{g}$ (**right panel**), for the TOV model D0. Curves same as in Fig. 7.1.

first notice that the value of $max\rho_b$ as a function of coordinate time differs between gauges. This is due to the change in slicing rate of the simulation (the lapse, α) for different gauge conditions. This is directly illustrated in Fig.7.2. Since the minimum lapse occurs at the origin (center of the stars and center of collapse), the integral of the lapse with respect to coordinate time represents the time elapsed as experienced by a coordinate observer at rest at the origin. Qualitatively, one can see that if the coordinate time is parametrized by values of the central baryon density ρ_b during collapse, then the integral of the lapse from the start of the simulation to some value of ρ_b is the same for different gauges. Another way of saying this is that it takes the same amount of proper time for the central baryon density to reach a given value independent of gauge.

In Figure 7.2 we also plot the maximum value of the spatial volume element, $\sqrt{g}$. This quantity determines how much physical volume is represented per unit of coordinate volume. Thus the larger the value of $\sqrt{g}$ the lower the effective resolution is, since a larger amount of physical volume is represented by a unit of coordinate volume. To have a well resolved simulation, $\sqrt{g}$ must not increase drastically; otherwise, the coordinate evolution is de-resolving the simulation (effectively the grid is being fatally stretched out and distorted in physical space). Note that one can see in Fig. 7.2 this grid stretching is exactly what happens during collapse in pure harmonic and frozen gauges. However, the damped harmonic gauge is designed to dynamically damp $\log(\sqrt{g}/\alpha)$ to zero, and thus drive $\sqrt{g}/\alpha$ to order unity. This is what we see happening in Figure 7.2. It is interesting to note that the damped harmonic shift condition (blue curve), has a lapse evolution the same as a harmonic or frozen gauge, but a distinct evolution for $\sqrt{g}$. Apparently, the damping of the coordinate dynamics imposed by this condition is enough to prevent the divergence of the volume element as the black hole forms for this spherically symmetric test case.

Consequently, in practice we find that the damped harmonic gauge is robust for our black hole formation runs. Figure 7.1 (right panel) illustrates the constraint violation in our TOV simulations at high resolution. An apparent horizon is first found at coordinate time $t = 48$ for the evolution in damped harmonic gauge. At coordinate time $t = 50$ after 8 successful apparent horizon finds, the collapse evolution is terminated as we have collected enough information to properly excise the black hole and initialize our ringdown simulations. By this time, the constraint violation has increased only by a factor of 10. In contrast, by the time the constraints have increased by the same factor in the harmonic gauge runs, an apparent horizon has yet to be found. This finding that damped harmonic gauge is a successful way to capture black hole formation extends and confirms the results of Sorkin [30], who found a damped harmonic gauge was particularly robust in the formation of black holes from a complex scalar field in axisymmetric simulations.

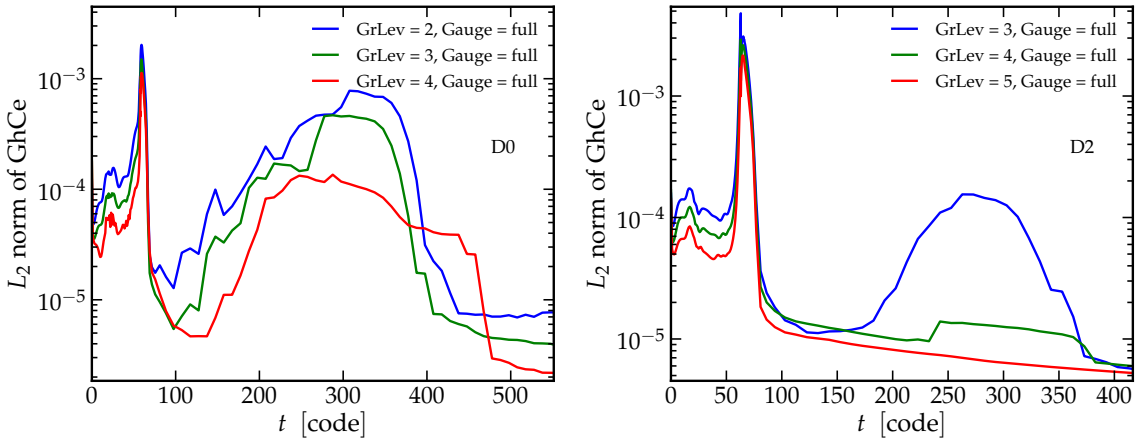

Figure 7.3: L_2 norm of the normalized generalized harmonic constraints ('GhCe') for the TOV model D0 (**left panel**) and the uniformly rotating model D2 (**right panel**). Note the strong 'peak' in the constraints corresponds to the time of black hole formation. GhCe is the sum of the squares of the components of the violations of the generalized harmonic equations Eqs. 7.13, 7.14, and 7.15.

7.A Plots documenting the robustness of the simulations

Here we show the robustness of the damped harmonic gauge by showing convergence in the constraints and waveforms of our simulations with resolution. Pressure depletion factor for these runs is $f_d = .9$

7.A.1 Convergence of simulations

In Figs. 7.3 and 7.4 we show plots which demonstrate the convergence of the simulations with resolution.

7.A.2 Gravitational waves from collapse

In Figs. 7.5 and 7.6 we show the gravitational waves from the collapse illustrated via the $(l, m) = (2, 0)$ mode of the Newman-Penrose scalar Ψ_4 at a finite radius.

7.B Definition of the 3-Velocity

There are often different definitions used for the fluid 3-velocity vector, v^i, in the literature. Here we clarify and compare these definitions. We use the 'transport velocity' (as denoted by Font in § 2.1.2 of [14]) definition for our 3-velocity, which can be written in terms of the fluid 4-velocity, **u**:

$$v^i = u^i/u^0. \tag{7.26}$$

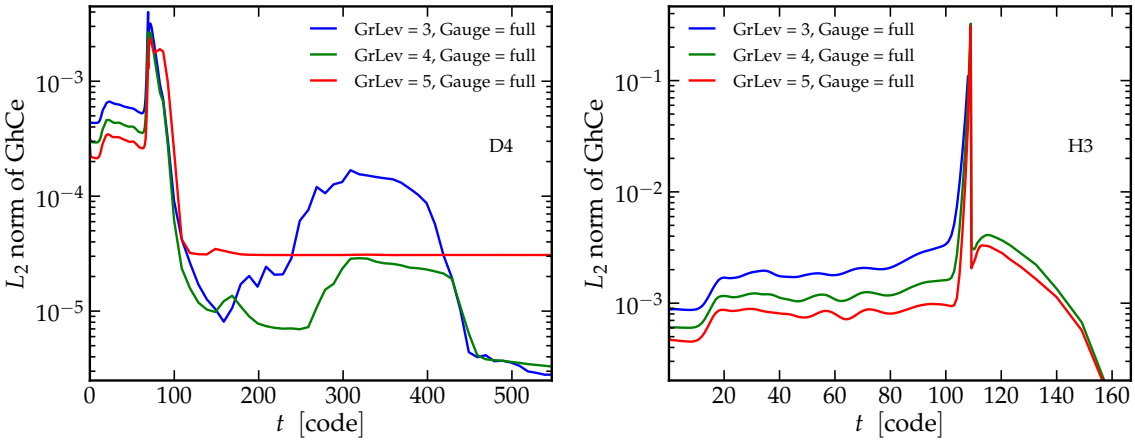

Figure 7.4: L_2 norm of the normalized generalized harmonic constraints ('GhCe') for the uniformly rotating model D4 (**left panel**) and the differentially rotating model H3 (**right panel**). The low resolution (Lev3) simulation for the differentially rotating model H3 was not well resolved enough to capture at least 8 apparent horizon finds before the code crashed, and thus could not be continued to ringdown. GhCe is the sum of the squares of the components of the violations of the generalized harmonic equations Eqs. 7.13, 7.14, and 7.15.

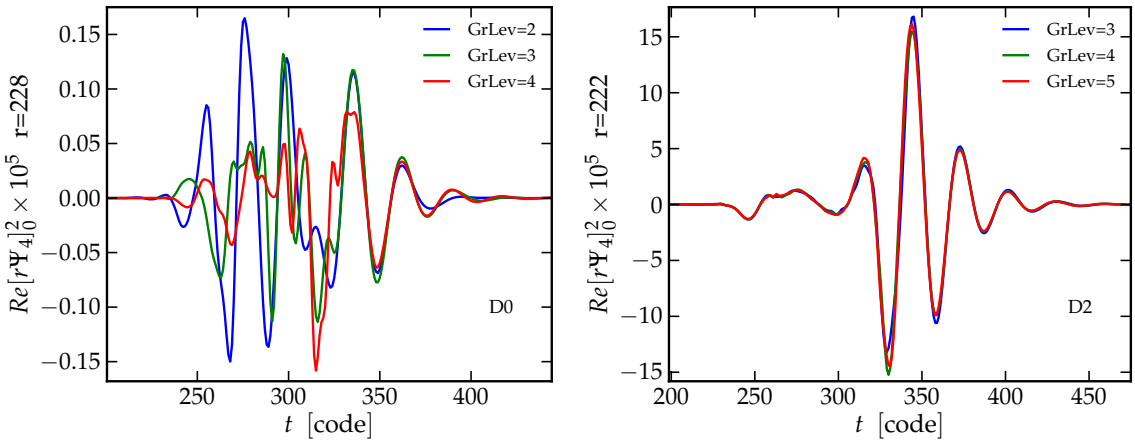

Figure 7.5: Gravitational waves for the TOV model D0 (**left panel**) and the uniformly rotating model D2 (**right panel**). Note for the spherically symmetric TOV model, the waves represent numerical noise from the relaxation of the neutron star on the grid. Initially unresolved, the effects of this noise become resolved as the simulation becomes that of black hole ringdown. All simulations here used the 'full' damped harmonic gauge.

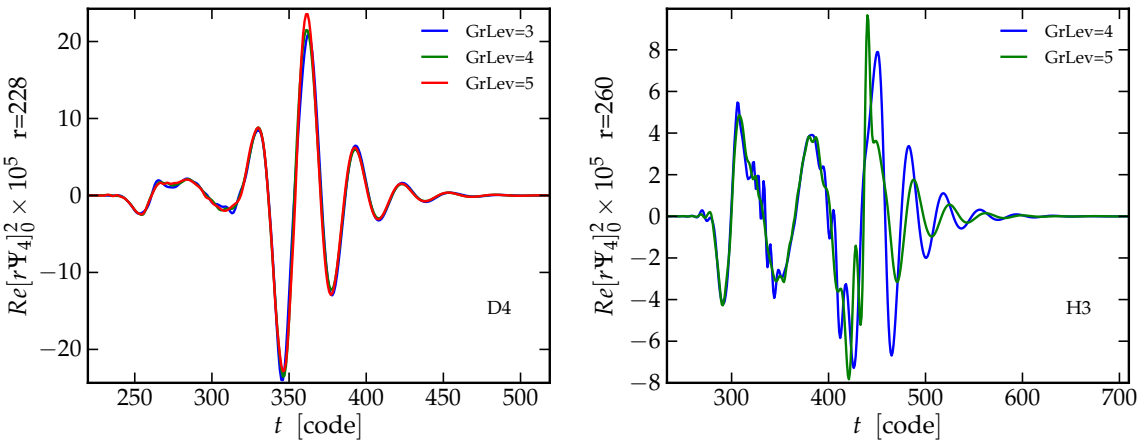

Figure 7.6: Gravitational waves for the uniformly rotating model D4 (**left panel**) and the differentially rotating model H3 (**right panel**). All simulations here used the 'full' damped harmonic gauge.

The 'transport velocity' can be interpreted as the Newtonian velocity relative to a fixed coordinate value; i.e., if a fluid element has transport velocity $v^i = 0$, then its coordinate location will remain fixed. However, this does *not* imply that the fluid element is 'at rest' in the slice (freely falling).

The 'Eulerian 3-velocity', V^i, is the velocity measured by normal-to-the-slice moving Eulerian observers [32]; that is, an Eulerian observer has $\mathbf{n}$, the unit timelike normal, as its 4-velocity. This yields the definition:

$$V_i = \frac{\mathbf{u} \cdot \partial_i}{-\mathbf{u} \cdot \mathbf{n}} \tag{7.27}$$

Note that an Eulerian observer is 'at rest' in the slice (is freely falling). By using the definition of the Lorentz factor, $w = \alpha u^0$ (Eq. 7.6), this equation becomes,

$$V_i = u_i / w. \tag{7.28}$$

Furthermore, raising V_i with the ADM 3-metric, one can obtain,

$$V^i = \frac{u^i}{w} + \frac{\beta^i}{\alpha}. \tag{7.29}$$

Finally, combining the definition of w, Eq. 7.26 and Eq. 7.29, we obtain an expression relating the 'Eulerian 3-velocity', V^i to the 'transport velocity', v^i:

$$\alpha V^i = v^i + \beta^i. \tag{7.30}$$

7.C Resolving the constraint equations

Here we present our novel method of adjusting the initial data configuration to produce a pressure depletion for inducing collapse without changing the constraints. The general procedure for this method is the following:

1. Generate your initial data configuration.
2. Calculate the Hamiltonian and Momentum sources as they appear in the Einstein Constraint equations.
3. Reduce the pressure terms contributing to the Hamiltonian and Momentum sources by some depletion factor, $f_d < 1$, where $f_d = 1$ represents no pressure reduction.
4. Adjust the remaining primitive variables (ρ,T,Y_e) such so that the Hamiltonian and Momentum sources obtain their original values.
5. Your new, pressure depleted configuration consists of the original fluid velocity, these adjusted primitive variables, plus the pressure and enthalpy calculated from your equation of state given the adjusted primitive variables.

Since we have adjusted the fluid configuration by hand (while fixing the metric variables) so that the Hamiltonian and Momentum sources remain unchanged, the constraint violation of the initial configuration will not change. Thus, if we started with constraint preserving initial data, our new pressure depleted data will also be constraint preserving.

In practice, for this work our initial data is cold ($T = 0$) and of fixed composition, Y_e. Thus, the process of adjusting the primitive variables in Step 4 amounts to a one dimensional root solve for a new adjusted density, ρ', which we then use to calculate a new Lorentz factor and set of conservative variables at each numerical grid-point to initialize our evolution. We derive the equation for this root solve in the following way. The Hamiltonian and Momentum constraints are respectively:

$$R + K^2 - K_{ij}K^{ij} = 16\pi GE, \tag{7.31}$$

$$\nabla_j \left(K^{ij} - g^{ij}K\right) = 8\pi G j^i. \tag{7.32}$$

We can then write the Hamiltonian source, E and the momentum source, j_i, in terms of primitive variables as:

$$E = \rho h w^2 - P, \tag{7.33}$$

$$j_i = \rho h w u_i. \tag{7.34}$$

Now is a good time to note that the momentum source, j_i differs from the evolved conservative momentum density, S_i (defined in Eq. 7.3), by a factor of $\sqrt{g}$: $j_i = S_i/\sqrt{g}$. We then solve Eq. 7.33 for the Lorentz factor and square Eq. 7.34 using $|u_i|^2 = w^2 - 1$,

$$w^2 = \frac{E+P}{\rho h}, \tag{7.35}$$

$$j^2 = |j_i|^2 = \rho^2 h^2 w^2 (w^2 - 1), \tag{7.36}$$

Eliminating w from the latter Eq., we obtain,

$$j^2 = (E+P)\left(E + P - \rho h\right), \tag{7.37}$$

which has derivative with respect to rho,

$$\frac{dj^2}{d\rho} = \frac{dP}{d\rho}(E + P - \rho h) + (E+P)\left(\frac{dP}{d\rho} - h\rho - \frac{dh}{d\rho}\right). \tag{7.38}$$

In these equations $P, h, dP/d\rho$, and $dh/d\rho$ are calculated via the equation of state given ρ.

Then, to achieve Step 3, we replace all the numerical values of $P, h-1, dP/d\rho$, and $dh/d\rho$ in 7.37 and 7.38 by their values multiplied by the depletion factor, f_d. Now, we have an equation (Eq. 7.37) where we can solve for a new baryon density, ρ', pointwise using a 'rtsafe'[22] style root solver (with the help of Eq. 7.38). We bracket the new ρ' in the root solver with $[0.1\rho, 10\rho]$ (except when $\rho = 0$ where we set $\rho' = 0$) which works well for moderate depletion factors. Completing the root solve and obtaining ρ' lets us calculate updated fluid variables where the configuration is adjusted in a way which is constraint preserving (as long as our original initial data was constraint preserving) and has a pressure depletion on the order of f_d.

Bibliography

[1] B. van Leer A. Harten, P. D. Lax. On upstream differencing and godunov-type schemes for hyperbolic conservation laws. *SIAM Rev.*, 25:35, 1983.

[2] B. Baiotti, I. Hawke, P. J. Montero, F. Löffler, L. Rezzolla, N. Stergioulas, J. A. Font, and E. Seidel. Three-dimensional relativistic simulations of rotating neutron star collapse to a Kerr black hole. *Phys. Rev. D*, 71:024035, 2005.

[3] L. Baiotti, I. Hawke, and L. Rezzolla. On the gravitational radiation from the collapse of neutron stars to rotating black holes. *Class. Quantum Grav.*, 24:187, June 2007.

[4] L. Baiotti, I. Hawke, L. Rezzolla, and E. Schnetter. Gravitational-Wave Emission from Rotating Gravitational Collapse in Three Dimensions. *Phys. Rev. Lett.*, 94:131101, April 2005.

[5] L. Baiotti, R. D. Pietri, G. M. Manca, and L. Rezzolla. Accurate simulations of the dynamical bar-mode instability in full general relativity. *Phys. Rev. D*, 75:044023, February 2007.

[6] T. W. Baumgarte and S. L. Shapiro. *Numerical Relativity: Solving Einstein's Equations on the Computer*. Cambridge University Press, Cambridge, UK, 2010.

[7] J. M. Centrella, K. C. B. New, L. L. Lowe, and J. D. Brown. Dynamical Rotational Instability at Low T/W. *Astrophys. J. Letters*, 550:L193, April 2001.

[8] M. W. Choptuik and F. Pretorius. Ultrarelativistic Particle Collisions. *Physical Review Letters*, 104(11):111101, March 2010.

[9] G. Corvino, L. Rezzolla, S. Bernuzzi, R. De Pietri, and B. Giacomazzo. On the shear instability in relativistic neutron stars. *Class. Quantum Grav.*, 27(11):114104, June 2010.

[10] M. D. Duez, F. Foucart, L. E. Kidder, H. P. Pfeiffer, M. A. Scheel, and S. A. Teukolsky. Evolving black hole-neutron star binaries in general relativity using pseudospectral and finite difference methods. *Phys. Rev. D*, 78:104015, November 2008.

[11] M. D. Duez, Y. T. Liu, S. L. Shapiro, and B. C. Stephens. General relativistic hydrodynamics with viscosity: Contraction, catastrophic collapse, and disk formation in hypermassive neutron stars. *Phys. Rev. D*, 69:104030, May 2004.

[12] M. D. Duez, P. Marronetti, S. L. Shapiro, and T. W. Baumgarte. Hydrodynamic simulations in 3+1 general relativity. *Phys. Rev. D*, 67:024004, January 2003.

[13] Matthew D. Duez, Stuart L. Shapiro, and Hwei-Jang Yo. Relativistic hydrodynamic evolutions with black hole excision. *Phys. Rev. D*, 69:104016, May 2004.

[14] J. A. Font. Numerical Hydrodynamics and Magnetohydrodynamics in General Relativity. *Liv. Rev. Rel.*, 11:7, September 2008.

[15] D. Garfinkle. Harmonic coordinate method for simulating generic singularities. *Phys. Rev. D*, 65(4):044029, February 2002.

[16] B. Giacomazzo, L. Rezzolla, and N. Stergioulas. Collapse of differentially rotating neutron stars and cosmic censorship. *Phys. Rev. D*, 84:024022, Jul 2011.

[17] L. Lindblom, K. D. Matthews, O. Rinne, and M. A. Scheel. Gauge drivers for the generalized harmonic Einstein equations. *Phys. Rev. D*, 77(8):084001, April 2008.

[18] L. Lindblom, M. A. Scheel, L. E. Kidder, R. Owen, and O. Rinne. A new generalized harmonic evolution system. *Class. Quantum Grav.*, 23:447, August 2006.

[19] L. Lindblom and B. Szilágyi. Improved gauge driver for the generalized harmonic Einstein system. *Phys. Rev. D*, 80(8):084019, October 2009.

[20] G. M. Manca, L. Baiotti, R. DePietri, and L. Rezzolla. Dynamical non-axisymmetric instabilities in rotating relativistic stars. *Class. Quantum Grav.*, 24:171, June 2007.

[21] T. Matsumisha and P.S. Marcus. A spectral method for polar coordinates. *J. Comput. Phys.*, 120(2):365–374, 1995.

[22] William H. Press, Saul A. Teukolsky, William T. Vetterling, and Brian P. Flannery. *Numerical Recipes, 3rd. edition*. Cambridge University Press, Cambridge, U. K., 2007.

[23] F. Pretorius. Evolution of Binary Black-Hole Spacetimes. *Phys. Rev. Lett.*, 95:121101, 2005. gr-qc/0507014.

[24] M. Saijo, T. W. Baumgarte, and S. L. Shapiro. One-armed Spiral Instability in Differentially Rotating Stars. *Astrophys. J.*, 595:352, September 2003.

[25] M. Saijo and I. Hawke. Collapse of differentially rotating supermassive stars: Post black hole formation. *Phys. Rev. D*, 80(6):064001, September 2009.

[26] M. Shibata. Collapse of Rotating Supramassive Neutron Stars to Black Holes: Fully General Relativistic Simulations. *Astrophys. J.*, 595:992–999, October 2003.

[27] M. Shibata, T. W. Baumgarte, and S. L. Shapiro. Stability and collapse of rapidly rotating, supramassive neutron stars: 3D simulations in general relativity. *Phys. Rev. D*, 61(4):044012, February 2000.

[28] M. Shibata and S. L. Shapiro. Collapse of a Rotating Supermassive Star to a Supermassive Black Hole: Fully Relativistic Simulations. *Astrophys. J. Letters*, 572:L39, June 2002.

[29] Masaru Shibata, Keisuke Taniguchi, and Koji Uryu. Merger of binary neutron stars of unequal mass in full general relativity. *Phys. Rev. D*, 68:084020, 2003.

[30] E. Sorkin. Axisymmetric generalized harmonic evolution code. *Phys. Rev. D*, 81(8):084062, April 2010.

[31] B. Szilágyi, L. Lindblom, and M. A. Scheel. Simulations of binary black hole mergers using spectral methods. *Phys. Rev. D*, 80(12):124010, December 2009.

[32] J. W. York, Jr. The initial value problem and dynamics. In N. Deruelle and T. Piran, editors, *Gravitational radiation*, pages 175–201. North-Holland Publishing Company, 1983.

[33] B. Zink, N. Stergioulas, I. Hawke, C. D. Ott, E. Schnetter, and E. Müller. Nonaxisymmetric instability and fragmentation of general relativistic quasitoroidal stars. *Phys. Rev. D*, 76(2):024019, July 2007.

Chapter 8

The Influence of Thermal Pressure on Hypermassive Neutron Star Merger Remnants

The merger of two neutron stars leaves behind a rapidly spinning hypermassive object whose survival is believed to depend on the maximum mass supported by the nuclear equation of state, angular momentum redistribution by (magneto-)rotational instabilities, and spindown by gravitational waves. The high temperatures ($\sim 5 - 40\,\mathrm{MeV}$) prevailing in the merger remnant may provide thermal pressure support that could increase its maximum mass and, thus, its life on a neutrino-cooling timescale. We investigate the role of thermal pressure support in hypermassive merger remnants by computing sequences of spherically-symmetric and axisymmetric uniformly and differentially rotating equilibrium solutions to the general-relativistic stellar structure equations. Using a set of finite-temperature nuclear equations of state, we find that hot maximum-mass critically spinning configurations generally do not support larger baryonic masses than their cold counterparts. However, subcritically spinning configurations with mean density of less than a few times nuclear saturation density yield a significantly thermally enhanced mass. Even without decreasing the maximum mass, cooling and other forms of energy loss can drive the remnant to an unstable state. We infer secular instability by identifying approximate energy turning points in equilibrium sequences of constant baryonic mass parametrized by maximum density. Energy loss carries the remnant along the direction of decreasing gravitational mass and higher density until instability triggers collapse. Since configurations with more thermal pressure support are less compact and thus begin their evolution at a lower maximum density, they remain stable for longer periods after merger.

Jeffrey D. Kaplan, Christian D. Ott, Evan P. O'Connor, Kenta Kiuchi, Luke Roberts, and Matthew Duez. Submitted for publication to The Astrophysical Journal, June 2013, arXiv:1306.4034

8.1 Introduction

Coalescing double neutron stars (NSs) are prime candidate progenitors of short-hard gamma-ray bursts (GRBs, e.g., [42] and references therein). The strong gravitational wave emission driving the coalescence makes NSNS systems the primary targets of the network of second-generation gravitational-wave interferometers currently under construction (Advanced LIGO [[26]], Advanced Virgo [[1]], and KAGRA [[59]]).

Until the last moments of inspiral, the constituent NSs may essentially be treated as cold neutron stars. Tidal heating is mild and the NS crust may not fail until the NSs touch ([48], but see [68] and [71]). Merger results in the formation of a shocked, extremely rapidly differentially spinning central object, commonly referred to as a hypermassive NS (HMNS), since it comprises the vast majority of the baryonic mass of the two premerger NSs and is thus expected to be more massive than the maximum mass supported by the nuclear equation of state (EOS) in the spherical and uniformly rotating limits limit (see, e.g., [17] for a review of NSNS mergers). The subsequent evolution of the HMNS has important ramifications for gravitational wave emission and the possible transition to a short-hard GRB. If the HMNS survives for an extended period, nonaxisymmetric rotational instability may enhance the high-frequency gravitational-wave emission, possibly allowing gravitational-wave observers to constrain the nuclear EOS (e.g., [7]). On the other hand, the neutrino-driven wind blown off a surviving HMNS, producing mass loss at a rate of order $10^{-4}\,M_\odot\,\mathrm{s}^{-1}$, will lead to strong baryon loading in polar regions [16], making the formation of the relativistic outflows needed for a GRB more difficult, even if a black hole with an accretion disk forms eventually. If the HMNS collapses to a black hole within milliseconds of merger, baryon loading will not hamper a GRB, but strong gravitational-wave and neutrino emission would be shut off rapidly.

The long-term survival of the HMNS depends sensitively on the maximum mass of a nonrotating cold neutron star supported by the nuclear EOS, which most certainly is above $\sim 2\,M_\odot$ [3, 15] and very likely below $\sim 3.2\,M_\odot$ [38]. At its formation, the HMNS is rapidly and strongly differentially rotating. Extreme differential rotation alone may increase the maximum HMNS mass by more than 100% [e.g., 6]. Angular momentum redistribution by (magneto-)rotational instabilities and spindown by gravitational wave emission are expected to remove this additional support. This will ultimately lead to black hole formation if the HMNS mass is above the maximum mass that can be supported by the nuclear EOS and uniform rotation ($\lesssim$20% greater than the maximum in the nonrotating limit; [6]).

Recently, [53], [47], [8], and, in earlier work, [4], have argued that there may be a significant enhancement of the HMNS maximum mass by thermal pressure support due to the moderately high temperatures of $\sim 5-40\,\mathrm{MeV}$ [44, 53] prevailing in the shock-heated HMNS. If true, the HMNS may survive on the neutrino cooling timescale provided that the combined premerger mass of the NSs is sufficiently close to the thermally-enhanced maximum HMNS mass. These authors estimate the neutrino cooling timescale to be comparable to or longer than the timescale for angular momentum redistribution and spindown by gravitational waves.

The focus of this paper is on the role of thermal pressure support in hypermassive NS merger remnants. Postmerger HMNS configurations that survive for multiple dynamical times quickly assume dynamical equilibrium and, after the extremely dynamic merger phase, show only mild deviation from axisymmetry (e.g., [53, 58]). Hence, instead of performing computationally expensive full merger simulations, we investigate the role of thermal effects by approximating HMNS configurations as sequences of rotational equilibrium solutions, which we compute with the relativistic self-consistent field method [11, 33, 34]. We consider the spherical limit (Tolman-Oppenheimer-Volkoff [TOV] solutions), uniform, and differential rotation. We employ multiple finite-temperature microphysical nuclear EOS and, since the equilibrium solver requires a barotropic equation of state, a range of temperature and composition parametrizations that are motivated by the merger simulations of [53]. An overall similar approach, though only considering isothermal and isentropic configurations, has been used in the past to study thermal effects on uniformly and differentially rotating proto-neutron stars [24, 25].

The key quantity relevant in the secular evolution of HMNSs is the baryonic mass (M_b; also called "rest mass") that can be supported by a given combination of EOS, thermal/compositional structure, and rotational setup. The gravitational mass (M_g) is not conserved and is reduced by cooling and angular momentum loss. *Our results show that the maximum baryonic mass of TOV, uniformly rotating, and differentially rotating configurations is essentially unaffected by thermal pressure support.* Thermal pressure support is negligible at supranuclear densities and becomes significant only at densities below nuclear saturation density. Since maximum-mass configurations always have maximum and mean densities above nuclear, thermal pressure support is minimal. The thermal contribution to the stress-energy tensor (which sources curvature) may, depending on the EOS, even lead to a net decrease of the $M_\mathrm{b}^\mathrm{max}$ with increasing temperature.

We find thermal enhancement of M_b for configurations with mean densities less than a few times nuclear saturation density that are nonrotating or rotating subcritically (i.e., below the mass-shedding limit). A hot configuration in this regime will support the same baryonic mass at a lower mean (and maximum) density. However, hot rotating configurations are spatially more extended than their cold counterparts, and thus reach mass shedding at lower angular velocities. This counteracts the thermal enhancement and results in $M_\mathrm{b}^\mathrm{max}$ that are within a few percent of cold

configurations.

The secular evolution of a HMNS towards collapse is driven by energy losses to gravitational waves and neutrinos, and, potentially, by loss of angular momentum transported to the surface by processes such as the MRI. It proceeds along trajectories of constant (or nearly constant) baryonic mass and in the direction of decreasing total energy (i.e., gravitational mass $M_{\rm g}$) and increasing maximum baryon density $\rho_{\rm b,max}$ (i.e., more compact configurations). We conjecture, based on established results of the theory of rotating relativistic stars ([22]), that instability to collapse occurs when the configuration reaches an unstable part of the parameter space and not necessarily because the maximum supportable baryonic mass $M_{\rm b}^{\rm max}$ drops below $M_{\rm b}$. We formalize this via an approximate variant of the turning-point theorem (e.g., [22, 60]): The turning-point theorem states that for uniformly rotating neutron stars, a local extremum in $M_{\rm g}$ at fixed angular momentum, entropy, and baryonic mass constitutes a point at which secular instability to collapse must set in. We argue that the turning point theorem carries over to differentially rotating hot HMNSs. The precise turning points become approximate and are distributed over a narrow range of $\rho_{\rm b,max}$ and $M_{\rm g}$ for all degrees of differential rotation and temperature prescriptions that we consider here. The regime of instability is thus largely independent of HMNS temperature. However, a hotter configuration will be less compact initially and, hence, will begin its secular evolution to its turning point at a lower $\rho_{\rm b,max}$ than a colder one. It will thus have to evolve further until it reaches its turning point and, at a fixed rate of energy loss, will survive for longer.

This paper is structured as follows. In §8.2, we introduce the set of EOS we employ and discuss the relative importance of thermal pressure as a function of density. We also introduce the temperature and composition parametrizations and the methods used for constructing equilibrium models without and with rotation. In §8.3, we lay out our results for nonrotating NSs and then discuss uniformly and differentially rotating configurations in §8.4.1 and §8.4.2, respectively. We consider evolutionary sequences of HMNSs at constant baryonic mass in the context of an approximate turning point theorem and compare with results from recent merger simulations in §8.5. Finally, in §8.6, we summarize our results and conclude.

8.2 Methods and Equations of State

8.2.1 Equations of State

We use a set of 8 EOS in this study. All EOS produce cold neutron stars in β-equilibrium that can have gravitational masses $M_{\rm g}$ above $2\,M_\odot$. These include two EOS from [39], the $K_0 = 220\,$MeV and $K_0 = 375\,$MeV variants (where K_0 is the nuclear compressibility modulus), denoted LS220 and LS375; the relativistic mean field (RMF) model EOS from [57], denoted HShen; two RMF models based on the NL3 and the FSUGold parameter set [55, 56] denoted GShen-NL3 and GShen-

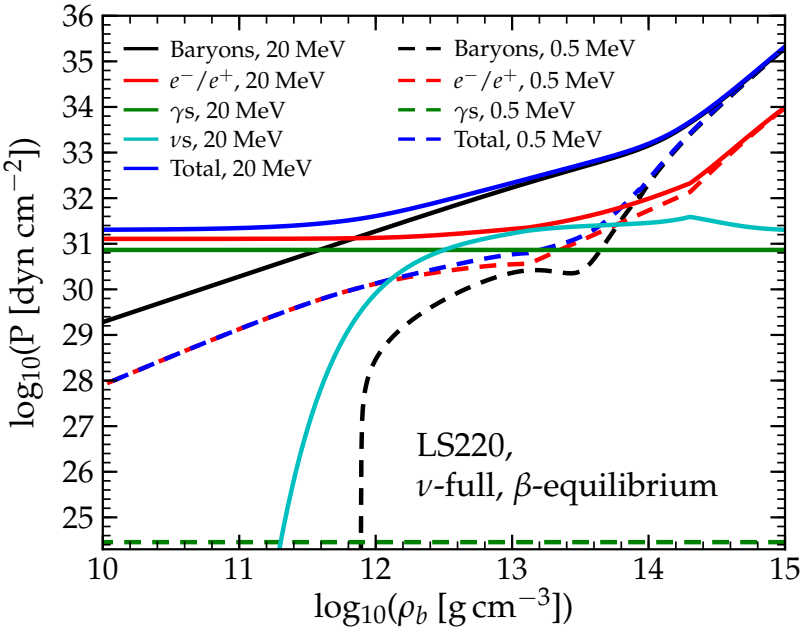

Figure 8.1: Individual pressure contributions of baryons, electrons/positrons, photons, and trapped neutrinos and the total pressure as a function of baryon density in the LS220 EOS for ν-full β-equilibrium as described in the text and $T = 0.5\,\mathrm{MeV}$ (dashed lines) and $T = 20\,\mathrm{MeV}$ (solid lines). The qualitative and quantitative behavior of the LS220 EOS with increasing temperature is representative for all EOS considered in this study. Note that the baryon pressure becomes negative at $\rho_\mathrm{b} \lesssim 10^{12}\,\mathrm{g\,cm^{-3}}$, and dips around $10^{13.5}\,\mathrm{g\,cm^{-3}}$ due to Coulomb effects at low temperatures [39].

FSU2.1; an unpublished[1] RMF model based on the DD2 interaction denoted HSDD2; and two recent RMF model EOS fit to astrophysical measurements of neutron star masses and radii [61], denoted SFHo and SFHx. All of these EOS are available in a common format for download from `http://www.stellarcollapse.org`.

The EOS of finite-temperature nuclear matter in nuclear statistical equilibrium (NSE) has contributions from a baryonic component (nucleons and nuclei), a relativistic electron/positron Fermi gas, a photon gas, and, if neutrinos are trapped, a neutrino gas. The Helmholtz free energies of these components add linearly, and the pressure is then the sum of the partial pressures and a function of baryon density ρ, temperature T and electron fraction Y_e,

$$P = P_{\rm baryon} + P_e + P_\gamma + P_\nu \ . \tag{8.1}$$

While $P_{\rm baryon}$ varies between the employed EOS, we add P_e and P_γ using the Timmes EOS [67] available from `http://cococubed.asu.edu`. In hot HMNSs, like in protoneutron stars, neutrinos are trapped and in equilibrium with matter. We include their pressure contribution to the EOS by treating them as a non-interacting relativistic Fermi gas with chemical potential μ_{ν_i}. For a single species of neutrinos and antineutrinos, the neutrino pressure in equilibrium is

$$P_{\nu_i} = \frac{4\pi(k_B T)^4}{3(hc)^3} \left[F_3\left(\eta_{\nu_i}\right) + F_3\left(-\eta_{\nu_i}\right)\right] \times \exp\left(-\frac{\rho_{\rm trap}}{\rho}\right) \ , \tag{8.2}$$

where $\eta_{\nu_i} = \mu_{\nu_i}/(k_B T)$ is the neutrino degeneracy parameter. For HMNS conditions, all neutrino species are present, but ν_μ and ν_τ have $\mu_{\nu_i} = 0$, since they appear only in particle–anti-particle pairs that have equal and opposite chemical potentials. For electron neutrinos we use $\mu_{\nu_e} = \mu_e + \mu_p - \mu_n$, for electron antineutrinos we use $\mu_{\bar{\nu}_e} = -\mu_{\nu_e}$. We include an attenuation factor $\exp(-\rho_{\rm trap}/\rho)$ to account for the fact that neutrinos decouple from matter at low densities. We set $\rho_{\rm trap} = 10^{12.5}\,{\rm g\,cm^{-3}}$, which is a fiducial trapping density for protoneutron stars (e.g., [40]). Taking the exact expression for the difference of the Fermi integrals from [9], we have the total neutrino pressure summed over all three species,

$$P_\nu = \frac{4\pi(k_B T)^4}{3(hc)^3} \left[\frac{21\pi^4}{60} + \frac{1}{2}\eta_{\nu_e}^2\left(\pi^2 + \frac{1}{2}\eta_{\nu_e}^2\right)\right] \times \exp\left(-\frac{\rho_{\rm trap}}{\rho}\right) \ . \tag{8.3}$$

We note that due to the neutrino statistical weight $g = 1$, for a single species of relativistic non-degenerate $\nu - \bar{\nu}$ pairs, the pressure is a factor of two lower than for $e^- - e^+$ pairs, since e^- and e^+ have statistical weight (spin degeneracy) 2.

Figure 8.1 illustrates the contributions of the partial pressures to the total pressure as a function of baryon density $\rho_{\rm b}$ for neutron-rich HMNS matter at two temperatures, 0.5 MeV (a representative "cold" temperature) and 20 MeV (a representative "hot" temperature for HMNSs). For the 0.5 MeV

[1] Available from `http://phys-merger.physik.unibas.ch/~hempel/eos.html`, based on [27, 28].

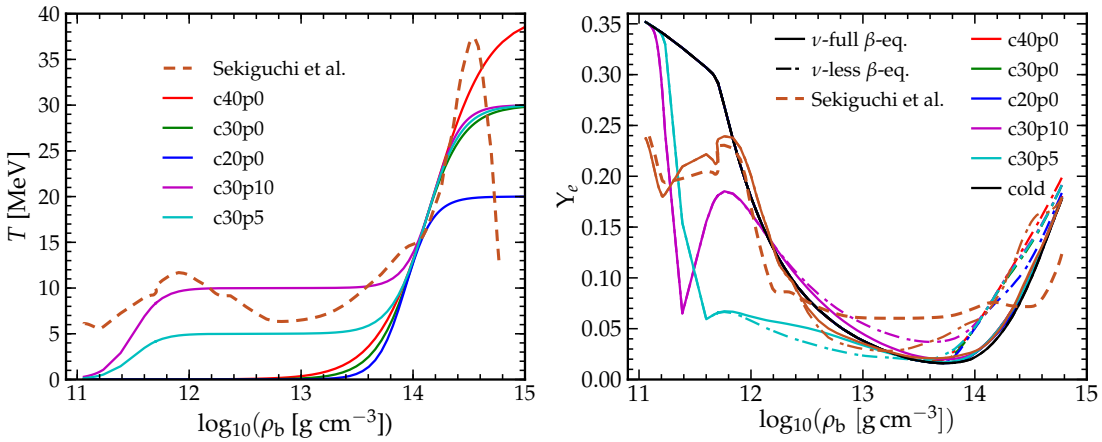

Figure 8.2: Temperature (T, left panel) and electron fraction (Y_e, right panel) as a function of baryon density for the T and Y_e prescriptions we explore in this work compared to 3D NSNS simulation data of [53] (dashed brown graphs). The profiles are created by taking T, Y_e, and ρ_b data along the $+x$-axis from their low-mass (two 1.35-$M_\odot$ progenitor NSs) simulation at 12.1 ms after merger. In the right panel, the dashed brown graph denotes the Y_e obtained from the simulation, while the solid and the dash-dotted graphs are Y_e obtained from the simulation temperature profile for ν-full and ν-less β-equilibrium, respectively.

EOS, we set the electron fraction Y_e by solving for ν-less β-equilibrium ($\mu_{\nu_e} = 0$). The resulting EOS describes ordinary cold neutron stars (at 0.5 MeV any thermal effects are negligible). For the 20 MeV case, we solve for Y_e by assuming ν-full β-equilibrium. We do so by making the assumption that any neutrinos produced during the merger are immediately trapped in the HMNS core, but stream away from regions below trapping density. The procedure is discussed in the next section 8.2.2 and detailed in Appendix 8.B.

Near and above nuclear saturation density, $\rho_{\rm nuc} \simeq 2.6 \times 10^{14}\,{\rm g\,cm^{-3}}$ for the LS220 EOS, the baryon pressure is due to the repulsive core of the nuclear force and dominates in both cold and hot regimes. The thermal enhancement above $\rho_{\rm nuc}$ remains small even at 20 MeV. In the cold case, relativistically degenerate electrons ($\Gamma = (d\ln P)(d\ln\rho)^{-1} = 4/3$) dominate below $\rho_{\rm nuc}$. At 20 MeV, relativistic non-degenerate electron/positron pairs and photons (for both, $P \propto T^4$, independent of $\rho_{\rm b}$; see, e.g., [69]) are the primary contributors at low densities, while the baryon pressure is significantly thermally enhanced below nuclear saturation density and dominates above $\sim 10^{12}\,{\rm g\,cm^{-3}}$. The neutrino pressure is comparable to the degenerate electron pressure between $\sim 10^{12.5} - 10^{14}\,{\rm g\,cm^{-3}}$, but still subdominant to the nuclear component. The contribution of pairs and photons gradually becomes more important at all densities as the temperature increases. We note that for $T = 0.5$ MeV, the neutrino chemical potentials are all zero and the pressure of trapped neutrinos is $3 \times (7/8) \times P_\gamma$, thermodynamically insignificant at $T = 0.5$ MeV.

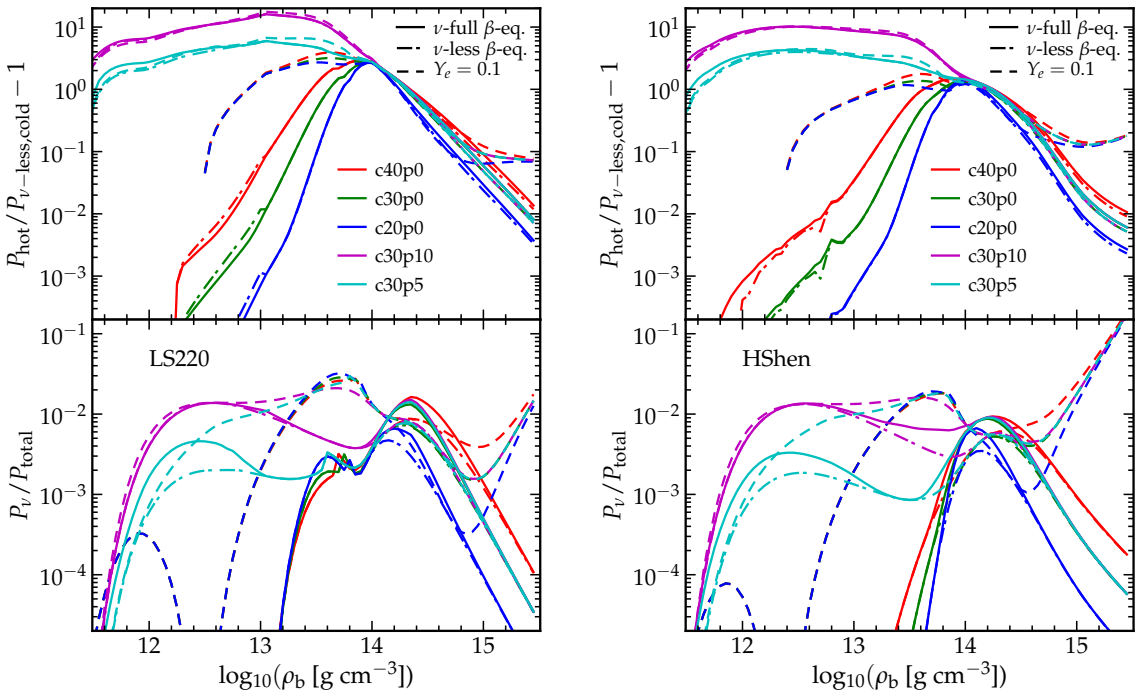

Figure 8.3: Effects of temperature and Y_e parametrizations on the pressure and relevance of the neutrino pressure component. **Top panels:** Fractional increase of the pressure over the cold ν-less β-equilibrium pressure for the LS220 EOS (left panel) and the HShen EOS (right panel). The different line styles correspond to $Y_e(\rho)$ obtained in ν-full β-equilibrium (solid), ν-less β-equilibrium (dash-dotted), and constant $Y_e = 0.1$ (dashed). **Bottom panels:** Relative contribution of the neutrinos to the total pressure (cf. Eq. 8.3) in the five temperature and three Y_e parametrizations and the LS220 EOS (left panel) and the HShen EOS (right panel).

8.2.2 Temperature and Composition Parametrizations

The hydrostatic and rotational equilibrium equations that we solve in this study assume a barotropic EOS ($P = P(\rho)$) and do not provide constraints on thermal structure and composition (Y_e is the only relevant compositional variable in NSE). We must make some assumptions to be able to proceed and obtain $P = P(\rho, T(\rho), Y_e(\rho))$ for our general finite-temperature microphysical EOS. Old NSs in isolation are nearly isothermal (e.g., [49]) and so are coalescing neutron stars until tidal heating becomes significant (e.g., [32, 35]). During merger, the NS matter is shock-heated to tens of MeV and results of the few merger simulations that have been carried out with temperature-dependent EOS (e.g., [8, 44, 51–53]) indicate that the HMNS is far from being isothermal or isentropic. It has a very hot dense core with $T \sim 20 - 40\,\mathrm{MeV}$ surrounded by a lower-density cooler envelope/torus of $5 - 20\,\mathrm{MeV}$, which may also be almost Keplerian and, hence, centrifugally supported. This result appears to be robust for equal-mass or near equal-mass NSNS systems (which may dominate the population; e.g., [36] and references therein). Mergers of non-equal mass systems in which the lower-mass NS is tidally wrapped around its more massive companion reach similar temperatures, but generally tend to have more mass at lower densities in the disk/torus [44].

There is no unique model/EOS independent mapping $T = T(\rho)$, thus we must explore a variety of possibilities. In Fig. 8.2, we contrast our set of temperature parametrizations with a $T(\rho)$ profile obtained from a $1.35 - 1.35\,M_\odot$ simulation using the HShen EOS by [53] at $\sim$12 ms after merger. We consider very hot cores at 20, 30, and 40 MeV with cold envelopes (parametrizations c20p0, c30p0, and c40p0) and two parametrizations with very hot cores at 30 MeV and cool envelopes at 10 MeV and 5 MeV, c30p10 and c30p5, respectively. Since low-density regions have shorter neutrino cooling times, the c30p10 and c30p5 parametrization may represent early HMNSs, while the cold-envelope parametrizations c20p0, c30p0, and c40p0 may correspond to late-time HMNSs. Note that the c30p10 parametrization fits the temperature profile from the [53] simulation quite well. Details on the functional forms of our parametrizations can be found in Appendix 8.A. For the TOV case we also consider isothermal configurations as a limiting case.

The choice of $Y_e(\rho)$ is equally difficult. Before merger, the NSs are in ν-less β-equilibrium ($\mu_\nu = \mu_e + \mu_p - \mu_n = 0$). After merger, neutrinos are present. They are trapped in hot dense matter ($\mu_\nu \neq 0$) and are streaming away from low-density regions. The equilibrium Y_e will shift and mixing due to non-linear hydrodynamics in the HMNS phase will distort any initial $Y_e(\rho)$ profile.

We deem the following prescription for Y_e to be the physically most sensible: We assume that the NSNS merger occurs so rapidly that the electron fraction Y_e of the ν-less β-equilibrium in the NSs becomes the trapped postmerger lepton fraction $Y_{\mathrm{lep}} = Y_e + Y_{\nu_e} - Y_{\bar{\nu}_e}$ above ρ_{trap}. Using the β-equilibrium condition with nonzero μ_ν, we solve for Y_e. At densities below ρ_{trap} we transition to Y_e given by ν-less β-equilibrium. Details of this procedure are given in Appendix 8.B. We refer to this parametrization of Y_e as ν-full β-equilibrium. In addition and for comparison, we consider

choices of constant $Y_e = 0.1$ and Y_e set according to ν-less β-equilibrium. The right panel of Fig. 8.2 depicts $Y_e(\rho)$ as obtained from the simulation of [53] contrasted with Y_e profiles computed under the assumption of ν-less and ν-full β-equilibrium for various temperature parametrizations and for the $T(\rho)$ as given by the simulation. None of the prescriptions fit the simulation-Y_e particularly well, which indicates that mixing neutrino transport effects are important (but cannot be included here). The Y_e obtained using the temperature data from the simulation naturally fits best, in particular at low densities where neutrinos have decoupled from the matter and ν-less β-equilibrium holds.

In the top panels of Fig. 8.3, we show the fractional pressure increase due to thermal effects as a function of baryon density for our set of temperature parametrizations for the LS220 EOS (left panel) and the HShen EOS (right panel) as two representative example EOS. We also distinguish between the choices of Y_e parametrization. For the parametrizations with cold "mantles" (cXp0), thermal effects are most important at densities near $\sim\rho_{\rm nuc}$ and quickly lose significance at lower and higher densities in both EOS. The thermal pressure enhancement is at most a factor of three (for the HShen) to five (for the LS220 EOS) for these parametrizations. The situation is different for the cases with hot plateaus, c30p10 and c30p5. For these, the thermal pressure is up to 20 times larger at low densities than predicted by the cold EOS. The Y_e parametrizations corresponding to ν-full and ν-less β-equilibrium yield qualitatively and quantitatively very similar results for both EOS.

At low densities, the ν-full and ν-less β-equilibrium cases both lead to $Y_e > 0.1$ (cf. Fig. 8.2). As a consequence, the pressure in the unrealistic $Y_e = const. = 0.1$, cXp0 parametrizations is lower than in the cold ν-less case at $\rho_b \lesssim 10^{12.2}\,{\rm g\,cm^{-3}}$. Due to the logarithmic scale of Fig. 8.3, the graphs of cXp0 with $Y_e = 0.1$ start only there and the predicted pressure enhancement is higher than in the β-equilibrium cases, which lead to lower Y_e above $\sim 10^{12.2}\,{\rm g\,cm^{-3}}$ and below $\sim\rho_{\rm nuc}$. In the cases with hot plateau (c30p10 and c30p5), thermal effects dominate over differences in Y_e at low densities. Finally, at $\rho > \rho_{\rm nuc}$, where temperature effects are smaller, differences in Y_e become important. Since the nuclear component dominates there, lower Y_e corresponds to higher pressure (e.g., [37]) and both β-equilibrium cases yield $Y_e > 0.1$.

The lower panels of Fig. 8.3 depict the relative contribution of the neutrinos to the total (hot) pressure in the HMNS temperature and Y_e parametrizations considered in this study. While there are clear temperature (see Eq. 8.3) and Y_e (through μ_{ν_e}) dependences, neutrino pressure plays only a minor role, making up at most $\sim$2% of the total pressure of the LS220 EOS. This is true also for the HShen EOS with the exception of the unrealistic $Y_e = 0.1$ case in which the neutrino pressure contribution grows to $\gtrsim$10% of the total pressure at supranuclear densities.

Finally, we note that the temperature and Y_e prescriptions discussed here lead to regions that may be unstable to convection if not stabilized by a positive specific angular momentum gradient (e.g., [64]). The spherically and axially symmetric equilibrium models that we construct in this study cannot account for convection and we leave an analysis of convective instability to future work.

8.2.3 Spherically Symmetric Equilibrium Models

We solve the Tolman-Oppenheimer-Volkoff (TOV) equation (e.g., [54]),

$$\frac{dP}{dr} = -\frac{G}{r^2}\left[\rho_{\rm b}\left(1+\frac{\epsilon}{c^2}+\frac{P}{\rho_{\rm b}c^2}\right)\right]\left[M_{\rm g}(r)+4\pi r^3\frac{P}{c^2}\right]\left[1-\frac{2GM_{\rm g}(r)}{rc^2}\right]^{-1}, \tag{8.4}$$

where r is the areal (circumferential) radius, $\rho_{\rm b}$ is the baryon density, ϵ is the specific internal energy, and $M_g(r)$ is the gravitational mass enclosed by radius r, determined via

$$\frac{dM_{\rm g}}{dr} = 4\pi r^2\rho_{\rm b}\left[1+\frac{\epsilon}{c^2}\right] \ . \tag{8.5}$$

The baryonic mass is larger and given by

$$\frac{dM_{\rm b}}{dr} = 4\pi r^2\rho_{\rm b}\left(1-\frac{2GM_{\rm g}(r)}{rc^2}\right)^{-1/2} \ . \tag{8.6}$$

We construct the TOV solutions using a standard fourth-order Runge-Kutta integrator on an equidistant grid with $\delta R = 10^2\,$cm zones. After each integration sub-step, the equation of state $P = P(\rho_{\rm b})$ is inverted to obtain $\rho_{\rm b}$. We use a variety of $P(\rho_{\rm b})$ parametrizations: (*i*) $T = const.$ (isothermal) with ν-full β-equilibrium above $\rho_{\rm trap}$ and ν-less β-equilibrium below, (*ii*) $T = const.$ with ν-less β-equilibrium, (*iii*) $T = const.$ with constant $Y_e = 0.1$, and (*iv*) the phenomenological cXpX temperature parametrizations with ν-full β-equilibrium above $\rho_{\rm trap}$ and ν-less equilibrium below. We compute TOV solutions for all EOS and define the surface of the neutron star as the areal radius at which the pressure drops below $\sim 2\times10^{22}\,$dyne cm^{-2}, which is typically one part in 10^{11} of the central pressure.

Besides the EOS, temperature, and Y_e prescription, the central baryon density $\rho_{\rm b,c}$ is the only other free parameter. Since we are interested in the maximum mass that can be supported, we compute sequences with varying $\rho_{\rm b,c}$ for each EOS, but limit ourselves to $\rho_{\rm nuc} < \rho_{\rm b,c} \leq \rho_{\rm max,EOS}$, where the latter is just the maximum density entry in the respective EOS table. HMNSs with central densities below $\rho_{\rm nuc}$ are not realistic (cf. [53]).

We make our TOV solver, all $P = P(\rho_{\rm b})$ tables, and the `Python` scripts used to create the results in this paper available on `http://www.stellarcollapse.org`.

8.2.4 Axisymmetric Equilibrium Models

We generate axisymmetric equilibrium models using the code originally presented in [11] (hereafter CST; see also [12, 13]), which is based on the relativistic self-consistent field method of Komatsu, Eriguchi & Hachisu (1989a). The axisymmetric equilibrium equations are solved iteratively on a grid in (s,μ), where s is a compactified radial coordinate and $\mu = \cos\theta$, where θ is the usual spherical

polar angle. Additionally, metric functions are solved using Green's functions integrals expanded in terms of N_l Legendre polynomials. Consequently, the total numerical resolution is specified via a tuple of (N_s, N_μ, N_l), which we set to (500, 300, 16). The resolution is chosen so that the resulting integral quantities of the equilibrium solution (e.g., its gravitational mass) are precise to about one part in 10^3.

An axisymmetric HMNS equilibrium configuration is constructed by the CST code based on choices of (i) a barotropic EOS, (ii) a rotation law, (iii) the rotation rate, and, (iv) the maximum mass-energy density $E_{\rm max} = [\rho_b(1+\epsilon/c^2)]_{\rm max}$ of the configuration.

In order to keep the size of the parameter space manageable, we restrict rotating configurations to the LS220 and HShen EOS and set up barotropic versions using the temperature and composition parametrizations described in §8.2.2. Since the EOS obtained with ν-full and ν-less β-equilibrium differ only very mildly (cf. Fig. 8.3), we construct rotating configurations under the simple assumption of ν-less β-equilibrium.

We employ the '$j-const.$' rotation law (see, e.g., CST), which is commonly used in the literature for HMNS models (e.g., [6]). The degree of differential rotation is parametrized by $\tilde{A}$ [2]. In the Newtonian limit, this rotation law becomes $\Omega = \Omega_c/(1+\tilde{A}^2\varpi^2/r_e^2)$, where ϖ is the cylindrical radius (a coordinate), r_e is the equatorial radius of the star (a constant for a given model), and Ω_c is the central angular velocity. For $\tilde{A}=0$, one recovers uniform rotation, while for large $\tilde{A}$, the specific angular momentum becomes constant (i.e., $\Omega \propto \varpi^{-2}$ in the Newtonian limit). We explore values of $\tilde{A}$ between 0 and 1. The latter value of $\tilde{A}$ corresponds to roughly a factor of two decrease of the angular velocity from the center to the HMNS surface, which is in the ball park of what is found in merger simulations (e.g., [58]). Once the rotation law is fixed, the rotation rate is determined by specifying the *axis ratio* $r_{\rm p/e}$, defined as the ratio of the HMNS radius along the pole $r_{\rm p}$ divided by the radius at the equator $r_{\rm e}$.

The final parameter to be chosen is the maximum energy density of the configuration. For simplicity and consistency with the choice of variables for the TOV solutions discussed in §8.2.3, we set $E_{\rm max}$ by choosing a maximum baryon density $\rho_{\rm b,max}$ and obtain $E(\rho_{\rm b,max})$ from the EOS.

For each choice of EOS, $\rho_{\rm b,max}$, and $\tilde{A}$, we compute a sequence of models with increasing rotation rate, stepping down from $r_{\rm p/e}=1$ (the nonrotating TOV case) until we reach mass shedding or until the code fails to converge to an equilibrium solution. In the case of uniform rotation ($\tilde{A}=0$) the sequence always ends at mass shedding, the resulting rotating neutron star has spheroidal shape, and the maximum and central density coincide ($\rho_{b,\rm max}=\rho_{\rm c}$). Differentially rotating sequences, on the other hand, can bifurcate into two branches: one with $\rho_{b,\rm max}=\rho_{\rm c}$ and spheroidal geometry and one with an off-center location of $\rho_{b,\rm max}$ and quasitoroidal shape. For differentially rotating models, the CST solver generally fails to converge to a solution at $r_{\rm p/e}$ before mass shedding and,

[2] Note that $\tilde{A}=1/\hat{A}$, where $\hat{A}$ is the same $\hat{A}$ as used in [6].

therefore, possibly before the maximum mass for a given configuration is reached. This limitation means that the maximum masses we state for differentially rotating models are to be interpreted as lower bounds on the true maximum masses. The code developed by [2] is far more robust than CST for such extreme configurations and these authors have argued that with increasing degree of differential rotation, arbitrarily large masses could be supported in extremely extended tori, but such configurations are unlikely to be astrophysically relevant.

8.3 Results: Spherically Symmetric Models

Our main interest is in how temperatures in the range encountered in HMNS of NSNS postmerger simulations change the maximum mass that can be supported. Since baryonic mass is a conserved quantity and can be related to the number of baryons present in the individual NSNS before merger (modulo a small amount of potential ejecta), we treat it as a the most important variable and define the maximum gravitational masses $M_{\rm g}^{\rm max}$ as the gravitational mass at which $M_{\rm b}^{\rm max}$ is maximal. We consider the isothermal TOV solution as a limiting case of maximal thermal support but note that such configurations with $T \gtrsim 5 - 8\,{\rm MeV}$ develop very large, non-degenerate envelopes at the low end of the central baryon densities $\rho_{\rm b,c}$ considered here. With increasing temperature, degeneracy is more and more lifted at those densities and the TOV model approaches an isothermal sphere whose pressure is dominated by relativistic non-degenerate pairs and whose mass and radius become infinite. We discard such solutions.

The results of our TOV calculations are summarized by Fig. 8.4 for all considered EOS. We provide numerical results in Tab. 8.1 for fiducial isothermal cold ($T = 0.5\,{\rm MeV}$) and parametrized temperature choices.

In the top panel of Fig. 8.4, we show the maximum gravitational mass (defined as $M_{\rm g}$ at $M_{\rm b}^{\rm max}$) as a function of isothermal temperature for our three Y_e prescriptions. The considered EOS show a great degree of variation in their sensitivity to Y_e prescriptions, but the overall trend is clear: increasing temperature generally leads to increasing $M_{\rm g}^{\rm max}$. The fractional increase over the cold value, however, is not large, as shown by the center panel. The HShen and GShen-FSU2.1 RMF TOV stars are the most sensitive to temperature variations[3], but even their maximum gravitational TOV mass increases only by $\sim 12 - 15\%$ at isothermal $T = 50\,{\rm MeV}$. The cXpX temperature parametrizations, shown as symbols in Fig. 8.4 located at their respective central temperatures, generally follow the trend of the isothermal sequences for each EOS, but their $M_{\rm g}^{\rm max}$ enhancement is systematically lower, since they are only centrally hot.

The lower panel of Fig. 8.4 depicts the change of the maximum baryonic TOV mass $M_{\rm b}^{\rm max}$ with increasing temperature. For most EOS, $M_{\rm b}^{\rm max}$ stays roughly constant at low temperatures, but

[3] See, e.g., [27] for a discussion of EOS physics and temperature dependence of various EOS models.

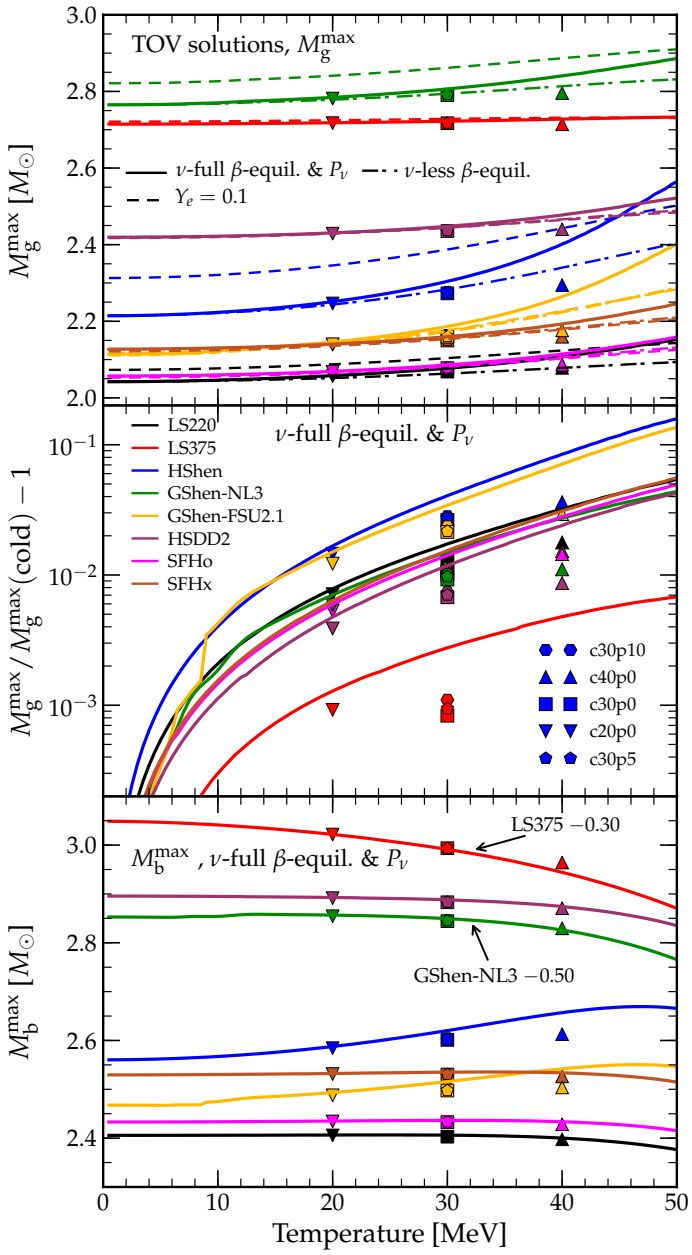

Figure 8.4: Effect of temperature T on the maximum masses of TOV solutions. **Top panel**: gravitational mass $M_{\rm g}^{\rm max}$ at the maximum baryonic mass for $T = const.$ configurations (lines) and parametrized cXpX profiles (symbols). The cXpX solutions are computed only for ν-full β-equilibrium. With increasing T, $M_{\rm g}^{\rm max}$ increases. This trend is independent of Y_e prescription, but the sensitivity to Y_e is highly EOS dependent. **Center panel**: Relative increase of $M_{\rm g}^{\rm max}$ with T for solutions in ν-full β-equilibrium. The increase is modest and below $\sim 10\%$ even in the $T = const.$ case. **Bottom panel:** Maximum baryonic mass $M_{\rm b}^{\rm max}$ that can be supported as a function of temperature. For most EOS, there is little variation in $M_{\rm b}^{\rm max}$ at low T, but the increasing thermal contribution to the TOV energy density (cf. Eq. 8.4) leads to a *decrease* of $M_{\rm b}^{\rm max}$ for *high*-T solutions. A linear vertical shift of -0.30 (-0.50) $M_\odot$ has been applied to the LS375 (GShen-NL3) curves to enhance the vertical dynamic range of the plot.

EOS	T(ρ)	$M_{\rm b}^{\rm max}$ ($M_\odot$)	$M_{\rm g}^{\rm max}$ ($M_\odot$)	R (km)	ρ_c ($10^{15}\,{\rm g\,cm^{-3}}$)
LS220, ν-less	0.5 MeV	2.406	2.042	10.63	1.863
LS220, ν-full	c20p0	2.434	2.068	10.69	1.873
	c30p0	2.433	2.078	10.89	1.840
	c30p10	2.433	2.079	11.86	1.840
	c30p5	2.433	2.078	11.23	1.840
	c40p0	2.428	2.087	11.07	1.808
LS375, ν-less	0.5 MeV	3.349	2.715	12.34	1.243
LS375, ν-full	c20p0	3.322	2.717	12.59	1.232
	c30p0	3.294	2.717	12.68	1.221
	c30p10	3.293	2.718	13.49	1.221
	c30p5	3.293	2.717	12.95	1.221
	c40p0	3.264	2.714	12.75	1.210
HShen, ν-less	0.5 MeV	2.560	2.214	12.59	1.357
HShen, ν-full	c20p0	2.584	2.246	13.17	1.321
	c30p0	2.601	2.273	13.48	1.276
	c30p10	2.604	2.277	15.08	1.276
	c30p5	2.603	2.275	14.01	1.276
	c40p0	2.613	2.295	13.69	1.243
GShen-NL3, ν-less	0.5 MeV	3.353	2.765	13.34	1.115
GShen-NL3, ν-full	c20p0	3.354	2.781	13.51	1.098
	c30p0	3.344	2.791	13.70	1.081
	c30p10	3.346	2.793	15.04	1.081
	c30p5	3.345	2.792	14.30	1.081
	c40p0	3.330	2.796	13.86	1.070
GShen-FSU2.1, ν-less	0.5 MeV	2.468	2.114	11.67	1.505
GShen-FSU2.1, ν-full	c20p0	2.488	2.140	12.15	1.474
	c30p0	2.497	2.159	12.40	1.428
	c30p10	2.502	2.164	14.30	1.420
	c30p5	2.497	2.160	12.44	1.428
	c40p0	2.504	2.176	12.56	1.398
HSDD2, ν-less	0.5 MeV	2.896	2.419	11.92	1.395
HSDD2, ν-full	c20p0	2.891	2.429	12.28	1.381
	c30p0	2.883	2.436	12.43	1.367
	c30p10	2.884	2.437	13.47	1.367
	c30p5	2.883	2.436	12.79	1.367
	c40p0	2.871	2.440	12.55	1.353
SFHo, ν-less	0.5 MeV	2.433	2.057	10.31	1.906
SFHo, ν-full	c20p0	2.434	2.068	10.67	1.884
	c30p0	2.433	2.078	10.86	1.862
	c30p10	2.434	2.079	11.81	1.862
	c30p5	2.433	2.078	11.21	1.851
	c40p0	2.428	2.087	11.03	1.829
SFHx, ν-less	0.5 MeV	2.529	2.127	10.79	1.722
SFHx, ν-full	c20p0	2.531	2.139	11.18	1.705
	c30p0	2.530	2.150	11.37	1.688
	c30p10	2.531	2.151	12.39	1.688
	c30p5	2.531	2.150	11.72	1.688
	c40p0	2.527	2.160	11.51	1.671

Table 8.1: "ν-less" indicates neutrino-less β-equilibrium, which we use only for the "cold" configurations. "ν-full" indicates neutrino-full β-equilibrium with neutrino pressure. $T(\rho)$ is the temperature parametrization, $M_{\rm b}^{\rm max}$ is the maximum baryonic mass, $M_{\rm g}^{\rm max}$ is the gravitational mass at the maximum baryonic mass, R is the radius of the $M_{\rm b}^{\rm max}$ configuration, and ρ_c is the central baryon density at which $M_{\rm b}^{\rm max}$ obtains.

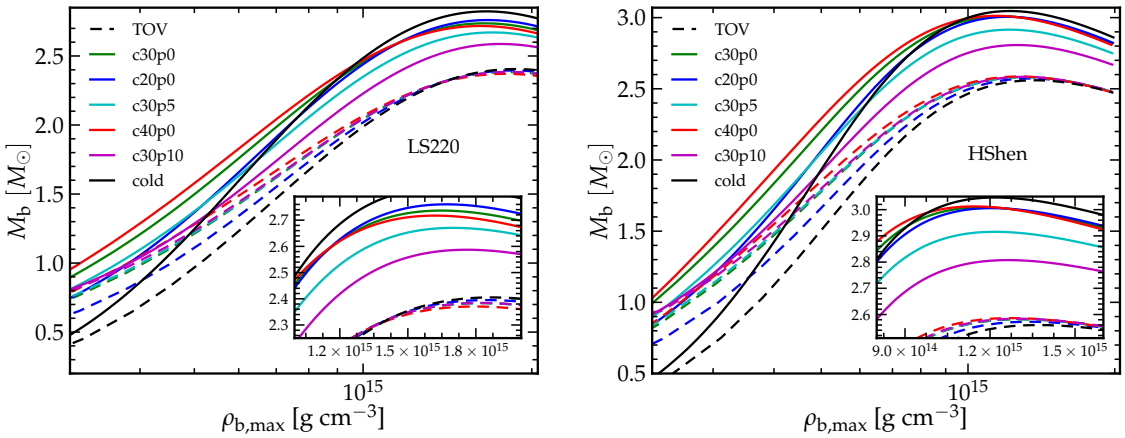

Figure 8.5: Baryonic mass M_b as a function of maximum baryon density $\rho_{b,max}$ of uniformly rotating ($\tilde{A} = 0$) equilibrium models at the mass-shedding limit for different temperature prescriptions (solid lines). We also plot the corresponding TOV sequences (dashed lines) and show results for the the LS220 EOS (**left panel**) and HShen EOS (**right panel**). There is a large thermal enhancement of M_b at low densities, but the sequences converge towards the cold supramassive limit as the maximum density increases and the configurations become more compact.

decreases at high temperatures. This shows that the increase in M_g^{max} in the TOV solutions is primarily due to thermal contributions to the total mass-energy density. Since it is the mass-energy density, and not just the baryonic mass, which sources curvature (the relativistic gravitational field), the thermal effects lead to a decrease in M_b^{max} with temperature even if M_g^{max} is still increasing. The HShen and GShen-FSU2.1 are the only two EOS that exhibit an increase of M_b^{max} at intermediate to high temperatures, but they too reverse this trend at isothermal $T \gtrsim 50\,\mathrm{MeV}$. The LS375 EOS, on the other hand, has monotonically decreasing M_b^{max} with T, which was seen before by [43]. The more realistic cXpX temperature parametrizations show a similar trend as their isothermal counterparts, but for the HShen and GShen-FSU2.1 EOS, the increase in M_b^{max} at intermediate T is smaller in these only centrally-hot parametrized models.

It is interesting to compare our findings with the results of [43], who studied black hole formation through protoneutron star collapse in failing core-collapse supernovae. These authors found much larger maximum baryonic and gravitational masses of their protoneutron stars at the onset of collapse than reported here. The collapsing protoneutron stars in their study have moderately-high central temperatures $T \lesssim 40\,\mathrm{MeV}$. However, at $\rho \approx 4 \times 10^{14} - 10^{15}\,\mathrm{g\,cm^{-3}}$, a region of extremely hot material with $T \gtrsim 80 - 100\,\mathrm{MeV}$ is present due to compression of multiple $M_\odot$ of accreted shock-heated material. [43] demonstrated that this extremely hot region is responsible for the observed thermal enhancement of the maximum protoneutron star mass. In NSNS mergers the situation is quite different and fully dynamical NSNS merger simulations have not found such extremely hot high-density regions [e.g., 44, 53]. It is thus unlikely that the findings of [43] apply to the merger HMNS case.

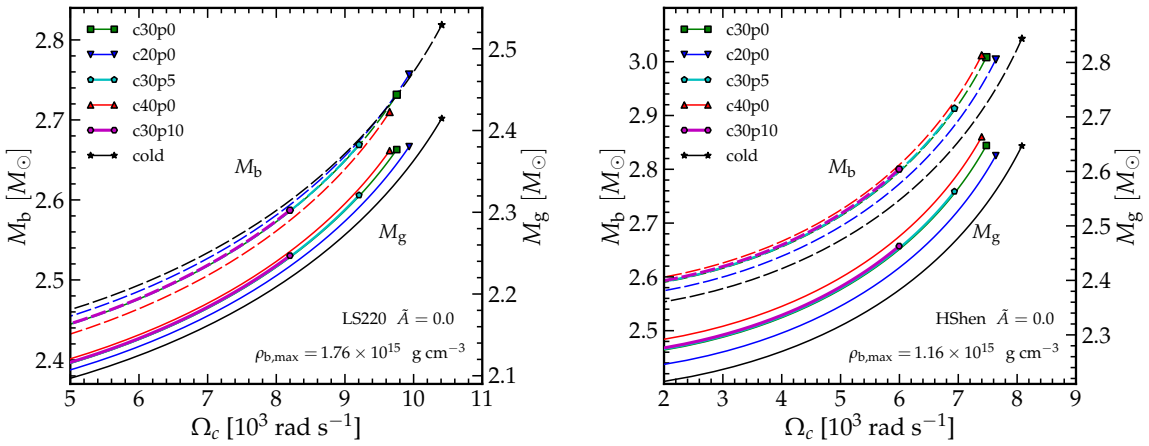

Figure 8.6: The gravitational mass (M_g, solid lines, right ordinate) and baryonic mass (M_b, dashed lines, left ordinate) as a function of angular velocity Ω for uniformly spinning models at a fixed density near the density that yields the maximum M_b for the LS220 (left panel) and the HShen EOS (right panel). The sequences terminate at the mass-shedding limit, which is the point with the maximum angular velocity for a specific temperature prescription. Configurations with higher temperatures and, in particular, the c30p5 and c30p10 models with high-temperature plateaus at low densities, have larger radii than colder models and thus reach the mass-shedding limit at lower angular velocities. Hence, such models have lower maximum masses at the supramassive limit than colder models. Note that hotter models with the LS220 have lower baryonic masses than colder models.

8.4 Results: Axisymmetric Models in Rotational Equilibrium

8.4.1 Uniformly Rotating Configurations

It has been widely recognized that uniform rotation can support a supramassive neutron star against gravitational collapse (see, e.g. [19, 21]). A supramassive neutron star is defined as a stable neutron star with a mass greater than the maximum mass of a TOV star with the same EOS (CST). At a given central density, the mass that may be supported rises with increasing angular velocity until the material on the NS's equator becomes unbound (the mass-shedding limit). This leads to the *supramassive limit*, a well defined maximum mass for uniformly rotating NSs with a specified EOS.

In Fig. 8.5, we plot the baryonic mass M_b as a function of maximum baryon density for TOV and uniformly rotating mass-shedding sequences obtained with the LS220 EOS (left panel) and the HShen EOS (right panel). Focusing first on the TOV sequences, one notes that at low central densities ($\rho_b \lesssim$ few $\times \rho_{nuc}$), M_b is significantly increased by thermal effects. This is because the mean density $\bar{\rho}_b$ of such configurations is in the regime in which thermal pressure is of greatest relevance (cf. Fig. 8.3) and can alter the structure of the bulk of the NS. This carries over to the uniformly rotating case. The extended hot configurations reach mass shedding at lower angular velocities than their cold counterparts, but the extended, low $\bar{\rho}_b$ cores of hot configurations receive

Model	$\rho_{\rm b,max}$ ($10^{15}\,{\rm g\,cm^{-3}}$)	$M_{\rm b}^{\rm max}$ ($M_\odot$)	$M_{\rm g}^{\rm max}$ ($M_\odot$)	r_e (km)	$r_{p/e}$	Ω ($10^3\,{\rm rad\,s^{-1}}$)	$T/\|W\|$
LS220 cold	1.653	2.823	2.419	14.429	0.566	10.096	0.118
LS220 c20p0	1.652	2.760	2.384	14.788	0.574	9.647	0.106
LS220 c30p0	1.652	2.737	2.382	15.000	0.576	9.441	0.103
LS220 c30p5	1.710	2.671	2.322	15.300	0.587	9.031	0.088
LS220 c30p10	1.769	2.587	2.247	16.130	0.599	8.215	0.066
LS220 c40p0	1.625	2.717	2.383	15.201	0.577	9.262	0.101
HShen cold	1.220	3.046	2.649	17.101	0.564	8.233	0.117
HShen c20p0	1.196	3.006	2.629	17.760	0.573	7.745	0.105
HShen c30p0	1.171	3.009	2.648	18.173	0.574	7.511	0.103
HShen c30p5	1.228	2.916	2.564	18.665	0.588	7.086	0.084
HShen c30p10	1.261	2.808	2.467	20.070	0.604	6.238	0.060
HShen c40p0	1.139	3.012	2.664	18.474	0.574	7.355	0.101

Table 8.2: Summary of mass-shedding uniformly rotating supramassive neutron star configurations at the maximum mass for each EOS and temperature prescription. These models are in ν-less β-equilibrium (see §8.2.2). $\rho_{\rm b,max}$ is the central density of the model with the maximum baryonic mass $M_{\rm b}^{\rm max}$. $M_{\rm g}^{\rm max}$ is the gravitational mass at the $\rho_{\rm b,max}$ at which $M_{\rm b}^{\rm max}$ occurs. r_e is the equatorial radius, $r_{p/e}$ is the axis ratio, Ω is the angular velocity, and $T/|W|$ is the ratio of rotating kinetic energy T to gravitational energy $|W|$.

sufficient rotational support to yield a higher $M_{\rm b}$. This, however, is the case only for centrally-hot cXp0 configurations. Models with hot envelopes (with parametrizations c30p5 and c30p10) benefit less from rotational support.

With increasing maximum density, the baryonic masses of the TOV models for different temperature parametrizations converge for a given EOS. Near the density at which the maximum mass is reached, the increase in $M_{\rm b}$ in hot configurations has turned into a slight decrease for models computed with the LS220 EOS and has dropped to $\lesssim$5% for the HShen EOS (see also Fig. 8.4). The mass-shedding sequences show a more complex behavior with increasing maximum density. As in the TOV case, the mean density $\bar{\rho}_b$ of the NSs increases and less material is experiencing enhanced pressure support due to high temperatures in the cXp0 models. Hence, these models move towards the $M_{\rm b}^{\rm max}$ of the cold supramassive limit (see the inset plots in Fig. 8.5). For both EOS, the $M_{\rm b}^{\rm max}$ of hot configurations are all lower than the cold value. The cXp0 models reach supramassive limits that are within less than 2% of the cold supramassive limit for both EOS. The c30p10 and c30p5 models, on the other hand, have $M_{\rm b}^{\rm max}$ that are $\sim 5-10\%$ lower than the cold supramassive limit for both EOS. Table 8.2 summarizes key parameters of the hot and cold configurations at the supramassive limit.

The systematics of the supramassive limit with temperature prescription becomes clear when considering Fig. 8.6. This figure shows the baryonic mass $M_{\rm b}$ and gravitational mass $M_{\rm g}$ for uniformly rotating NSs as a function of angular velocity Ω for the LS220 and HShen EOS at fixed densities near the maximum of $M_{\rm b}(\rho_{\rm b,max})$ (see Table 8.2). At fixed angular velocity below mass

shedding, hotter configurations always yield higher $M_{\rm g}$ than their colder counterparts. For the LS220 EOS, as in the TOV case discussed in the previous section 8.3, hotter configurations have lower $M_{\rm b}$. In the case of the HShen EOS, which generally yields less compact equilibrium models, the opposite is true, but the increase in $M_{\rm b}$ caused by thermal support is smaller than the increase in $M_{\rm g}$.

With increasing Ω, the mass-shedding limit is approached and hotter configurations systematically reach the mass shedding limit at lower angular velocities. The reason for this is best illustrated by comparing c30p0 models with c30p10 and c30p5 models, which have a high-temperature plateau at low densities of 10 MeV and 5 MeV, respectively. At low angular velocities, all c30pX models show the same thermal increase in $M_{\rm g}$. However, the high pressure at low densities in the c30p10 and c30p5 models leads to significantly larger radii compared to the model without temperature plateau. Consequently, as Ω is increased, the configurations with plateau reach the mass-shedding limit at lower Ω. For the LS220 EOS, the c30p10 sequence terminates at $\sim$8200 rad s^{-1}, the c30p5 sequence terminates at $\sim$9200 rad s^{-1}, while the c30p0 sequence does not terminate before $\sim$9800 rad s^{-1}. The HShen model sequences show the same qualitative trends.

8.4.2 Differentially Rotating Configurations

Differential rotation can provide centrifugal support at small radii while allowing a NS configuration to stay below the mass-shedding limit at its equatorial surface. Differentially rotating equilibrium configurations have been shown to support masses well in excess of the supramassive limit [e.g., 6, 41, 45]. Such configurations are referred to as "hypermassive". However, since there is (mathematically speaking) an infinite number of possible differential rotation laws, it is impossible to define a formal "hypermassive limit" for the maximum mass of HMNSs in the way it is possible for uniformly rotating supramassive NSs. Nevertheless, we can study the systematics of the supported baryonic (and gravitational) masses with variations in the HMNS temperature profile, maximum baryon density, and degree and rate of differential rotation for the rotation law considered in this study, which is not drastically different from what is found in merger simulations (e.g., [58]).

In Fig. 8.7, we show the supported baryonic mass $M_{\rm b}$ as a function of maximum baryon density $\rho_{\rm b,max}$ for cold, c20p0, and c40p0 temperature prescriptions, both EOS, and for different choices of $\tilde{A}$. The curves represent configurations with the minimum $r_{\rm p/e}$ at which an equilibrium solution is found by the CST solver (i.e., the most rapidly spinning setup). Note that the peaks of these curves represent only *lower* limits on the maximum HMNS mass. In addition, we plot only solutions with ratios $T/|W|$ of rotational kinetic energy T to gravitational energy $|W|$ below 25%, since more rapidly spinning models would be dynamically nonaxisymmetrically unstable [5, 10]. It is this limit which defines the rising branch of the $M_{\rm b}(\rho_{\rm b,max})$ curve at the lowest densities in Fig. 8.7 for $\tilde{A} = 1.0$. Note that many of these configurations may still be unstable to secular rotational instabilities or rotational shear instabilities (e.g., [14, 46, 70]).

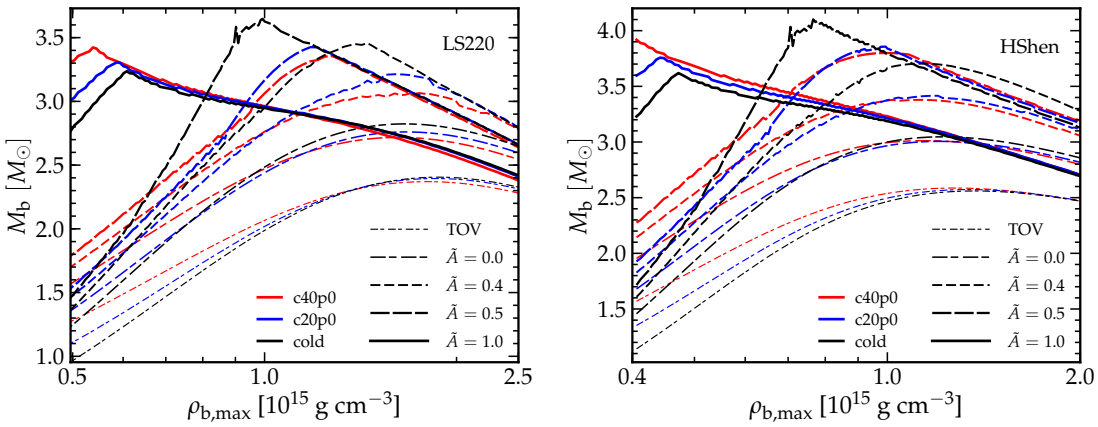

Figure 8.7: Maximum baryonic mass configurations for sequences of uniformly rotating ($\tilde{A} = 0$) and differentially rotating ($\tilde{A} = \{0.4, 0.5, 1.0\}$) models with cold, c20p0, and c40p0 temperature parametrizations and the LS220 EOS (left panel) and HShen EOS (right panel). We note that for differentially rotating models these curves represent lower limits on the maximum baryonic mass. We limit the sequences to models with $T/|W| \lesssim 0.25$ and this limit defines the rising part of the graphs for $\tilde{A} = 1$ at low densities. We show the TOV case (thinnest and shortest dash-dotted lines) for comparison. The raggedness of the curves with $\tilde{A} \gtrsim 0.4$ is a consequence of finite resolution in the parameter $r_{p/e}$ that is varied to find the maximum mass at a given $\rho_{\rm b,max}$. Thermal effects are most pronounced at low densities and for high $\tilde{A}$. For uniform and moderate differential rotation, hotter models have lower global maximum $M_{\rm b}$ than colder models.

The overall shape of the $M_{\rm b}(\rho_{\rm b,max})$ curves in Fig. 8.7 is qualitatively similar to what is shown in Fig. 1 of [6] for $\Gamma = 2$ polytropes and Fig. 2 of [41] for the cold FPS EOS [18]. The LS220 and HShen EOS yield qualitatively very similar results, but the supported HMNS masses found by the CST solver are, as expected, systematically higher for models with the HShen EOS than for those using the LS220 EOS. One notes, however, interesting variations with temperature prescription. At low $\rho_{\rm b,max}$, thermal pressure support leads to increased $M_{\rm b}$ and more differentially rotating configurations have higher $M_{\rm b}$. Sequences with $\tilde{A} \lesssim 0.5$ show similar systematics with density and temperature prescription as the uniformly spinning ones discussed in §8.4.1: As the density increases, hot configurations converge towards the cold sequence and reach their maximum $M_{\rm b}$ near and below the maximum of the cold sequence. Models with $\tilde{A} \gtrsim 0.5$, on the other hand, have more steeply rising curves with $\rho_{\rm b,max}$ and are discontinuous (i.e., exhibit a "kink") at their global maxima. At these points quasitoroidal solutions appear. Furthermore, the slope of the curve describing (as a function of $\rho_{\rm b,max}$) the axis ratios $r_{\rm p/e}$ at which the solver stops converging discontinuously changes sign. We attribute this behavior, which was also observed by [41], to a bifurcation of the sequence between models, which continue shrinking in axis ratio until they become completely toroidal ($r_{\rm p/e} = 0$), and less extreme models that stay quasitoroidal or spheroidal . Beyond the "kink" in $\tilde{A} \gtrsim 0.5$ sequences, thermal effects play little role.

The lower bounds of the range of $\rho_{\rm b,max}$ shown in the two panels of Fig. 8.7 (and also Fig. 8.8)

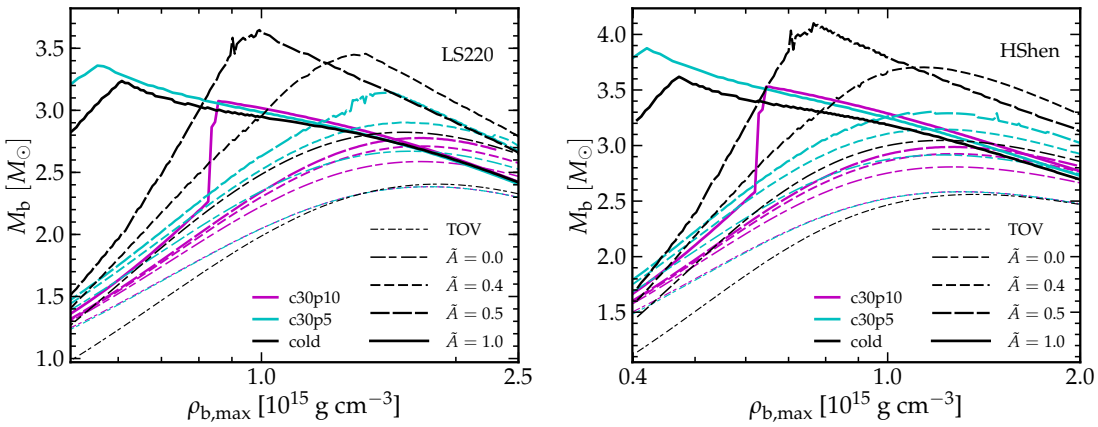

Figure 8.8: Same as Fig. 8.7, but comparing cold configurations with models with the c30p5 and c30p10 temperature prescriptions, which have a hot plateau at low densities. The overall systematics are the same for the LS220 EOS (left panel) and the HShen EOS (right panel). In the TOV case, M_b is thermally enhanced at low densities, but the global maximum of M_b of hot configurations is near that of the cold TOV solution. Uniformly and moderately differentially rotating sequences of c30p10 and c30p5 models have systematically smaller maximum masses than cold models throughout the considered density range. Only very differentially rotating models ($\tilde{A} \gtrsim 0.7$; $\tilde{A} = 1.0$ shown here) exhibit a thermal enhancement of the maximum mass at low to intermediate densities. The c30p10 sequence for $\tilde{A} = 1.0$ exhibits a discontinuous jump, which occurs when the sequence transitions from spheroidal to quasitoroidal shape. See text for discussion.

are chosen for the following reason: Fully dynamical merger simulations by, e.g, [4, 7, 31, 53, 58, 65], all suggest a rule of thumb that the postmerger maximum baryon density of the HMNS is typically not less than ∼80% of the central density of the progenitor NSs. We can derive a rather solid EOS-dependent lower limit on $\rho_{b,max}$ for HMNS remnants from (equal mass) NSNS mergers in the following way: In order to form a HMNS, constituent equal-mass NSs must at the very least have a mass that is 50% of the maximum mass in the cold TOV limit. Hence, the premerger central density must at least be that of a TOV solution with $M_b = 0.5 M_b^{max,TOV}$. Using the aforementioned empirical result from merger simulations, we arrive at

$$\rho_{b,min} = 0.8 \rho_{b,TOV}(M_b = M_{b,max}/2) \ . \tag{8.7}$$

For the LS220 EOS, $\rho_{b,TOV}(M_b = M_{b,max}/2) \sim 5.8 \times 10^{14}\,\mathrm{g\,cm^{-3}}$ and occurs at M_b (M_g) of 1.19 $M_\odot$ (1.10 $M_\odot$). For the HShen EOS, $\rho_{b,TOV}(M_b = M_{b,max}/2) \sim 4.4 \times 10^{14}\,\mathrm{g\,cm^{-3}}$ and occurs at M_b (M_g) of 1.28 $M_\odot$ (1.20 $M_\odot$). Applying the density cut given by Eq. (8.7) excludes most dynamically nonaxisymmetrically unstable configurations.

Figure 8.8, like Fig. 8.7, shows baryonic mass as a function of maximum baryon density for both EOS and a variety of $\tilde{A}$, but contrasts models c30p5 and c30p10, which have hot plateaus at low densities, with cold models. The qualitative features discussed in the following are identical for both EOS. In the TOV case and at low densities, M_b is enhanced primarily by the hot core, since

Model	$\rho_{\rm b,max}$ ($10^{15}\,{\rm g\,cm^{-3}}$)	$M_{\rm b}^{\rm max}$ ($M_\odot$)	$M_{\rm g}^{\rm max}$ ($M_\odot$)	r_e (km)	$r_{p/e}$	$\tilde{A}$	Ω_c ($10^3\,{\rm rad\,s^{-1}}$)	$T/\|W\|$
LS220 cold	0.993	3.648	3.140	17.258	0.376	0.5	15.476	0.244
LS220 c20p0	0.852	3.573	3.124	18.538	0.364	0.6	15.047	0.243
LS220 c30p0	0.706	3.568	3.167	19.611	0.344	0.7	14.888	0.249
LS220 c30p5	0.600	3.413	3.064	21.870	0.320	0.9	14.461	0.250
LS220 c30p10	0.990	3.090	2.723	19.208	0.421	0.9	16.330	0.187
LS220 c40p0	0.692	3.597	3.211	19.931	0.344	0.7	14.677	0.249
HShen cold	0.766	4.101	3.562	19.800	0.372	0.5	13.450	0.245
HShen c20p0	0.641	4.076	3.585	21.352	0.360	0.6	13.042	0.245
HShen c30p0	0.532	4.099	3.650	22.305	0.344	0.7	13.131	0.249
HShen c30p5	0.517	3.942	3.527	24.371	0.340	0.8	12.426	0.243
HShen c30p10	0.646	3.529	3.141	23.521	0.400	1.0	13.934	0.196
HShen c40p0	0.514	4.148	3.708	22.701	0.344	0.7	12.888	0.249

Table 8.3: Summary of the differentially rotating HMNS configurations with the largest baryonic masses for each EOS and temperature prescription. These configurations are obtained in a sequence from $\tilde{A} = 0$ to $\tilde{A} = 1$ with spacing $\delta\tilde{A} = 0.1$ and are to be seen as lower bounds on the maximum achievable masses. The sequences considered here exclude dynamically nonaxisymmetrically unstable models with ratio of rotational kinetic energy to gravitational energy $T/|W| > 0.25$. The quantities listed in the table are the following: $\rho_{\rm b,max}$ is the baryon density at which the maximum baryonic mass $M_{\rm b}^{\rm max}$ occurs, $M_{\rm g}^{\rm max}$ is the gravitational mass at that density, r_e is the equatorial radius of the configuration, $r_{p/e}$ is its axis ratio, $\tilde{A}$ is the differential rotation parameter at which $M_{\rm b}^{\rm max}$ obtains. Ω_c is the central angular velocity of the configuration and $T/|W|$ is its ratio of rotational kinetic energy to gravitational energy. We note that the accuracy of the results listed in this table is set by the step size in $r_{p/e}$, which we set to $\delta r_{p/e} = 0.004$.

nonrotating solutions are compact and dominated by $\rho_{\rm b} \gtrsim 10^{14}\,{\rm g\,cm^{-3}}$, where the high-temperature plateaus play no role. At higher densities, the $M_{\rm b}$ curves of hot models converge to near or below the cold TOV maximum $M_{\rm b}$. The situation is different for uniformly and moderately differentially rotating models ($\tilde{A} \lesssim 0.5$). Rotation shifts these configurations to lower mean densities and the hot plateaus lead to equatorially bloated solutions. These reach their minimum $r_{\rm p/e}$ for which a solution can be found at lower angular velocities. Hence, centrifugal support is weaker and the configuration with the hottest plateau has the lowest $M_{\rm b,max}$. The behavior is different at high degrees of differential rotation ($\tilde{A} = 1$). The cold and the c30p5 models are HMNSs and quasitoroidal already at the lowest densities shown in Fig. 8.8. The c30p5 sequence has slightly larger $M_{\rm b}$ than the cold sequence. The c30p10 sequence, however, is spheroidal at low $\rho_{\rm b,max}$ and then discontinuously transitions to the quasitoroidal branch, which is marked by a large jump in $M_{\rm b}$.

In order to illustrate this discontinuous behavior further, we plot in Fig. 8.9 the equatorial radius of equilibrium solutions as a function of central angular velocity at $\tilde{A} = 1$ and for three different fixed $\rho_{\rm b,max}$. We show curves obtained with the LS220 EOS for the cold, c30p5, and c30p10 temperature prescriptions. The curves are parametrized by decreasing $r_{\rm p/e}$ and terminate at the smallest value at which the solver converges. The three densities are chosen so that the first two are below and the third is above the jump of the c30p10 curve in Fig. 8.8. At all $\rho_{\rm b,max}$, the hot configurations have

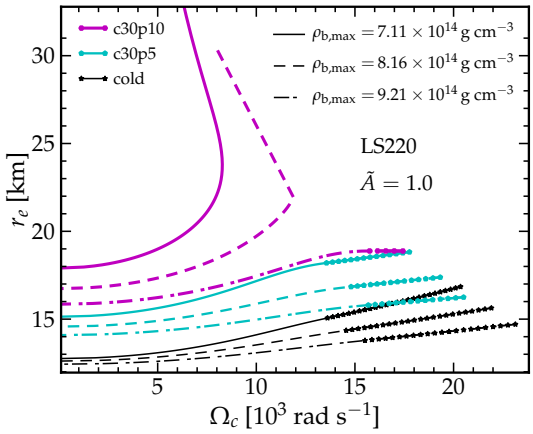

Figure 8.9: Equatorial radii r_e vs. central angular velocity Ω_c in sequences parametrized by the axis ratio $r_{p/e}$ for models using the LS220 EOS, differential rotation parameter $\tilde{A} = 1.0$, and cold, c30p5, and c30p10 temperature parametrizations. We show curves for three densities, two below the discontinuous jump of the c30p10 curve in Fig. 8.8 and one above. At the same density, hotter configurations have larger radii and transition to quasitoroidal shape (marked by dots) at higher Ω_c. The transition between spheroidal and quasitoroidal shape is discontinuous in $\rho_{\rm b,max}$ for critical models at the minimum $r_{p/e}$ that can be found (shown in Figs. 8.7 and 8.8), but smooth in $r_{p/e}$ at fixed $\rho_{\rm b,max}$. The low-density sequences with the c30p10 temperature prescription (10-MeV plateau at low densities; see §8.2.2) become double valued in Ω_c with increasing $r_{\rm p/e}$, stay spheroidal and have very large r_e.

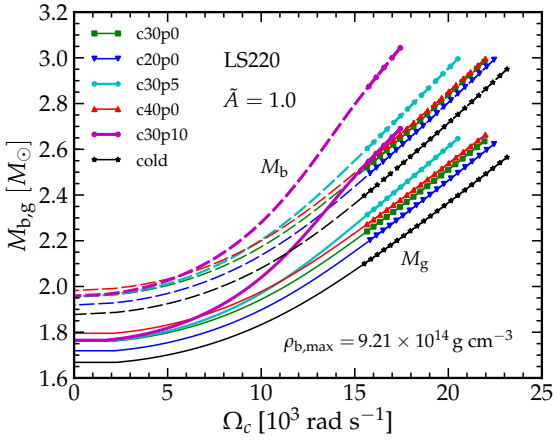

Figure 8.10: Baryonic mass $M_{\rm b}$ and gravitational mass $M_{\rm g}$ vs. central angular velocity Ω_c parametrized by the axis ratio $r_{\rm p/e}$ at fixed degree of differential rotation $\tilde{A} = 1$, and fixed maximum density of $\rho_{\rm b,max} = 9.21 \times 10^{14}\,{\rm g\,cm^{-3}}$. Curves for all temperature parametrizations are shown for the LS220 EOS. Quasitoroidal configurations are marked by symbols and the transitions between spheroidal and quasitoroidal solutions are smooth. The end points of all graphs correspond to the values plotted in Figs. 8.7 and 8.8 for the various temperature prescriptions at $\tilde{A} = 1.0$ and the $\rho_{\rm b,max}$ chosen here. Sequences with hot plateaus (using temperature prescriptions c30p5 and c30p10) exhibit significant thermal enhancements of $M_{\rm b}$ and $M_{\rm g}$ at rapid rotation rates, but have lower maximum rotation rates due to their larger radii.

significantly larger radii than the cold models, but decreasing $r_{\rm p/e}$ leads to increasing Ω_c and only modest radius changes for cold and c30p5 models. This is very different for the c30p10 sequence. At $\rho_{\rm b,max} = 7.11 \times 10^{14}\,{\rm g\,cm^{-3}}$ these models do not become quasitoroidal and the $r_e - \Omega_c$ mapping becomes double-valued as the decrease in $r_{\rm p/e}$ turns from a decrease of $r_{\rm p}$ at nearly fixed $r_{\rm e}$ and increasing Ω_c into a steep increase of $r_{\rm e}$ and a decrease of Ω_c. As $\rho_{\rm b,max}$ increases, less material is at low densities where thermal pressure support is strong in the c30p10 models. Consequently, the solutions are more compact and stay so to smaller $r_{\rm p/e}$. $\rho_{\rm b,max} = 8.16 \times 10^{14}\,{\rm g\,cm^{-3}}$ is the critical density at which the very last point in the sequence of decreasing $r_{\rm p/e}$ (the one shown in Fig. 8.8) jumps discontinuously to large $r_{\rm e}$. At $\rho_{\rm b,max} = 9.21 \times 10^{14}\,{\rm g\,cm^{-3}}$, which is above the critical density for c30p10 in Fig. 8.8, the c30p10 models become quasitoroidal as $r_{\rm p/e}$ decreases and Ω_c increases. They exhibit the same systematics as the c30p5 and cold models. We note that what we have described for the c30p10 models also occurs for the c30p5 models, although at significantly lower densities $\rho_{\rm b,max} \lesssim 5 \times 10^{14}\,{\rm g\,cm^{-3}}$ and even the cold models show similar trends at low densities.

The sequences shown in Figs. 8.7 and 8.8 are extreme configurations in the sense that models with smaller $r_{\rm p/e}$ cannot be found by the CST solver and may not exist for the rotation law that we consider here. Real HMNS may not by such critical rotators. In Fig. 8.10, we plot $M_{\rm b}$ and $M_{\rm g}$ for the LS220 EOS as a function of central angular velocity Ω_c and temperature prescription. We fix the degree of differential rotation to $\tilde{A} = 1$ and show sequences in Ω_c for a fixed maximum density $\rho_{\rm b,max} = 9.21 \times 10^{14}\,{\rm g\,cm^{-3}}$, which is the highest density shown in Fig. 8.9. The transition to quasitoroidal shape is smooth and quasitoroidal configurations are marked with symbols. The end points of the $M_{\rm b}$ curves shown in Fig. 8.10 and in Fig. 8.9 correspond to the $M_{\rm b}$ values of the $\tilde{A} = 1$ curves in Figs. 8.7 and 8.8 at $9.21 \times 10^{14}\,{\rm g\,cm^{-3}}$.

Fig. 8.10 shows that, as in the case of uniform rotation (cf. Fig. 8.6), hotter *subcritically* differentially spinning configurations have higher $M_{\rm g}$. At the density chosen for this plot, they also have higher $M_{\rm b}$, but at the higher densities at which the masses of uniformly spinning models peak, the $M_{\rm b}$ of hotter configurations are smaller than those of colder ones. It is particularly remarkable that the models with the hot plateau at low densities show the greatest thermal enhancement. They also transition to a quasitoroidal shape last but terminate the earliest in Ω_c. Nevertheless, for the $\rho_{\rm b,max}$ chosen here, they can support slightly more mass at critical rotation than their counterparts without low-density temperature plateau.

8.5 Discussion and comparison with 3D NSNS simulations

8.5.1 The Stability of HMNS Equilibrium Sequences

The existence of a maximum mass for equilibrium sequences of nonrotating (TOV) neutron stars is one of the most important astrophysical consequences of general relativity and, hence, is well known

in the study of compact objects. The parameter space of hot differentially rotating HMNS models studied here is vast and complex. In the following, we briefly review the classical results on the stability of stationary neutron stars and formulate how one may reason regarding the stability of HMNS equilibrium models.

The equilibrium models we generate in this study are extrema of the total mass-energy, $M_{\rm g}$, with respect to adiabatic perturbations to the metric and fluid quantities ([22]). If perturbed, a particular equilibrium model will oscillate around its initial state (or diverge from its initial state) if it is stable (unstable). In this case, the extremum of the mass-energy of the model is at a minimum (maximum if unstable). A particular useful approach to the stability problem is the *turning-point method* of [60]. The turning-point method allows one to reason about the stability of sequences of equilibrium solutions solely by examining the parameter space of equilibrium models without dynamical simulations or linear perturbation analysis. The turning-point method has been used extensively in previous work on the stability of cold and uniformly rotating neutron stars (e.g., CST, [20, 50, 62]).

An equilibrium sequence is a one dimensional slice from the space of equilibrium models indexed by some parameter. Here we use $\rho_{\rm b,max}$ as our sequence parameter. A model in the space of equilibrium models may be defined by the following conserved quantities: the gravitational mass $M_{\rm g}$, baryonic mass $M_{\rm b}$, total angular momentum J, and total entropy S. Generally, as one changes the sequence parameter, $\rho_{\rm b,max}$, the quantities ($M_{\rm g}$, $M_{\rm b}$, J, S) will vary. A *turning point* in the sequence occurs when 3 out of 4 of the derivatives $d/d\rho_{\rm b,max}$ of ($M_{\rm g}$, $M_{\rm b}$,J, S) vanish. For this point in $\rho_{\rm b,max}$, the turning point theorem shows (i) that the derivative of the fourth quantity in the tuple also vanishes, and (ii) that the sequence must have transitioned from stable to unstable ([60] and [30]). This characterization of the space of equilibrium models relies on the assumption that the change in $M_{\rm g}$ depends to first order only on the *total* changes in baryonic mass $M_{\rm b}$, angular momentum J, and entropy S, and not on changes to their higher moments. That is, changes in the distribution of entropy, baryonic mass and angular momentum. In nature, this will generally not be the case, since cooling and angular momentum redistribution will change the entropy and angular momentum distributions, respectively. However, these changes will be slow and not drastic so that changes to the total energy due to changes in these higher order moments will be small. We account for such changes approximately by considering different degrees of differential rotation and a range of temperature prescriptions in the following.

If we are considering the special case of zero-temperature configurations, then the entropy S is no longer relevant to the equilibrium's stability, since the change to the configuration's energy due to a change in entropy is also zero. In this case, a turning point may be identified when two out of three of the set $d/d\rho_{\rm b,max}(M_{\rm g}, M_{\rm b}, J)$ are zero. Zero temperature is a very good approximation for our cold equilibrium models. In Fig. 8.11, we plot $M_{\rm g}$ along constant $M_{\rm b}$ sequences with $M_{\rm b} = 2.9 M_\odot$ for the

HShen EOS ($M_{\rm b} = 2.9 M_\odot$ corresponds to $M_{\rm b}$ of a HMNS formed from two NSs of $M_{\rm g} = 1.35 M_\odot$, assuming no mass loss). All of these curves have a minimum located at $\rho_{\rm b,max} \gtrsim 1 \times 10^{15} {\rm g\,cm^{-3}}$.

For the cold sequences, these minima are turning points because $dM_{\rm g}/d\rho_{\rm b,max}$ and $dM_{\rm b}/d\rho_{\rm b,max}$ are both zero. Any models along those curves at densities in excess of $\rho_{\rm b,max}$ at the minima are secularly unstable to collapse. For the hot temperature parametrizations[4], the minima are only approximations to the turning point (which we shall call *approximate turning points*) because only two out of four ($dM_{\rm g}/d\rho_{\rm b,max}$ and $dM_{\rm b}/d\rho_{\rm b,max}$) of the derivatives of ($M_{\rm g}$, $M_{\rm b}$, J, S) are zero. We argue that these approximate turning points are good indicators of the onset of instability for the equilibrium sequences for several reasons. (i) We find that the approximate turning points for all considered temperature parametrizations and measures of differential rotation ($\tilde{A} = 0$ to $\tilde{A} = 1.1$ with spacing $\delta\tilde{A} = 0.1$) lie within the same $\sim 25\%$ range in $\rho_{\rm b,max}$ indicated by the blue lines in Fig. 8.11 (similarly within a $\sim 25\%$ range in $\rho_{\rm b,max}$ for the LS220 EOS). (ii) In cold uniformly rotating NS models, approximate turning points occur where one out of three of $d/d\rho_{\rm b,max}(M_{\rm g}, M_{\rm b}, J)$ vanish. The study of such models shows that the actual turning point density is within only $\sim 1\%$ of the approximate turning point density (where $dM_{\rm g}/d\rho_{\rm b,max} = 0$ along the mass-shed sequence; cf. Fig. 10 of [62]). (iii) The turning-point condition is a sufficient, but not necessary, criterion for secular instability. Thus instability must set in at $\rho_{\rm b,max}$ greater than the turning-point $\rho_{\rm b,max}$, but may set in already at lower densities (see, e.g., [63] for an example). It is thus conservative to use the approximate turning point located at the highest $\rho_{\rm b,max}$ over all sequences for a given EOS as an upper bound for the maximum stable $\rho_{\rm b,max}$ of HMNS models for that EOS.

8.5.2 The Secular Evolution of HMNS from Mergers

A HMNS remnant resulting from the merger of two NSs that does not promptly collapse into a black hole will settle to a quasiequilibrium state. More precisely, this is a state in which the HMNS is no longer in dynamical evolution, measured, for example, by oscillations in the HMNS maximum density. This should occur several dynamical times after merger. From this point on, the HMNS will evolve secularly along some sequence of equilibrium models. A secular evolution is, by definition, a dissipative process that may involve energy loss from the system. Consequently, we may parametrize the secular evolution of the HMNS towards a turning point via the change in its total mass-energy, which, in our case, is the change in gravitational mass of the equilibrium model. This occurs in HMNSs via neutrino cooling and the emission of gravitational radiation. In addition, the rotational energy of the HMNS may be reduced by angular momentum redistribution via the MRI, provided this occurs sufficiently slowly to be characterized as as secular process. This can lead to a build up of magnetic field, or dissipation of the free energy of differential rotation as heat (see, e.g., [66] for

[4]We show only the c40p0 and cold temperature parametrizations in Fig. 8.11, because we find them to be the limiting cases. All other parametrizations have minima at intermediate locations in the ($M_{\rm g}$, $\rho_{\rm b,max}$) plane.

a detailed discussion), which may lead to increased neutrino cooling. Furthermore, specific angular momentum transported to the HMNS surface may unbind surface material, leading to a decrease in J and $M_{\rm b}$.

A secularly evolving HMNS will, in general, evolve in the direction of decreasing gravitational mass $M_{\rm g}$ while conserving its total baryonic mass $M_{\rm b}$. This results in an increasing density and compactness of the star. Figure 8.11 shows, for a fixed temperature prescription and differential rotation parameter, that the gravitational mass $M_{\rm g}$ of a sequence with fixed baryonic mass $M_{\rm b} = 2.9\,M_\odot$ (using the HShen EOS; we find qualitatively the same for the LS220) is decreasing with increasing density. This continues until, $M_{\rm g}$ reaches a minimum at an approximate turning point for $\rho_{\rm b,max} \gtrsim 1 \times 10^{15}\,{\rm g\,cm^{-3}}$. Here, $\delta M_{\rm g} = 0$, and $\delta M_{\rm b}$ vanishes by our choice of a constant $M_{\rm b}$ sequence.

The curves in Fig. 8.11 are shown for constant differential rotation parameter $\tilde{A}$. However, a HMNS of $M_{\rm b} = 2.9 M_\odot$ is not necessarily constrained to a specific curve. One would expect the HMNS to evolve to neighboring curves of less extreme differential rotation (decreasing $\tilde{A}$), in accordance with its loss of angular momentum due to gravitational waves and its redistribution of angular momentum due to other secular processes. Nevertheless, consider the limit in which the HMNS is constrained to a curve of constant $\tilde{A}$. Then it would evolve secularly until reaching the curve's minimum. At this point, any further energy loss implies that the HMNS must either (a) secularly evolve to a nearby equilibrium sequence with lower temperature or lower degree of differential rotation and higher density (another curve on the plot) *or* (b) undergo collapse to a black hole. Note that the densities at which the minimum occurs for different $\tilde{A}$ and temperatures are remarkably close to each other. For the sequences using the HShen EOS shown in Fig. 8.11, the approximate turning points lie in the range $1.05 \times 10^{15}\,{\rm g\,cm^{-3}} < \rho_{\rm b,max} < 1.30 \times 10^{15}\,{\rm g\,cm^{-3}}$ for all considered $\tilde{A}$ and both shown temperature prescriptions. The constant-$M_{\rm b}$ curves for other temperature parametrizations (c20p0, c30p0, c30p5, c30p10) are all located in-between the curves for the c40p0 and cold cases shown. Thus, we expect that the point of collapse for a HMNS will be marked by its evolution to this density regime regardless of the temperature distribution of the model.

From the above findings, we conclude that thermal effects have little influence on the stability of HMNSs in rotational equilibrium against gravitational collapse. However, our results do imply that thermal support *will* affect at what density the HMNS first settles to its quasiequilibrium state. The discussion in §8.4.2 and, in particular, Fig. 8.10, illustrates that at subcritical rotation rates and densities significantly below those of the approximate turning points, models with hot temperature profiles have a larger $M_{\rm b}$ compared to models with cooler temperatures at the same $\rho_{\rm b,max}$. Thus a HMNS with greater thermal support will reach a quasiequilibrium at a lower $\rho_{\rm b,max}$, and thus have more energy to lose before it can evolve to the critical density regime for collapse.

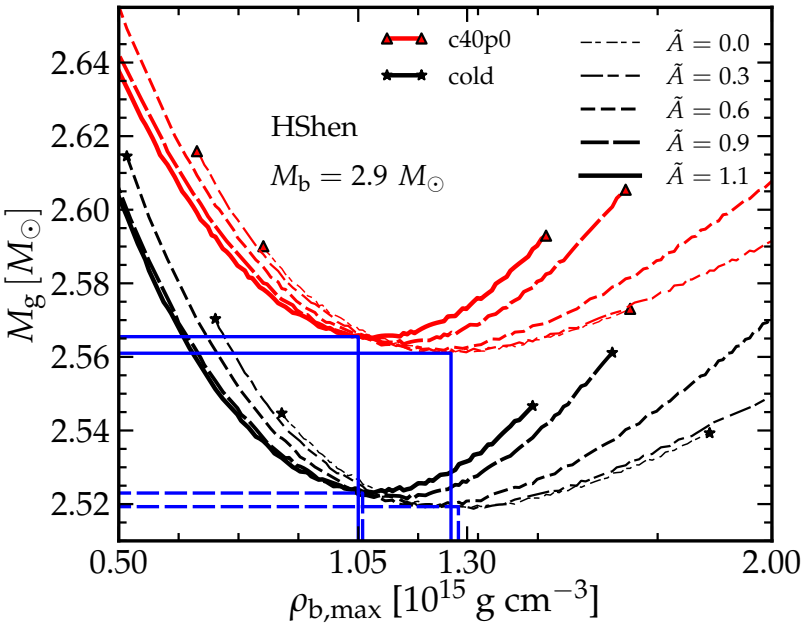

Figure 8.11: Gravitational mass M_g as a function of maximum baryon density $\rho_{b,max}$ for models with $M_b = 2.9 M_\odot$. Each curve is for a fixed degree of differential rotation $\tilde{A}$, with the axis ratios $r_{p/e}$ chosen such that $M_b = 2.9 M_\odot$. Symbols mark equilibrium solutions at the minimum $r_{p/e}$ for which a solution can be found for a $M_b = 2.9$ and a given $\tilde{A}$. The local minima of these curves are approximate turning points of the sequences. For the cold (c40p0) models, we have noted the range in M_g and $\rho_{b,max}$ across models with different amounts of differential rotation with dashed (solid) blue lines. Consequently, $\rho_{b,max} = 1.30 \times 10^{15} g\,cm^{-3}$ represents the upper limit for the baryon density of a stable HMNS with the HShen EOS. Note also that the difference in M_g of the approximate turning points between sequences with the same temperature prescription is only $\sim 0.005 M_\odot$

While thermal effects may be important in setting the initial conditions for the secular evolution of a HMNS, they appear to be of little consequence to the stability of a HMNS in quasiequilibrium. Once in a quasiequilibrium state, the energy lost by a HMNS during its secular evolution is the most robust indicator for its progress towards instability and collapse. Fig. 8.11 shows that this is true regardless of the degree of differential rotation of the HMNS. For a fixed temperature parametrization, the difference in M_g between different degrees of differential rotation is at most $\sim 0.005\,M_\odot$, corresponding to $\lesssim 10\%$ of the total energy lost during the HMNS's secular evolution.

8.5.3 Comparison with NSNS Merger Simulations

[53] conducted simulations of NSNS mergers using the HShen EOS and included neutrino cooling via an approximate leakage scheme. They considered three equal-mass binaries with component NS gravitational (baryonic) masses of $1.35 M_\odot$ ($1.45 M_\odot$), $1.50 M_\odot$ ($1.64 M_\odot$), $1.60 M_\odot$ ($1.77 M_\odot$) denoted as L, M, and H, respectively. The HMNS formed from their high-mass binary collapses to a black hole within $\lesssim 9$ ms of merger. The low-mass and the intermediate-mass binaries, however, form hot

($T \sim 5 - 30\,\mathrm{MeV}$) spheroidal quasiequilibrium HMNSs that remain stable for at least 25 ms, the duration of their postmerger simulations.

[53] argue that thermal pressure support could increase the maximum mass of HMNSs with $T \gtrsim 20\,\mathrm{MeV}$ by $20-30\%$. The results that we lay out in §8.3 and §8.4 of our study suggest that it is not straightforward to disentangle centrifugal and thermal effects for differentially rotating HMNS. Our findings show that critically spinning configurations (i.e., configurations at which the maximum M_b is obtained for a given $\tilde{A}$) of hot models do not lead to an increase in the maximum supported baryonic mass by more than a few percent and in most cases predict a lower maximum mass than in the cold case. We find it more useful to consider the results of [53] in the context of the evolutionary scenario outlined in §8.5.2.

In Fig. 8.12, we plot $M_{\rm b}$ as a function of $\rho_{\rm b,max}$ for select sequences of uniformly and differentially rotating models obtained with the HShen EOS with the cold and c40p0 temperature prescriptions. We also mark the immediate postmerger densities of the L, M, and H models of [53] and their evolutionary tracks (in $\rho_{\rm b,max}$). The high-mass model H never settles to a quasiequilibrium and collapses to a black hole during the dynamical early postmerger phase. Its $\rho_{\rm b,max}$ evolves within $\sim$9 ms from $0.58\times10^{15}\,\mathrm{g\,cm^{-3}}$ to values beyond the range of the plot. Our secular-evolution approach cannot be applied to this model since it never reaches a quasiequilibrium state. The lower-mass M and L models enter Fig. 8.12 at successively lower densities. Their "ring-down" oscillations are damped by $\sim$9 ms after which the HMNSs evolve secularly with $\rho_{\rm b,max}$ that increase roughly at the same rate in both models, suggesting that their rate of energy loss is comparable. At such early times, gravitational waves are most likely dominating energy loss (cf. the discussion of timescales in [47]), and, indeed, model M and L exhibit similar gravitational wave amplitudes and frequencies ([53], Fig. 4). Focusing on model L, we now consider Fig. 8.11, which shows sequences of constant $M_{\rm b}$ (for model L with $M_{\rm b} \sim 2.9\,M_\odot$). As the HMNS loses energy, $M_{\rm g}$ decreases and the HMNS evolves to the right (towards higher $\rho_{\rm b,max}$). Model L enters its secular evolution at a central density of $\sim0.56\times10^{15}\,\mathrm{g\,cm^{-3}}$ and evolves secularly to $\sim0.68\times10^{15}\,\mathrm{g\,cm^{-3}}$ within $\sim$16 ms. Largely independent of its specific angular momentum distribution and thermal structure, Fig. 8.11 suggests that this model will reach its global minimum $M_{\rm g}$ and, thus, instability in a small density range of $\sim 1.05 - 1.30\ \times 10^{15}\,\mathrm{g\,cm^{-3}}$. Linearly extrapolating the density evolution of model L in [53], we expect a possible onset of collapse at $t \gtrsim 58$ ms after merger (and $\gtrsim$49 ms after the start of the secular evolution). However, depending on its angular momentum when entering its secular evolution, its cooling rate, angular momentum redistribution and loss, this model may evolve into a long-term stable supramassive neutron star, since a baryonic mass of $\sim2.9\,M_\odot$ can in principle be supported by the HShen EOS at the supramassive limit (cf. Table 8.2).

The role of thermal effects in all of the above is relatively minor (cf. the very similar $\rho_{\rm b,max}$ locations of the $M_{\rm g}$ minima in hot and cold configurations shown in Fig. 8.11). However, when

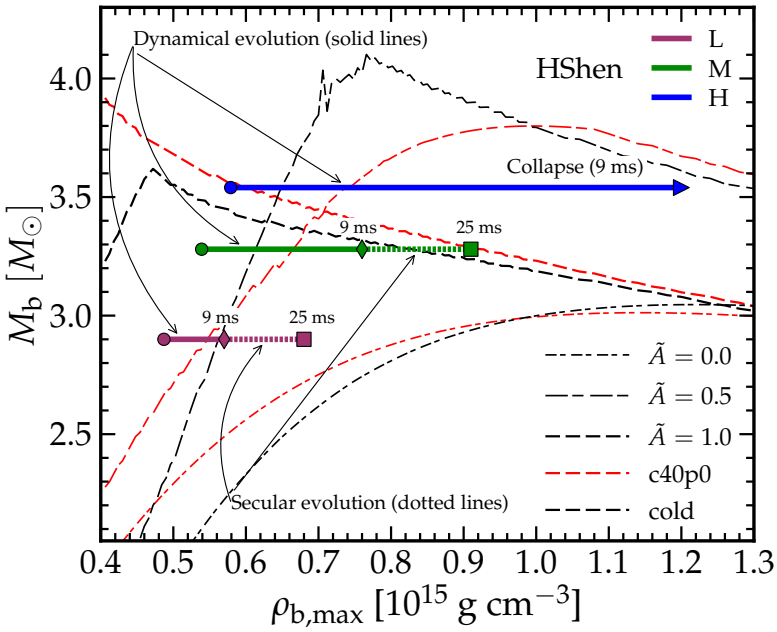

Figure 8.12: Similar to Fig. 8.7 but for the HShen EOS and showing the evolution of HMNSs from [53]. We show the evolution of maximum density of the HMNS for the low, medium and high mass configurations (thick lines L, M and H) starting from the premerger density (noted by circles), and ending at the simulation termination densities (squares, or, in the H configuration, an arrow indicating collapse to a black hole). After approximately 9 ms (noted with diamonds), the L and M models show negligible dynamical oscillations and have settled to a quasiequilibrium state. From there until the end of the simulation, the L and M HMNS are evolving secularly (indicated by thick dotted lines).

first entering the secular regime as a subcritical HMNS, a configuration with higher temperature and stronger thermal pressure support will be less compact and will have a lower $\rho_{\rm b,max}$ at a fixed $M_{\rm b}$ than a colder one. Hence, in the picture of secular HMNS evolution discussed in §8.5.2, such a configuration would have to evolve "farther" in $\rho_{\rm b,max}$ to reach criticality and, thus, can survive longer at fixed energy loss rates.

[47] performed NSNS merger simulations of $\Gamma = 2$ polytropes in which they approximated a thermal pressure component with a $\Gamma = 2$ Γ-law. Their postmerger HMNS enters its secular evolution in a quasitoroidal configuration with two high-density, low-entropy cores, a central, lower-density, hot region and a high-entropy low-density envelope. The total mass of their model can be arbitrarily rescaled, but in order to estimate temperatures and thermal pressure contributions, the authors scaled their HMNS remnant to a gravitational mass of $2.69\,M_\odot$. With this, they estimated in their quasitoroidal HMNS peak and rms temperatures of $\sim$20 MeV and $\sim$5 MeV, respectively. [47] studied the effect of neutrino cooling on the HMNS evolution by introducing an ad-hoc cooling function that removes energy proportional to the thermal internal energy (neglecting the stiff temperature dependence of neutrino cooling). In order to capture effects of cooling during the limited simulated

physical postmerger time, they drained energy from their HMNS at rates $\sim 100 - 200$ times higher than realistic cooling by neutrinos.

The authors considered cases without cooling and with two different accelerated cooling timescales. As cooling is turned on in their simulations, the slope of the maximum baryon density $\rho_{\rm b,max}(t)$ of the HMNS increases discontinuously and the higher the cooling rate, the faster the evolution to higher $\rho_{\rm b,max}(t)$. The HMNSs in both cases with cooling become unstable at different times, but roughly at the same $\rho_{\rm b,max}$. This is consistent with the secular HMNS evolution picture laid out in §8.5.2. Cooling reduces the total energy of the system ($M_{\rm g}$) and drives the HMNS to higher $\rho_{\rm b,max}$ at fixed $M_{\rm b}$ until the (approximate) turning point is reached and collapse ensues. However, losses due to gravitational wave emission and angular momentum redistribution and shedding will have the same effect and may dominate in nature, since they are likely to operate more rapidly than neutrino cooling (cf. the discussion of timescales by [47]).

[8] carried out smoothed-particle hydrodynamics simulations of HMNSs in the conformal-flatness approximation to general relativity. They compared simulations using the full temperature dependence of the HShen and LS180 EOS[5] with an approximate treatment of thermal pressure via a Γ-law, $P_{\rm th} = (\Gamma_{\rm th} - 1)\epsilon_{\rm th}\rho_{\rm b}$. Although [8] do not provide a figure showing the evolution of maximum baryon density, they show (in their Fig. 5) graphs of cumulative mass as a function of distance from the center of the LS180-EOS HMNS at 8 ms after merger, roughly the time when the dynamical early postmerger phase is over and the secular HMNS evolution begins. From this, it may be observed that the HMNS with the lower thermal gamma ($\Gamma_{\rm th} = 1.5$) is more compact than the model with $\Gamma_{\rm th} = 2$. The HMNS evolved with the fully temperature-dependent LS180 EOS is in between the two, but closer to the $\Gamma_{\rm th} = 2$ model. [8] found that the more compact HMNS with $\Gamma_{\rm th} = 1.5$ collapses after 10 ms, while the less compact $\Gamma_{\rm th} = 2.0$ and full-LS180 cases collapse after $\sim$20 ms. This is consistent with the picture of secular HMNS evolution drawn in §8.5.2: Given a fixed number of baryons, a less compact configuration has a lower maximum baryon density after merger and, therefore, begins its secular evolution (in the sense of Figs. 8.11 and 8.12) at a lower density than a more compact configuration. Consequently, it must lose more energy before reaching the critical density for collapse.

The above illustrates how thermal pressure effects may increase the lifetime of a HMNS by affecting the initial conditions for its secular evolution. From §8.4 one notes that hot configurations, at densities below $\lesssim 10^{15}\,{\rm g\,cm^{-3}}$ (the exact value being EOS dependent), may support significantly larger masses than their cold counterparts at the same $\rho_{b,\rm max}$. Thus, during the dynamical settle-down of two merging neutron stars to a secularly-evolving HMNS remnant, a configuration with lower thermal pressure will need to evolve to higher $\rho_{b,\rm max}$ to reach an equilibrium configuration.

[5] The LS180 is the variant of the [39] EOS with nuclear compressibility modulus $K_0 = 180\,{\rm MeV}$.

8.6 Summary and Conclusions

The merger of double neutron stars with component masses in the most commonly observed mass range ($\sim 1.3 - 1.4\,M_\odot$; [36]) is most likely to result in a hot, differentially spinning hypermassive neutron star (HMNS) remnant that is stable against collapse on a dynamical timescale, but likely secularly evolving towards instability, driven by energy loss. While a number of merger simulations in approximate or full general-relativity with the necessary microphysics are now available, the role of thermal pressure support on the postmerger HMNS and its stability is not well understood.

In this study, we have attempted to gain insight into the role of thermal pressure support by constructing nonrotating, uniformly rotating and differentially rotating axisymmetric equilibrium solutions with multiple microphysical, fully temperature and composition dependent equations of state (EOS) and parametrized temperature distributions motivated by results from full merger simulations. Such axisymmetric equilibrium models are acceptable approximations to merger remnants that have survived the initial highly dynamical and strongly nonaxisymmetric postmerger evolution and have settled down into longer-term stable quasiequilibrium.

In the secular postmerger phase, the baryonic mass $M_{\rm b}$ of the hypermassive merger remnant is conserved. Thus the dependence of the maximum of $M_{\rm b}$ on temperature is the most interesting quantity to study. In spherical symmetry (the TOV case), we find that at densities significantly lower than the density at which the maximum mass configuration occurs, thermal enhancement of the NS mass can be strong. Generally, hotter configurations yield the same $M_{\rm b}$ at lower central densities than their colder counterparts. However, when considering compact maximum-$M_{\rm b}$ configurations, thermal effects are small. For reasonable temperature prescriptions, hot temperatures lead to a small ($\lesssim 1\%$) decrease of $M_{\rm b}^{\rm max}$ for five out of the seven EOS that we consider. The two other EOS, the HShen EOS and the GShen-FSU2.1 EOS, show up to $\sim 2\%$ thermal enhancement of $M_{\rm b}$. As expected, none of the considered EOS could support a remnant of the merger of a canonical double NS system with typical masses.

Rapidly uniformly spinning configurations can support supramassive NSs. We have studied uniformly spinning sequences generated with the LS220 and HShen EOS. As in the TOV case, we find significant thermal enhancement of $M_{\rm b}$ at low central densities and rotation rates up to mass shedding. At high densities, however, thermal pressure is much less important for the support of the inner NS core, but bloats the envelope. This results in hotter configurations reaching mass shedding at lower angular velocities than colder configurations. Hence, at the mass-shedding supramassive limit, $M_{\rm b}$ and $M_{\rm g}$ decrease with increasing temperature for uniformly spinning NSs. For the LS220 EOS (HShen EOS), the cold supramassive $M_{\rm b}$ limit is $\sim 2.823\,M_\odot$ ($\sim 3.046\,M_\odot$). This corresponds to component gravitational masses in an equal-mass progenitor binary of $M_{\rm g} \sim 1.287\,M_\odot$ ($M_{\rm g} \sim 1.403\,M_\odot$). On the other hand, a supramassive LS220 (HShen) NS with a 30-MeV core and a 10-

MeV envelope has a supramassive limit $M_{\rm b} \sim 2.587\,M_\odot$ ($M_{\rm b} \sim 2.808\,M_\odot$), which corresponds to binary component $M_{\rm g} \sim 1.185\,M_\odot$ ($M_{\rm b} \sim 1.300\,M_\odot$). Hence, cold maximally uniformly rotating configurations of LS220 and HShen NSs may barely support the merger remnant of canonical double NS binaries, but hot ones might not.

Differential rotation adds yet another layer of complexity, but is the most interesting scenario, since hypermassive merger remnants are born with differential rotation. The notion of a maximum mass of a differentially rotating HMNS is somewhat misleading, since different rotation laws will give different masses and different solvers may converge to different branches in the solution space. Hence, all "maximum" masses quoted are lower limits. For the commonly used $j - const.$ rotation-law, parametrized by the dimensionless parameter $\tilde{A}$, we find $M_{\rm b}$ up to $\sim 3.65\,M_\odot$ and $\sim 4.10\,M_\odot$, for the LS220 EOS and the HShen EOS, respectively. These high-mass configurations generally occur at densities that are up to a factor of two lower than those of maximum-$M_{\rm b}$ TOV and uniformly rotating models. Even higher masses could be found, but such configurations would be dynamically nonaxisymmetrically unstable.

Our results indicate that the role of thermal effects depends very much on the degree of differential rotation in addition to maximum density and (central) angular velocity. All qualitative findings are identical for the LS220 EOS and the HShen EOS. For critically rotating models (with minimum axis ratio $r_{\rm p/e}$ for which a solution is found) the dependence on differential rotation is as follows: (i) For a low degree of differential rotation ($\tilde{A} \lesssim 0.4$), the same systematics as found for the uniformly rotating case hold. (ii) In models with intermediate degree of differential rotation ($\tilde{A} \sim 0.5 - 0.7$), hot configurations have systematically lower "maximum" $M_{\rm b}$ than colder ones. (iii) Models with high degree of differential rotation ($\tilde{A} \gtrsim 0.7$) are mostly quasitoroidal and the "maximum" $M_{\rm b}$ occurs at low densities ($\lesssim 5 \times 10^{14}\,{\rm g\,cm^{-3}}$) and is mildly enhanced by thermal pressure support for models with hot cores, but cold envelopes. Models with high-temperature envelopes remain spheroidal until higher densities and have lower "maximum" $M_{\rm b}$. The situation is yet different for differentially rotating configurations that are rotating rapidly, but subcritically. For example, for LS220 EOS configurations with $\tilde{A} = 1$, models with thermally supported envelopes have the highest $M_{\rm b}$ at subcritical rotation, but their sequences terminate at lower angular velocities (higher $r_{\rm p/e}$) than the cold configuration, which ultimately catches up in $M_{\rm b}$ at critical rotation.

To summarize all of the above: The forecast is mixed – the role of thermal effects on the baryonic mass that is supported by a given configuration depends sensitively and in a complicated way on its details, that is, central/mean baryon density, temperature distribution, degree of differential rotation and rotation rate, to name the most important parameters. Configurations that yield "maximum" $M_{\rm b}$ are essentially unaffected by thermal effects. Beyond that, no simple general statements can be made.

A more useful way to reason about the role of thermal pressure support is to consider evolutionary

sequences of equilibrium models representing the secular quasiequilibrium evolution of a HMNS. This evolution occurs along tracks of constant baryonic mass $M_{\rm b}$ parametrized by maximum baryon density $\rho_{\rm b,max}$. Since energy is lost by gravitational wave and neutrino emission, a configuration always evolves into the direction of decreasing total energy (i.e. decreasing gravitational mass $M_{\rm g}$ and increasing $\rho_{\rm b,max}$). The turning point theorem [22, 60] says that an extremum in $M_{\rm g}$ may mark the point at which the sequence becomes secularly unstable to collapse. While this can be proven rigorously only for uniformly rotating (or nonrotating) configurations, we conjecture that it also holds at least approximately for the much more complex HMNS case. Provided this is true, we can define approximate turning points using constant-$M_{\rm b}$ sequences with different degrees of differential rotation and temperature parametrizations. With this, we find that the approximate turning points for a given $M_{\rm b}$ always lie in narrow ranges of $\rho_{\rm b,max}$ and $M_{\rm g}$, which define the $M_{\rm g} - \rho_{\rm b,max}$ space in which collapse to a black hole occurs. Furthermore, the approximate turning point density at which collapse must set in depends only very weakly on temperature. Finally, we note that all approximate turning points found in this work are at baryon densities below the cricial value for stable TOV stars. This may suggest that HMNS with maximum densities at or higher than the critical TOV central density could always be unstable to collapse. This possibility should be investigated further in future work.

The secular evolution of a HMNS can then be described by the progressive decrease of its gravitational mass $M_{\rm g}$ and increase of its maximum density $\rho_{\rm b,max}$. Our results show that a HMNS with more thermal pressure support will enter its secular evolution at a higher $M_{\rm g}$ and lower $\rho_{\rm b,max}$ than a colder one (with the same rotational setup). Hence, the hot HMNS will have to evolve further in $\rho_{\rm b,max}$ until reaching its approximate turning point. This explains the effects of thermal pressure observed in merger simulations (e.g., [8, 53]). We note that the same argument may also be applied to differences in HMNS spin: a more rapidly spinning HMNS will enter its secular evolution at lower $\rho_{\rm b,max}$ and higher total energy and, hence, will have to evolve further in $\rho_{\rm b,max}$ to reach its approximate turning point.

The goal of the work presented in this paper was to elucidate the role of thermal pressure support in hypermassive NSNS merger remnants on the basis of stationary spherically symmetric and axisymmetric equilibrium solutions of the Einstein-Euler equations. While yielding new insights, our present approach is limited in multiple ways: (*i*) Even in the secular quasiequilibrium evolution phase, HMNS are not exactly axisymmetric. The CST solver used in this study does not support nonaxisymmetric configurations, which makes it impossible for us to test how sensitive our results are to symmetry assumptions. (*ii*) The equilibrium sequences considered here rely on an ad-hoc rotation law and ad-hoc temperature and composition parametrizations motivated by the simulations of [53]. In general, the angular velocity distribution will be more complex (see, e.g., [23]) and the thermal and compositional structure of a HMNS will not be a single-parameter function of density. (*iii*) The

CST solver has difficulties converging for configurations with a high degree of differential rotation and it is not clear if the terminating axis ratio $r_{\rm p/e}$ is set by the formulation and implementation of the equations by the CST solver or if the termination occurs for physical reasons. This could be checked only by a comparison study with a more robust solver, e.g., the one of [2]. (*iv*) The approximate turning point theorem that we have used to reason about the evolution and stability of HMNSs is heuristic and lacks rigorous foundation. Fully reliable statements about the stability of differentially rotating HMNSs with complex temperature and compositional distributions will require at least perturbative stability analysis or direct non-linear simulation.

Future work should address the above limitations (*i*-*iv*) and should also consider rotating configurations constructed with a broader set of finite-temperature microphysical equations of state.

Acknowledgements

We thank Eliot Quataert for inspiration and acknowledge helpful discussions with Lars Bildsten, Jim Lattimer, Lee Lindblom, Sterl Phinney, Jocelyn Read, Yuichiro Sekiguchi, Masaru Shibata, Saul Teukolsky, Kip Thorne, and especially Aaron Zimmerman. This work was initiated at a Palomar Transient Factory Theory Network meeting at the Sky House, Los Osos, CA. CDO wishes to thank the Yukawa Institute for Theoretical Physics for hospitality during the long-term workshop Gravitational Waves and Numerical Relativity 2013 when this work was completed. This research is supported in part by NASA under the Astrophysics Theory Grant no. NNX11AC37G, by the National Science Foundation under grant nos. AST-1205732, PHY-1151197, AST-1212170, PHY-1068881, by the Alfred P. Sloan Foundation, and by the Sherman Fairchild Foundation. The calculations underlying the results presented in this paper were performed on the Caltech compute cluster "Zwicky" (NSF MRI award No. PHY-0960291). The EOS tables, driver and TOV solver routines used in this work are available for download at `http://www.stellarcollapse.org`. The solver for axisymmetric equilibrium configurations of rotating HMNSs is not open source, but a similar solver may be obtained form `http://www.lorene.obspm.fr/`. The figures in this paper were generated with the `matplotlib` library for `Python` [29].

8.A Temperature Parametrizations

We consider temperature prescriptions with only a hot core at and above nuclear density and with a hot core and a more extended high-density plateau at lower densities. We emphasize that these prescriptions are rather ad-hoc and motivated primarily by the data from the simulations of [53]. All high-temperature regions are smoothly tapered-off ("rolled-off") using tanh functions.

Model	$T_{\rm max}$ [MeV]	Midpoint m $\log_{10}(\rho_{\rm b}[{\rm g\,cm^{-3}}])$	Scale s $\log_{10}(\rho_{\rm b}[{\rm g\,cm^{-3}}])$	Plateau Temperature T_p [MeV]
cold	–	–	–	–
c20p0	20	$14.0 - 0.07$	0.25	0
c30p0	30	$14.125 - 0.07$	0.375	0
c30p5	30	$14.1875 - 0.07$	0.3125	5
c30p10	30	$14.25 - 0.07$	0.25	10
c40p0	40	$14.25 - 0.07$	0.5	0

Table 8.4: Parameters used for the temperature parametrizations used in this study. The notation is c¡core temperature¿p¡plateau temperature¿. All low-density temperature plateaus are tapered off at densities below $\sim 10^{12}\,{\rm g\,cm^{-3}}$ with a tanh function with a midpoint at $\log_{10}(\rho_{\rm b}[{\rm g\,cm^{-3}}]) = 11.5$ and an e-folding width of $\log_{10}(\rho_{\rm b}[{\rm g\,cm^{-3}}]) = 0.25$. All minimum temperatures are 0.01 MeV. See Fig. 8.2 for a comparison of the various temperature prescriptions. The functional form of the prescriptions is given by (8.8) and (8.10).

The prescriptions with only a hot core (i.e. prescriptions cXp0) are given by the

$$T_{\rm roll}(\rho_{\rm b}; T_1, T_2, m, s) = T_2 + \frac{(T_1 - T_2)}{2}\left(\tanh\frac{(\log_{10}(\rho_{\rm b}) - m)}{s} + 1\right), \tag{8.8}$$

where m is the roll-off midpoint (in $\log_{10}(\rho_{\rm b}[{\rm g\,cm^{-3}}])$ and s is the roll-off e-folding scale (also in $\log_{10}(\rho_{\rm b}[{\rm g\,cm^{-3}}])$. For prescriptions that only have hot cores, T_1 is set to the peak temperature $T_{\rm max}$ and T_2 is set to $T_{\rm min} = 0.01\,{\rm MeV}$. The prescriptions with a high-temperature plateau at lower densities, i.e. c30p5 and c30p10, are constructed as the sum of two of the above functions as follows:

$$\begin{aligned} T(\rho_{\rm b}; T_{\rm max}, T_{\rm min}, T_p, m', s') &= T_{\rm min} + T_{\rm roll}(\rho_{\rm b}; T_1 = T_p, T_2 = 0, m = 11.5, s = 0.25) \\ &\quad + T_{\rm roll}(\rho_{\rm b}; T_1 = T_{\rm max} - T_p, T_2 = 0, m', s'), \end{aligned} \tag{8.9}$$

where m' is the roll-off midpoint, s' is the roll-off scale, and T_p is the plateau temperature. Writing this out more explicitly, we have:

$$\begin{aligned} T(\rho_{\rm b}; T_{\rm max}, T_{\rm min}, T_p, m, s) &= T_{\rm min} + \frac{T_p}{2}\left(\tanh\frac{(\log_{10}(\rho_{\rm b}) - 11.5)}{0.25} + 1\right) \\ &\quad + \frac{T_{\rm max} - T_p}{2}\left(\tanh\frac{(\log 10(\rho_{\rm b}) - m)}{s} + 1\right). \end{aligned} \tag{8.10}$$

Table 8.4 summarizes the parameters for generating the temperature prescriptions used in this study.

8.B Solving for the Electron Fraction

For a given EOS and temperature prescription, we find the electron fraction Y_e by first solving for Y_e assuming neutrino-less β-equilibrium for the cold case ($T = 0.01\,\mathrm{MeV}$ or the lowest temperature point available in the EOS table), using the condition

$$\mu_\nu = 0 = \mu_n + \mu_p - \mu_e \ , \tag{8.11}$$

for the chemical potentials. In the absence of neutrinos, the lepton fraction $Y_{\rm lep} = Y_e$. In the hot case, neutrinos are trapped in the HMNS matter above $\rho = \rho_{\rm trap} \approx 10^{12.5}\,\mathrm{g\,cm^{-3}}$ and $Y_{\rm lep} = Y_e + Y_\nu$, where $Y_\nu = Y_{\nu_e} - Y_{\bar{\nu}_e}$.

We then take $Y_{\rm lep}$ and solve for Y_e in the hot case with neutrinos by treating the latter as a relativistic Fermi gas in equilibrium for which Y_ν can be calculated from the neutrino number density $n_\nu = n_{\nu_e} - n_{\bar{\nu}_e}$ via

$$Y_\nu = \frac{n_\nu}{\rho N_A} \ . \tag{8.12}$$

The neutrino number density is

$$n_\nu = 4\pi \left(\frac{k_B T}{hc}\right)^3 \left[F_2(\eta_\nu) - F_2(-\eta_\nu)\right] \ , \tag{8.13}$$

where $\eta_\nu = \mu_\nu/(k_B T)$ is the neutrino degeneracy parameter [9]. Note that in equilibrium, ν_e and $\bar{\nu}_e$ have equal and opposite chemical potentials. F_2 is a Fermi integral given by

$$F_k(\eta) = \int_0^\infty \frac{x^k dx}{e^{x-\eta} + 1} \ . \tag{8.14}$$

In practice, we use

$$F_2(\eta) - F_2(-\eta) = \frac{1}{3}\eta(\eta^2 + \pi^2) \ , \tag{8.15}$$

which is given in [9] and is exact for any degeneracy parameter η.

We find Y_e by finding the root

$$0 = Y_{\rm lep} - (Y_e + Y_\nu) \ . \tag{8.16}$$

$Y_{\rm lep}$ is a fixed input. We set $Y_e = Y_{\rm lep}$ as an initial guess and Y_ν is calculated using Eqs. (8.12), (8.13), and (8.15), with $\mu_\nu = \mu_n + \mu_p - \mu_e$ obtained from the EOS. Y_e is then adjusted and we iterate until convergence.

Since neutrinos begin to stream freely below $\rho_{\rm trap}$, we also compute Y_e using the ν-less β-

equilibrium condition (Eq. 8.11). We then compute a final effective Y_e using

$$Y_{e,\mathrm{eff}}(\rho, T[\rho]) = Y_{e,\nu-\mathrm{less}\,\beta}(\rho, T[\rho]) \times (1 - e^{-\rho_{\mathrm{trap}}/\rho}) + Y_{e,\beta}(\rho, T[\rho]) \times e^{-\rho_{\mathrm{trap}}/\rho} \,. \tag{8.17}$$

Bibliography

[1] T. Accadia et al. (Virgo Collaboration). Status of the Virgo project. *Class. Quantum Grav.*, 28(11):114002, June 2011.

[2] M. Ansorg, A. Kleinwächter, and R. Meinel. Highly accurate calculation of rotating neutron stars. Detailed description of the numerical methods. *Astron. & Astrophys.*, 405:711–721, July 2003.

[3] J. Antoniadis, P. C. C. Freire, N. Wex, T. M. Tauris, R. S. Lynch, M. H. van Kerkwijk, M. Kramer, C. Bassa, V. S. Dhillon, T. Driebe, J. W. T. Hessels, V. M. Kaspi, V. I. Kondratiev, N. Langer, T. R. Marsh, M. A. McLaughlin, T. T. Pennucci, S. M. Ransom, I. H. Stairs, J. van Leeuwen, J. P. W. Verbiest, and D. G. Whelan. A Massive Pulsar in a Compact Relativistic Binary. *Science*, 340:448, April 2013.

[4] L. Baiotti, B. Giacomazzo, and L. Rezzolla. Accurate evolutions of inspiralling neutron-star binaries: Prompt and delayed collapse to a black hole. *Phys. Rev. D*, 78:084033, October 2008.

[5] L. Baiotti, R. D. Pietri, G. M. Manca, and L. Rezzolla. Accurate simulations of the dynamical bar-mode instability in full general relativity. *Phys. Rev. D*, 75:044023, February 2007.

[6] T. W. Baumgarte, S. L. Shapiro, and M. Shibata. On the Maximum Mass of Differentially Rotating Neutron Stars. *Astrophys. J. Letters*, 528:L29, January 2000.

[7] A. Bauswein, H.-T. Janka, K. Hebeler, and A. Schwenk. Equation-of-state dependence of the gravitational-wave signal from the ring-down phase of neutron-star mergers. *Phys. Rev. D*, 86(6):063001, September 2012.

[8] A. Bauswein, H.-T. Janka, and R. Oechslin. Testing approximations of thermal effects in neutron star merger simulations. *Phys. Rev. D*, 82(8):084043, October 2010.

[9] S. A. Bludman and K. A. van Riper. Diffusion approximation to neutrino transport in dense matter. *Astrophys. J.*, 224:631, September 1978.

[10] S. Chandrasekhar. *Ellipsoidal Figures of Equilibrium.* Yale University Press, New Haven, USA, 1969. revised edition 1987.

[11] Gregory B. Cook, Stuart L. Shapiro, and Saul A. Teukolsky. Spin-up of a rapidly rotating star by angular momentum loss: Effects of general relativity. *Astrophys. J.*, 398:203, 1992.

[12] Gregory B. Cook, Stuart L. Shapiro, and Saul A. Teukolsky. Rapidly rotating polytropes in general relativity. *Astrophys. J.*, 422:227, 1994.

[13] Gregory B. Cook, Stuart L. Shapiro, and Saul A. Teukolsky. Recycling pulsars to millisecond periods in general relativity. *Astrophys. J. Letters*, 423:117, 1994.

[14] G. Corvino, L. Rezzolla, S. Bernuzzi, R. De Pietri, and B. Giacomazzo. On the shear instability in relativistic neutron stars. *Class. Quantum Grav.*, 27(11):114104, June 2010.

[15] P. B. Demorest, T. Pennucci, S. M. Ransom, M. S. E. Roberts, and J. W. T. Hessels. A two-solar-mass neutron star measured using Shapiro delay. *Nature*, 467:1081, October 2010.

[16] L. Dessart, C. D. Ott, A. Burrows, S. Rosswog, and E. Livne. Neutrino Signatures and the Neutrino-Driven Wind in Binary Neutron Star Mergers. *Astrophys. J.*, 690:1681, January 2009.

[17] J. A. Faber and F. A. Rasio. Binary Neutron Star Mergers. *Liv. Rev. Rel.*, 15:8, July 2012.

[18] B. Friedman and V. R. Pandharipande. Hot and cold, nuclear and neutron matter. *Nuc. Phys. A*, 361:502, May 1981.

[19] J. L. Friedman and J. R. Ipser. On the maximum mass of a uniformly rotating neutron star. *Astrophys. J.*, 314:594–597, March 1987.

[20] J. L. Friedman, J. R. Ipser, and R. D. Sorkin. Turning-point method for axisymmetric stability of rotating relativistic stars. *Astrophys. J.*, 325:722–724, February 1988.

[21] J. L. Friedman, L. Parker, and J. R. Ipser. Rapidly rotating neutron star models. *Astrophys. J.*, 304:115, May 1986.

[22] J. L. Friedman and N. Stergioulas. *Rotating Relativistic Stars*. March 2013.

[23] F. Galeazzi, S. Yoshida, and Y. Eriguchi. Differentially-rotating neutron star models with a parametrized rotation profile. *Astron. & Astrophys.*, 541:A156, May 2012.

[24] J. O. Goussard, P. Haensel, and J. L. Zdunik. Rapid uniform rotation of protoneutron stars. *Astron. & Astrophys.*, 321:822–834, May 1997.

[25] J.-O. Goussard, P. Haensel, and J. L. Zdunik. Rapid differential rotation of protoneutron stars and constraints on radio pulsars periods. *Astron. & Astrophys.*, 330:1005–1016, February 1998.

[26] G. M. Harry (for the LIGO Scientific Collaboration). Advanced LIGO: the next generation of gravitational wave detectors. *Class. Quantum Grav.*, 27(8):084006, April 2010.

[27] M. Hempel, T. Fischer, J. Schaffner-Bielich, and M. Liebendörfer. New Equations of State in Simulations of Core-collapse Supernovae. *Astrophys. J.*, 748:70, March 2012.

[28] M. Hempel and J. Schaffner-Bielich. A statistical model for a complete supernova equation of state. *Nuc. Phys. A*, 837:210, June 2010.

[29] J. D. Hunter. Matplotlib: A 2d graphics environment. *Computing In Science & Engineering*, 9(3):90–95, 2007.

[30] J. Kaplan. *Topics in Numerical Relativity.* PhD thesis, California Institute of Technology, Pasadena, CA, USA, 2013.

[31] K. Kiuchi, Y. Sekiguchi, M. Shibata, and K. Taniguchi. Long-term general relativistic simulation of binary neutron stars collapsing to a black hole. *Phys. Rev. D*, 80(6):064037, September 2009.

[32] C. S. Kochanek. Coalescing binary neutron stars. *Astrophys. J.*, 398:234, October 1992.

[33] H. Komatsu, Y. Eriguchi, and I. Hachisu. Rapidly rotating general relativistic stars. I - Numerical method and its application to uniformly rotating polytropes. *MNRAS*, 237:355, March 1989.

[34] H. Komatsu, Y. Eriguchi, and I. Hachisu. Rapidly rotating general relativistic stars. II - Differentially rotating polytropes. *MNRAS*, 239:153, July 1989.

[35] D. Lai. Resonant Oscillations and Tidal Heating in Coalescing Binary Neutron Stars. *MNRAS*, 270:611, October 1994.

[36] J. M. Lattimer. The Nuclear Equation of State and Neutron Star Masses. *Ann. Rev. Nuc. Part. Sc.*, 62:485, November 2012.

[37] J. M. Lattimer and M. Prakash. Neutron Star Structure and the Equation of State. *Astrophys. J.*, 550:426, March 2001.

[38] J. M. Lattimer and M. Prakash. Neutron star observations: Prognosis for equation of state constraints. *Phys. Reports*, 442:109, April 2007.

[39] J. M. Lattimer and F. D. Swesty. A Generalized Equation of State for Hot, Dense Matter. *Nucl. Phys. A*, 535:331, 1991.

[40] M. Liebendörfer. A Simple Parameterization of the Consequences of Deleptonization for Simulations of Stellar Core Collapse. *Astrophys. J.*, 633:1042, November 2005.

[41] I. A. Morrison, T. W. Baumgarte, and S. L. Shapiro. Effect of Differential Rotation on the Maximum Mass of Neutron Stars: Realistic Nuclear Equations of State. *Astrophys. J.*, 610:941, August 2004.

[42] E. Nakar. Short-hard gamma-ray bursts. *Phys. Reports*, 442:166, April 2007.

[43] E. O'Connor and C. D. Ott. Black Hole Formation in Failing Core-Collapse Supernovae. *Astrophys. J.*, 730:70, April 2011.

[44] R. Oechslin, H.-T. Janka, and A. Marek. Relativistic neutron star merger simulations with non-zero temperature equations of state. I. Variation of binary parameters and equation of state. *Astron. & Astrophys.*, 467:395, May 2007.

[45] J. P. Ostriker, P. Bodenheimer, and D. Lynden-Bell. Equilibrium Models of Differentially Rotating Zero-Temperature Stars. *Phys. Rev. Lett.*, 17:816, October 1966.

[46] C. D. Ott, H. Dimmelmeier, A. Marek, H.-T. Janka, I. Hawke, B. Zink, and E. Schnetter. 3D Collapse of Rotating Stellar Iron Cores in General Relativity Including Deleptonization and a Nuclear Equation of State. *Phys. Rev. Lett.*, 98:261101, June 2007.

[47] V. Paschalidis, Z. B. Etienne, and S. L. Shapiro. Importance of cooling in triggering the collapse of hypermassive neutron stars. *Phys. Rev. D*, 74:064032, 2012.

[48] A. J. Penner, N. Andersson, D. I. Jones, L. Samuelsson, and I. Hawke. Crustal Failure during Binary Inspiral. *Astrophys. J. Letters*, 749:L36, April 2012.

[49] M. Prakash, J. M. Lattimer, J. A. Pons, A. W. Steiner, and S. Reddy. Evolution of a Neutron Star from Its Birth to Old Age. In D. Blaschke, N. K. Glendenning, & A. Sedrakian, editor, *Physics of Neutron Star Interiors*, volume 578 of *Lecture Notes in Physics, Berlin Springer Verlag*, page 364, 2001.

[50] J. S. Read, B. D. Lackey, B. J. Owen, and J. L. Friedman. Constraints on a phenomenologically parametrized neutron-star equation of state. *Phys. Rev. D*, 79:124032, June 2009.

[51] S. Rosswog and M. Liebendörfer. High-resolution calculations of merging neutron stars—II. Neutrino emission. *MNRAS*, 342:673, July 2003.

[52] M. Ruffert and H.-T. Janka. Coalescing neutron stars - A step towards physical models. III. Improved numerics and different neutron star masses and spins. *Astron. & Astrophys.*, 380:544, December 2001.

[53] Y. Sekiguchi, K. Kiuchi, K. Kyutoku, and M. Shibata. Gravitational Waves and Neutrino Emission from the Merger of Binary Neutron Stars. *Phys. Rev. Lett.*, 107(5):051102, July 2011.

[54] L. S. Shapiro and S. A. Teukolsky. *Black Holes, White Dwarfs and Neutron Stars.* John Wiley & Sons, New York U. S. A., 1983.

[55] G. Shen, C. J. Horowitz, and E. O'Connor. Second relativistic mean field and virial equation of state for astrophysical simulations. *Phys. Rev. C*, 83:065808, June 2011.

[56] G. Shen, C. J. Horowitz, and S. Teige. New equation of state for astrophysical simulations. *Phys. Rev. C*, 83:035802, March 2011.

[57] H. Shen, H. Toki, K. Oyamatsu, and K. Sumiyoshi. Relativistic Equation of State for Core-collapse Supernova Simulations. *Astrophys. J.*, 197:20, December 2011.

[58] Masaru Shibata, Keisuke Taniguchi, and Koji Uryu. Merger of binary neutron stars with realistic equations of state in full general relativity. *Phys. Rev. D*, 71:084021, 2005.

[59] K. Somiya (for the KAGRA collaboration). Detector configuration of KAGRA-the Japanese cryogenic gravitational-wave detector. *Class. Quantum Grav.*, 29(12):124007, June 2012.

[60] R. D. Sorkin. A Stability Criterion for Many Parameter Equilibrium Families. *Astrophys. J.*, 257:847, June 1982.

[61] A. W. Steiner, J. M. Lattimer, and E. F. Brown. The Neutron Star Mass-Radius Relation and the Equation of State of Dense Matter. *Astrophys. J. Letters*, 765:L5, March 2013.

[62] N. Stergioulas and J. L. Friedman. Comparing models of rapidly rotating relativistic stars constructed by two numerical methods. *Astrophys. J.*, 444:306–311, May 1995.

[63] K. Takami, L. Rezzolla, and S. Yoshida. A quasi-radial stability criterion for rotating relativistic stars. *MNRAS*, 416:L1–L5, September 2011.

[64] J.-L. Tassoul. *Theory of Rotating Stars*. Princeton University Press, Princeton U. S. A., 1978.

[65] M. Thierfelder, S. Bernuzzi, and B. Brügmann. Numerical relativity simulations of binary neutron stars. *Phys. Rev. D*, 84(4):044012, 2011.

[66] T. A. Thompson, E. Quataert, and A. Burrows. Viscosity and Rotation in Core-Collapse Supernovae. *Astrophys. J.*, 620:861, February 2005.

[67] F. X. Timmes and D. Arnett. The Accuracy, Consistency, and Speed of Five Equations of State for Stellar Hydrodynamics. *Astrophys. J.*, 125:277, November 1999.

[68] D. Tsang, J. S. Read, T. Hinderer, A. L. Piro, and R. Bondarescu. Resonant Shattering of Neutron Star Crusts. *Phys. Rev. Lett.*, 108(1):011102, January 2012.

[69] K. A. van Riper and S. A. Bludman. Composition and equation of state of thermally dissociated matter. *Astrophys. J.*, 213:239, April 1977.

[70] A. L. Watts, N. Andersson, and D. I. Jones. The Nature of Low $T/|W|$ Dynamical Instabilities in Differentially Rotating Stars. *Astrophys. J. Letters*, 618:L37, January 2005.

[71] N. N. Weinberg, P. Arras, and J. Burkart. An Instability due to the Nonlinear Coupling of p-modes to g-modes: Implications for Coalescing Neutron Star Binaries. *Astrophys. J.*, 769:121, June 2013.

Chapter 9

Supplements to The Influence of Thermal Pressure on Hypermassive Neutron Star Merger Remnants

---

First publication. Jeffrey D. Kaplan (2013).

9.1 Expanded discussion on the stability of HMNS equilibrium sequences

The existence of a maximum mass for equilibrium sequences of stationary neutron stars is one of the most important astrophysical consequences of general relativity and, hence, is well known in the study of compact objects. However we find that the intuition gleaned through studying the stability of spherically symmetric neutron stars can be misleading when studying the vastly larger and more general parameter space of hot, differentially rotating HMNS models. Thus, we review here the classic results on the stability of stationary neutron stars and formulate how we may reason about the stability of our HMNS equilibrium models.

9.1.1 Review on established applications of the turning-point method to neutron star stability

Cold, non-rotating TOV models form a one-dimensional sequence of equilibrium models parametrized by the model's central baryon density (which is the same as the maximum baryon density $\rho_{\mathrm{b,max}}$ in NSs without differential rotation); it is well known that neutron stars correspond to stable models

of this sequence with densities on the order of 10^{14}-10^{15} g cm^{-3} (e.g., see [5]). It can be shown via the *turning-point* method, that the extrema in $M_{\rm g}$ along this one-dimensional sequence are sufficient indicators of a change in the stability of equilibrium models; it is this result which proves that, for a given EOS, the neutron star with the maximum mass is marginally unstable and any equilibrium models at higher central densities are unstable.

When expanding configuration space of equilibrium models to two dimensions by including cold uniformly-rotating neutron stars, it is tempting to locate the equilibrium model with the global maximum in $M_{\rm g}$ and declare it the maximum stable mass for cold uniformly rotating neutron stars. However, it is possible for the equilibrium model with the maximum $M_{\rm g}$ to be secularly unstable (e.g., see Fig 10. of [9]). While practically the difference in $M_{\rm g}$ (and $\rho_{\rm b,max}$) between the global maximum in $M_{\rm g}$ for all equilibrium models and the maximum $M_{\rm g}$ ($\rho_{\rm b,max}$) for the subset of stable models is $\sim 0.1\%$ ($\sim 1\%$), the two models no longer precisely coincide. To diagnose secular instability in this two-dimensional configuration space, one must use the turning point theorem as written by [2] (or the corollary in CST; see also Sec. 9.2 of [3]) that identifies *specific one-dimensional sequences* (here, sequences of constant total angular momentum J) sliced from the two-dimensional configuration space along which an extremum of $M_{\rm g}$ implies a change in stability of the equilibrium models. In the case above, the equilibrium model with the global extremum in mass lies along the mass-shedding sequence. We coin the term "approximate turning point" to denote such extrema, that is, extrema along sequences which formally do not prove the onset of instability but are expected to be close to the actual onset of instability in the parameter space.

Since we wish to understand which areas of the parameter space of HMNS models we study exhibit the onset of instability, we must examine the intuition which underlies the turning-point method in greater detail. Equilibrium models in general relativity are solutions of the Einstein-Euler system, which are an extrema of the gravitational mass, $M_{\rm g}$ at fixed total baryon mass $M_{\rm b}$, total angular momentum J, and total entropy S ([3]). A specific equilibrium configuration is stable if the extremum in $M_{\rm g}$ is a local minimum with respect to linear dynamical perturbations (i.e., with respect to variations of the action which conserve $M_{\rm b}$, J, and S). Consider that we now have some sequence of equilibrium models parametrized by an arbitrary parameter λ.[1] Usually, for different values of λ, the equilibria must represent distinct stellar configurations since the values of $M_{\rm b}$, J and S will vary with λ. However, if one can demonstrate that there exist two equilibrium models with the same $M_{\rm b}$, J and S, *but different* $M_{\rm g}$, separated by an infinitesimal separation $d\lambda$, then the model with the greater $M_{\rm g}$ cannot be at a local minimum (since the other model in its neighborhood has a lower $M_{\rm g}$); thus the model with the greater $M_{\rm g}$ must be secularly unstable. Such a demonstration is how the turning-point method identifies the onset of instability along a sequence of equilibrium

[1] Here we assume the functions $M_{\rm b}$, J, S, and $M_{\rm g}$ of the equilibrium models are sufficiently smooth so that we may take first and second derivatives of the functions with respect to the parameter λ.

models ([3, 8]).

The turning-point method requires a 'thermodynamic like' relationship on the configuration space of equilibrium models relating the change in mass-energy for an infinitesimal change to the dynamically conserved quantities, i.e., a relationship of the form,

$$\delta M_{\rm b} = \beta_\alpha \delta E^\alpha, \tag{9.1}$$

where α is an index running over the conserved quantities of the model, E^α represent the 'conserved quantities' and the β^α are sometimes called the 'conjugate functions' to the conserved quantities. A general relation which is nearly in this form is provided by The 'First Law of Thermodynamics for Relativistic Stars' (see [1, 3]), which relates the infinitesimal change in gravitational mass $\delta M_{\rm g}$, to the change in conserved quantities of a rotating relativistic equilibrium model by,

$$\delta M_{\rm g} = \int \frac{g}{u^t} \delta dM_{\rm b} + \int \frac{T}{u^t} \delta dS + \int \Omega \delta dJ, \tag{9.2}$$

where the notation $\int \delta dM_{\rm b}$ means the integral over the star of changes to $M_{\rm b}$ in each infinitesimal element $dM_{\rm b}$, and where g is the specific Gibbs energy per unit baryon mass, u^t is the t component of the fluid's 4-velocity, S is entropy, T is the temperature, Ω is the angular velocity and J is angular momentum.[2] However, if the integrands (i.e. the conjugate functions) in the first law are constant over the star, then we may write it as,

$$\delta M_{\rm g} = \frac{g}{u^t} \delta M_{\rm b} + \frac{T}{u^t} \delta S + \Omega \delta J, \tag{9.3}$$

where $\delta M_{\rm b}$, δS and δJ are defined as the change in the total value of the conserved quantities for the star:

$$\delta M_{\rm b} = \int \delta dM_{\rm b}, \quad \delta J = \int \delta dJ, \quad \delta S = \int \delta dS. \tag{9.4}$$

Note, our Eq. 9.3 is the same as Eq. (8) of [4]. Although it limits one to equilibrium models where the conjugate functions are constant over the star, Eq.9.3 is a relation of the kind required to use the turning-point method.

Since the core of the turning-point method works by identifying infinitesimally separated equilibrium models of the same $M_{\rm b}$, J, S, the theorem can only be applied to a point on a sequence where the derivatives (with respect to the sequence parameter) of the conserved quantities, $dM_{\rm b}/d\lambda$, $dJ/d\lambda$, $dS/d\lambda$, vanish. Thus it is often employed in multidimensional configuration spaces by examining sequences of models where all but one of the dynamically conserved quantities ($M_{\rm b}$, J, S) are fixed ([2], CST). Then, the first law in the form of Eq. 9.3 yields the vanishing of the final conserved quantity at an extremum of the gravitational mass along the sequence, and this point

[2] In this section, we use geometric units which set $G = c = 1$.

on the sequence is a turning point. This is how the turning-point method is employed to show the classic criterion that the one dimensional sequence of cold TOV equilibrium models transitions from stable to unstable at a maximum in $M_{\rm g}$. Note that it is the limited dimensionality of the sequence (the vanishing of J and S) that leads to the coincidence between the model with maximum mass and the transition to instability of the sequence.

9.1.2 Applying the turning-point method in more general cases

In "The influence of thermal pressure on hypermassive neutron star merger remnants" (Chapter 8), we invoke the turning-point method to reason about the stability of our equilibrium sequences. There we make two important approximations which prevent us from using the turning-point theorem for a formal proof of instability for the sequences in Fig. 8.11.[3]

The first approximation made is where we note that our "characterization of the space of equilibrium models relies on the assumption that the change in $M_{\rm g}$ depends to first order only on the *total* changes in baryonic mass $M_{\rm b}$, angular momentum J, and entropy S, and not on changes to their higher moments." The mathematical embodiment of this statement is that we expect that Eq. 9.2 to be well approximated by Eq. 9.3. In general, this would be an extremely restrictive requirement. Let us examine what is happening using the third term of Eq. 9.2 as a representative example. Here we are replacing the infinite degrees of freedom in the integral, represented by the *distribution of changes* to each angular momentum element δdJ, by a single degree of freedom, the *total change* in angular momentum δJ. Note that each infinitesimal change δdJ that has a contribution to the change in total energy ($\delta M_{\rm g}$) is weighted by the conjugate quantity Ω. When this 'weight' is constant over the star, the infinite degrees of freedom represented by the distribution of changes to each angular momentum element ($\delta M_{\rm g}$) collapses to a single degree of freedom represented by the total change in angular momentum (δJ).

The full, relativistic version of the rotation law we use is,

$$\frac{r_e^2}{\tilde{A}^2}\left(\Omega_c - \Omega\right) = F(\Omega) = u^t u_\phi, \tag{9.5}$$

where $\tilde{A}$ is our differential rotation parameter, r_e is the equatorial radius of the star, and u^t and u_ϕ are the contravariant time component of the 4-velocity and u_ϕ is the covariant azimuthal component of the 4-velocity (cf. [3]). Solving for Ω, substituting the resulting expression into $\int \Omega \delta dJ$, and integrating the term with Ω_c (which is a constant), we obtain,

$$\int \Omega \delta dJ = \Omega_c \delta J - \frac{\tilde{A}^2}{r_e^2}\int u^t u_\phi \delta dJ. \tag{9.6}$$

[3] with the exception of the $\tilde{A} = 0$ (uniformly rotating) sequence for the 'cold' temperature parametrization; in this case the minima of $M_{\rm g}$ in the sequence, in fact, *does satisfy* all of the criteria necessary to be identified as a turning point.

In Eq. 9.6, note the second term on the RHS of the equation vanishes for $\tilde{A} = 0$. This term almost achieves what we intend when we say "the higher moments" of $\int \Omega \delta dJ$; unfortunately, aside from the factor of $\tilde{A}$, the above example, the integral on the RHS is on the same order of magnitude as the first term on the RHS of the equation. This can be observed by rewriting it as,

$$\frac{\tilde{A}^2}{r_e^2} \int u^t u_\phi \delta dJ = \tilde{A}^2 \int \frac{w^2}{\alpha^2} \hat{\varpi}^2 (\Omega - \omega) \delta dJ. \tag{9.7}$$

Here, $\hat{\varpi} = \varpi / r_e$ is the dimensionless cylindrical radius, w is the relativistic Lorentz factor of the fluid, α is the ADM lapse, and ω is the metric frame dragging potential (again, cf. [3]). Though the above expression only shows the obvious, that the term is only of "higher order" for $\tilde{A}$ small, the author notes this is because we are expanding about one of the *extrema* of the angular velocity, that is, the value at the center which is the maximum value of the angular velocity.

One attempt at correcting this would be to expand around the *average* value of Ω weighted by the perturbation to dJ:

$$\bar{\Omega} = \frac{\int \Omega \delta dJ}{\int \delta dJ} = \frac{\int \Omega \delta dJ}{\delta J}. \tag{9.8}$$

Unfortunately, this is a *bad* idea for applications to the turning-point method, since the turning-point method requires locating where $\delta J = 0$! In fact, this suggests that attempting to expand the integrals in the first law, Eq. 9.2, in a series of moments may be the wrong approach, or at least the expansion must be done with careful consideration for its application to the turning-point method.

Although we have failed to write a formal proof "that the change in $M_{\rm g}$ depends to first order only on the *total* changes in baryonic mass $M_{\rm b}$, angular momentum J, and entropy S, and not on changes to their higher moments," we would like to convince the reader that the use of an approximate turning point theorem is still appropriate for this application. In Sec. 8.5.1, we note that a turning point occurs when 3 out of 4 of the derivatives of ($M_{\rm g}$, $M_{\rm b}$, J, S) vanish along a sequence. This is formally only the case when Eq. 9.3 holds. However we note that by limiting our angular momentum distribution to a *fixed* differential rotation law, we are essentially *leaving fixed* the number of degrees of freedom in the configuration space (i.e. our 4-dimensional set of ($M_{\rm g}$, $M_{\rm b}$, J, S)). This is because any change to the angular momentum distribution δdJ must be *completely specified* by the rotation law. In practice, there will be an additional contribution to the energy, which in our example of the rotational energy amounts to the second term in the RHS of Eq. 9.6, which we deem $T_{\rm HO}$ with HO for 'higher order.' Now, a turning point will be where 4 of the 5 of the derivatives along the sequence of ($M_{\rm g}$, $M_{\rm b}$, J, S, $T_{\rm HO}$) vanish. While this effectively makes the use of approximate turning points "more approximate", we note that it still adheres to the method underlying the turning point theorem; that is, we are locating the area of parameter space for which the energy and conserved quantities are an extremum. Thus in this area, we must be in the vicinity of models with the same conserved quantities, ($M_{\rm g}$, $M_{\rm b}$,J, S, $T_{\rm HO}$), but different energies, and thus

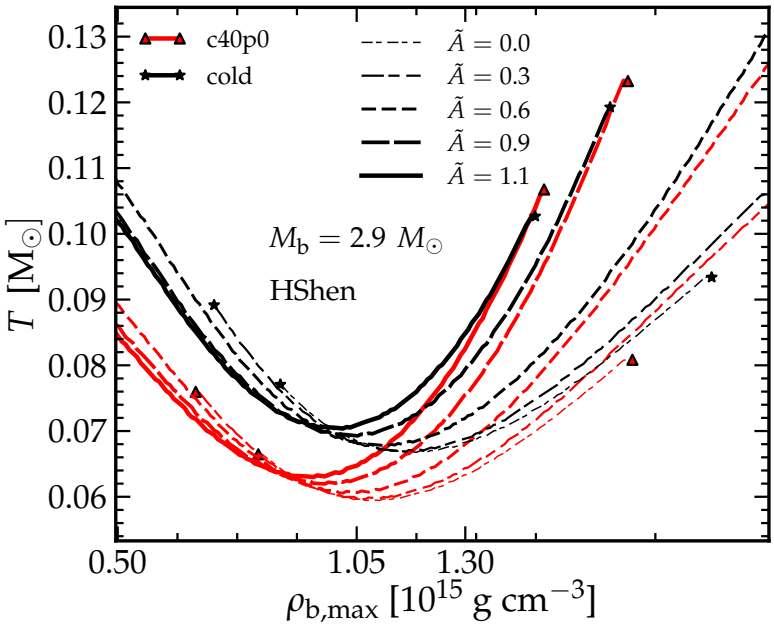

Figure 9.1: Same as Fig. 8.11, except showing approximate turning points where $d/d\rho_{b,max}$ of (M_b, T) vanishes.

'close' in parameter space to the unstable models. We provide numerical evidence for this claim by plotting the total rotational kinetic energy, T, versus $\rho_{b,max}$ in Fig. 9.1. Here we see that the approximate turning points for T & M_b also lie in the same small range of central densities close to those as in Fig. 8.11.

Finally, the reader may object that a physical HMNS need not obey a specific rotation law or maintain the same amount of differential rotation. We argree, this is true, however it is also true that the distribution of angular momentum in the HMNS may not change arbitrarily; it will change according to laws specified by the physical processes driving the secular evolution of the HMNS remnant. This will similarly restrict the degrees of freedom of the equilibrium sequences along which the HMNS will evolve. While this makes the astrophysical configuration space larger than the 4-dimensional configuration space we study, it is still highly restricted in its dimensionality. Our thorough analysis of approximate turning points should build confidence that we have 'honed in' on region of parameter space in which HMNSs become unstable to gravitational collapse.

9.1.3 Approximate turning points for alternate tuples of conserved quantities

Here we briefly address the second approximation made, that of using 'approximate' turning points where only 2 (instead of 3 for a proper turning point) out of the 4 quantities (M_g, M_b, J, S) vanish along a sequence. In Fig. 8.11, we show where the derivatives of M_g & M_b vanish; the choice of M_g,

and $M_{\rm b}$ is particularly suited for discussing the secular stability of models. However we have also checked (cf. Fig. 9.2) that the range of densities is nearly identical for approximate turning points using both tuples of ($M_{\rm g}$, J) and ($M_{\rm b}$, J).

In Fig. 9.2, we see that the $\rho_{\rm b,max}$ of these approximate turning points are very close (within a few percent) of the turning points in the ($M_{\rm g}$, $M_{\rm b}$) slice of parameter space. This shows that for $\rho_{\rm b,max}$ values where the turning points occur, they are *very nearly* locations along the sequence where the derivatives of $M_{\rm g}$, $M_{\rm b}$ *and* J vanish. This directly verifies our assertion that these approximate turning points are very good approximations to the true turning points of the sequence.

9.2 Properties of quasitoroidal models

Here we use the Newtonian approximation in spherical symmetry with a centrifugal force term to show three properties of quasitoroidal equilibrium models. They are all concerned with the location of the off-center density maxima, the presence of which is the technical requirement for classifying the model as quasitoroidal.

9.2.1 Criterion which implies a model must be quasitoroidal

First, note that the mass shed limit provides the following restriction on the equatorial angular velocity at the star's surface, Ω_e:

$$\Omega_e^2 \leq \frac{GM}{R^3} = \frac{4\pi}{3} G\bar{\rho}. \tag{9.9}$$

Now we write the equation of force balance (the Euler equation) in the following form,

$$\frac{1}{r\rho}\frac{dP}{dr} = -\frac{Gm(r)}{r^3} + \Omega^2, \tag{9.10}$$

and examine the limit of this equation as $r \to 0$. Here, $\Omega = \Omega_c$, the central angular velocity, and $m(r)$ is very well approximated by $m(r) = 4\pi/3\,\rho_c r^3$, where ρ_c is the central density. In this limit, Eq 9.10 becomes:

$$\left(\frac{1}{r\rho_c}\frac{dP}{dr}\right)_{r\to 0} = -\frac{4\pi}{3} G\rho_c + \Omega_c^2. \tag{9.11}$$

Note that since r and ρ_c are always positive, the sign of dP/dr is determined by the sign of the RHS of this equation. Usually one expects this dP/dr to be negative in a stellar model, however, if

$$\Omega_c^2 > \frac{4\pi}{3} G\rho_c, \tag{9.12}$$

then the sign of dP/dr at the star's center is positive. Given any reasonable EOS (i.e. $dP/d\rho$ is always positive) this means the density is initially *increasing* as one moves out towards the star's equator. This implies that the stellar model has its density maximum off-center and must be a

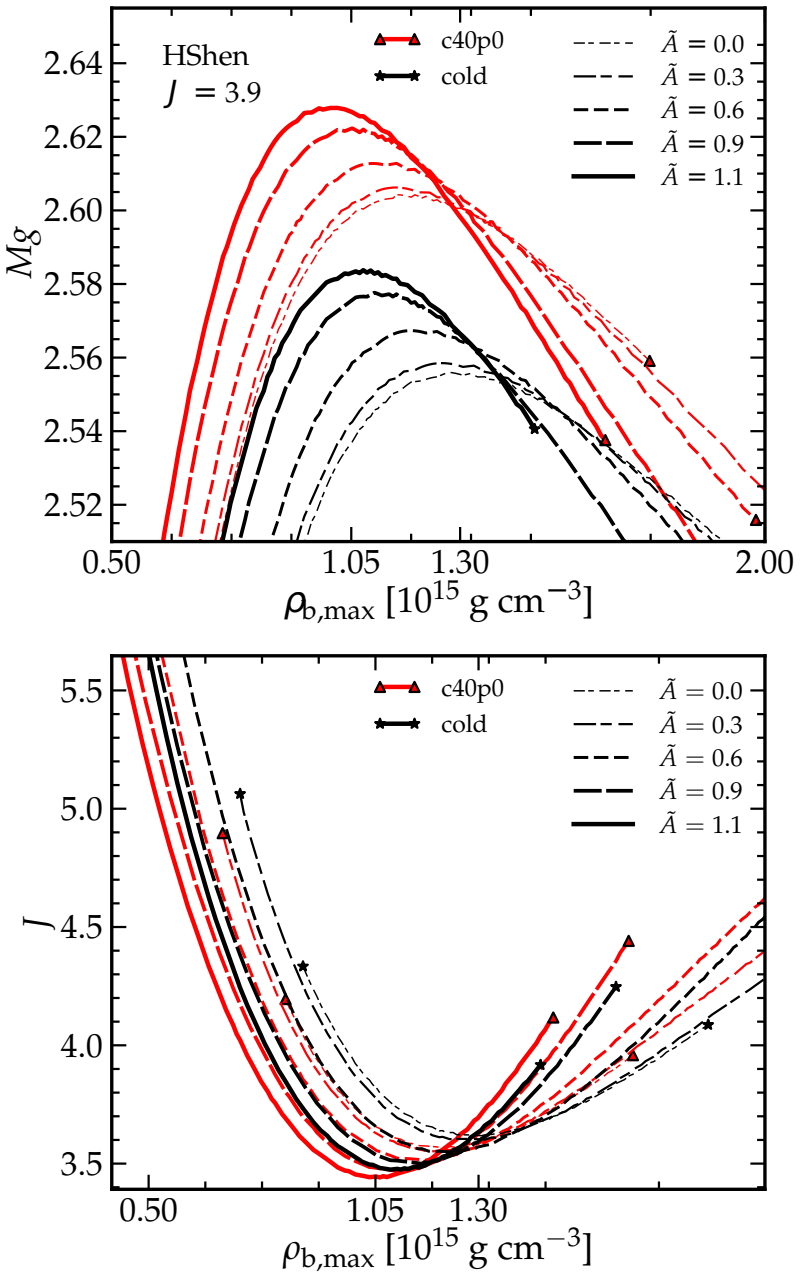

Figure 9.2: Same as Fig. 8.11, except showing approximate turning points where $d/d\rho_{\rm b,max}$ of ($M_{\rm g}$, J) vanishes (**top panel**), and where $d/d\rho_{\rm b,max}$ of ($M_{\rm b}$, J) vanishes (**bottom panel**). The **top panel** plots $M_{\rm g}$ for a fixed value of the dimensionless angular momentum $J = 3.9$, which we see is representative of the $M_{\rm b} = 2.9 M_\odot$ sequence by examining the **bottom panel**, where we plot the dimensionless angular momentum, J, at fixed $M_{\rm b} = 2.9 M_\odot$.

quasi-toroid. If we combine Eqs. 9.9 and 9.12, then we obtain a condition which, if it is true, indicates that the stellar model must be quasitoroidal:

$$\bar{\rho}\left(\frac{\Omega_c}{\Omega_e}\right)^2 > \rho_c. \tag{9.13}$$

Note that this equation contains the same terms as the RHS terms of Eq. (17) of [6].

9.2.2 The fluid element at $\rho_{\rm b,max}$ is freely falling.

A second closely related fact is the following statement in the equatorial plane of an axisymmetric rotating stellar model:

The fluid element at the location of maximum density is freely falling.

This follows from the fact that at the location of maximum density $\nabla P = 0$, which means that centrifugal and gravitational forces must exactly balance. Technically, this fact is mathematically true for both quasitoroidal and spheroidal models; however, it only is physically interesting for the quasitoroidal case.

9.2.3 Maximum of the centrifugal support with differential rotation

Here we present a simple calculation which identifies (in the Newtonian limit) the location (as a fraction of equatorial radius) at which the centrifugal force is maximized. The calculation is of interest in providing an estimate of the amount of differential rotation necessary for the appearance of quasitoroidal configurations. Note that for a uniformly rotating configuration, there is *no* maximum in the centrifugal force; it simply increases without bound as one moves outward in the equatorial plane. However, as one 'dials up' the differential rotation (in our case in terms of $\tilde{A}$), at some point, we expect the maximum of the centrifugal force to be at some point inside the star. Here we answer the question *what is the critical value of $\tilde{A}$, $\tilde{A}_c$ such that for $\tilde{A} > \tilde{A}_c$ the maximum of the centrifugal force lies within the star?*

We write the Newtonian limit of the differential rotation law in its usual form,

$$\Omega = \frac{\Omega_c}{1 + \tilde{A}^2\varpi^2/r_e^2}, \tag{9.14}$$

with Ω_c the angular velocity at the center of the model, $\tilde{A}$ is the differential rotation parameter, ϖ the cylindrical radius (a coordinate), and r_e is the equatorial radius of the model (a constant). First, we rewrite this equation such that it is expressed in terms of the equatorial angular velocity,

Ω_e, instead of the central angular velocity:

$$\Omega = \Omega_e \frac{1+\tilde{A}^2}{1+\tilde{A}^2\varpi^2/r_e^2}. \tag{9.15}$$

Next, we define $\hat{\varpi} = \varpi/r_e$ as the dimensionless cylindrical radius and write the centrifugal force on a mass element in terms of the Eq. 9.15 for Ω:

$$F_{\rm cent} = \Omega_e^2 r_e \hat{\varpi} \left(\frac{1+\tilde{A}^2}{1+\tilde{A}^2\hat{\varpi}^2} \right)^2. \tag{9.16}$$

Now we maximize the above expression with respect to $\hat{\varpi}$. The derivative of $F_{\rm cent}$ with respect to $\hat{\varpi}$ is,

$$\frac{dF_{\rm cent}}{d\hat{\varpi}} = \Omega_e^2 r_e \left(1 - \frac{4\tilde{A}^2\hat{\varpi}^2}{1+\tilde{A}^2\hat{\varpi}^2} \right) \left(\frac{1+\tilde{A}^2}{1+\tilde{A}^2\hat{\varpi}^2} \right)^2, \tag{9.17}$$

which we set equal to zero and solve for $\hat{\varpi}_{\rm max}$ obtaining:

$$\hat{\varpi}_{\rm max} = \frac{1}{\sqrt{3}\tilde{A}}. \tag{9.18}$$

For $\hat{\varpi}_{\rm max} \leq 1$, the location of maximum centrifugal force is inside the star. Thus the critical value for $\tilde{A}$, is $\tilde{A}_c = 1/\sqrt{3} \simeq 0.577$. It is interesting to note that, as we 'dial up' $\tilde{A}$ in our equilibrium solver, we indeed begin observe the appearance of quasitoroidal equilibrium configurations starting at around $\tilde{A} > \tilde{A}_c$.

9.3 Changes in energy and density of a configuration

In the text we claim that a decrease in total energy of a stellar configuration with a fixed number of baryons necessarily results in the configuration becoming more compact; here we present our argument to support this claim. First, this idea is firmly rooted in intuition. If one removes thermal energy from a star, one would expect it to start to contract and hence increase its density (by density here we mean both average and central density). Note we are careful to phrase this explicitly as a loss of thermal energy and not as a 'cooling'; as stars have an inverse heat capacity, a loss of thermal energy is distinct from a decrease in temperature! Second, imagine a rotating star from which rotational energy and angular momentum are extracted. Here we would expect the ellipticity of the star to decrease, causing it to contract and increase its density.

In the Newtonian case, we may prove that the loss of thermal energy leads to an increase in density of the star. From [7] Eqs. 3.2.10 and 3.2.11, the virial theorem lets us write the total energy

of a polytropic stellar model in terms of its potential energy as:

$$E = -\frac{3\Gamma - 4}{5\Gamma - 6}\frac{GM^2}{R}, \tag{9.19}$$

where Γ is the adiabatic index in the polytropic equation of state $P = K\rho_{\rm b}^{\Gamma}$. Note that the energy of a stable star is always negative, and so a decrease in energy at fixed M must result in a decrease in R. With a fixed number of baryons, M is also fixed (in the Newtonian limit), and hence an energy loss must increase the density of the star.

9.4 Relation of average density to mass-shed centrifugal support

High temperatures affect the baryonic mass $M_{\rm b}$ of supramassive NSs (with $M_{\rm b} > M_{\rm b}^{\rm max,TOV}$ in two competing ways: (i) an increase in $M_{\rm b}$ due to thermal pressure, and (ii) a decrease in $M_{\rm b}$ due to a reduction in the mass-shedding angular velocity caused by an increase in radius. In order to estimate the net result of these two effects, one may consider the Newtonian mass-shedding condition. Along the equatorial plane, the Newtonian centrifugal force per unit mass is $\Omega^2\vec{\varpi}$. The baryonic mass of a spheroid with axis ratio $r_{\rm p/e}$ and average baryonic density $\bar{\rho}_{\rm b}$ is given by:

$$M_{\rm b} = \frac{4\pi}{3} r_e^2 r_p \bar{\rho}_{\rm b} = \frac{4\pi}{3} r_e^3 r_{\rm p/e} \bar{\rho}_{\rm b} \ . \tag{9.20}$$

We can then write the mass-shedding (Keplarian) $\Omega_{\rm K}^2$ as:

$$\Omega_{\rm K}^2 = \frac{GM_{\rm b}}{r_e^3} = \frac{4\pi}{3} G r_{p/e} \bar{\rho}_{\rm b} \ . \tag{9.21}$$

Thus, for uniform rotation at mass shedding, the rotational support $\Omega^2\varpi$ is directly proportional to the average baryonic density $\bar{\rho}_{\rm b}$. Consequently, one can understand the relative increase in maximum $M_{\rm b}$ from the maximum-mass TOV solution to supramassive NSs between NS models with different EOS and temperature prescriptions simply by measuring $\bar{\rho}_{\rm b}$ (see [6] for a similar idea). This measure correlates well with our findings. Centrally-hot models with cXp0 temperature prescriptions are slightly more extended than cold variants, thus have lower $\bar{\rho}_{\rm b}$, resulting in slightly lower maximum $M_{\rm b}$. On the other hand, the models with high-temperature plateaus at low densities (c30p10 and c30p5) have more extended low-density envelopes, but about the same thermal pressure support in the bulk of the NS as the c30p0 model (cf. Fig. 8.6). This results in a lower $\bar{\rho}_{\rm b}$, a lower mass shedding angular velocity and, hence, a lower $M_{\rm b}$ at their supramassive limit.

9.5 Newtonian estimate of angular momentum at coalescence

Here we use freshman physics to estimate the angular momentum of two equal mass neutron stars at coalescence. A special thanks goes out to Aaron Zimmerman, who sketched this out for me in about ~ 5 minutes. The calculation is that of two sphere each with the same mass, M, radius, R, and moment of inertia, I. The two spheres touch at a point; they rotate about this point at the Keplarian frequency, and we wish to calculate the angular momentum of the configuration. First, we may write the Keplarian frequency as:

$$\Omega_k = \sqrt{\frac{GM_{\rm total}}{a^3}} = \frac{1}{2}\sqrt{\frac{M}{R^3}}, \tag{9.22}$$

where we have set $G = 1$, $M_{\rm total} = 2M$ and the orbital separation a to $a = 2R$. Next, we calculate the moment of inertia of the total configuration. The parallel axis theorem lets us calculate the moment of inertia of a body rotating around an axis which is a perpendicular distance, $r_\perp$ from its center of mass, as $I_{r_\perp} = I_{\rm cm} + Mr_\perp^2$. This is precisely what we have for each neutron star with $r_\perp = R$, and thus the total moment of inertia is:

$$I_{\rm total} = 2I + 2MR^2, \tag{9.23}$$

where I sans-subscript is the moment of inertia of one of our neutron stars. The angular momentum estimate of the configuration is then just $\Omega_k I_{\rm total}$:

$$J^{\rm corot}_{\rm Newt} = \sqrt{\frac{M}{R^3}}\left(I + MR^2\right) = M^{3/2}R^{1/2}\left(1 + \frac{I}{MR^2}\right) = C^{-1/2}\left(1 + \frac{I}{MR^2}\right)M^2, \tag{9.24}$$

where in the final expression, we've substituted the compaction $C = M/R$ for the radius.

Above we assumed that the two neutron stars were approximately in rigid rotation about the center of mass; this is the corotating limit. If instead we assume the neutron stars are irrotational, then we must correct our expression. We can do this by subtracting the spin angular momentum, $I\Omega_k$, for each neutron star. This yields:

$$J^{\rm irrot}_{\rm Newt} = \sqrt{\frac{M}{R^3}}\left(MR^2\right) = M^{3/2}R^{1/2} = C^{-1/2}M^2. \tag{9.25}$$

Bibliography

[1] J. M. Bardeen. A Variational Principle for Rotating Stars in General Relativity. *Astrophys. J.*, 162:71, October 1970.

[2] J. L. Friedman, J. R. Ipser, and R. D. Sorkin. Turning-point method for axisymmetric stability of rotating relativistic stars. *Astrophys. J.*, 325:722–724, February 1988.

[3] J. L. Friedman and N. Stergioulas. *Rotating Relativistic Stars*. March 2013.

[4] J. O. Goussard, P. Haensel, and J. L. Zdunik. Rapid uniform rotation of protoneutron stars. *Astron. & Astrophys.*, 321:822–834, May 1997.

[5] B. K. Harrison, K. S. Thorne, M. Wakano, and J. A. Wheeler. *Gravitation Theory and Gravitational Collapse*. 1965.

[6] N. D. Lyford, T. W. Baumgarte, and S. L. Shapiro. Effects of Differential Rotation on the Maximum Mass of Neutron Stars. *Astrophys. J.*, 583:410, January 2003.

[7] S. L. Shapiro and S. A. Teukolsky. *Black holes, white dwarfs, and neutron stars: The physics of compact objects*. 1983.

[8] R. D. Sorkin. A Stability Criterion for Many Parameter Equilibrium Families. *Astrophys. J.*, 257:847, June 1982.

[9] N. Stergioulas and J. L. Friedman. Comparing models of rapidly rotating relativistic stars constructed by two numerical methods. *Astrophys. J.*, 444:306–311, May 1995.